Unsteady Jet Dynamics with Implications for Volcanic Plumes

by

Kirsten Chojnicki

A Dissertation Presented in Partial Fulfillment
of the Requirements for the Degree
Doctor of Philosophy

Approved November 2012 by the
Graduate Supervisory Committee:

Amanda Clarke, Chair
Jeremy Phillips
Stanley Williams
Ronald Adrian
Harindra Fernando

ARIZONA STATE UNIVERSITY

December 2012

ABSTRACT

Assessments for the threats posed by volcanic eruptions rely in large part on the accurate prediction of volcanic plume motion over time. That predictive capacity is currently hindered by a limited understanding of volcanic plume dynamics. While eruption rate is considered a dominant control on volcanic plume dynamics, the effects of variable eruption rates on plume rise and evolution are not well understood. To address this aspect of plume dynamics, I conducted an experimental investigation wherein I quantified the relationship between laboratory jet development and highly-variable discharge rates under conditions analogous to those which may prevail in unsteady, short-lived explosive eruptions. I created turbulent jets in the laboratory by releasing pressurized water into a tank of still water. I then measured the resultant jet growth over time using simple video images and particle image velocimetry (PIV). I investigated jet behavior over a range of jet Reynolds numbers which overlaps with estimates of Reynolds numbers for short-duration volcanic plumes. By analysis of the jet boundary and velocity field evolution, I discovered a direct relationship between changes in vent conditions and jet evolution. Jet behavior evolved through a sequence of three stages - jet-like, transitional, and puff-like - that correlate with three main injection phases - acceleration, deceleration and off. While the source was off, jets were characterized by relatively constant internal velocity distributions and flow propagation followed that of a classical puff. However, while the source was on, the flow properties - both in the flows themselves and in the induced ambient flow - changed abruptly with changes at the source. On the

basis of my findings for unsteady laboratory jets, I conclude that variable eruption rates with characteristic time scales close to eruption duration have first-order control over volcanic plume evolution. Prior to my study, the significance of this variation was largely uncharacterized as the volcanology community predominately uses steady eruption models for interpretation and prediction of activity. My results suggest that unsteady models are necessary to accurately interpret behavior and assess threats from unsteady, short-lived eruptions.

ACKNOWLEDGMENTS

With sincere gratitude, I thank my advisor and my committee for countless hours spent working through many aspects of this work. Todd Veach, an astrophysics graduate student specializing in instrumentation, designed and built the timing circuit that synchronized the camera, laser, and flowmeter. Stan Klonowski and Chris Skiba contributed significant efforts to the design and construction of the rest of the apparatus. Finally, I would like to thank my friends and family for their unwavering support and encouragement.

TABLE OF CONTENTS

Page

CHAPTER Page

CHAPTER Page

LIST OF TABLES

LIST OF FIGURES

Figure Page

PREFACE

Models of volcanic plumes are used to interpret observations of their behavior as well as to assess the potential impact of hazards associated with explosive eruptions. While most models currently assume that eruption rates remain constant over the duration of an eruption, observations of volcanic activity suggest that variable eruption rates may be common. Moreover, theoretical work suggests that variations in eruption rates may be dynamically significant, that is, plume behavior from variable-rate eruptions may significantly deviate from the behavior of plumes generated by constant-rate eruptions. For situations in which this deviation may be large, incorrect interpretations of volcanic plume behavior or grossly inaccurate assessments of volcanic plume hazards may result from the analysis of steady model predictions.

One situation in which this deviation may be large is for a class of eruptions which is characterized by short durations over which the eruption rate may strongly vary. The general effect, however, of variable eruption rates on volcanic plumes is not well understood. Consequently, whether or not volcanic plume behavior deviates substantially from the predictions of steady models when eruption rates vary is not well established for any class of eruptions. Unsteady eruption rates may be of first-order significance for short-duration eruptions, and, thus, the principal focus of this work is to understand the development of volcanic plumes from this particular class of eruptions. The findings from the investigation of this class may then illustrate the potential significance of unsteady eruption rates on the development of volcanic plumes in general.

I note here that my aim is to provide insight into a problem relevant to volcanology rather than provide a new understanding of a particular eruption. My purpose is to identify the essential features of volcanic plumes from this eruption class such that the controls on the dynamics in transient conditions may be clarified and the attributes of the class may serve to identify real situations in which eruption rate variations may be important. In other words, rather than providing a complicated theoretical result for the description of volcanic plumes from this eruption class, I suggest a general suite of observables and qualitative relationships which may be indicative of volcanic plume behavior from transient eruptions. The results may then be used to understand the general issues and questions unsteady eruption rates may raise for understanding and measuring volcanic activity.

I present the results from this investigation in the following manner. In Chapter 1, I begin with a discussion of volcanic plumes in order to emphasize the potentially distinct nature of volcanic plumes from transient eruptions with short durations. I then discuss the limitations of observations and current theoretical models for consideration of the effects from transient eruption rates, and therefore propose an experimental investigation to derive insight for this problem. While a number of experimental investigations provide background for this problem, as demonstrated by the discussion in Chapter 2, the conditions which may prevail in volcanic plumes from transient eruptions are beyond the range, scope and certainty of most of the problems of interest to these investigations and therefore the results of these previous investigations may not necessarily apply to the

volcanic situation. Consequently, I conducted the experimental investigation outlined in Chapter 3 to obtain results which may be more appropriate for understanding volcanic plume dynamics.

These results, in turn, are discussed in Chapters 4, 5 and 6; each focuses on a different aspect of the results and their potential application for understanding the volcanic system. In Chapter 7, I conclude that variable eruption rates may influence volcanic plume behavior to first order when the variations are strong and vary on the same time scale as eruption duration. Furthermore, the resultant behavior will likely be specific to the form of the time variation. This result is significant; it implies that hazards associated with volcanic plumes, such as plume collapses, may depend on precisely how the eruption rate varies in time; thus, current theoretical models which do not account for time varying eruption rates may not provide accurate hazard assessments for plumes from this eruption class. A new theoretical model for volcanic plumes which can account for time variations is therefore necessary to constrain the potential hazards associated with this class as well as for interpreting time-dependent plume observations.

Chapter 1

INTRODUCTION

1.1 Motivation

The rise behavior and transport capabilities of volcanic plumes may be severely impacted by unsteady generation conditions at the source [e.g., *Sparks et al*., 1997; *Scase* 2009]. Unsteady source conditions sometimes lead to greater momentum and energy losses than steady source conditions in otherwise equivalent flow configurations [e.g., *Johari and Paduano*, 1997; *Ruiz et al*., 2007]. As a result, the moving fluid experiences larger rates of energy and momentum dissipation and ultimately a decrease in the transport capacity of mass, momentum, and energy [e.g., *Musculus*, 2009]. A reduction such as this in the motion or transport capacity of volcanic plumes may suppress or enhance their potential for disaster. For example, a reduction in the transport capacity of a plume may limit the rise of the plume in the atmosphere [e.g., *Wilson and Sparks*, 1976; *Wilson et al.*, 1978] and thereby limit the interference of the plume with air traffic [e.g., *Mastin*, 2009], or decrease the area impacted by particulate dispersal [e.g., *Carey and Sparks*, 1986]. On the other hand, an increase in momentum loss during unsteady flow conditions may also culminate in a collapse of the volcanic plume under the force of gravity [e.g., *Sparks et al*., 1997], leading to gravity-driven currents (pyroclastic density currents), which are extremely dangerous for people living on and around volcanoes. It is imperative, therefore, to establish

whether, and the extent to which, unsteady generation conditions influence a volcanic plume, as well as to characterize the nature of the influence.

1.2 Unsteady Volcanic Plumes

Observations suggest that mass flux rates may vary in time during volcanic eruptions [e.g., *Druitt et al.*, 2002; *Clarke et al.*, 2002; *Iguchi et al.*, 2008; *Gottsman et al*., 2012]. For eruptions that generate volcanic plumes, time-varying mass flux rates may lead to unsteady dynamic conditions in the plume [e.g., *Sparks et al*., 1997]. These conditions most likely arise when the mass flux variations are on the order of $1/N$ where N is atmospheric buoyancy frequency. The value of N is typically ~ 0.01 seconds [e.g., *Sparks et al*., 1997] and thus variations in source conditions that occur over a duration less than 100 seconds *may* lead to unsteady conditions in the volcanic plume. However, the response of volcanic plumes to variable volume fluxes is not well understood [e.g., *Scase et al*., 2009; *Kitamura and Sumita*, 2011]. Without this understanding, the hazards associated with plumes from this class of eruption cannot be adequately assessed [e.g., *Mastin et al*., 2009]. Furthermore, most models of volcanic plumes now include an assumption that volume fluxes remain constant over the eruption duration [e.g., *Woods*, 1988; Suzuki et al., 2005; *Ogden et al*., 2008; *Kaminski et al*., 2011]. Yet these volcanic plume models are based on simple turbulent models of steady jets, which do not accurately predict experimental observations of unsteady jets [e.g., *Boree et al*. 1996; *Zhang and Johari*, 1996; *Querzoli*, 2010]. Thus, ignoring the dependence of turbulent dynamics on time-varying volume

fluxes may lead to inaccurate hazard predictions for volcanic plumes from time-varying eruption conditions. Volcanic plume rise, dilution, and collapse are all processes important to effectively evaluating volcanic plume hazards [e.g., *Sparks et al*., 1997; *Mastin et al*., 2009]. Therefore, understanding whether and to what extent variable volume fluxes influence these processes will enrich our understanding of the response of volcanic plumes to variable volume fluxes and will improve the analysis of hazards from plumes generated by time-varying eruption conditions.

Characterizing the response of a plume to unsteady generation conditions first requires an identification of the relationship between the unsteady source condition and the evolution of the plume. The relationship between source conditions and plume rise is also critical for developing accurate, as well as predictive, models of volcanic plumes [e.g., *Woods*, 1988; *Sparks et al*., 1997; *Mastin et al*., 1999]. While the relationship between steady source conditions and volcanic plume evolution has been reasonably well established for long-duration or sustained eruptions [e.g., *Morton et al.*, 1956; *Wilson et al.*, 1978; *Sparks et al.*, 1997], such a relationship has yet to be developed for volcanic plumes generated from unsteady source conditions during discrete volcanic eruptions that last a few tens of seconds [e.g., *Patrick et al*., 2007; *Scase*, 2009]. During discrete eruptions, the plume is fed by material discharged from the volcanic vent at rates that vary with time [*Druitt et al*., 2002; *Caplan-Auerbach et al.*, 2009; *Mori and Burton*, 2009; *Gottsman et al.*, 2011]. Once material stops discharging from the vent, the

eruption ends, but short-lived volcanic plumes continue to ascend for several minutes after the discharge stops. Volcanic plume behavior is readily observed with UV [e.g., *Yamamoto et al*., 2008; *Mori and Burton*, 2009; *Nadeau et al.*, 2011], visible [e.g., *Wilson and Self*, 1980; *Sparks and Wilson*, 1982; *Clarke et al*. 2002; *Formenti et al*., 2003; *Bluth and Rose* 2004; *Johnson et al.*, 2005*; Peterson et al*., 2012], and thermal [e.g., *Ripepe et al*., 1993; *Patrick et al*., 2007; *Sahetapy-Engel and Harris*, 2009] imaging techniques, as well as satellite [e.g., *Watson et al.*, 2004; *Peterson et al*., 2012] and radar measurements [e.g., *Hort and Seyfried*, 1998; *Schraff et al*., 2008; *Gouhier and Donnadieu*, 2008]. However, the source conditions at the volcanic vent are more difficult to observe and constrain in the field [e.g., *Johnson et al.*, 2005*; Iguchi et al*., 2008; *Nadeau et al.*, 2011; *Donne and Ripepe*, 2012]. Thus, the range of variability in discharge rate over time remains relatively uncertain.

Nevertheless, there is evidence that some short-duration eruptions emit plumes that evolve in two phases: a phase where the plume velocity decreases with time, followed by a phase where the velocity remains relatively constant in time. While the duration of the first phase is on the order of a tenth of a second, the duration of the second phase can be much longer and is on the order of seconds to tens of seconds [e.g., *Patrick et al*., 2007; *Mori and Burton*, 2009; *Donne and Ripepe*, 2012]. Without more specific information on the source conditions for these plumes, it is difficult to determine the character of unsteady conditions in nature, as well as to speculate on what their frequency distribution

may be. Furthermore, without such measurements, the diversity of generation conditions within an existing plume class is relatively uncertain. Therefore, the focus of this study is not on an existing class of volcanic plumes but on a theoretical class of short-duration, unsteady plumes that is defined, described, and analyzed here.

This work analyzes the dynamics of transient jet flow focusing on the role of unsteady force contributions. The analysis of turbulence in unsteady jets has both a theoretical interest, with regard to velocity profiles and turbulence characteristics, and a practical one, for improving models of volcanic plume motion. Volcanic plume models are needed to accurately and reliably forecast the location, movement, and stability of volcanic plumes, in order to assess and define potential hazards to aircraft and communities downwind [*Mastin et al*., 2009]. However, volcanic plume behavior is very complex, non-linear, and not well constrained; cumulatively, these factors limit the effective use of models for hazards management. Moreover, direct observations of explosive processes are difficult so indirect measurements are used instead to quantify and characterize fluid flow in volcanic systems [*Gilbert and Lane*, 2012]. However, this approach complicates the task of uniquely identifying source mechanisms for observed signals and limits the extent to which we can interpret them [e.g., *Gilbert and Lane*, 2012]. If we desire an improved management strategy for volcanic plume hazards, we must take a new approach.

Our current approach is to manipulate and analyze our understanding of the underlying plume dynamics to build conceptual models for classes of volcanic plumes [e.g., *Sparks and Wilson*, 1976; *Woods*, 1988; *Woods*, 1995; *Clarke et al*., 2002; *Bonnadonna and Phillips*, 2003; *Bonnadonna et al.*, 2005; *Ogden et al*., 2008]. For each class, a very general suite of observables and qualitative relationships is used to construct indicators of dynamics. These indicators are first-order controls on plume dynamics which can be studied using analytical models [e.g., *Sparks and Wilson*, 1976; *Kieffer*, 1982; *Carey and Sparks*, 1986; *Woods*, 1988; *Turcotte et al*., 1990; *Woods*, 1995; *Scase et al*., 2009]. Some of the complex relationships among variables are then investigated statistically with numerical models [e.g., *Valentine and Wohletz*, 1989; *Dobran et al.*, 1993; *Neri and Macedonio*, 1996; *Clarke et al*., 2002; *Suzuki et al*., 2005; *Ogden et al*., 2008] and systematically with experimental models [e.g., *Kieffer and Sturtevant*, 1984; *Kaminski et al*., 2005; *Clarke et al*., 2009; *Kitamura and Sumita*, 2011] to identify the extent to which they influence the evolution of the plume. At the outset, this methodology may appear robust; however, the break-down manifests in the current lack of compatibility among the relationships and variables which may be tested *across* techniques.

Incompatibility occurs for three main reasons: first, volcanic plumes are described with turbulent models that relate their generation conditions to their *internal* dynamics; second, volcanic plumes are typically opaque so only their *boundaries*, not their internal dynamics, are accessible for direct measurement;

and, finally, the generation conditions for which turbulent models are most robust are *steady* conditions, while the generation conditions for which volcanic plumes occur most frequently are *unsteady*. Consequently, the literature contains an increasing number of observations of unsteady plume boundaries to which, lacking a suitable unsteady model, steady or instantaneous models are applied for the purposes of analysis and interpretation [e.g, *Johnson et al.*, 2005; *Patrick et al*., 2007; *Terada and Ida*, 2007; *Yamamoto et al*., 2008; *Caplan-Auerbach et al*., 2009; *Peterson et al*., 2012]. Therefore, there is an immediate need for a model that can relate unsteady volcanic plume generation conditions to the evolution of internal dynamics and external observable boundaries.

1.3 Explosive Volcanic Eruptions

Volcanic plumes are generated during explosive volcanic eruptions. Volcanic eruptions occur when molten rock, or magma, reaches the surface of the Earth. As the magma rises to the surface, it experiences depressurization due to a decrease in the lithostatic pressure gradient. Magma depressurization results in the exsolution of gases that were once dissolved in the magma. If the magma viscosity is low or the system is permeable, then these gases may easily move through the magma and leak out into the atmosphere [e.g., *Sparks et al*., 1997]. In this case an eruption will generally result in an effusive and non-violent emission of lava flows or domes. If, however, the magma is impermeable and very viscous, then the gases may be trapped in the magma, and an eruption will result in an explosive expansion of a mixture of gas and magma fragments into the Earth's

atmosphere. This mixture may then form a volcanic plume [e.g., *Sparks et al*., 1997]. A range of plume styles is shown in Figure 1.1.

While this is a very simple description of volcanic eruptions, it serves to illustrate the critical role of gas expansion in the plume formation process. Explosive eruptions can then be further divided into classes based on the particular composition of the magma, style of explosion, behavior of the plume, and the types of deposits and hazards that may result. Three styles of explosive eruptions are briefly discussed here - Plinian, Strombolian and Vulcanian – to illustrate the features which distinguish different eruption types [e.g., *Sparks et al*., 1997].

Eruption classification schemes [*Walker*, 1973; *Newhall and Self* ,1982] are based on eruption size. On the large end of the explosive eruption spectrum are called Plinian- and sub-Plinian-style eruptions, which produce volcanic plumes that reach altitudes above 10 kilometers and last for tens of hours [*Newhall and Self*, 1982]. At the opposite end of the spectrum are Strombolian-style eruptions, which last for tens of seconds and may or may not generate plumes. If plumes are generated by Strombolian eruptions, they typically rise less than 5 km above the volcanic vent [*Newhall and Self*, 1982]. Strombolian-style eruptions are referred to as discrete explosions to distinguish them from the continuous ejection of magma during Plinian- and sub-Plinian-style eruptions. Vulcanian-style eruptions are also discrete explosions, but they may last from tens of seconds to tens of minutes and eject plumes to altitudes between 5 and 20 km

above sea level [*Newhall and Self*, 1982]. Thus, Vulcanian-style eruptions are classified between Plinian- and Strombolian-styles, in terms of magnitude.

As these systems were derived to classify eruption deposits as well as the events themselves, each class is associated with an approximate erupted volume expressed in units of dense rock equivalent (DRE) ejecta volume, which is calculated by taking the total mass erupted and assuming it has the density of the vesicle-free magma. While Plinian-style eruptions eject over 10^9 m^3 of material, Strombolian eruptions eject less than 10^7 m^3 [*Newhall and Self*, 1982]. Vulcanian-style eruptions erupt somewhere between 10^7 and 10^9 m^3 of material [*Newhall and Self*, 1982]. A modified classification system for explosive eruption magnitude, called the volcanic explosivity index (VEI), was proposed by *Newhall and Self* [1982]. The VEI ranks the magnitude of an eruption on a scale from 0 to 8. A VEI of 0 represents a non-explosive eruption and a VEI of 8 represents a cataclysmically explosive eruption with a stratospheric injection of a plume (height is greater than 25 km above sea level) [*Newhall and Self*, 1982]. According to this scale, Strombolian-style eruptions are VEI 1 to 2, Vulcanian-style eruptions are VEI 2 to 4, and Plinian-style eruptions are VEI 4 to 8 [*Newhall and Self*, 1982]. While this scale does not clarify the boundaries between these eruption classes, it does illustrate that there is variation within and between classes and is included here because it is commonly used in volcanology when describing the behavior of an eruption or a volcanic plume.

Considering that the behavior exhibited by each of these classes is in theory distinct, different eruption mechanisms are thought to underlie them. For example, bursting of large gas slugs at the volcanic vent may result in Strombolian-style eruptions [e.g., *Sparks et al*., 1997]. Vulcanian-style eruptions, in contrast, may result from the disruption of a seal or cap near the volcanic vent which results in the rapid decompression of a gas-rich column of magma contained within the shallow conduit [e.g., *Sparks et al*., 1997]. Plinian-style eruptions may result from a significant change in the magma system at depth, such as an injection of hot mafic magma into a cooling magma reservoir, which induces a continuous rise and vesiculation of magma from the reservoir to the surface [e.g., *Sparks et al*., 1997]. In practice, however, the boundaries of these classes are uncertain and eruption behavior varies greatly such that it may not fit neatly into one of these eruption classes. For example, under certain situations mafic magmas that typically erupt as Strombolian-style eruptions may erupt in violent Vulcanian- [e.g., *Calvari et al*., 2012] or Plinian-style eruptions [e.g., *Williams*, 1983] and generate large ash plumes.

1.4 Volcanic plumes

According to the standard model for steady volcanic plumes [e.g., *Sparks and Wilson*, 1976; *Carey and Sparks*, 1986; *Woods*, 1988], the structure of steady volcanic plumes can be divided into three regions on the basis of the factors that govern their dynamics. At the vent, the volcanic plume motion may be dominated by the force of momentum derived from the expansion of gas that was formerly

contained in the magma [e.g., *Sparks and Wilson*, 1976; *Woods*, 1988]. As the plume ascends, it entrains atmospheric air through turbulent eddies at the edges of the plume. Turbulent eddies internal to the plume then transport and mix the ambient air with the material in the plume [e.g., *Sparks and Wilson*, 1976; *Woods*, 1988]. The plume contains gas and hot tephra particles (quenched magma) that transfer heat to the cooler atmospheric air during the mixing process. The process of turbulent entrainment and mixing results in the dilution of the initial momentum forces, a decrease in the bulk density of the plume, and the production of momentum due to buoyancy forces [e.g., *Sparks and Wilson*, 1976; *Carey and Sparks*, 1986; *Woods*, 1988]. If the momentum generated by the buoyancy forces is sufficient then buoyancy forces dominate the plume dynamics and the plume continues to ascend [e.g., *Sparks and Wilson*, 1976]. Otherwise the plume collapses under the force of gravity once the initial momentum is diluted below a threshold necessary to support the rise [e.g., *Sparks et al*., 1997].

Dilution of the initial momentum, including the entrainment process, therefore, may play a role in the rise and collapse of volcanic plumes. Nevertheless, this contribution has been neglected in some volcanic plume models on the basis that, for large volcanic plumes (rise >20 km), buoyancy-driven dynamics may dominate over 90% of the motion [*Sparks and Wilson*, 1976]. It is similarly neglected for very small volcanic plumes (rise ~ 1 km), which likely have very small amounts of initial momentum [e.g., *Sparks et al*., 1997]. It is included in some volcanic plume models [e.g., *Woods*, 1988; *Sparks et al*., 1997;

Scase 2009] to account for the initial decrease in velocity that occurs from dissipation of the eruption energy. These results suggest that the overall significance of the momentum-driven rise regime may be non-trivial even for large volcanic plumes [e.g., *Scase* 2009]. Moreover, if the source momentum flux strongly varies, then the plume may experience large and sudden variations in the mean rate of flow, and momentum dilution may have a nontrivial control on dynamics. In this situation, the volcanic plume is unsteady in the mean as well as turbulent. Processes like turbulent entrainment and mixing directly depend on the mean flow rate and may therefore vary in response to flow rate changes. Turbulent entrainment and mixing are important for achieving buoyant rise conditions; thus, collapse conditions may also change in response to flow rate changes. As the flow adjusts to the changes, flow structure may change, as may the ways mass, momentum, and energy are transported through the flow. Thus, understanding the controls on momentum dilution when volume flux varies may provide insight into the potential consequences of variable volume flux on volcanic plumes and their overall evolution.

In particular, understanding the length and time-scales over which momentum dominates volcanic plumes and the processes that contribute to entrainment and mixing during that dynamic phase, is critical for understanding the threshold conditions that separate buoyant rise from collapse conditions [e.g., *Valentine et al.*, 1991; *Kaminski et al.*, 2005; *Suzuki et al.*, 2005]. Some insight into the length and time-scales over which momentum dominates can be provided

by field-based studies of volcanic plumes. In these studies, a variety of optical-based instrumentation is used to investigate the behavior of volcanic plumes [e.g., *Johnson*, 2005; *Patrick*, 2007; *Yamamoto et al*., 2008; *Mori and Burton*, 2009]. From these studies, we know that volcanic plumes vary in shape, size, temperature, velocity, final rise heights, complexity, and their evolution in time. Photographs of short-lived plumes are shown in Figure 1.2 to demonstrate the wide variety of plumes produced in nature. These techniques typically focus on the change in the external boundaries of the plume. The motion of the boundaries reflects the net effect of a number of external and internal processes that may vary as the mean flow varies. Because of this proposed complexity, it may be difficult to detect, derive, or quantify changes in the flow rate using observable changes in the external boundaries of the flow. This difficulty complicates the task of understanding the response of turbulent flows to transient source conditions for situations where the internal structure of a flow is not accessible, as is the case with volcanic plumes. While techniques such as Doppler radar can be used to investigate some aspects of the internal behavior of volcanic plumes [e.g., *Scharff et al*., 2008; *Gouhier and Donnadieu* (2008)], these techniques are limited to relatively dilute plumes. Studies use other bands of the electromagnetic spectrum (i.e., infrasound) to investigate other aspects of plume motion, including the energy imparted to the atmosphere during eruption initiation [e.g., *Johnson et al*., 2005; *Caplan-Auerbach et al*., 2010] and the turbulence characteristics of the plumes [e.g., *Matoza et al*., 2009].

All of these studies address aspects of time-varying plume motion: however, a simple dynamic model that can describe the evolution of time-varying vent flux in terms of easily observable parameters such as plume front propagations and radial expansion does not yet exist. Moreover, images of volcanic plumes from short-duration eruptions are becoming increasingly common in volcanology, in part because they are more common in general than steady, continuous, long-lived eruptions. As a result, additional motivation for a study of transient source effects on near-vent volcanic plume dynamics comes from a desire to effectively interpret field observations of transient eruptions.

Simple analytical and empirical models of turbulent plumes, thermals, and puffs are currently used to interpret volcanic plume observations. Turbulent plumes are generated from a continuous release of buoyancy while thermals are generated from an instantaneous release of buoyancy [*Morton et al*., 1956]. Puffs are instantaneous releases of momentum [*Richards*, 1965]. A generalized analytical model derived by *Morton et al*. [1956] for continuous and instantaneous sources of buoyancy rising through a stratified atmosphere is most commonly used. According to this model, the rise of continuous sources is dependent on the flux of material at the vent, whereas the rise of an instantaneous source is dependent on the total amount of material released. They also have a different dependence on time: continuous sources rise at a rate proportional to the square root of time, while instantaneous sources rise at a rate proportional to the fourth root of time. This model has been modified in the form of variations in the

empirical constants [e.g., *Sparks et al*., 1997] to account for atmospheric conditions common for volcanic plumes. In general, empirical models are in good agreement with observations of some well-documented volcanic plumes [e.g., *Wilson et al*., 1978; *Sparks et al*., 1997; *Mastin et al*., 2009].

However, some eruptions deviate from this model for reasons that are not distinguishable within the simple structure of the model [*Mastin et al*., 2009], such as Vulcanian-style eruptions [e.g., *Caplan-Auerbach et al.*, 2010], which cannot be easily classified as steady and continuous or instantaneous. It is important here to note that volcanic plumes are classified by eruption type or magnitude. In other words, Plinian-style plumes are plumes generated from Plinian-style eruptions. Thus it is assumed that all plumes generated by Plinian-style eruptions have the same governing dynamics. This classification system poses problems for short-lived plumes characterized by time-varying source conditions. Plumes from these eruptions are diverse, suggesting that plume behavior arises from specific rather than universal governing dynamics. A new classification system may therefore be required for short-lived plumes.

One alternative to simple analytical and empirical models, would be a numerical approach that accounts for transient volume fluxes [e.g., *Clarke et al*., 2002], but such models have been applied only to single, well-characterized eruptions at individual volcanoes. Nevertheless, these results show that large changes in vent and plume conditions may occur on very short time scales in agreement with other observations of similar eruptions [*Gottsman et al*., 2012].

This result suggests that strong fluctuations in the volume flux may be possible or even typical for many eruptions.

In contrast, a more general model developed recently by *Scase* [2009] extends existing theoretical volcanic plume models [*Woods*, 1988] to account for time-varying volume flux. Though this model relies on important assumptions that are most appropriate for steady turbulent flows, in particular, Taylor's turbulent entrainment hypothesis [*Morton et al.*, 1956], the *Scase* [2009] approach clearly demonstrates that time-varying volume flux may produce plume behavior that is distinct from eruptions with steady and long-lived source conditions. Along the same lines, experimental work by *Kieffer and Sturtevant* [1984] and *Kitamura and Sumita* [2011] indicate that volume flux which are suddenly initiated and then remain constant result in turbulent jets where the fluid at the front of the flow is affected by the transient condition, but the fluid behind the front is essentially steady. In contrast, the source condition in this study remains unsteady after it is suddenly initiated. While the source conditions investigated by *Kieffer and Sturtevant* [1984] and *Kitamura and Sumita* [2011] vary from the source conditions considered here, their results are valuable for understanding evolution when the flow rate is quasi-steady.

Additional studies using numerical approaches have demonstrated that significant variations in the evolution process can arise even when the momentum flux is constant if the jet is overpressured [e.g., *Valentine*, 1988; *Odgen et al*., 2008], the vent geometry changes [e.g., *Odgen et al*., 2011], the atmospheric

conditions vary [e.g., *Tupper et al*., 2009], or the plume partially collapses [e.g., *Valentine et al*., 1991; *Kaminski et al*., 2011]. Thus, it may be difficult to distinguish the variations in volcanic plume behavior caused by variable volume fluxes from those caused by a variety of other variables, such as atmospheric changes, that could simultaneously enter the problem.

In response to the above discussion, work presented here aims to investigate time-dependence in volcanic eruptions by considering the conditions in which Vulcanian-plumes are generated. This type of eruption is expected to produce a strongly time-dependent, momentum-driven jet phase that may not be accurately described by a volcanic plume model based on buoyancy-driven turbulence alone and underlain by assumptions of constant momentum flux. In fact, observations of transient Vulcanian eruptions suggest an increase in volume flux after eruption initiation (~10-30 s) that peaks and then declines to negligible values on the order of tens to hundreds of seconds later [e.g., *Druitt et al*. 2002; *Iguchi et al*., 2008; *Clarke et al*. 2002; *Scase*, 2009]. These conditions may also exist for Strombolian-style eruptions [e.g., *Donne and Ripepe,* 2012, *Mori and Burton*, 2009].

I therefore suggest the existence of a class of eruptions characterized by durations which are short and mass flux rates that may strongly vary. I define a short duration as less than 1/N or ~ 100 seconds. While limitations in our ability to carry out measurements of momentum flux during eruptions also limits a quantitative definition of ‘strong’, I offer a conceptual definition of ‘strong’ as a

condition characterized by large accelerations. The purpose of this study is to understand the potential consequences of the time-varying flux on plumes that may be generated from this eruption class. Specifically, my aim is to learn whether the controls on the motion of the plume are influenced by time-varying source conditions and if they differ from the controls that dominate plume motion when the source conditions are steady.

To investigate the effects of variable driving dynamics on turbulent motion, I considered the simplified problem of a jet resulting from time-varying momentum flux. Jets are relevant to volcanic plumes, since they are used as analog models [e.g., *Sparks and Wilson*, 1976; *Woods*, 1988; *Sparks et al*., 1997; *Kaminski et al*., 2005; *Ogden et al*., 2008], and jets can be used to study the isolated effect of time-variation on turbulent motion. This effect must be examined by conducting laboratory experiments because turbulent flows do not respond in a universal manner to unsteady driving conditions [e.g., *Bernard and Wallace*, 2002]. Moreover, this effect cannot be studied in nature, as the source conditions for explosive eruptions are difficult to measure directly [*Sparks et al*., 1997]. Time can be isolated in jets because, according to steady jet theory [*Fischer et al*., 1979], when there are no external forces acting on a jet, the motion of the jet is a function of two factors: the initial flux of momentum at the source, and the rate at which it is diluted by the turbulent mixing and entrainment process [*Fischer et al*., 1979]. Thus, in theory, if both the flux of momentum and the motion of the jet are accurately measured, the turbulent mixing and entrainment

process can be investigated [e.g., *Fischer et al*., 1979; *Papanicolaou, and List*, 1988; *Johari and Paduano*, 1997; *Mi et al*., 2007]. This process depends on the mean flow rate of the jet and may vary if the flow rate varies [*Fischer et al*., 1979; *Johari and Paduano*, 1997; *Breidenthal*, 2008]. Consequently, the motion of a jet arising from unsteady source conditions may differ from the motion that arises in steady conditions [e.g., *Boree et al.*, 1996; *Johari and Paduano*, 1997; *Breidenthal*, 2008; *Ruiz et al*., 2007; *Musculus*, 2009]. To investigate jet motion from unsteady sources, I conducted a series of analogue lab experiments to examine the behavior of turbulent jet rise resulting from time-varying injections of momentum into a still ambient fluid. I specifically considered an injection with a Gaussian-like time history that may be similar to volcanic eruptions. This source time-history has not been examined previously for experimental conditions analogous to volcanic plumes. The results I present here, therefore, contribute to narrowing this knowledge gap.

1.5 Overview

The work I present considers the behavior common to a theoretical class of volcanic plumes which I define to be those that are generated at a variable rate during short-lived explosive eruption events and are driven by inertia. Both the external and internal dynamics of this flow class are considered here through the use of laboratory experiments. The purpose of the study is, first, to facilitate the understanding of whether and to what extent variable source conditions impact short-duration volcanic plume evolution, and, second, to describe the dynamics

and evolution of analogous laboratory flows which may help identify and understand volcanic plumes that belong to this theoretical class of flows.

In the laboratory, I specifically examined the role that time-dependent discharge rates play in the development of turbulent jets generated under conditions analogous to those that may prevail in discrete volcanic eruptions. I generated these jets by injecting pressurized water into a tank of still water. Injections were Gaussian-like in time with durations shorter than jet rise times. Jet behavior was tested over a range of conditions corresponding to an order of magnitude change in the source Reynolds number (10^3-10^5), a parameter that characterizes the relative effects of inertia and viscous forces in controlling the motion of the jet. These Reynolds numbers correspond to those expected for smaller volcanic plumes, providing the range of applicability for the results of this study. The evolution of the flow boundaries and the internal flow fields were investigated using the experimental techniques best suited to each study, which are flow visualization and particle image velocimetry, respectively. I discuss these methods in more detail in Chapter 3.

The results of the jet boundary evolution are discussed in Chapter 4. These jets evolved in three main phases: an injection phase lasting the duration of the source, a transition phase immediately following the source termination, and a final phase during which the source was off. The injection phase was further subdivided into two distinct sub-phases, acceleration and deceleration. Scaling of the results indicates that individual characteristic velocities dominate each of the

acceleration, deceleration, and transition phases of the short-lived unsteady jet development. However, the final phase of development tended toward the behavior of a finite-volume release of momentum, or a puff. As such, it was determined that time-dependent source conditions had dominant first-order effects on flow evolution during the injection and transition phases, but had little control over dynamics during the final phase where the integrated total volume injected played a dominant role.

In addition to variable characteristic velocities, each flow phase had a unique velocity distribution, as discussed in Chapter 5. During the accelerating phase, the flow field reflected expansion of the source fluid into the ambient fluid and also indicated significant movement of the ambient fluid in front of the source fluid. During the decelerating phase, the flow field was dominated by two large-scale vortices at the front of the flow with multiple smaller scale vortices near the vent. The motion of the front of the large-scale vortices was consistent with expansion, but the motion at their base indicated significant movement of ambient fluid into the flow (entrainment) at that location. Motion of ambient fluid into the flow was also observed for the smaller scale trailing vortices, although at much smaller scales. This flow pattern indicates that two types of ambient fluid entrainment operated during this phase: large-scale entrainment (engulfment) occurred in the largest eddies, and small-scale entrainment (nibbling) occurred in the smaller eddies. In eddies of both sizes, entrainment occurred on the side of the eddy closest to the source. Once the source was off, the flow was dominated by a

large number of small-scale vortices. Evidence for small-scale diffusive entrainment was visible in eddies at the flow boundaries.

The addition of a buoyancy force does not appear to modify unsteady jet velocities significantly in the near-source region for the flow conditions observed here, as described in Chapter 6. This is most likely due to the fact that the momentum generated by the buoyancy force is small compared to the momentum imparted to the jet during the release. Thus, if buoyancy is acting on the velocity field, the effects are not first-order. In contrast, both the buoyant jet morphology and concentration patterns were different from the non-buoyant jets. This result suggests that mixing in the unsteady jets is enhanced by the presence of positive buoyancy. However, this mixing does not significantly influence the velocity field. The flow front velocities and internal velocity distributions evolved in a similar way to the evolution pattern observed for non-buoyant unsteady jets. That is, when plotted together, the height time series of the unsteady buoyant jets are inseparable from the unsteady non-buoyant jets; when plotted together, the near-source velocity fields for both the non-buoyant and buoyant unsteady jets are inseparable. Thus, the influence of buoyancy on unsteady jets remains unresolved and should be the subject of future work, perhaps focusing on stronger initial buoyancy contrasts or regions farther from source where buoyancy may play a larger role.

As summarized in Chapter 7, the flow fields indicate the following sequence of events in the evolution of unsteady turbulent jets: 1) Initially, the high

pressure of the source fluid causes it to expand vertically and radially into the ambient without entraining much ambient fluid. 2) Once the source volume flux starts to wane, the flow becomes unstable and begins breaking up into eddies of two main sizes: large-scale at the flow front and small-scale nearer the source. During this waning phase, the flow simultaneously entrains a significant amount of ambient fluid though two different modes of entrainment associated with the two eddy sizes: large-scale eddies engulf; small-scale eddies nibble. 3) After the source ends, the flow becomes more unstable and begins to break into a large number of small eddies, then dissipates. The sequence of events indicated by the internal velocity fields is supported by the evolution of the flow front where the height changes rapidly at the initiation of the flow and then continues to change less rapidly as the momentum flux decreases and eventually stops. Once the source ends, the height evolves constantly in time according to theory for an instantaneous release of fluid or a puff. Scaling arguments indicate that height initially depends on the momentum injection rate in the acceleration phase, then on the cumulative momentum of the injection during the deceleration phase, and finally on the total momentum injected once the source is off.

There are many implications of this work for the volcanic system that are discussed in Chapter 7. Most importantly, however, there are at least two phases of development for plumes with source durations shorter than their rise times. In the first phase, the flow evolution will depend directly on conditions at the source and the front of the flow will evolve variably in time. During the second phase

(source off), the time-dependence of the source has no control on the dynamics, and the flow will evolve dynamically as if it were driven by an instantaneous source. Short-duration plumes, therefore, record time-dependent source conditions only in the initial phases of eruptions. Consequently, field studies intending to relate short-duration volcanic plume evolution to source conditions should capture plume motion from the eruption initiation; in other words, observations must be continuous to ensure the initiation is captured. Furthermore, observations for both the vent and plume parameters must be made simultaneously in order to correlate changes in the plume with changes at the source. Another implication of the short duration of source dominance is that geophysical observations may not be good indicators of the magnitude or the final rise height of a short-lived plume. If source momentum is the only dominant control on plume dynamics, the final rise height will depend on the total amount of momentum injected into the plume. Thus, the injected momentum must be quantified before total rise heights can be estimated. This point is significant for those interested in forecasting eruption hazards from geophysical observations. The model presented here may provide a means to calculate that parameter once the laboratory results are scaled to the natural system by comparison with an appropriate field data set. This data set needs to simultaneously constrain vent and plume behavior in a calm ambient environment.

Figure 1.1. Volcanic plumes range from (a) isolated spheres of material rising < 1 kilometer above sea level at Santiaguito Volcano, Guatemala (from *Yamamoto et al.*, 2008); (b) cylinders of material rising < 5 kilometer above sea level at Santiaguito Volcano, Guatemala (photo by author); (c) large cylinders of material rising > 5 kilometers above sea level; and (d) conical columns of material rising > 25 km at Mount St. Helens, U.S.A. (USGS).

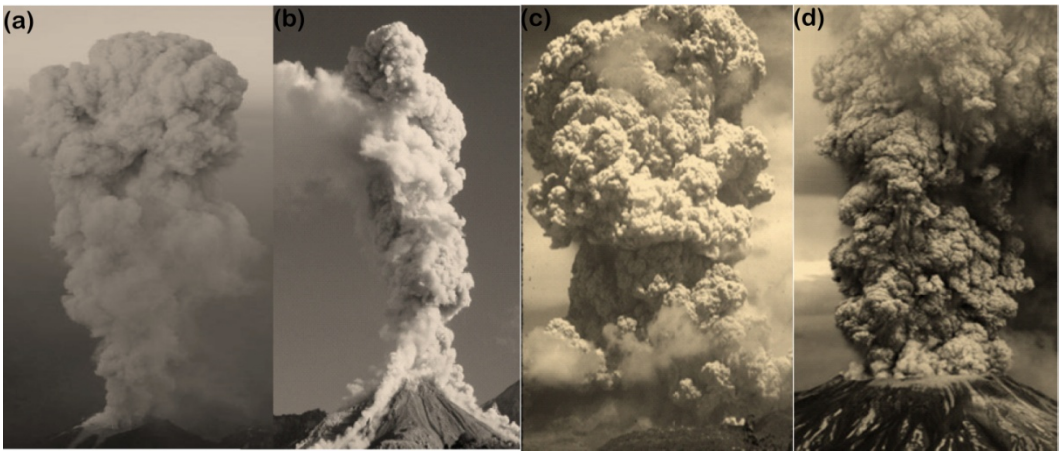

Figure 1.2. Variation in short-lived volcanic plumes. From left to right: Santiaguito Volcano, Guatemala (photo by author); Stromboli Volcano, Italy [*Patrick et al*., 2007); Semeru Volcano, Indonesia [*Nishimura et al.*, 2012]; Santiaguito Volcano, Guatemala [*Schraff et al*., 2008] ; Fuego Volcano, Guatemala [*Lyons et al.*, 2009]; Soufriere Hills Volcano, Montserrat [*Clarke et al*., 2002].

Chapter 2

BACKGROUND

2.1 Turbulence

I begin with a brief overview of turbulent flow. Turbulence may be defined as a condition of a flowing fluid in which the fluid elements have velocities that fluctuate continuously and thereby transport mass, momentum and energy by their continuous movements [*Taylor*, 1915]. These fluctuations lead to variations in velocity of neighboring fluid elements, and since the fluid behaves as a continuum (there can be no gap in the fluid), the fluid elements must respond to these velocity variations by rotating around one another [*Bernard and Wallace*, 2002]. Rotating fluid elements are called vortices or eddies and lead to small regions of fluid moving together in a way that may be different from the movement of the flowing fluid as a whole [*Bernard and Wallace*, 2002]. Eddies distribute mass, momentum, and energy from one part of a turbulent flow to another and dissipate momentum and energy as they rotate [*Bernard and Wallace*, 2002]. Thus, they are the mechanism by which the velocity distributions within the flowing fluid are established and modified.

Eddies are typically described by their strength, defined as the rate at which they rotate, and their size; both are indicators for the transport capacity of the eddy [*Bernard and Wallace*, 2002]. Eddy sizes in any given flowing fluid range from the molecular scale to the largest length scales of the flow, which are usually set by the conditions at the edges of the flow where the flowing fluid may

be bound by a physical barrier, as in the case of pipe walls, or one established by changes in fluid properties, such as the surface between ocean water and atmospheric air [*Fischer et al*., 1979]. Each configuration of flowing fluid has a span in eddy sizes that are specific to that configuration, and a distribution between the smallest and largest eddies that is also specific to that configuration [*Bernard and Wallace*, 2002]. Thus, experiments are necessary to investigate the behavior of turbulent flows in specific configurations of interest.

Typically, flows with similar configurations generate similar behaviors. Thus, turbulent flows within a particular class are assumed to behave similarly enough that mathematical tools may be developed to describe the behaviors common to all flows in that class [*Fischer*, 1979]. For example, jets are a class of turbulent flows which distribute mass, momentum and energy by turbulent motions. These motions are generated by momentum forces associated with the transport of the jet fluid from a source environment to a second environment of ambient fluid [*Fischer*, 1979]. Model formulations within this flow class are typically derived under the assumption that the mean flow is steady; that is, the motion of the fluid is considered over a sufficiently long time interval during which the variations in velocity associated with turbulent motions tend to average out [*Fischer*, 1979]. The magnitude of the fluctuations tends to remain within a relatively narrow range such that a mean velocity can be determined when the instantaneous values of velocity are averaged over the sufficiently long time interval. In this situation, an instantaneous measurement of flow velocity can then

be thought of as containing two separate components: a contribution from the mean, and a contribution from a fluctuation about that mean [*Fischer et al*., 1979]. This process of dividing the instantaneous velocity into a mean and fluctuating component is called Reynolds decomposition [*Fischer et al*., 1979]. The mean value is determined by averaging all the instantaneous velocity measurements taken within an interval of time over that interval; the fluctuations about that mean are then derived from the difference between the velocity at any instant and the mean value over the interval [*Fischer et al*., 1979]. When the motion of the flow behaves in such a way that this conceptualization does a reasonable job of capturing the overall behavior of the fluid, the relationships between the processes that drive and resist the fluid motion can be related through their modification of the mean flow behavior.

In some cases, predictions of the mean flow behavior are sufficient to address fluid problems. For example, if there is a question about the average discharge rate of a river, perhaps for consideration of whether the river can handle thermal efflux from a proposed power plant, then an estimate of the mean behavior would provide the relevant information on which to base the evaluation [*Fischer*, 1979]. However, other situations require more information, such as the consideration of a toxin moving within the river. In this case, the variations about the mean could lead to lethal concentrations of the toxin in certain places at certain times which might not be predicted by considering the motion of the mean alone, as the mean flow could remain below lethal concentrations at all times

[*Fischer*, 1979]. In short, the level of complexity required to model a turbulent flow depends on the problem that the calculations will be used to address [*Fischer*, 1979].

2.2 Turbulence Models

The Navier-Stokes equations govern the motion of turbulent fluids in three spatial dimensions and over time [*Fischer*, 1979]. To find solutions to these equations that may appropriately describe the motion of fluid in a problem of interest, the problem of interest must be simplified by making assumptions about factors that contribute most to the motion [*Fischer*, 1979]. These assumptions then lead to approximations about which terms in the governing equations to neglect. This process may allow the system of partial differential equations to be simplified to a system of ordinary differential equations; finding solutions to latter equations is relatively easier [*Fischer*, 1979]. Ordinary differential equations involve the solution of one function or set of functions for one variable, but partial differential equations involve the solution of two or more variables, adding complexity to the solution process. Common assumptions used to simplify dynamic problems relate to how quickly flow properties vary over time and how large the variations are in space. If flow properties vary slowly in time, then a steady assumption is made wherein derivatives with respect to time are neglected. Similarly, if flow properties vary significantly in the direction of flow but minimally in the other two spatial dimensions, then the properties and variations

in those directions are often neglected in a one-dimensional assumption [*Fischer*, 1979]. These assumptions are discussed further below.

2.2.1 Time

Equations which describe the motion of fluids relate the relative magnitudes of all the processes contributing to the motion such that their net effect on fluid motion can be estimated [*Fischer*, 1979]. For steady flows, these equations are often derived based on the assumption that the forces driving and resisting the flow are balanced, and therefore there are no net accelerations of the fluid [*Fischer*, 1979]. When the forces are balanced, forces contributing to the motion that are difficult to quantify can be calculated using theory, if the theory relates the unknown forces to forces that can be quantified more easily [*Fischer*, 1979]. For example, a jet working against the force of gravity must supply enough thrust to the fluid to overcome the net force of gravity and other forces that resist the fluid motion in order to propel the fluid to a certain height. If the thrust is constant and continuous and can be measured along with the height, then the total resistance acting against the mean motion of the fluid can be calculated. However, if the thrust varies or is intermittent, then the flow may have a mean flow that varies in time in addition to being turbulent. This state complicates the analysis of the flow, because the theoretical models for turbulent flows relate the forces driving a flow to its time-averaged mean motion. For flows with unsteady means, flow properties may vary greatly in space and over time, and thus predictions of

the time-averaged behavior may not adequately represent the physical state of the flow at any time [*Bernard and Wallace*, 2002].

2.2.2 Space

Turbulent models are carried out with one-, two- and three-dimensional models. One-dimensional models use the one-dimensional turbulent transport equation where only variations in the flow velocity with distance from source and along the direction of flow are considered [*Fischer et al*., 1979]. The value of the velocity at a particular distance represents the average value of the velocity over the cross-section at that distance. Solutions of the one-dimensional transport equations may be accurate when cross-sectional mixing due to turbulent motions occurs relatively quickly and equally in all directions. Thus, most one-dimensional models assume that mixing occurs instantaneously over the entire cross-section [*Fischer et al.*, 1979]. In reality, mixing over a cross-section requires a finite amount of time over which the degree of mixing may be spatially variable. If the mixing timescale is much less than the timescale of the transport process then the assumption of instantaneous mixing may still result in a reasonable computation of the flow behavior.

In one-dimensional models, the net result of all the mixing processes that occur in the turbulent flow are expressed as coefficients of turbulent diffusion in the transport equation. These coefficients, or eddy diffusivities, are considered constants for steady flow conditions, but the processes they describe may vary in space and time in unsteady flow conditions [*Fischer et al.*, 1979]. Thus, steady

one-dimensional models are based on time and space averages of the velocity field and may not be reasonable for use with unsteady flows in which large spatial gradients in the velocity field may arise and change significantly over time. Quasi-steady flow conditions may also be considered in one-dimensional flow models where velocity changes occur in time; however, the spatial averages are still maintained, and thus only the variation in the vertical coordinate is considered [*Fischer et al.*, 1979]. Consequently, quasi-steady one-dimensional models may not accurately represent the changes in the velocity field if the evolution depends on the spatial variations in the velocity field that are not considered explicitly in one-dimensional models.

The analysis carried out by one-dimensional models with steady or quasi-steady formulas tends to accurately predict the general trends in Plinian volcanic plume behavior [e.g., *Sparks and Wilson*., 1976; *Woods*, 1988; *Carazzo et al.*, 2005]. One-dimensional models tend to overestimate plume motion because they consider only the variation of the vertical component of velocity in the flow direction. Thus, any processes that contribute to variations over the cross-section are ignored [*Fischer et al.*, 1979]. If these processes result in a damping of the motion by friction forces, then neglecting them will result in an overestimate of the motion. Two-dimensional models include the potential effects of such processes and account for variation of the vertical velocity over the cross-section in addition to the variation in the direction of flow. However, two-dimensional models often require more information. In particular, they require information

about how the variation in the vertical component of velocity along the direction of flow relates to the variation in the radial component of velocity along the cross section of the flow at various distances from the source. These distributions are related by the action of turbulence, and though there is no model which can exactly describe this action in detail, turbulence models have been developed to account for the general effects and thereby relate the vertical motion to the radial motion through reasoned arguments [*Fischer et al.*, 1979].

Taylor's entrainment hypothesis is most common for turbulent jets and plumes [e.g., *Carey and Sparks*, 1986; *Woods*, 1988; *Carazzo et al*., 2005; *Scase*, 2009]. According to Taylor's hypothesis, as plumes travel, they entrain ambient fluid with low momentum relative to the plume fluid. Thus, momentum must be expended by the flow to increase the momentum of the ambient fluid to that of the jet fluid [*Morton et al*., 1956]. Ambient fluid is entrained by the action of vortices at the edge of the plume that derive their rate of motion from the higher momentum fluid near the center of the plume. Thus, there should be a relationship between the velocity of the fluid at the center of the flow and the velocity at which ambient fluid is brought into the plume [*Morton et al*., 1956]. For steady flow conditions, it is assumed that the rate of advection of plume properties in the vertical direction is balanced by the rate at which they are diffused along the radial direction [*Morton et al*., 1956]. Thus, the vertical component of velocity at the center of the flow should be directly proportional to the radial component of velocity at the flow boundary, the radial velocity at which ambient fluid is brought

into the plume [*Morton et al*., 1956]. Therefore, Taylor proposed that a characteristic velocity of the flow center, typically taken as the vertical component of velocity along the centerline of the flow, should then be directly related to the radial component of velocity at the edge of the flow by a constant of proportionality [*Morton et al*., 1956].

This simple relationship has been very effective for a wide range of turbulent flows including jets, plumes, puffs and thermals [*Turner*, 1986]. The relationship is usually expressed as a percentage. For example, the radial component of velocity or the entrainment velocity is 5% of the velocity at the jet center. Typical values of this constant for the behavior of steady turbulent flows far away from their sources are 0.05 [*Papanicolaou and List*, 1988] for jets, 0.09 for plumes [*Papanicolaou and List*, 1988], 0.25 for thermals [*Fischer et al.*, 1979] and 0.30 for puffs [*Fischer et al.*, 1979]. These values assume the turbulent flows have a Gaussian profile for the vertical velocity distribution across the jet. It is important to point out that, although the velocity of an element of plume or jet fluid moving along the center of the jet will decrease as it moves away from the source, as long as the flow is steady, the vertical transport will be equal to the radial transport and the velocity of the element at the center will remain directly proportional to the velocity of the elements at the edge, though the magnitudes of both will decrease [*Fischer et al.*, 1979]. Also, the expected velocity decrease is slower for jets than for plumes, since the value of the constant is greater for the plume [*Fischer et al.*, 1979]. However, there are a number of situations where the

assumption of equilibrium between the axial and radial transport are not strictly valid and lead to the over or underestimation of velocity depending on the situation [*Turner*, 1979]. Furthermore, these formulations neglect a number of other potential contributions to this process, such as the magnitude of the density difference between the plume fluid and the ambient fluid, which is now known to be an important factor in determining ambient fluid entrainment [e.g., *Carazzo et al.*, 2005]. These values are also different near the source of the turbulent flow, as the dynamics are typically not yet in equilibrium. Estimates for the near-source values of this constant for plumes are around 0.2-0.3 and jets around 0.3 [e.g., *Solovitz and Mastin*, 2009]. Thus the rate at which fluid is entrained into the turbulent flow is greater near its source. How this value may change for flows with time-varying source conditions is unclear, considering the fundamental assumption of equilibrium between the axial and radial transport may no longer be valid. In other words, axial and radial transport may not be in equilibrium in unsteady flows.

Two-dimensional models also include the role of the radial component of velocity along the cross-section in contributing to the motion of the plume [*Fischer*, 1979]. Two-dimensional motion tends to occur when the fluid is near boundaries, causing the magnitude of the radial component of velocity to be of the same order of magnitude as the vertical component [*Fischer*, 1979]. It can also occur in specific flow geometries, such as fluid passing through a rectangular opening where the length is much greater than the width. In this situation, both the

radial component of velocity and its distribution over the cross-section must be known. Two-dimensional models of round plumes and jets tend to assume a circular cross-section to the plume, with distributions having a geometrical similarity around the central axis, called an axisymmetric approximation [*Fischer*, 1979]. The two-dimensional approximation works best for flows with minor variations in the third component of velocity (azimuthal), such that the bulk of the dynamics are determined by the vertical and radial components.

From the outset, it may not be known whether unsteady flow conditions introduce significant variations in the radial and azimuthal components of velocity within the volume of a plume. However, their presence can be confirmed by comparing predictions from two-dimensional theoretical models with experimental data. If there is a difference between the predictions and the observations, and if the processes considered in the two-dimensional model are the only ones acting on the system, then it may be inferred that motion in the direction of the azimuthal coordinate is important for that flow configuration [*Fischer*, 1979]. Any losses experienced by the flow due to the motion in the direction of the azimuthal coordinate would not be accounted for in the two-dimensional model, and thus the losses experienced by the flow would be under estimated.

Three-dimensional models, on the other hand, account for these losses. Three-dimensional models explicitly consider azimuthal variations in velocity along the azimuthal coordinate, rather than assuming a particular distribution and

assuming that this distribution is the same for all directions around the central axis of the flow [*Fischer et al*., 1979]. As a result, three-dimensional models may account for a velocity distribution that is not centered on the plume axis or that is non-circular in cross-section, which may be characteristic of plumes and jets in nature. In addition to information about how the vertical component of velocity varies along the radial coordinate at a given location for a given direction from the central axis, three-dimensional models also require information about how the velocity varies along the radial coordinate. Three-dimensional models of steady Plinian volcanic plumes agree well with the results of one-dimensional models [e.g., *Suzuki and Koyaguchi*, 2010], suggesting that the one-dimensional models include the dominant controls on Plinian plume dynamics. The three-dimensional models offer a refined characterization of losses due to processes acting out of the main direction of flow, such as entrainment [e.g., *Suzuki et al*., 2005].

2.3 Steady Turbulent Jets

Three classes of turbulent flows are considered here: steady turbulent jets, puffs, and vortex rings. In all three flows, turbulent motions are generated by momentum forces. They differ in their shapes and the dominant controls on their dynamics. These flows are summarized in the schematic in Figure 2.1 and are discussed below.

Steady turbulent jets are generated by a continuous source of momentum. As jet fluid moves away from the source, it slows down and spreads wider. As it moves, it incorporates ambient fluid into the jet through the process of turbulent

entrainment. The rates at which jets slow, spread, and entrain are governed by the rate momentum is supplied to the jet at the source. This momentum is diluted as the high-momentum jet fluid mixes with the low-momentum ambient fluid, causing a decrease in velocity and an increase in jet width [*Fischer et al.*, 1979].

Consequently, jets from steady source conditions have velocities that are large near the source and near the center of the flow as shown in Figure 2.2. The vertical component of velocity along the centerline of the jet decreases with distance from the source. The rate of decrease depends on the rate at which the jet momentum is diluted by turbulent motion and the entrainment and mixing of ambient fluid. Close to the source of the jet, the velocity distribution across the jet is uniform; in other words, all of the fluid at the source has the same velocity. However, in the far field of the jet, the time-averaged vertical velocity distribution across the jet has a Gaussian distribution in space. This distribution has a maximum velocity at the center of the jet and minima at the edges of the jet. This velocity distribution is shown in the schematic in Figure 2.2d. This schematic shows the distribution of the time-averaged vertical component of velocity in the transition region of an arbitrary steady jet. The jet moves from the bottom to the top of the figure. Fast jet fluid is located nearest to the source and nearest to the center of the jet fluid. This cross-sectional distribution represents the transfer of momentum from the center to the edges of the flow. This transfer occurs by the action of turbulent mixing. As the source momentum dissipates with increasing

distance from source, the Gaussian cross-sectional distribution decreases in amplitude and increases in width.

The transitional region is between the near-field and far-field. In this region, large coherent structures are located in the shear layer, separating the jet fluid from the surrounding ambient fluid. Coherent structures are regions of the flow where the fluid moves together in a pattern, or coherently, rather than moving at random. These structures are formed by the roll-up of the shear layer of the jet fluid. This process is illustrated in Figure 2.3. These structures dominate the dynamics in this region and control the rate at which ambient fluid is brought into the jet as well as the rate at which momentum is transferred throughout the flow. These large structures are formed by the large radial velocity gradients that form in the near-field within the boundary layer between the high-velocity jet fluid and the ambient fluid. In steady jets, these gradients are reduced by the action of turbulent mixing, which leads to the breakdown of the large structures to small structures in the transition region.

Large structures dominate motion in the near-field and transition regions of a steady jet, and also dominate the motion of puffs and vortex rings from the near-field into the far-field, as shown in Figure 2.1. Puffs and rings are generated by an instantaneous release of momentum, and their motions are governed by the total amount of momentum imparted to the puff or ring during release. For small-volume injections, vortex rings are formed, and at intermediate volumes, puffs are formed [e.g., *Olcay and Krueger*, 2008]. The structure of vortex rings is shown in

Figure 2.4. In the experiments of *Ghaem-Maghami and Johari* [2010], this difference was attributed to the presence of a tail of fluid in the puff case that was absent in the vortex ring case. The vortex ring entrains fluid across its bottom surface by large-scale eddies, and thus the presence of the tail limits the surface area across which fluid can be entrained [*Ghaem-Maghami and Johari*, 2010]. Entrainment at the sides of the puff tail occurred by small-scale eddies [*Ghaem-Maghami and Johari*, 2010]. This difference in entrainment behavior is illustrated in Figure 2.1, where the small vortices near the bottom of the puff represent the fact that fluid is brought in by small eddies at that location. Furthermore, the experiments of *Ghaem-Maghami and Johari* [2010] showed that above the cores of each of these structures, fluid was always directed radially away from the structure, while below the cores fluid was brought into the structure. This behavior is also included in Figure 2.1 where the core location is represented by the horizontal line through the middle of the flow. Above the line, fluid is directed radially away from the core, and below it fluid is directed toward the core. The fluid entrained is ambient fluid in the case of the ring and tail fluid plus ambient fluid in the case of the puff [*Ghaem-Maghami and Johari*, 2010]. For the ring, ambient fluid is incorporated into the structure at a greater rate than it is forced out at the top; conversely for puffs, the rate at which fluid is forced out the top is greater than the entrainment rate [*Ghaem-Maghami and Johari*, 2010]. Each of the *Ghaem-Maghami and Johari* [2010] experiments was conducted at the same

constant injection velocity, which was maintained over the injection duration, and greater volumes were achieved simply by increasing this injection duration.

The far-field velocity distributions for rings and puffs from steady sources were investigated by *Ghaem-Maghami and Johari* [2010] who found that velocities were greatest in the center of a ring or puff and decreased radially from the center. This distribution is shown in Figure 2 for arbitrary rings and puffs based on the results of *Ghaem-Maghami and Johari* [2010]. Larger volume puffs, or elongated puffs, also had the largest velocities near the center of the flow, but had a velocity distribution that was elongated in the direction of the flow due to the presence of the head and the tail.

Vortex rings, turbulent puffs, and jets may all be created by the impulsive injection of fluid through an outlet. To classify the flow that will result from a particular injection, the non-dimensional parameter, *P*, was developed by *Hermanson et al*. [2000]. This parameter treats the volume of injected fluid as if it were injected as a cylinder with the same volume as the injected fluid and a base diameter equal to the orifice diameter. The length of the cylinder, *L*, is computed by dividing the total volume injected Q by the orifice area *A*. Then *P* is defined according to the following expression:

$$P = (L/d)^{1/3} = (Q/Ad)^{1/3} \ . \tag{2.1}$$

For *P* values greater than 8, flows form long cylindrical shapes (cigars) that behave as starting jets, whereas *P* values less than 1.6 generate flat-cylinders or vortex rings [*Hermanson et al*., 2000; *Ghaem-Maghami and Johari*, 2010]. For

intermediate values of *P*, puff-like structures are formed that can be compact puffs (spherical), elongated puffs (spherical front with conical tail), or cigar-like [*Hermanson et al*., 2000; *Ghaem-Maghami and Johari*, 2010]. For a constant value of outlet area, the value of *P* can be changed by changing the total volume injected, and thus the total volume injected determines the structure resulting from the injection. However, this parameter does not depend on time and may not describe the behavior of the unsteady jets well.

The time over which vortices form delineates the time during which entrainment occurs by advection. This time is commonly referred to as the 'formation time' following *Gharib et al*. [1998]. For steady flow conditions, in experiments with smooth contraction nozzles where fluid was injected using a piston-cylinder mechanism, *Gharib et al*. [1998] found that the formation time was affected only by the velocity of fluid that forms the vortex and the geometry of the outlet. Thus, if the vortex motion is non-dimensionalized on these scales, a universal non-dimensional formation time results, with a value around 4.0.

2.4 Simple Models of Steady Turbulent Jets

Two simple models for turbulence generated by the action of momentum forces are most appropriate for the experiments presented here: a starting jet and a puff. The starting jet model is based on the starting plume model of *Turner* [1962]. *Turner* [1962] proposed a theoretical model for starting plumes entering neutral surroundings as an intermediate theory to continuous and instantaneous models. This theory allowed for the jet width and height to grow in time, unlike a

continuous model, but includes a steady source flux, unlike an instantaneous model. He described the structure of a starting plume as composed of a spherical vortex ball atop a conical jet. The spherical front or cap was different from an isolated instantaneous puff or a thermal, in its influx of mass and momentum supplied to it by the conical jet below; the conical jet, or tail, region was considered to have properties like that of a steady jet. *Turner* [1962] then reasoned that rotational motion in the cap resulted in the turbulent entrainment of ambient fluid into the cap as well as entrainment of fluid from the tail below. *Turner* [1962] further suggested that the cap entrains equal amounts from each region (ambient and tail). As a consequence, the momentum of the starting jet was diluted more rapidly than an established jet but less rapidly than a puff. By experiment, *Turner* [1962] found that the front of the starting plume evolved at 72% of the steady plume velocity in the tail. He also maintained that the shape of the starting plume – a spherical cap atop a conical tail – was sustained for the entire duration while its size was increasing.

Experimental work has extended *Turner*'s [1962] conceptual model to momentum-driven jets. By dimensional analysis, *Hill and Ouellette* [1999] derived an expression to estimate the rise rate of a starting jet as a function of the momentum flux at the source:

$$h(t) = C_1 \dot{M}_0{}^{1/4} t^{1/2} \tag{2.2}$$

where $h(t)$ is the jet height at time t, $\dot{M}_0$ is the momentum flux at the source, that is, the rate momentum is being added to the jet at the source, and t is the time

from the start of the release. The parameter C_1 is a coefficient of proportionality with an empirical value of approximately 3.0 for steady starting jets with circular cross-sections [*Hill and Ouellette*, 1999]. However, *Hill and Ouellette* [1999] estimate this value to range from 2.89 to 3.04 and experimental work by *Sangras et al*. [2002] estimate it at 2.6 - 2.8. *Sangras et al*. [2002] noted that although the value was similar, there was disagreement about when the expression was valid. While *Hill and Ouellette* [1999] reported the appropriate range of application is for distances greater than 20 or 30 times the source diameter, the observations of *Sangras et al*. [2002] suggested the appropriate range was at distances greater than 60 times the source diameter. This distance refers to the location from the source where the self-similar assumption can be reasonably made based on the observation that the ratio between the maximum width of the jet at any time to its height at that time remains constant.

A constant aspect ratio suggests that the internal forces driving the rise and the spread are in direct balance with each other at all distances from the source, and thus the flow is said to be in a state where its dynamics are self-similar [*Morton et al*., 1956]. From this assumption of self-similarity, *Morton et al*. [1956] reasoned that the vertical momentum flux driving the rise of the flow was balanced by the radial diffusion of momentum by turbulence which governed the spread. To relate the vertical motion to the radial motion, they formulated the entrainment hypothesis, which states that if the width grows by the turbulent entrainment of ambient fluid and if the width is growing in direct proportion to

the height, then the radial component of velocity at which fluid is entrained at the edge of the jet is directly proportional to a characteristic vertical component of velocity interior to the jet. This can expressed mathematically as

$$V = \alpha u \tag{2.3}$$

where V is the vertically directed velocity at the center of the jet at a given height, u is the radially directed velocity at the edge of the jet at that height, and α is the entrainment constant. Thus the entrainment hypothesis follows directly from an assumption of self-similar dynamics [*Morton et al*., 1956]. This assumption of self-similarity is commonly used in mathematical models of turbulent flow from constant sources. As evidenced by the experimental results of *Hill and Ouellette* [1999] and *Sangras et al*. [2002], starting jets from continuous sources arrive at self-similar states many vent diameters away from the source. While self-similarity seems to apply to jets started impulsively with a volume flux that remains constant, it may not apply to flows started impulsively with a volume flux that remains variable.

Self-similarity is also achieved in the far-field of puffs, instantaneous rather than continuous releases of momentum. Puffs take on two main geometries: axial (spherical) and cylindrical [*Richards*, 1965]. A puff is analogous to a thermal. Similarity scaling for puffs moving in a still and uniform ambient in the self-preserving regions is

$$h(t) = C_1 {M_T}^{1/4} t^{1/4} \tag{2.4}$$

where h is the height of the flow at time t, C_1 is a constant that is specific for experiment conditions, and M_T is the total mass specific momentum of the injection [*Sangras et al*., 2002]. The total momentum can be calculated by integrating the instantaneous mass specific source flux of momentum $\dot{M}_0\ (t)$ over the duration of the injection T according to

$$M_T = \int_0^T \dot{M}_0(t)dt \tag{2.5}$$

It is of note that for both starting jets and puffs, the height of the flow has a power law dependence on time; however, the power ½ in the starting jet case (equation 2.2) indicates a greater rise rate than the power ¼ in the puff case (equation 2.4). It is also of note that the height to which the flow travels in a given amount of time is related to the source momentum flux, the power of time, and a coefficient of proportionality, and not explicitly related to the injection pressure, velocity, or nozzle diameter. This suggests that various combinations of injection pressure, nozzle diameter, and velocity (which may not be independent of the first two) that produce the same amount of momentum flux should produce jets with similar rise behaviors.

2.5 Unsteady Turbulent Jets

In unsteady jets, the large structures discussed above may persist rather than be broken down into smaller eddies [e.g., *Ruiz et al*., 2011; *Hu et al*., 2012]. This is because the unsteady conditions maintain the presence of radial gradients in the velocity field [e.g., *Ruiz et al*., 2011; *Hu et al*., 2012]. Unsteady jets can be generated by source momentum fluxes that vary in time [e.g., *Boree et al*., 1997;

Johari and Paduano, 1997; *Breidenthal*, 2008] but may also occur when ambient or exit conditions vary in time. The factors that govern their behavior depend on the situation in which the jets were generated. Thus, to understand the effect of unsteadiness for a specific situation, experiments must be conducted for that situation. However, in general, the effect of source unsteadiness depends on whether the jet is being accelerated or decelerated. Relative to a steady jet, spreading and mixing are observed to decrease in accelerating laboratory jets [e.g., *Kouros et al*., 1993; *Zhang and Johari*, 1996], but increase in decelerating laboratory jets [e.g., *Boree et al*. 1996; *Johari and Paduano*, 1997; *Musculus*, 2009]. *Ruiz et al*. [2011] attribute the observed differences between steady and unsteady jets to the rate at which the shear layer between the jet and ambient fluid grows and forms large-scale structures. *Ruiz et al*. [2011] observe that steady jets develop a slowly growing shear layer that rolls up approximately one diameter from the source into many small-scale structures. These observations are consistent with previous observations of near-field structures in steady jets [e.g., *Crow and Champagne*, 1971; *Hussain and Husain*, 1989]. However, the shear layer from a pulsed jet – created by a sequence of pulses of fluid – develops more rapidly and forms large-scale coherent structures with characteristic length scales on the order of the total flow width [*Ruiz et al*., 2011]. *Ruiz et al*. [2011] also observe that the magnitude of the vorticity near the source is increased in unsteady jets by over 50% compared to a steady jet at the same Reynolds number.

These results suggest that unsteady discharge rates may lead to greater strain rates in the direction of flow within the fluid in the shear layer. These increased strain rates may in turn generate larger magnitudes of vorticity that lead to the observed large-scale structures. An alternative explanation, proposed by *Soteriou et al.*, [2002], suggests that unsteady volume fluxes result in the production of local circulation maxima in the shear layer. While flow above the local maxima is decelerated by the presence of the local maxima, flow below it is accelerated, and the difference in velocity induces the local flow to rotate around the maxima. *Soteriou et al.*, [2002] suggest local maxima do not occur in steady jets because the production of circulation in the shear layer increases monotonically with height at an approximately constant rate. *Soteriou et al.*, [2002] also propose that the magnitude of the circulation or the strength of the rotation depends on the relative rates between the local turbulent diffusion and convection processes. Turbulent diffusion acts to reduce gradients and prevent the development of local maxima so large rates of turbulent diffusion work against the generation of structures. Convection may lead to large local strain rates and thus stretch the circulation in the direction of flow and prevent local maxima from forming.

In other experiments investigating unsteady vortex generation, *Olcay and Krueger* [2008] observed that accelerating a forming vortex results in a more tightly wound vortex with a smaller core as compared to the steady formation of a vortex. Similarly, decelerating flow during vortex formation results in a more

loosely wound vortex with a fatter core [*Olcay and Krueger*, 2008]. As observed by *Ruiz et al.* [2011] and noted by *Maxworthy* [1972], forming vortices entrain ambient fluid through advection whereas fully formed, steady vortex rings entrain ambient fluid through the much slower process of diffusion. Other factors such as unsteady flow conditions, the specific vortex-generation mechanism, and the outlet type have all been shown to influence the formation time [e.g., *Ai et al*., 2005; *Yu et al*., 2007].

When pressure drives vortex generation, there seems to be an additional contribution of pressure to the circulation of the rings during the initial roll-up phase [*Krueger*, 2005]. Because the propagation velocity of a vortex ring is directly related to circulation, pressure-driven rings should propagate faster than piston-cylinder or gravity-driven rings. Orifice plates tend to delay the formation time, that is, to lengthen the duration of advective entrainment, and to produce larger rings that persist for longer times than vortex structures formed by flow through smooth contraction nozzles or flat plate orifices [e.g., *Ai et al*., 2005; *Mi et al*., 2007]. These observations suggest that pressure-driven rings generated in jets issuing from orifice plates should form rings that propagate further from the outlet before they finish forming, all the while entraining ambient fluid through advection.

The effect of unsteadiness on vortex formation depends on the nature of the unsteadiness. In general, acceleration tends to decrease formation time that results in structures forming close to the source. Deceleration results in an

increase in the formation time, resulting in structures that form far from the vent. Flows that quickly accelerate and then slowly decelerate entrain large amounts of ambient fluid and form rings with small cores [*Olcay and Krueger*, 2008]. Flows that slowly accelerate and then quickly decelerate form rings with fat cores that entrain less ambient fluid.

In contrast to experiments in steady jets that involve a constant rate of injected volume, the injection rate in an unsteady jet may vary in time such that the volume flux may change considerably from one instant to the next. It is unknown whether such source conditions will result in flow structure evolution from ring to puff to jet over time. However, experiments by *Sangras et al*. [2002] observed that interrupted starting jets, jets where the source was on long enough to achieve starting jet behavior before the source was suddenly stopped, evolved from starting jets to puffs for short times after the source was stopped. This result suggests that a changing source condition may result in structure evolution through time.

While most of the above experiments utilize constant velocity or schematic (e.g., trapezoidal) acceleration schemes, in natural flows the volume flux increases, gradually peaks, and then decreases before it stops. Natural flows include jellyfish and squid locomotion, cardiovascular flows [e.g., *Querzoli et al*., 2011] and perhaps flows from some volcanic eruptions. As the injection time history is an important control on the formation of vortices in the near-field of these flows, the gradual changes in velocity are expected to affect the formation

of structures and the shear layer in nontrivial ways. Thus, it is important to understand the dynamics of the vortices generated from this type of unsteady source condition, in order to understand the overall unsteady jet dynamics.

The application of similarity solutions for relating the motion of flow to its generation conditions strictly applies to conditions where the momentum flux is constant or instantaneous, and thus the flow reaches a dynamic state that can be approximated by a self-similar assumption. It is not obvious whether these relationships may be extended to include the effect of variable injection rates. However, experimental work by *Querzoli et al*. [2010] suggests that this theory can be extended to varying volume fluxes by subdividing the volume flux behavior into intervals on the basis of whether the volume flux is increasing in time or decreasing. The volume flux studied in *Querzoli et al*. [2010] has a Gaussian-like distribution in time, with an injection duration lasting 1.0 second. They found that the rise of the resultant jets was governed by two momentum scales in sequence. Initially, the jet rise was governed by the momentum flux, but once the volume flux neared the peak of the Gaussian, the jet rise was governed by the total amount of momentum that was injected to that point. This result is supported by the observation that once the instantaneous flux of momentum fell below the time-averaged flux of momentum, the shear layer that separated the jet fluid from the ambient fluid broke, allowing ambient fluid to be entrained directly into the jet core rather than into the shear layer. In other words, while the shear layer was continuous, the instantaneous flux from the vent drove the rise

behavior, but once the shear layer broke, a cap formed and the total amount of momentum injected dominated the rise behavior. This result suggests that unsteady jet rise is controlled by the dynamics of the cap, which may depend on but differ from the dynamics of the flow behind it.

This breaking or separation of the shear layer is consistent with other experimental observations that observe the formation of a vortex ring at the start of an impulsively started jet. Starting vortex rings are known to form in impulsively-started flows ejected from circular outlets (i.e., orifice plates, nozzles, open pipes, etc.) into still ambient fluids [e.g., *Richards,* 1965]. A boundary layer forms between the moving fluid and the still ambient fluid generating high rates of shear at the jet boundary. This boundary layer is unstable and the fluid in the shear layer rolls back on itself to create the leading vortex ring. Driving the flows with pressure, relative to piston-cylinder or gravity-driven mechanisms, increases the strength of a vortex [*Krueger,* 2005]. Using a circular orifice plate, as opposed to, for example, a square orifice plate, as an outlet [*Mi et al.*, 2001] increases the strength as well. In many situations, the starting vortex rings separate from the jet fluid beneath it and move separately from the rest of the jet fluid [*Gharib et al.*, 1998]. These isolated vortex rings are similar to puffs, in that their motion is governed by the total amount of momentum contained within the structure. They differ, however, in the distribution of vorticity within the structure; vorticity surrounds a core in a vortex ring but is distributed uniformly through a puff. Recent experimental work by *Ghaem-Maghami and Johari* [2010] indicate that

rings and puffs also differ in the rates at which they expand and entrain: rings entrain at a greater rate than they expand, while puffs expand at a greater rate than they entrain.

Ghaem-Maghami and Johari [2010] also observed that as the total volume of a puff increases, the rate at which it expands increases relative to the rate it entrains; in other words, as the puff volume increases, it entrains fluid at a decreasing rate. The ratio of expansion to entrainment was greatest for established steady jets. The study by *Ghaem-Maghami and Johari* [2010] was limited to jets driven by constant volume fluxes so the volumes did not change over time. Instead, the effects of volume were studied by conducting separate experiments with different injection durations of a constant volume flux. It is therefore not clear how these results may apply to jets driven by variable volume fluxes when the volume changes over time.

2.6 Velocity Measurements in Turbulent Jets

In turbulent flows, the overall motion of the flow may differ from the motion of the fluid elements that make up the flow. Fluid elements may undergo translation, rotation, linear deformation, and angular deformation. The motion of a fluid element from one instant to the next may be due to one of these or some combination of any or all of them. As the overall motion of the flow is the net result of the individual motions of all of the elements, a greater understanding of the overall motion can be achieved by understanding the motion of the elements. The relative motion of fluid elements within a turbulent flow can be measured

using a technique called Particle Image Velocimetry (PIV) that involves adding particles to an otherwise clear fluid to make the motion of that fluid visible [e.g., *Adrian* 1984; *Adrian* 1991].

PIV is a measurement method used to measure the distribution of velocity within a moving fluid for the purpose of visualizing the structure of the flow and understanding the mechanics of its motion [e.g., *Adrian*, 1991; *Adrian and Westerweel*, 2011]. This technique provides velocity measurements over a whole flow field at a particular instant in time; other techniques for measuring fluid motion involve measurements of the flow at a single location or over a large interval of time. Thus PIV captures snap-shots of the continuous fluid motion. Analysis of these snap-shots can then be used to inspect the mechanics of the continuous motion. The results of these measurements are typically represented as vector plots that show the differential motion of the fluid elements as well as the motion of the overall flow [e.g., *Adrian*, 1991; *Adrian and Westerweel*, 2011]. These vector plots can then be used to understand how the motions of the fluid elements combine to generate the overall motion of the flow.

PIV is also a nonintrusive measurement technique, as long as the particles do not interfere with the motion of the fluid, so the flow is not altered when taking the measurement [e.g., *Adrian and Westerweel*, 2011]. This feature is important for unsteady flows, which may change abruptly and unsystematically by the presence of a measuring device in the field [e.g., *Adrian and Westerweel*, 2011]. The ability to make instantaneous measurements of the flow field is also an

important feature for unsteady flows [e.g., *Adrian and Westerweel*, 2011]. Unsteady flows may involve the generation of very large instantaneous forces that impact the motion of a fluid in a non-trivial way such that the motion cannot be understood without considering the contribution from the unsteady forces. For example, the sudden opening of a valve in a water pipeline may lead to a burst pipe if the strength of the pipe material cannot withstand the large pressures that are generated in the pipeline during the valve opening. The average pressures in the pipeline, however, may remain below that peak value, and thus a rupture would not be considered if the peak force was not considered [*Mays*, 1999]. Consequently, making instantaneous measurements of the flow enables the measurement of large instantaneous forces.

To use PIV to understand unsteady dynamics, a set of experiments must be performed under identical conditions [*Adrian and Westerweel, 2011*]. Even for identical conditions, the inherent randomness in turbulent flow behavior will lead to variations in the measurements acquired from each individual experiment. Consequently, the contributions to the motion from variations in the measurements between different runs of that condition need to be eliminated before the motion can be analyzed [*Adrian and Westerweel, 2011*]. However, this task must be accomplished without eliminating the contributions to the motion from time-varying dynamics. Ensemble averages are used for this purpose.

An ensemble average is computed for each instant that measurements are acquired [as described in *Adrian and Westerweel, 2011*]. To compute the average,

an instantaneous velocity distribution from an individual experiment is averaged with those at the same instant from all other experiments in the set. The result is an average velocity field that represents the average motion of a flow at a particular instant for a given experimental condition. This average is computed so that the mechanics of the flow that results from a particular experimental condition can be studied rather than the mechanics of the flow that resulted from a single experiment.

The difference between velocity fields, or realizations, from an individual experiment and that from an ensemble average over all experiments in a set, or ensemble, is belabored here because each volcanic plume is equivalent to the result of a single experiment. Thus an understanding of the laboratory flows based on their ensemble average behavior may not provide information about the detailed dynamics of any single plume, but rather information about the behavior common to an entire class of plumes generated from identical eruption conditions.

This fact presents problems when trying to compare the laboratory data with volcanic plume observations; because plumes are classified according the style of eruption that generated the plume rather than the observable behavior of the plume itself. So while there are conceptual models for plumes formed during Vulcanian-, or Strombolian-style eruptions, each of these eruption styles can generate a wide variety of plume behaviors. *Patrick et al.* [2007] reported four different plume ‘morphologies’ - jets, starting plumes, thermals and rooted thermals - that were observed from Strombolian-style eruptions at Stromboli

Volcano in Italy. Each of these ‘morphologies’ is an individual class of turbulent flow with general theory and methods of solution specific to each class. Moreoever, each of these classes has a distinct source condition, which implies that each morphology type has a distinct source condition. However, these morphologies were defined based on observations of plumes without observations of the source conditions. While observations of ‘source conditions’ for volcanic eruptions can be difficult to collect and interpret, their omission does present a problem when trying to understand how to model the resultant plumes. For example, it must be known whether each morphology class requires a separate set of equations, or simply a change in the initial conditions for a single set of equations.

It is not yet understood if all of these morphologies are present or common at all volcanoes, or if they are specific to Stromboli Volcano in Italy. *Gottsmann et al.* [2009] present evidence for two different plume types generated during Vulcanian-style eruptions at Soufriere Hills Volcano on the island of Montserrat in the British West Indies. Their analysis, however, was of the source condition and they did not provide any detailed information about the corresponding plumes except to mention that they were different. Moreover, publications which do consider plume behavior rarely consider the behavior common to more than ten plumes, with the exception of *Patrick et al*. [2007] who used approximately 80 plumes on which they base their classification. Consequently, there are currently not enough plume observations in the literature with which to distinguish volcanic

plumes based on the details of their vent flux conditions, rather than on their broadly-defined generation mechanisms.

Thus, my work considers the behavior common to a theoretical class of volcanic plumes that are generated at a variable rate during short-lived explosive eruptions and are driven by inertia. Both the results from individual experiments and ensemble-averages are considered here. This is to facilitate, first, an understanding of what contributes to variability from the average behavior, and, second, an understanding of the evolution of an individual jet which may help identify which volcanic plumes belong to this theoretical plume class.

Additionally, this work aims to measure the internal velocity fields of jets generated under unsteady conditions that may be analogous to those that prevail in short-duration volcanic eruptions. The purpose of the measurements is to characterize the velocity structure of the resultant unsteady jets over time. The evolution of the structure is then analyzed to improve the understanding of the mechanics of these flows that is derived from the analysis of the external flow behavior. These results are then used to improve understanding of volcanic plume behavior in terms of volume flux variations.

Figure 2.1 Simple models of turbulent flows driven by momentum.

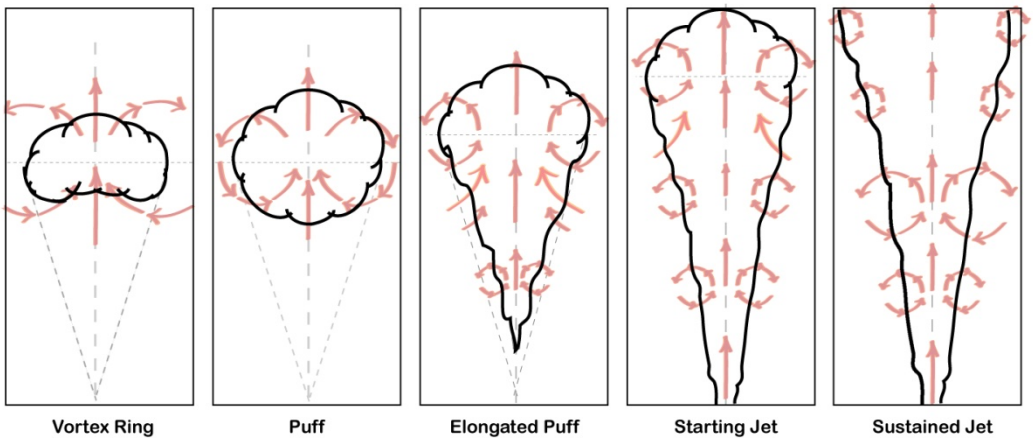

Figure 2.2 Vertical velocity contours for simple models of turbulent flows driven by momentum. Velocity distributions are time-averaged and correspond with the far-field behavior. These distributions are schematic and show the variation in the distributions among the models. Distributions are based on the experimental results of [*Ghaem-Maghami and Johari*, 2010].

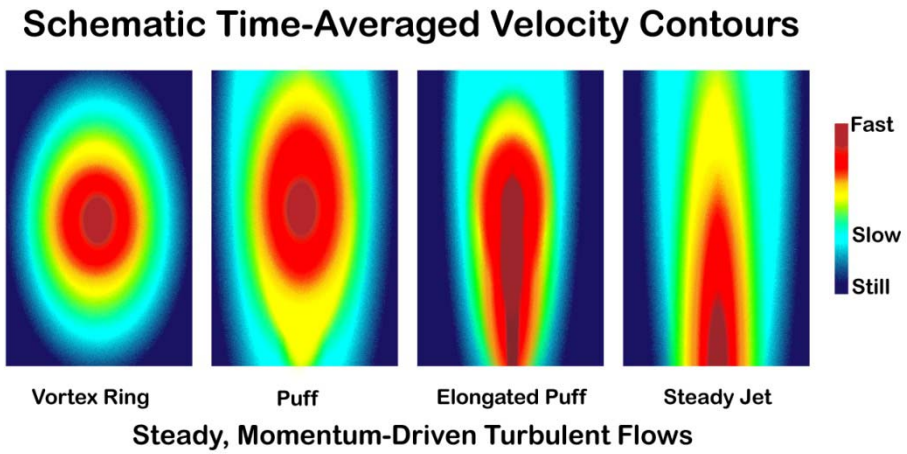

Figure 2.3 Formation process of a starting vortex.

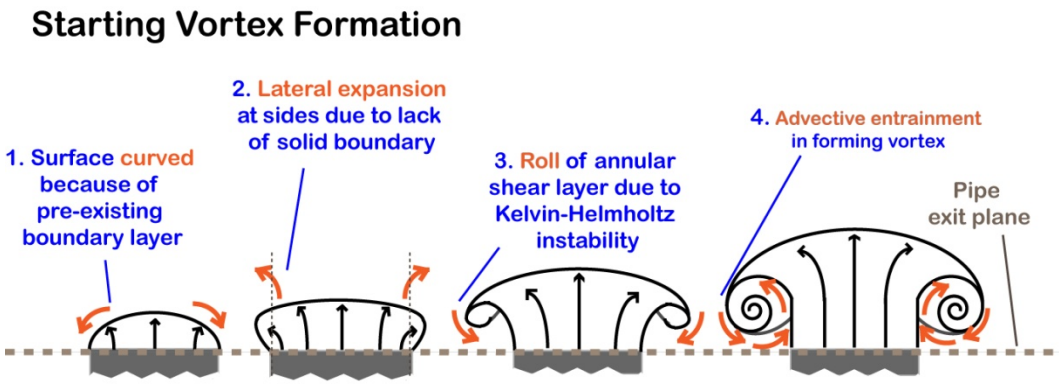

Figure 2.4 Structure of a vortex ring.

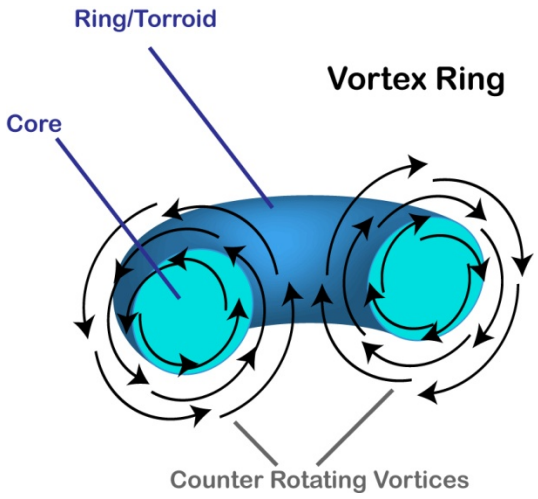

Chapter 3

EXPERIMENTAL METHODS

3.1 External Jet Measurements

The experiments described in this chapter investigate the effects of strongly varying volume fluxes on the rise characteristics of turbulent jets. Jets were generated by injecting water into a tank of still water through a vertically oriented pipe. Injection rates were measured with a mass flow meter. The bulk properties of the resultant jet - jet height and width - were then measured from time-resolved video records of jet motion in the tank.

A sketch of the apparatus used to generate the jets is shown in Figure 3.1. The fresh water bath filled a tank with dimensions 0.6 x 0.6 x 1.2 m deep to a depth of ~ 0.95 m. Both the bath and the source reservoir were filled from the lab water supply and brought to room temperature before experiments were run to get rid of any dissolved air. Therefore, one value of the water volume, 1000 kg/m^3, was used for calculations in all experiments as the room temperature was 23 +/- 5 ^oC for all experiments.

During a run, the pump used to generate the initial source pressure was turned off before the valve was opened. Since the pump was operated with a dial, a hard object (a dead 9V battery) was taped in the path of the dial, such that turning the dial until it contacted that object allowed approximately the same initial pressures to be reached in each experiment. The initial pressure (the

pressure just prior to vent opening) was read from a pressure gauge positioned inline prior to the mass flow meter. This value was then manually recorded.

Then approximately three minutes were allowed to pass between the pump turn-off time and the valve opening time to allow transient motion in the plumbing system to subside. The valve was an electronically controlled pneumatic ball valve that opened in 80 milliseconds according to the manufacturer's specifications on the valve. The addition of the electronic valve aided in the reproducibility of the injections. It was added after the experiments described in *Clarke et al*. [2009] in which a ball valve was manually opened. The increase in reproducibility was necessary to ensure multiple experiments could be run under identical conditions so that their results could be ensemble averaged. The operation time of the valve was investigated by recording a 3.5-volt signal when the valve was triggered on a second channel on the digitizer for the mass flow meter. The time difference between the 3.5 volt signal and the first non-zero flow rate was 0.14 +/- 0.04 seconds. The source of the difference between the 0.08 seconds indicated by the manufacturer and the measured difference of 0.14 seconds is unknown. Following the valve opening, source fluid entered the tank through an orifice that was raised 8 cm from the bottom of the tank.

I measured the mass flux of water that entered the tank with a Coriolis mass flow meter (Kueppers KCM3000) sampling at 100 hertz. I did not set the form of the source time function or its duration; both were determined by the release of the pressurized fluid. I divided the mass flux by the density of water to

calculate the volume flux. The resulting functions, shown in Figure 3.2, are best described as a Gaussian distribution in time, and lasted for approximately 400 milliseconds.

There was some variability in the beginning of the injection that contributed to error in identifying the start of the injection in the mass flow meter data. This variability led to an error of approximately 0.04 seconds in identifying the start time. The total volume injected was calculated by integrating the instantaneous volume flux $\dot{Q}_o\ (t)$ over the injection duration T according to the following expression:

$$Q_T = \int_0^T \dot{Q}_0(t)dt. \tag{3.1}$$

The total volume injected for all the experiments considered here ranged from 30 cm^3 to 100 cm^3 and depended on the initial pressure, vent diameter, and pressurization conditions for each run. “Pressurization conditions” refer to factors which may have contributed to variability between experiments run at seemingly identical pressures. The most significant contributor to this variation was likely the behavior of a flexible hose which connected the pump and the flowmeter. The effects of the pressurization conditions contributed unsystematic error to the measurement of flow rate and jet motion. The total volume of fluid pressurized in each experiment exceeded the volume of fluid released by a factor of approximately 100.

While the run procedure minimized variations in starting conditions, the nature of turbulent flows is such that they vary for every individual experiment

run. Nine runs were therefore performed for each starting condition. To reduce the influence of variation among the experiments and simultaneously retain the time variation information, averages were calculated for each flow condition by ensemble averaging the time series data over the nine runs for each flow condition for each time step. Specifically, the ensemble average of the volume flow rate $< \dot{Q}(t_1) >$ at time t_1 was calculated according to the following equation:

$$< \dot{Q}(t_1) > = \lim_{N\to\infty} \frac{1}{N} \sum_{i=1}^{N} \dot{Q}_i(t_1) \qquad (3.2)$$

where *N* is the number of experiments [e.g., *Adrian and Westerweel*, 2011], in this case *N* = 9. As *N* approaches infinity, the ensemble averaged value approaches the true value of the mean. This calculation was then repeated for all times in the time series. Here, the brackets are used to denote an ensemble average. Similarly, the ensemble average of the height $< h(t_1) >$ at time t_1 was found according to

$$< h(t_1) > = \lim_{N\to\infty} \frac{1}{N} \sum_{i=1}^{N} h_i(t_1). \qquad (3.3)$$

I recorded the motion of the resultant jets using a high-speed camera positioned perpendicular to one of the tank walls. On the opposite wall, I formed a backdrop by taping a sheet of translucent white paper to it. To increase the contrast between the source and ambient waters, I backlit the backdrop with a uniform light sheet. The light sheet was created using studio lights (Speedotron) and a light gel.

I imaged a field of view of 1000 mm by 1000 mm through a fixed focal point lens on a CCD camera (Redlake MotionPro 2000) with a chip of 1024 by 1024 pixels and a bitdepth of 8 bits. I recorded at 100 hertz yielding a spatial resolution of ~1 mm/pixel and temporal resolution of 10 milliseconds. Jet motion

was measured from the video record by identifying the location of the flow height in each video frame.

The video camera was not time-synchronized with the mass flow meter. Instead, it was initially assumed that the first mass flow meter measurement above background noise corresponded with the first video frame with visible dye movement. This assumption was later tested by adding an LED that illuminated when the vent was triggered to the video field of view. This trigger signal was also sent to the digitizer for the mass flow meter. It therefore served as a common reference time and enabled synchronization of the video and mass flow meter data. This test indicated that 9 +/- 3 video frames were recorded between the time the LED was lit and the first visible dye movement in the video.

I examined unsteady jet behavior in six experimental conditions characterized by the diameter of the circular orifice from which the jet entered the tank and the pressure in the system immediately prior to the valve opening. Three orifice diameters, 3, 9 or 15 mm, were used at each of two initial pressure conditions, 3.4 and 6.9 MPa. The orifice diameter influenced the Reynolds number largely via the inverse relationship between vent velocity and orifice diameter. Thus, these six conditions enabled a test of the Reynolds number effect on the unsteady rise of the jets. The ensemble-averaged values of the injection characteristics for each of the six flow conditions tested in the above apparatus are summarized in Table 1 for non-buoyant jets and Table 2 for buoyant jets. The resulting jet behavior is discussed for non-buoyant jets in Chapter 4 and buoyant

jets in Chapter 6. Buoyant jets were generated with an aqueous solution of methanol with a density of 970.0 +/- 5.0 kg m^{-3}.

3.2 Internal Jet Measurements

Velocity field measurements were obtained using Particle Image Velocimetry (PIV). PIV is a non-invasive technique for measuring velocities within a flowing fluid. A schematic illustrating this process is shown in Figure 3.3. In this technique, particles are added to a fluid to provide a means to track the motion of the fluid, which is otherwise not visible. Particles within a particular plane through the flow interior are then illuminated with a laser light sheet so the internal motion, rather than the motion of the edges, of the flow is visible. Images are then taken of the illuminated particles [technique summarized in *Adrian and Westerweel*, 2011]. Sequential images are then processed to determine the distance the particles moved between the times the images were taken. Processing involves dividing the image field of view into small subsections using a grid. Within each grid section, the average displacement of all the particles in a grid section is found by cross-correlating the images. Velocities are then computed by dividing the average displacement in that grid section over the time interval between the images. This computation is completed for all grid sections. The result is a velocity field for the flowing fluid in the plane of the laser [*Adrian and Westerweel*, 2011].

I conducted the PIV measurements in the Explosive Volcanology Laboratory at Arizona State University to characterize jets similar to those created

in the apparatus in Figure 3.1 and described in section 3.1. In contrast to the experiments described in section 3.1 in which the jet issued from a flat plate orifice, in the experiments described here, the jet issues from an open pipe; the flat plate orifices screw onto this pipe, so they were simply not installed while these experiments were conducted. This decision was made in order to limit the number of unknowns in the problem, since the behaviors of steady jets, puffs, and vortex rings from open pipe experiments were discussed more extensively than those from orifice plates in the literature at the time these experiments were conducted in January and February 2010.

The PIV arrangement is shown schematically in Figure 3.4. This arrangement consisted of a laser, optics for creating a laser sheet across the image area, and a digital camera for recording the PIV images. Silver-coated hollow glass spheres from Potters Industries were used to seed the source and ambient fluid. These particles had a diameter of 10 microns and a density of 1.1 grams per cubic centimeter. The laser sheet was created with a dual-powered double-pulse Nd:YAG laser from Litron, operated at a frequency of 14.1 hertz and power of 200 millijoules per pulse at a wavelength of 532 nanometers. The light sheet was aligned with the center of the pipe to illuminate the motion in the center plane of the jet. The light sheet was approximately 1 millimeter thick and approximately 30 centimeters tall at the location of the pipe. The time between laser pulses was 0.0075 s. Synchronization of the camera and laser were controlled with a timing unit.

Images were then taken of the particles that were illuminated in the plane of the laser. Images were taken with a HiSense4M camera from Dantec Dynamics at a frequency of 14.1 hertz. The camera was operated in triggered double-frame mode, which means a pair of images was collected every 0.07 seconds after the camera was triggered. Images were collected for a total record length of 7.0 seconds. The CCD in the HiSense4M camera is 2048 pixels high by 2048 pixels wide; however, images for this study are 2048 pixels high by 1000 pixels wide to limit the field of view to the jet motion. The narrow field of view increases the number of velocity measurements within the jet region. The optics for the camera consisted of a Zeiss macro lens with a fixed focal length of 50 millimeters that was coupled to the camera with an F-mount adapter. The camera field of view was 302 millimeters tall by 142 millimeters wide such that each pixel corresponded to 0.15 millimeters. This provided measurements over the region $0 < y < 15d$ where y is the vertical distance from the pipe exit plane and d is the inner diameter of the pipe. The pipe inner diameter was 20 millimeters. The center of the field of view was offset from the center of the pipe to capture the motion of the ambient fluid surrounding the jet boundary. The measurements corresponded to a radial distance of $-2.5d < r < 4.5d$, where r is the radial coordinate and $r = 0d$ corresponds to the center of the pipe. Separate high-speed video measurements of this same flow condition in this apparatus yielded maximum jet front velocities on the order of 1 meter per second within this field of view immediately following jet initiation.

The PIV images were analyzed using an interrogation window size of 32 by 32 pixels with a 25% overlap. Image pairs were cross-correlated and then filtered using a 3-by-3 pixel, moving-average filter. A multi-pass correlation algorithm was applied to minimize noise. This algorithm was set at 3 passes. The resulting vector fields have an array of 85 by 40 vectors (i.e., 3400 uniformly spaced vectors). For a single pass and without the moving average filter, there were erroneous vectors (outliers) in the PIV fields immediately following jet initiation. These outliers were usually located in the jet close to the pipe exit plane ($y < 1d$) or near the front of jet in the starting vortex. For times near the jet initiation, the outliers in the jet are likely associated with a combination of the very high seeding density in the jet fluid as it exited and large velocity gradients in the jet fluid. For intermediate times, the outliers in the jet are likely associated with a combination of the very high seeding density in the jet, large velocity gradients in the jet fluid, and the rotation of the jet fluid into and out of the plane of the laser. The number of outliers in the jet decreased as the time after injection increased. Outliers in the starting vortex are likely associated with the three-dimensional motion of the vortex. Regions of high shear (steep velocity gradients) also appear at various times and in various places throughout the flow and contributed to the generation of spurious vectors.

After three passes and the application of the moving average filter, up to 70% of the velocities in the fields consisted of interpolated vectors. This high percentage is attributed to the large dynamic range in the instantaneous velocity

fields generated in these unsteady experiments. The error may be minimized by optimizing the PIV technique in several ways: reducing the spatial extent of the camera field of view, reducing the timing between laser pulses, and calibrating the seeding density in the jet for particular instants and locations of interest in the jet. However, this optimization cannot be completed without *a priori* knowledge of the range and distributions of velocities to be expected in the flow fields at different locations and at different times. This information was not known before this study was undertaken, and it was therefore necessary to begin with a characterization of the overall flow behavior to establish a baseline. Due to the highly variable nature of the flows from this experimental setup, this characterization was time-consuming. Therefore, the work presented here lays the groundwork for additional studies in this same experimental setup, which may yield improved velocity measurements and detailed analysis of specific regions of the flow. Nevertheless, the interpretation of the flow behavior presented here should not be significantly altered with these improved measurements. In other words, it is expected that additional measurements may refine the details of the motion, but the broad characterization of flow behavior presented here significantly improves understanding of unsteady jets developed using the bulk visualization presented in section 3.1. Therefore, the interpolated values in the velocity field are considered acceptable for these broad characterization purposes. Accordingly, the data may be appropriate for qualitative comparison against

numerical models of analogous volcanic eruptions or other flows, but its utility in quantitative validation exercises may be limited.

The experiments described here were conducted at approximately 3.4MPa, the low momentum condition described in section 3.1. This maximized the time the jet front remained within the field of view of the camera. For non-buoyant and buoyant jets, instantaneous flow fields were measured for 100 experiments over a range of total injected volumes. As discussed in the introduction, the value of P, which is a parameter that identifies the structure that will form during a steady injection, depends only on total injected volume when the vent area remains constant. Thus, the total injected volume for each experiment was calculated according to equation 3.1 above. The frequency distributions of the calculated volumes for the non-buoyant and buoyant jets are shown in Figures 3.5 and 3.6, respectively. The mean injected volume for the non-buoyant jets was 64.0 cubic centimeters, and the mean injected volume for the buoyant jets was 67.9 cubic centimeters. Experiments within 5% of these means were chosen to ensemble average according to methods analogous to those described in Section 3.1. Ensemble averages of the instantaneous velocity fields were then calculated, over the 27 qualifying experiments for the non-buoyant jets and over the 31 qualifying experiments for the buoyant jets. These averages were computed for each instant data was acquired. The ensemble-averaged source conditions for the internal measurements of non-buoyant jets are summarized in Table 3, along with the source condition of a single, representative experiment from the ensemble. The

ensemble averaged source conditions for the internal measurements of buoyant jets are summarized in Table 4, along with the source condition of a representative, single experiment.

The accuracy of an ensemble average improves when more experiments are part of the ensemble. When a small number of realizations comprise the ensemble, there may be areas of low coherence or data loss where velocities strongly vary between realizations. A universal number does not exist for the exact number of realizations that need to comprise the ensemble to prevent data loss [*Adrian and Westerweel*, 2011]. The value depends on the flow situation and the purpose of measurements. Ensemble averages are meant to be taken over a set of experiments with identical initial conditions. Identical initial conditions in these experiments are defined as those experiments with similar total volumes injected. The purpose of this study was to investigate the evolution of the flow over time rather than to achieve a statistically convergent data set, and thus visual inspection of the ensemble of 27 or 31 experiments suggests the ensembles are sufficiently large for this purpose. However, areas of low coherence and data loss in the ensemble average field are expected with this ensemble size. The low coherence seems to affect the measurements in the jet more than the ambient fluid. Considering the low coherence in the ensemble for the motion of the jet fluid, an individual experiment was chosen to represent the evolution of all experimental runs in the ensemble and to illustrate the main features of the flow development that are not evident from the ensemble.

For perspective, a similar experimental study was published by *Ghaem-Maghami and Johari* [2010] after completion of their experiments which found that 2000 experimental runs were needed for convergence of the ensemble statistics for *steady* finite-volume flows, suggesting a much larger number would be required for unsteady flows. Based on the results from 100 experimental runs (realizations) in this apparatus, 27 experiments of every 100 would be similar enough to ensemble. Thus, to obtain the minimum of 2000 experiments for a convergent ensemble average, over 6000 experiments would be required. At peak efficiency, I ran one experiment in thirty minutes, which suggests that over 3000 hours of data collection alone would be required to obtain an experimental set of sufficient size. This estimate does not include a number of additional steps required to obtain this data, including data processing, which takes about four times longer than data collection. Obtaining that type of data set using this apparatus would require such a significant undertaking that it is cost-prohibitive on the grounds that I've outlined only bare requirements for the minimum number of experiments for a statistically convergent data set. Furthermore, there's no guarantee that these efforts would be sufficient to produce a statistically convergent set for *unsteady*, finite-volume flows. Furthermore, in the study referenced, the statistics converged for the velocity fields in the self-similar region of the far field, which indicates nothing about the convergence anywhere else in the flows. Additionally, due to the significant time variation in these flows, statistical convergence would likely be achieved at a *different* number of

experiments for *each* instant. Thus, statistically convergent data sets were not the objective of this study.

Figure 3.1. Schematic of the experimental apparatus for the external jet experiments.

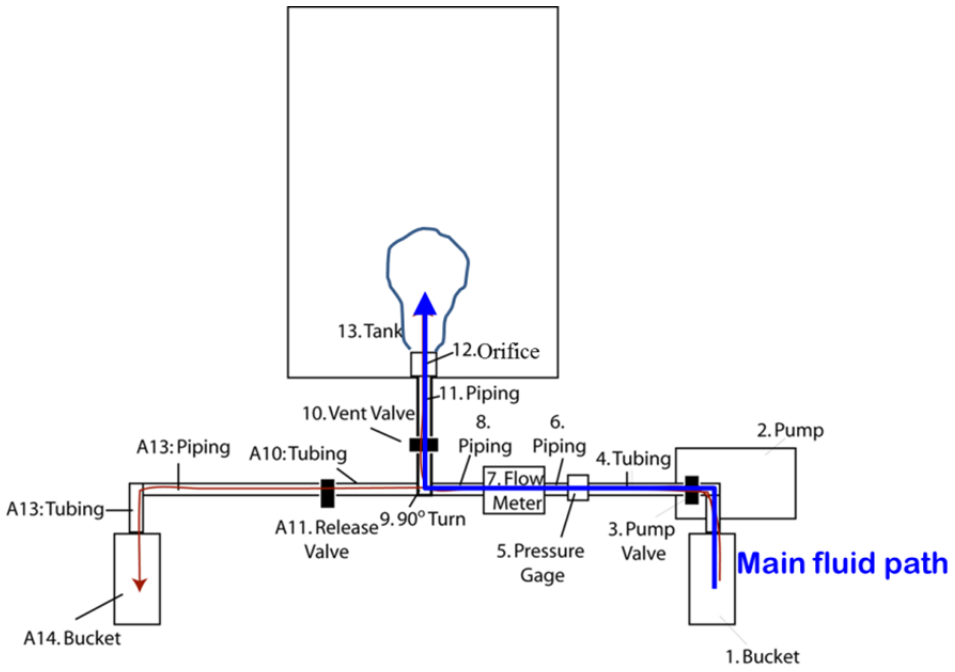

Figure 3.2. Mass-specific momentum flux at the source for the individual (grey) experiments, the ensemble average (red) for each experimental condition, and one standard deviation from the ensemble average (black). The experimental conditions are H3 (a), L3 (b), H9 (c), L9 (d), H15 (e), and L15 (f).

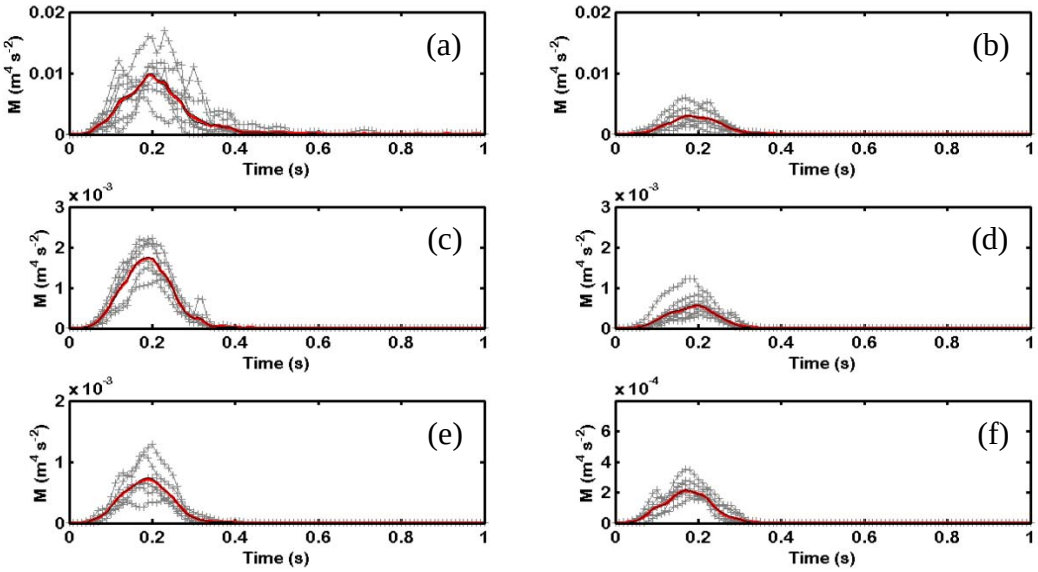

Figure 3.3. Schematic of the PIV process.

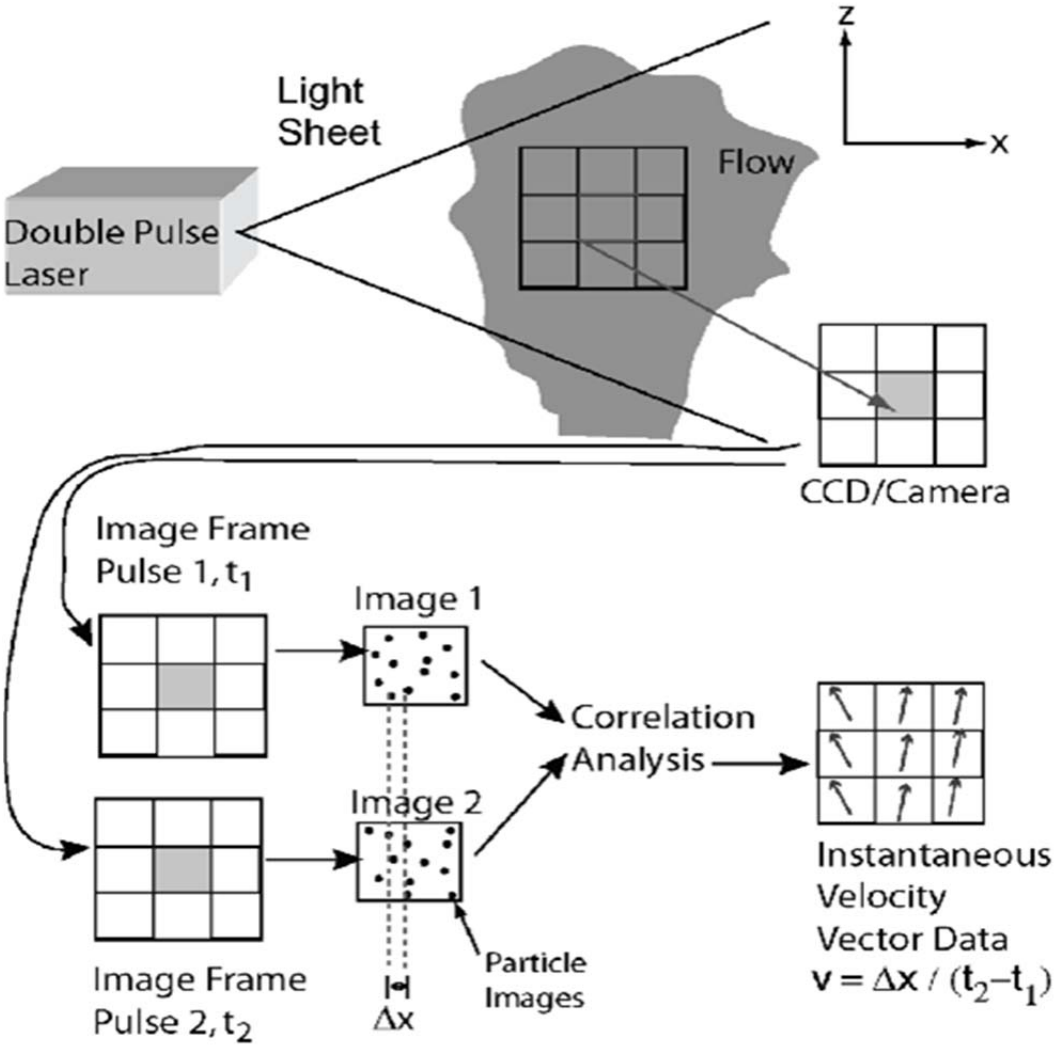

Figure 3.4. Schematic of experimental apparatus used for internal flow measurements.

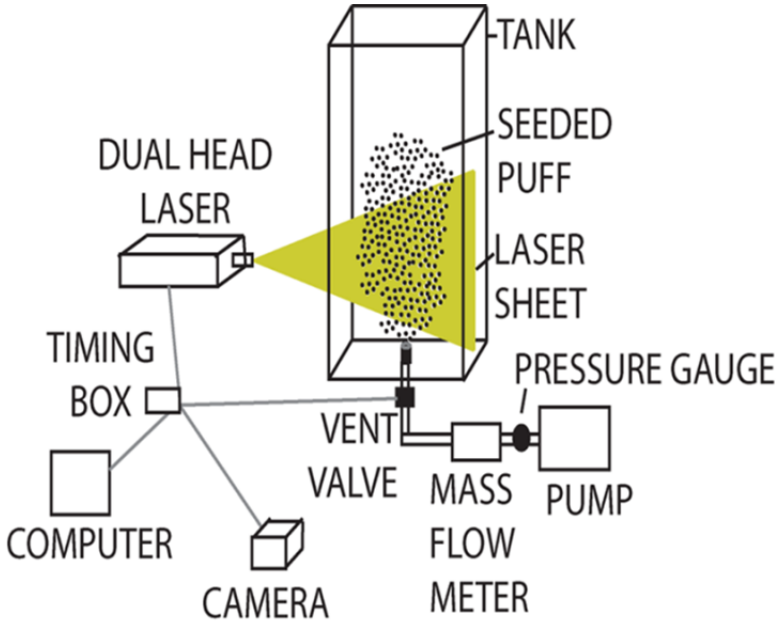

Figure 3.5. Histogram of injected volume for internal measurements of non-buoyant jets.

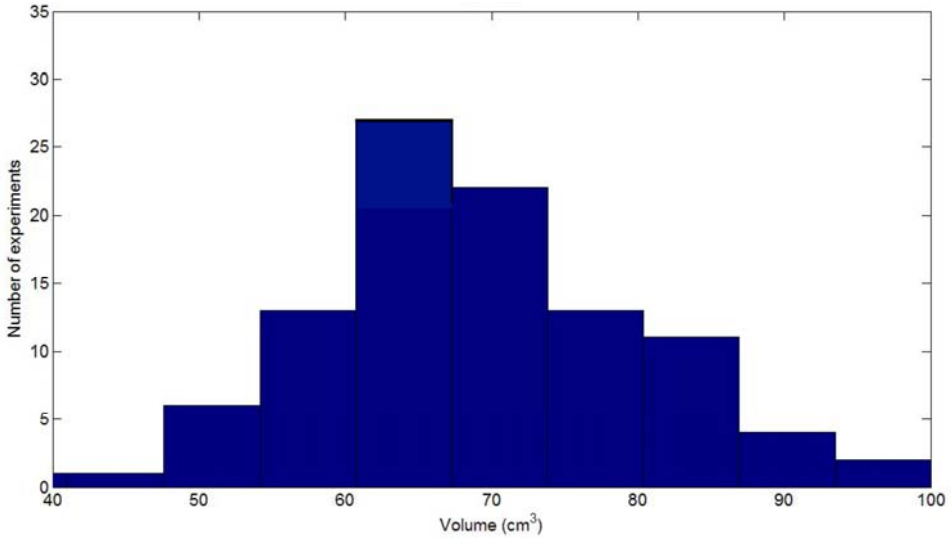

Figure 3.6. Histogram of injected volume for internal measurements of buoyant jets.

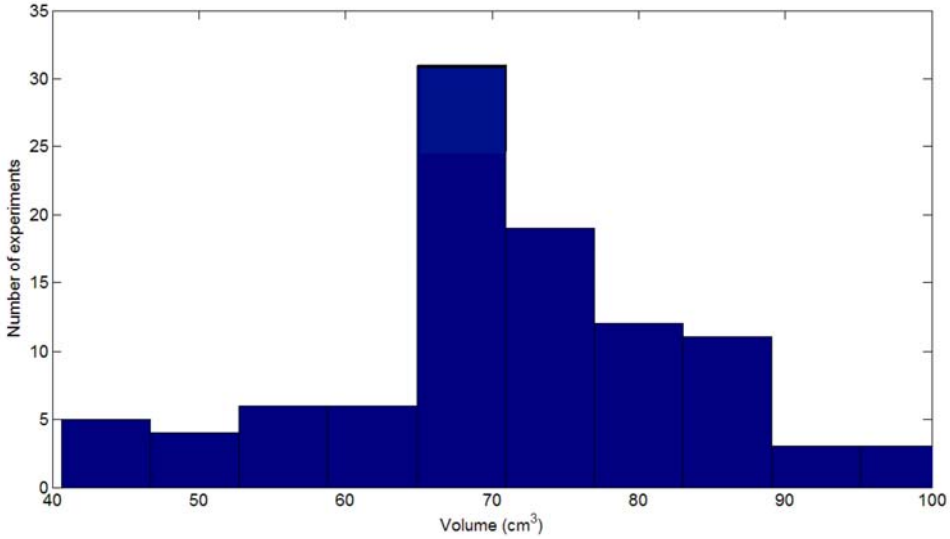

Table 3.1. Summary of ensemble-averaged source conditions for the external non-buoyant jet experiments.

Experiment Condition	$V_{0,max}$ (m s^{-1})	$Re_{0,max}$	Pulse (s)	Volume Injected (cm^3)	Momentum Injected (m^4 s^{-1})	P
H3	32.3	96,752	0.28	39.5	9.49 E-05	14.02
L3	20.7	62,041	0.25	24.0	3.59 E-05	11.20
H9	4.4	39,579	0.27	47.4	1.65 E-05	4.87
L9	3.0	26,720	0.29	33.4	8.93 E-05	3.97
H15	2.1	31,260	0.28	65.0	1.17 E-05	3.07
15	1.3	18,807	0.29	40.6	4.91E-05	2.42

Table 3.2. Summary of ensemble-averaged source conditions for the external buoyant jet experiments.

Experiment Condition	$V_{0,max}$ (m s^{-1})	$Re_{0,max}$	Pulse (s)	Volume Injected (cm^3)	Momentum Injected (m^4 s^{-1})	$Fr_{0,max}$
H3	29.4	88,294	0.53	50.4	1.01 E-03	980
L3	15.6	46,915	0.42	22.5	2.43 E-04	520
H9	4.4	39,885	0.50	56.2	1.72 E-04	85
L9	3.2	29,173	0.43	38.6	8.90 E-05	62
H15	1.6	23,260	0.49	54.3	5.96 E-05	24
L15	1.0	15,728	0.40	35.9	2.82E-05	15

Table 3.3. Summary of ensemble-averaged source conditions for the internal non-buoyant jet experiments.

Experiment Condition	$V_{0,max}$ (m s^{-1})	$Re_{0,max}$	Pulse (s)	Volume Injected (cm^3)	Momentum Injected (m^4 s^{-1})	$Fr_{0,max}$
20-mm ID*, Open Pipe, Single Experiment	0.96	19,213	0.49	62.1	4.33E-5	12.4
20-mm ID, Open Pipe, Ensemble	0.92	18,357	0.52	59.7	3.91E-5	11.9

*ID = inner diameter

Table 3.4. Summary of ensemble-averaged source conditions for the internal buoyant jet experiments.

Experiment Condition	$V_{0,max}$ (m s^{-1})	$Re_{0,max}$	Pulse (s)	Volume Injected (cm^3)	Momentum Injected (m^4 s^{-1})
20-mm ID* Open Pipe, Single Experiment	1.00	20,042	0.50	62.1	4.48 E-05
20-mm ID Open Pipe, Ensemble	0.94	18,716	0.52	61.6	4.08 E-05

*ID = inner diameter

Chapter 4

RESULTS FOR UNSTEADY JET EXTERNAL EVOLUTION

4.1. Introduction

Observations suggest that volume flux may vary in time during volcanic eruptions [e.g., *Druitt et al.*, 2002; *Clarke et al.*, 2002; *Iguchi et al*., 2008; *Gottsman et al*., 2012]. For eruptions which generate volcanic plumes, time-varying volume flux may lead to unsteady dynamic conditions in the plume [e.g., *Sparks et al*., 1997]. These conditions most likely arise when the volume flux variations are on the order of $1/N$ where N is atmospheric buoyancy frequency. The value of N is typically ~ 0.01 seconds [e.g., *Sparks et al*., 1997] and thus variations in source conditions that occur over a duration less than 100 seconds *may* lead to unsteady conditions in the volcanic plume. However, the response of volcanic plumes to variable eruption rates is not well understood [e.g., *Scase et al*., 2009; *Kitamura and Sumita*, 2011]. Without this understanding the hazards associated with plumes from this class of eruption cannot be adequately assessed [e.g., *Mastin et al*., 2009]. Furthermore, most models of volcanic plumes now include an approximation that eruption rates remain constant over the eruption duration [e.g., *Woods*, 1988; Suzuki et al., 2005; *Ogden et al*., 2008; *Kaminski et al*., 2011]. Yet these volcanic plume models are based on simple turbulent models of steady jets which do not accurately predict experimental observations of unsteady jets [e.g., *Boree et al*. 1996; *Zhang and Johari*, 1996; *Querzoli*, 2010]. Thus, ignoring the dependence of turbulent dynamics on time-varying eruption

rates may lead to inaccurate hazard predictions for volcanic plumes from variable-rate eruptions. Volcanic plume rise, dilution, and collapse, are all processes important to effectively evaluating volcanic plume hazards [e.g., *Sparks et al*., 1997; *Mastin et al*., 2009]. Therefore, understanding whether and to what extent variable eruption rates may influence these processes may enrich our understanding of the response of volcanic plumes to variable eruption rates and improve the analysis of hazards from plumes generated by variable-rate eruptions.

According to the standard model for steady volcanic plumes [e.g., *Sparks and Wilson*, 1976; *Carey and Sparks*, 1986; *Woods*, 1988], the structure of steady volcanic plumes can be divided into three regions on the basis of the factors that govern the dynamics. At the vent, the volcanic plume motion may be dominated by the force of momentum which is derived from the expansion of gas that was formerly contained in the magma [e.g., *Sparks and Wilson*, 1976; *Woods*, 1988]. As the plume ascends, it entrains atmospheric air through turbulent eddies at the edges of the plume. Turbulent eddies internal to the plume then transport and mix the ambient air with the material in the plume [e.g., *Sparks and Wilson*, 1976; *Woods*, 1988]. The plume contains gas and hot tephra particles (quenched magma) which transfer heat to the cooler atmospheric air during the mixing process. The process of turbulent entrainment and mixing results in the dilution of the initial momentum forces, a decrease in the bulk density of the plume and the production of momentum due to buoyancy forces [e.g., *Sparks and Wilson*, 1976; *Carey and Sparks*, 1986; *Woods*, 1988]. If the momentum generated by the buoyancy forces

is sufficient then buoyancy forces dominate the plume dynamics and the plume continues to ascend [e.g., *Sparks and Wilson*, 1976]. Otherwise the plume collapses under the force of gravity once the initial momentum is diluted below a threshold necessary to support the rise [e.g., *Sparks et al*., 1997].

Dilution of the initial momentum, including the entrainment process, therefore, may play a role in the rise and collapse of volcanic plumes. Nevertheless, this contribution has been neglected in some volcanic plume models on the basis that, for large volcanic plumes (rise >20 km), buoyancy-driven dynamics may dominate over 90% of the motion [*Sparks and Wilson*, 1976]. It is similarly neglected for very small volcanic plumes (rise ~ 1 km) which likely have very small amounts of initial momentum [e.g., *Sparks et al*., 1997]. It is included in some volcanic plume models [e.g., *Woods*, 1988; *Sparks et al*., 1997; *Scase* 2009] to account for the initial decrease in velocity that occurs as the inertia is dissipated that was imparted to the plume during eruption. These results suggest that the overall significance of the momentum-driven rise regime may be non-trivial even for large volcanic plumes [e.g., *Scase* 2009]. Moreover, if the eruption rate strongly varies, then the plume may experience large and sudden variations in the mean rate of flow and momentum dilution may have a nontrivial control on dynamics; in this situation, the volcanic plume is unsteady in the mean as well as turbulent. Processes like turbulent entrainment and mixing directly depend on the mean volume flux and may therefore vary in response to volume flux changes. Turbulent entrainment and mixing are important for achieving buoyant rise

conditions, thus, collapse conditions may also change in response to volume flux changes. As the flow adjusts to the changes, flow structure may change as may the way mass, momentum, and energy are transported through the flow. Thus, understanding the controls on momentum dilution when volume fluxes vary may provide insight into the potential consequences of variable volume fluxes on volcanic plumes and their overall evolution.

In particular, understanding the length and time-scales over which momentum dominates volcanic plumes and the processes that contribute to entrainment and mixing during that dynamic phase are critical for understanding the threshold conditions that separate buoyant rise from collapse conditions [e.g., *Valentine et al*., 1991; *Kaminski et al*., 2005; *Suzuki et al*., 2005]. Some insight into the length and time-scales over which momentum dominates can be provided by field-based studies of volcanic plumes. In these studies, a variety of optical-based instrumentation is used to investigate the behavior of volcanic plumes [e.g., *Johnson*, 2005; *Patrick*, 2007a; *Yamamoto et al*., 2008; *Mori and Burton*, 2009]. From these studies we know that volcanic plumes vary in shape, size, temperature, velocity, final rise heights, complexity, and their evolution in time. Photographs of short-lived plumes are shown in Figure 1.2 to demonstrate the wide variety of plumes produced in nature. These techniques typically focus on the change in the external boundaries of the plume. The motion of the boundaries reflects the net effect of a number of external and internal processes that may vary as the mean flow varies. Because of this proposed complexity, it may be difficult

to detect, derive or quantify changes in the volume flux using observable changes in the external boundaries of the flow. This difficulty complicates the task of understanding the response of turbulent flows to transient source conditions for situations where the internal structure of a flow is not accessible, as is the case with volcanic plumes. While techniques such as Doppler radar can be used to investigate some aspects of the internal behavior of volcanic plumes [e.g., *Scharff et al*., 2008; *Gouhier and Donnadieu* (2008)] these techniques are limited to relatively dilute plumes. Studies which use other bands of the electromagnetic spectrum (i.e., infrasound) are used to investigate other aspects of plume motion including the energy imparted to the atmosphere during eruption initiation [e.g., *Johnson et al*., 2005; *Caplan-Auerbach et al*., 2010] and the turbulence characteristics of the plumes [e.g., *Matoza et al*., 2009].

All of these studies address aspects of time-varying plume motion, however, a simple dynamic model that can describe the evolution of time-varying source flux in terms of easily observable parameters such as plume front propagations and radial expansion does not yet exist. Moreover, images of volcanic plumes from short-duration eruptions are becoming increasingly common in volcanology, in part because they are more common in general than steady, continuous, long-lived eruptions. As a result, additional motivation for a study of transient source effects on near-vent volcanic plume dynamics comes from a desire to effectively interpret field observations of transient eruptions.

Simple analytical and empirical models of turbulent plumes and puffs are currently used to interpret volcanic plume observations. A generalized analytical model derived by *Morton et al*. [1956] for continuous and instantaneous sources of buoyancy rising through a stratified atmosphere is most commonly used. According to this model, jet rise from a continuous source is dependent on the source volume flux whereas puff rise from an instantaneous source is dependent on the total amount of material released. They also have a different dependence on time: continuous sources rise at a rate proportional to the square root of time, while instantaneous sources rise at a rate proportional to the fourth root of time. This model has been modified in the form of variations in the empirical constants [e.g., *Sparks et al*., 1997] to account for atmospheric conditions common for volcanic plumes. In general, good agreement has been found between the empirical model and some well-documented volcanic plumes [e.g., *Wilson et al*., 1978; *Sparks et al*., 1997; *Mastin et al*., 2009].

However, there are some eruptions which deviate from this model for reasons that are not distinguishable within the simple structure of the model [*Mastin et al*., 2009], such as Vulcanian-style eruptions [e.g., *Caplan-Auerbach et al.*, 2010], which cannot be easily classified as steady and continuous or instantaneous. Alternative to simple analytical and empirical models, are numerical approaches that account for transient eruption rates [e.g., *Clarke et al*., 2002], but these have been applied only to single, well-characterized eruptions at individual volcanoes. Nevertheless, these results show that large changes in vent

and plume conditions may occur on very short time scales in agreement with other observations of similar eruptions [Gottsman et al., 2012]. This result suggests that strong fluctuations in the volume flux may be possible or even typical.

In contrast, a more general model developed recently by *Scase* [2009] extends existing theoretical volcanic plume models [*Woods*, 1988] to account for time-varying volume fluxes. Though this model relies on important assumptions that are most appropriate for steady turbulent flows, in particular, Taylor's turbulent entrainment hypothesis [*Morton et al.*, 1956], the *Scase* [2009] approach clearly demonstrates that time-varying volume fluxes may produce plume behavior that is distinct from eruptions with steady and long-lived source conditions. Along the same lines, experimental work by *Kieffer and Sturtevant* [1984] and *Kitamura and Sumita* [2011] indicate that volume fluxes which are suddenly initiated but then remain constant result in turbulent jets where the fluid at the front of the flow is affected by the transient condition but the fluid behind the front is essentially steady. While this source condition varies from one that is suddenly initiated and remains unsteady, these experiments provide valuable information on the variations that can arise in the evolution process when the volume flux is quasi-steady.

Additional studies using numerical approaches have demonstrated that significant variations in the evolution process can also arise even when the volume flux is constant if the jet is overpressured [e.g., *Valentine*, 1988; *Odgen et*

al., 2008], the vent geometry is changing [e.g., *Odgen et al*., 2011], the atmosphere is important [e.g., *Tupper et al*., 2009], or the plume is partially collapsing [e.g., *Valentine et al*., 1991; *Kaminski et al*., 2011]. Thus, it may be difficult to distinguish the variations in volcanic plume behavior relating to variable eruption rates from those associated with many of the other variables that could simultaneously enter the problem.

As a consequence of the above discussion, work presented here aims to investigate time-dependence in volcanic eruptions by considering the conditions in which Vulcanian-plumes are generated. This type of eruption is expected to produce a strongly time-dependent jet phase (momentum-driven) that may not be accurately described by a volcanic plume model based on buoyancy-driven turbulence alone and underlain by assumptions of constant volume flux. In fact, observations of transient Vulcanian eruptions suggest eruption rates increase for some period after eruption initiation (~10-30 s) after which they peak and then decline to negligible values on the order of tens to 100 seconds later [e.g., *Scase*, 2009; *Clarke et al*. 2002; *Druitt et al*. 2002].

To isolate time-variation in driving turbulent dynamics we therefore consider the rise of turbulent jets in a still ambient. In this situation there are no external forces acting on the jet and the motion of the jet is a function of two factors: the initial flux of momentum at the source and the rate it is diluted by the turbulent mixing and entrainment process. Thus, in theory, if both the flux of momentum and the motion of the jet are accurately measured, the turbulent

mixing and entrainment process and its dependence on the time-varying source conditions can be investigated. We therefore conducted a series of analogue lab experiments where we examined the behavior of turbulent jet rise resulting from time-varying injections of momentum flux. Injection characteristics and the resultant jet rise, spread, and shape were measured as functions of time for various source diameters, source Reynolds numbers and amounts of injected source fluid. The measurements of jet heights and widths were compared with predictions from steady similarity theory to evaluate the use of steady theory in approximating the flows described here. Finally, we used that evaluation to investigate the factors that control the dissipation of upward momentum for unsteady turbulent jets.

4.1.2 Simple Turbulent Jet Models

Two simple models for turbulence generated by the action of momentum forces are most appropriate for these experiments: a starting jet and a puff.

The starting jet model is based on the starting plume model of *Turner* [1962]. *Turner* [1962] proposed a theoretical model for starting plumes entering neutral surroundings as an intermediate theory to continuous and instantaneous models. This theory allowed for the jet width and height to grow in time, unlike a continuous model, but includes a steady source flux, unlike an instantaneous model. He described the structure of a starting plume as comprised of two parts – a spherical vortex ball atop a conical jet. The spherical front or cap was different from an isolated instantaneous puff or thermal by the influx of mass and

momentum that was supplied to it by the conical jet below; the conical jet, or tail, region was considered to have properties like that of a steady jet. *Turner* [1962] then reasoned that rotational motion in the cap resulted in the turbulent entrainment of ambient fluid into the cap as well as entrainment of fluid from the tail below. And, furthermore, the cap entrains equal amounts from each region (ambient and tail). As a consequence, the momentum of the starting jet was diluted more rapidly than an established jet but less rapidly than a puff. By experiment, *Turner* [1962] found that the front of the starting plume evolved at 72% of the steady plume velocity in the tail. He also maintained that the shape of the starting plume – a spherical cap atop a conical tail – was sustained while its size was increasing.

Experimental work has extended *Turner*'s [1962] conceptual model to momentum driven jets. Using an assumption of self-similarity and an argument based on the conservation of momentum, *Hill and Ouellette* [1999] derived an expression to estimate the rise rate of a starting jet as a function of the momentum flux at the source

$$h(t) = C_1 \dot{M}_0{}^{1/4} t^{1/2} \tag{4.1}$$

where $h(t)$ is the jet height at time *t*, $\dot{M}_0$ is the momentum flux at the source, that is, the rate momentum is being added to the jet at the source, and *t* is the time from the start of the release. The parameter C_1 is a coefficient of proportionality whose value was found by experiment to be approximately 3.0 for steady and starting jets with circular cross sections. Experimental work by *Sangras et al*.

[2002] measured this value to be 2.8. *Sangras et al*. [2002] noted that although the value was similar there was disagreement about when the expression was valid. While *Hill and Ouellette* [1999] reported the appropriate range of application is for distances greater than 20 or 30 times the distance of the source diameter, the observations of *Sangras et al*. [2002] suggested the range was greater than 60 times the diameter of the vent. This distance refers to the location from the vent where the self-similar assumption can be reasonably made based on the observation that the ratio between the maximum width of the jet at any time to its height at that time remains constant.

A constant aspect ratio suggests that the internal forces driving the rise and the spread are in direct balance with each other at all distances from the source and thus the flow is said to be in a state where its dynamics are self-similar. It is also by this assumption of self-similarity that *Morton et al*. [1956] reasoned that in this state the vertical momentum flux driving the rise of the flow was balanced by the radially directed turbulent diffusion of momentum which governed the spread. To relate the vertical motion to the radial motion they formulated the entrainment hypothesis which states that if the width grows by the turbulent entrainment of ambient fluid and if the width is growing in direct proportion to the height then the radial component of velocity by which fluid is entrained at the edge of the jet is directly proportional to a characteristic vertical component of velocity interior to the jet. Thus the entrainment hypothesis follows directly from an assumption of self-similar dynamics. This assumption is commonly used in

mathematical models of turbulent flow from constant sources. While it seems to apply to jets started impulsively with a momentum flux that remains constant, it may not apply to flows started impulsively with a momentum flux that remains variable.

A puff is an instantaneous release of momentum. Puffs take on two main geometries spherical (axial) and cylindrical [*Richards,* 1965]. A puff is analogous to a thermal, which is an instantaneous release of buoyancy. Similarity scaling for puffs moving in a still and uniform ambient in self preserving regions

$$h(t) = C_1 {M_T}^{1/4} t^{1/4} \tag{4.2}$$

where h is the height of the flow at time t, C_1 is a constant that is specific for experiment conditions, and M_T is the total mass specific momentum of the injection [*Sangras et al*., 2002]. The total momentum can be calculated by integrating the instantaneous mass specific source flux of momentum $\dot{M}_0\ (t)$ over the duration of the injection T according to

$$M_T = \int_0^T \dot{M}_0(t)dt. \tag{4.3}$$

It is of note that for both starting jets and puffs the height of the flow has a power law dependence on time; however, the power ½ in the starting jet case indicates a greater rise rate than the power ¼ in the puff case. It is also of note that the height to which the flow travels in a given amount of time is related to the source momentum flux, the power of time, and a coefficient of proportionality and not explicitly related to the injection pressure, velocity or nozzle diameter. This suggests that various combinations of injection pressure, nozzle diameter, and

velocity (which may not be independent of the first two) that produce the same amount of momentum flux should produce jets with similar rise behaviors.

4.1.3 Properties of Unsteady Jets

The expressions above strictly apply to conditions where the momentum flux is constant or instantaneous and thus the flow reaches a dynamic state that can be approximated by a self-similar assumption. Therefore it is not obvious whether these relationships may be extended to include the effect of variable injection rates. However, experimental work by *Querzoli et al.* [2010] suggests that this theory can be extended to varying momentum flux by subdividing the behavior into intervals on the basis of whether the momentum flux is increasing in time or decreasing. The momentum flux studied in *Querzoli et al.* [2010] has a Gaussian-like distribution in time with an injection duration lasting 1.0 second. They found that the rise of the resultant jets was governed by two momentum scales in sequence – initially the jet rise was governed by the momentum flux but once the volume flux neared the peak of the Gaussian the jet rise was governed by the total amount of momentum that was injected to that point. This result is supported by the observation that once the instantaneous flux of momentum fell below the time-averaged flux of momentum, the shear layer that separated the jet fluid from the ambient fluid broke allowing ambient fluid to be entrained directly into the jet core rather than into the shear layer. In other words, while the shear layer is continuous, the instantaneous flux from the vent drives the rise behavior, but once the shear layer breaks a cap forms and the total amount of momentum

injected dominates the rise behavior. This result suggests that unsteady jet rise at this time is controlled by the dynamics of the cap, which may depend on but differ from the dynamics of the flow behind it.

This breaking or separation of the shear layer is consistent with other experimental observations that observe the formation of a vortex ring at the start of an impulsively started jet. Starting vortex rings are known to form in impulsively-started flows ejected from circular outlets (i.e., orifice plates, nozzles, open pipes, etc.) into still ambient fluids [e.g., *Richards*, 1965]. A boundary layer forms between the moving fluid and the still ambient generating high rates of shear at the jet boundary. This boundary layer is unstable and the fluid in the shear layer rolls back on itself to create the leading vortex ring. Both driving the flows with pressure (relative to piston-cylinder or gravity-driven flows) [*Krueger*, 2005] and using a circular orifice plate (as opposed to square, for example) as an outlet [*Mi et al.*, 2001] are known to increase the strength of the vortex ring. In many situations the starting vortex rings separate from the jet fluid beneath it and move separately from the rest of the jet fluid [*Gharib et al.*, 1998]. These isolated vortex rings are similar to puffs in that their motion is governed by the total amount of momentum contained within the structure. They differ however in the distribution of vorticity within the structure; vorticity surrounds a core in vortex ring but is distributed uniformly through a puff. Recent experimental work by *Ghaem-Maghami and Johari* [2010] indicate that rings and puffs also differ in the rates at

which they expand and entrain - rings entrain at a greater rate than they expand while puffs expand at a greater rate than they entrain.

They also observed that as the total volume of a puff increases the rate at which it expands increases relative to the rate it entrains; in other words, as the puff volume increases it entrains fluid at a decreasing rate. The ratio of expansion to entrainment was greatest for established steady jets [*Ghaem-Maghami and Johari*, 2010]. The study by *Ghaem-Maghami and Johari* [2010] was limited to jets driven by constant volume fluxes so the volumes did not change over time. Instead, the effects of volume were studied by conducting separate experiments with different injection durations of a constant volume flux. It is therefore not clear how these results may apply to jets driven by variable volume fluxes when the volume changes over time.

4.2 Methods

Overview. The experiments here investigate the effects of strongly varying volume flux on the rise characteristics of turbulent jets. Jets were generated by injecting water into a tank of still water through a vertically oriented pipe. Injection rates were measured with a mass flow meter. The bulk properties of the resultant jet - jet height and width - were then measured from time-resolved video records of jet motion in the tank.

A sketch of the apparatus used to generate the jets is shown in Figure 3.1. The fresh water bath filled a tank with dimensions 0.6 x 0.6 x 1.2 m deep to a depth of ~ 0.95 m. Both the bath and the source reservoir were filled from the lab

water supply and brought to room temperature before experiments were run to get rid of any air dissolved in it. Therefore, one value of the water volume, 1000 kg/m^3, was used for calculations in all experiments as the room temperature was 75 +/- 5 F for all experiments.

During a run, the pump used to generate the initial source pressure was turned off before the valve was opened. Since the pump was operated with a dial, a hard object (a dead 9V battery) was taped in the path of the dial such that turning the dial until it contacted that object allowed approximately the same initial pressures to be reached in each experiment. The initial pressure (the pressure just prior to vent opening) was read from a pressure gauge positioned inline prior to the mass flow meter. This value was then manually recorded.

Then approximately three minutes were allowed to pass between the pump turn off time and the valve opening time to allow transient motion in the plumbing system to subside. The valve was an electronically controlled pneumatic ball valve that opened in 80 milliseconds according to the manufacturer's specifications on the valve. This time was investigated by recording a 3.5 volt signal when the valve was triggered on a second channel on the digitizer for the mass flow meter. The time difference between the 3.5 volt signal and the first non-zero volume flux was 0.14 +/- 0.04 seconds. The source of the difference between the 0.08 seconds indicated by the manufacturer and the measured difference of 0.14 seconds is unknown. The addition of the electronic valve aided in the reproducibility of the injections and was added after the experiments in

Clarke et al. [2009] in which a ball valve was manually opened. Following the valve opening, source fluid entered the tank through an orifice that was raised 8 cm from the bottom of the tank.

I measured the mass flux of water that entered the tank with a Coriolis mass flow meter (Kueppers KCM3000) sampling at 100 hz. I did not set the form of the source time function or its duration; both were determined by the release of the pressurized fluid. I divided the mass flux by the volume of water to calculate the volume flux. The resulting functions, shown in Figure 3.2, were best fit by a Gaussian distribution in time and lasted for approximately 400 milliseconds.

There was some variability in the beginning of the injection that contributed to error in identifying the start of the injection in the mass flow meter data. This error could lead to an error in the start of approximately 0.04 seconds. The total volume injected was calculated by integrating the volume flux curve over the injection duration. The total volume injected ranged from 30 cm^3 to 100 cm^3 and depended on the initial pressure, vent diameter, and pressurization conditions for each run. The total volume of fluid pressurized in each experiment exceeded the volume of fluid released by a factor of approximately 100.

While the run procedure minimized variations in starting conditions, the nature of turbulent flows is such that they vary for every individual experiment run. Nine runs were therefore performed for each starting condition. To reduce the influence of variation in each experiment and simultaneously retain the time variation information, averages were calculated for each flow condition by

ensemble averaging the time series data over the nine runs for each flow condition. The ensemble average of the volume volume flux $< \dot{Q}(t_1) >$ at time t_1 was calculated according to the following equation

$$< \dot{Q}(t_1) > = \lim_{N\to\infty} \frac{1}{N} \sum_{i=1}^{N} \dot{Q}_i(t_1) \quad (4.4)$$

where *N* is the number of experiments, in this case *N* = 9. This calculation was then repeated for all times in the time series. Here, the brackets are used to denote an ensemble average. Similarly, the ensemble average of the height $< h(t_1) >$ at time t_1 was found according to the following equation

$$< h(t_1) > = \lim_{N\to\infty} \frac{1}{N} \sum_{i=1}^{N} h_i(t_1) \quad (4.5)$$

I recorded the motion of the resultant jets using a high-speed camera positioned perpendicular to one of the tank walls. On the opposite wall, I formed a backdrop by taping a sheet of translucent white paper to it. Then to increase the contrast between the dyed source and ambient waters I backlit the backdrop with a uniform light sheet using studio lights (Speedotron) and a light gel.

I imaged a field of view of 1000 mm by 1000 mm through a fixed focal point lens on a CCD camera (Redlake MotionPro 2000) with a chip of 1024 by 1024 pixels and a bitdepth of 8 bits. I recorded at 100 hz yielding a spatial resolution of ~1 mm/pixel and temporal resolution of 10 milliseconds. Jet motion was measured from the video record by identifying the location of the flow height in each video frame.

The video camera was not time synchronized with the mass flow meter. Instead, it was assumed that the first mass flow meter measurement above

background noise corresponded with the first video frame with visible dye movement. This assumption was later tested by adding an LED that lit when the vent was triggered to the video field of view. This trigger signal was also sent to the digitizer for the mass flow meter. It therefore served as a common reference time and enabled synchronization of the video and mass flow meter data. This test indicated that 9 +/- 3 video frames were recorded between the time the LED lit and the first visible dye movement in the video.

I examined unsteady jet behavior in six experimental conditions characterized by the diameter of the circular orifice from which the jet entered the tank and the pressure in the system immediately prior to the valve opening. Three orifice diameters, 3, 9 or 15 mm, were used at each of two initial pressure conditions, 3.4 and 6.9 MPa. The orifice diameter influenced the Reynolds number via the inverse relationship between vent velocity and orifice diameter which I discuss in more detail in the following section. Thus, these six conditions enabled a test of the Reynolds number effect on the unsteady rise of the jets. The ensemble averaged values of the injection characteristics for each of the six flow conditions tested in the above apparatus are summarized in Table 3.1, and discussed below.

4.3 Results and Discussion

4.3.1 Source Characteristics

The nature and duration of the subsequent release were not set a priori but were dependent on the fluid pressurization and release. The ensemble averaged

source momentum flux, $\langle \dot{M}_o(t) \rangle$, or the ensemble averaged momentum per unit mass passing through the plane of the orifice per unit time, was calculated according to the following equation

$$\langle \dot{M}_o(t) \rangle = \langle \dot{Q}(t) \rangle \langle V_o(t) \rangle = \langle \dot{Q}(t) \rangle \left(\frac{\langle \dot{Q}(t) \rangle}{A_o} \right) \tag{4.6}$$

where $\langle V_o(t) \rangle$ is the ensemble averaged flow velocity in the plane of the orifice and A_o is the cross sectional area of the orifice. The chevron brackets indicate and ensemble averaged quantity. By using the relationship $\langle V_o(t) \rangle = \langle \dot{Q}(t) \rangle / A_o$, I assume the fluid exits the vent with a velocity distribution that is equal for all positions within the cross section (i.e. uniform) and the losses sustained by the moving fluid between the mass flow meter and the orifice are negligible. Between the mass flow meter and the orifice are sections of rigid pipes of different materials with different internal diameters, a tee connection to transition the horizontal flow necessary for the mass flow meter to vertical flow necessary for the injection, and the valve. Consequently, the fluid likely sustains losses between the mass flow meter and the orifice. These losses are expected to be in direct proportion to the instantaneous Reynolds number of the flow. As the flow is unsteady, the velocity and thus the Reynolds number varies throughout the flow and over time and therefore these losses are difficult to quantify. Consequently, they are assumed negligible as a first approximation of the dynamics. Thus the velocity calculated by assuming that they are negligible yields a maximum estimate of the velocity.

The source momentum flux is shown as a function of time in Figure 3.1 for the individual experiment runs (gray), the ensemble mean of all the runs in each condition (red), and the variation of one standard deviation from the ensemble mean (black). Each ensemble average consists of nine experimental runs. The ensemble curves are not smooth most likely because there are only nine runs in the ensemble; more runs would result in a smoother curve. The delay time between the trigger and the flow initiation was determined for each experiment condition by identifying the first instant the ensemble averaged momentum flux exceeded the background noise level and ranged from 0.14 +/- 0.04 seconds. The delay time was used to adjust the ensemble averaged momentum flux for each condition so that the flow initiated at 0.01 seconds. The ensemble averaged source momentum flux rates for all experimental conditions are plotted in Figure 4.1. For all conditions, source momentum flux generally increased for the first 200 milliseconds, then decreased for 200 milliseconds and ceased at approximately 400 milliseconds. Source momentum flux was greatest for smaller orifice diameters and larger initial pressures.

The source Reynolds number for the experiment ensemble $\langle Re_o(t) \rangle$ was calculated as a function of time, *t*, according to the expression

$$\langle Re_o(t) \rangle = \frac{\langle V_o(t) \rangle \, d_o}{\upsilon} \tag{4.7}$$

where d_o is the diameter of the orifice and υ is the kinematic viscosity of water. The variation of the source Reynolds number over time is shown for each experimental condition in Figure 4.2. Minimum Reynolds numbers were observed

at the start of the flow and had values on the order of 10^2 to 10^3. Maximum Reynolds numbers were observed at the flux peak and had values on the order of 10^3 to 10^5. In each experiment the jet Reynolds number increases by a factor of 100 within the first 200 milliseconds of the experiment making it a strongly varying flux. Reynolds numbers for Vulcanian style eruptions are estimated to range from $10^4 – 10^7$ [*Sparks et al.*, 1997] based on estimates for the diameter of the circular volcanic vent, velocity of ejecta at the vent, and the bulk kinematic viscosity of the ejected material suggesting that the results of these experiments may apply only to smaller Vulcanian style events.

The average volume of fluid released during the injection, Q_T is listed in Table 3.1 for each condition. This value was calculated by integrating the ensemble averaged volume flux curve over the ensemble averaged pulse duration. The duration was difficult to define using a universal criterion for the end of the injection; however, the end of the injection was generally chosen as the time the ensemble averaged flux first fell below a critical value of ~0.2 kg/s. The time period between the adjusted starting time and threshold end time is described here as the injection time or pulse, *T*. The pulse was approximately constant for all experimental conditions as indicated in Table 3.1. The total volume injected during the pulse was calculated according to the following expression

$$Q_T = \overline{\langle \dot{Q}(t) \rangle} = \lim_{t\to\infty} \frac{1}{T} \sum_{i=1}^{T} \langle \dot{Q}(t_i) \rangle. \quad (4.8)$$

The overbar indicates a time-average. The total injected momentum, M_T, listed in Table 3.1, is the time-integrated momentum flux over the pulse and was calculated according to the following expression

$$M_T = \overline{\langle \dot{M}(t) \rangle} = \lim_{t\to\infty} \frac{1}{T} \sum_{i=1}^{T} \langle \dot{M}(t_i) \rangle. \quad (4.9)$$

When the ensemble averaged momentum flux time series for each condition is normalized by the peak value of the momentum flux for that condition, the curves for all experiments collapse together as shown in Figure 4.3. This collapse suggests that all conditions have a similar pulse history despite their differences in the magnitudes of the momentum flux and Reynolds number. Consequently, variations in flow behavior between experiment conditions is associated with the magnitudes of momentum flux and Reynolds number rather than the pulse history while the common behaviors for all conditions is associated with the pulse history.

4.3.2 Qualitative Observations of Jet Evolution

I now describe the morphological characteristics of the resulting turbulent jets. Flow patterns for the six experimental conditions were classified into two categories based on the generation of a vortex ring that separated from the rest of the flow. While experiments with the 3-mm and 9-mm-diameter orifices did not appear to generate separating vortex rings, experiments with the 15-mm diameter orifice did. The evolution of individual flows within each of these classes was generally similar and therefore the evolution of a representative experiment is used to illustrate the evolution of each class. The evolution sequence presented

here is interpreted from the video images of the motion of the jet and therefore describes the evolution of the jet boundary. In the video images, dyed jet fluid appears as dark pixels and the dye-less ambient fluid as light pixels. Variations in the pixel value of different regions of the flows are interpreted to reflect some combination of flow depth in the viewing direction and dye concentration, which can evolve in space and time due to mixing with the un-dyed ambient fluid. Round or elliptical features in the jet have been interpreted to be vortex structures.

4.3.2.1 Flows without leading vortex rings

The overall morphological evolution of the jets from experiments run with the 3-mm and 9-mm diameter orifices were generally the same. A representative experiment with a 3-mm orifice diameter and high momentum flux is shown in the photographs in Figure 4.4a and described below in order to give a reader a sense of the observable features of this flow pattern.

For the experiment from a 3-mm diameter orifice shown in Figure 4.4a, the first 0.30 seconds following the opening of the valve are characterized by rapid ascent of the injected (dyed) fluid. At 0.05 s the flow appears to be symmetric about the axis of injection and the flow spreads monotonically with distance from source. At 0.10 seconds, however, there is a visible structure to the flow which consists of a flattened ovoid cap, marked v1 for vortex structure 1, followed by a conical tail. The cap is wider than the conical tail. Then at 0.15 seconds there is another change in the flow pattern. The cap is now spherical and the width of the flow from the cap to the conical tail is approximately uniform

such that this region looks like a cylinder. Then at 0.20 seconds the cap structure begins to isolate itself from the tail below and a second structure, marked v2, appears to be forming a spherical shape which is complete by 0.25 seconds.

From 0.30 seconds to 1.0 seconds, structures 1 and 2 are maintained and evolve in different ways. From 0.30 seconds to 0.35 seconds the vertical extent of v1 increases as it separates from v2 as evidenced by the presence of colorless fluid beneath v1 indicating the presence of ambient rather than jet fluid between v1 and v2. Structure v2 does not appear to rise during this time but instead grows considerably in width. At 0.60 s v1 and v2 are both spherical and much wider than the conical fluid tail. While the tail appears to not change before 0.60 s, at 0.60 s it appears to be wavering off the flow axis. Then at 1.0 s v1 appears separated from v2 by a larger distance and it rotated off the axis of the flow. Structure v2 appears higher at 1.0 s than it does at 0.60 s, and its spherical structure is no longer distinguishable. In the quantitative analysis of flows from this class, the jet height refers to the height of the first structure, v1, over time.

4.3.2.2 Flows with leading vortex rings

Experiments run with the 15-mm diameter orifices are characterized by vortex rings that separate and evolve independently from the remaining/trailing source fluid. The observable features of this flow pattern are described below for a representative experiment with a 15-mm orifice diameter and high momentum flux. The jet from this experiment is shown in the photographs in Figure 4.4b.

For the experiment from a 15-mm diameter orifice shown in Figure 4.4b, the first 0.30 seconds following the opening of the valve are characterized by rapid ascent of the injected (dyed) fluid. At 0.05 seconds the flow appears to be symmetric about the axis of injection, and appears cylindrical rather than conical. It also appears to be one structure as evidenced by the continuous distribution of dyed fluid. However, by 0.10 seconds the distribution of dyed jet fluid is no longer continuous and colorless ambient fluid separates the front structure, again called v1, from the tail of the flow. At the front of the tail is a second round feature, structure v2. At 0.15 seconds v1 moves away from structure v2 which is now more visible due to the enhanced contrast between the dyed front and the colorless ambient fluid as compared to the contrast between v1 and v2. Structures v1 and v2 are approximately the same width. Then at 0.20 s a third structure, v3, becomes visible which appears wider than structure v2.

From 0.25 seconds to 1.0 seconds, structures v1 and v2 are maintained and evolve in different ways. From 0.25 – 0.35 v1 continues to rise though at a lower rate than in the previous time steps. Structure v2 does not seem to rise but grows slightly wider instead. This structure is a flattened ovoid not a sphere. Structure v3 continues to grow wider and has a more spherical like shape; it remains wider than v2. Behind v3 is a tail of fluid that appears cylindrical. At 0.40 s a v2 appears much further away from the source and is transitioning into a sphere. By 0.60 s the core of the vortex ring in v1 is clearly visible; structures v2 and v3 are more spherical and appear to be merging together. At 1.0 s v2 and v3 have formed a

very tall and wide spherical structure that sits on top of the tail of the fluid behind v3. In the videos of these experiments this tail fluid moves very little. In the quantitative analysis of flows from this class, the symbols v1 and v2 refer to the structures marked v1 and v2 in these images.

4.3.2.3 Summary of flow morphology

The unsteady jets from all six conditions are similar in that they create a sequence of distinct round structures as they evolve. The structures grow in height and width, at various rates, as they travel from the source. However, the different sets of experiments differ in the relative sizes (i.e. fluid volumes) of each of those structures.

The typical evolution of the unsteady jets is characterized by the formation of one or more toroidal vortices, the first of which is labeled v1 in the images. The vortices form as the source fluid initially exits the round orifice and are then driven away from the source by the fluid injected after its formation. Flow conditions with the highest discharge velocities generate vortex structures that propagate the farthest from the source during the time of the acceleration.

During the initial rapid ascent, the flow remains symmetric about the axis of the flow. This period of high ascent rates corresponds in time with the acceleration phase at the source, between 0.05 s and 0.20 s after flow initiation. As the flow continues, it breaks up into individual vortex elements that move in different directions with respect to one another, causing asymmetry in the overall flow pattern. The time at which the breakup becomes visible and the rate at which

it evolves are different for each condition but generally occur near the peak in the flux, approximately 0.20 s after flow initiation.

During the source deceleration phase, the vertical growth of the jet front is reduced, and the radial growth is enhanced at some heights above the orifice. Also during the deceleration phase, the first vortex separates, in five of the six conditions, from the rest of the flow and moves in isolation at a rate that exceeds the propagation of the fluid behind it. The first vortex does not separate in the low momentum, 9-mm experiment. I note here that the first vortex structure forms a ring vortex only in the experiments with the 15-mm diameter orifice; in the other conditions, the first vortex is an ovoid or spherical structure without evidence of being a ring.

During the 0.60 s time step, the source is off, and the flows are in a transitional state characterized by the continued radial growth of the individual structures that developed during the deceleration stage. The leading vortex v1 also grows wider at this time. Finally, the flow arrives at its final dynamic state characterized by radial growth of all the injected source fluid. This period has low vertical propagation and spreading rates.

This general evolution model, however, does not consider the effects of Reynolds number on the morphology. To illustrate this effect the outlines for representative experiments from each experimental condition are shown in Figure 4.5 at 1.0 seconds. The morphologies for the jets created in the experiments with the 3-mm diameter orifice follow a similar pattern to that expected for a starting

jet with a spherical head and conical tail. This morphology type also characterizes the shapes for jets generated in the experiments with a 9-mm diameter orifice and low momentum and the 15-mm diameter orifice at high momentum. In contrast, a cylindrical morphology is formed in the experiments with a 9-mm diameter orifice and high momentum and the 15-mm diameter orifice at low momentum. These jets have a relatively uniform width over their length. They also have seemingly different source conditions where the 9-mm jets have much higher peak Reynolds numbers (Table 3.1). However, as shown in Figure 4.2, they have similar ensemble averaged initial Reynolds number evolutions within the first 0.03 seconds which differs from the evolution of both the 9-mm diameter orifice and low momentum and the 15-mm diameter orifice at high momentum. This suggests that the main control on the final morphology is the initial Reynolds number evolution.

4.3.3 Quantitative Observations of Jet Behavior

4.3.3.1 Height

Jet rise behavior was quantified by measuring the position of the jet front in each image of the video record for each experimental run. The resulting height time series for all runs in a specific experimental condition were then ensemble averaged according to equation 2 to determine the average rise behavior for the condition while retaining the time-dependent information. The average rise behavior for each condition is shown in Figure 4.5. Jet height for the experiments with 3-mm and 9-mm orifice diameters is coincident with the starting vortex flow

front position (v1 in the individual experiments); for the experiments with a 15-mm orifice diameter two height measurements were recorded, one for the tip of the ring vortex (v1 in the individual experiments) and one for the vortex structure at the front of the tail (v2 in the individual experiments). The uncertainty of each measurement was of the order of the picture spatial accuracy (+/-0.3 mm) close to the nozzle, increasing up to +/-1.8 mm when the flow front reaches 0.6 meters above the bottom of the tank. The measurements at the farthest location, about 0.75 meters, show large scattering (~7 mm) because jet dilution by the surrounding water decreases the picture contrast and thus increases uncertainty in height measurements.

Initially the jets rise very rapidly and then the rise rate tapers off around 0.2 seconds. After that, the jets decelerate at progressively greater rates until the rise rates asymptote to a constant rate around 1.0 s. Flows with smaller vent sizes and larger pressures − high momentum conditions − have larger values of height at any given time. The trends in rise for v1 in the experiments with the 3-mm and 9-mm orifice diameters and v2 in the experiments with the 15-mm orifice diameters are nearly parallel, while the trends for the vortex rings created in the experiments with the 15-mm orifice diameters show a different rise behavior.

The relationship between height and time appears to be logarithmic for the conditions without vortex rings. To find the best fit line of the form $h = \ln(t)$, I used linear regression analysis to fit $x = \ln(t)$ and $y = h$. The resulting function is

of the form $y = a(x) + b$. After substituting ln (t) back in for x the function becomes

$$y = a\ln(t) + b. \tag{4.10}$$

In this form, I am taking the log of the dimensional quantity, time; however, the logarithmic function can only be used with pure numbers (i.e., dimensionless values). Thus, this equation must be rewritten to nondimensionalize time. First, I multiply b by a/a which results in the following expression

$$y = a\ln(t) + \frac{a}{a}b. \tag{4.11}$$

Then, a is factored out of the terms on the right hand side yielding the following expression

$$y = a\left(\ln(t) + \frac{b}{a}\right). \tag{4.12}$$

Next, I set $b/a = \ln(1/t_0)$ where t_0 is a characteristic time scale. Substituting this expression for b/a yields

$$y = a\left(\ln(t) + \ln(1/t_0)\right). \tag{4.13}$$

I can simplify this expression using the log property

$$\ln(f) + \ln(g) = \ln(fg) \tag{4.14}$$

to yield the following expression

$$y = a\ln(t/t_0). \tag{4.15}$$

In this expression, the quotient t/t_0 is nondimensional.

To return the expression to the unit of interest, height, I substitute h back in for y to yield

$$h = a\ln(t/t_0). \tag{4.16}$$

Since h has units of length, a must also. I can therefore treat a as h_0, a characteristic length scale. This length scale can then be used to nondimensionalize the height, h/h_0, which results in the expression

$$h/h_0 = \ln(t/t_0). \tag{4.17}$$

To find the time scale t_0 in terms of a and b, I take the exponential of both sides of the expression $b/a = \ln(1/t_0)$ to yield

$$\exp(b/a) = \exp(\ln(1/t_0)) = 1/t_0\ . \tag{4.18}$$

I then solve for t_0 yielding

$$t_0 = \exp(-b/a). \tag{4.19}$$

The quotient b/a, is nondimensional as both b and a have units of length. Thus, expressions for the two characteristic scales h_0 and t_0 can be calculated directly from the regression analysis. The results of the regression analysis and the norm of the residuals are listed in Table 4.1. A plot comparing the predictions of these fits with the observations is shown in Figure 4.6. With the exception of the fits for the v1 conditions (purple and magenta), the rest of the fits are reasonable. The logarithmic functions fit the data over the entire duration of 0.0 to 1.0 seconds. There is more disagreement between the fit and the data for times less than 0.1 seconds and close to 1.0 s. Unsteady jet height therefore has a logarithmic dependence on time for the entire observation duration, rather than the power law dependence observed for the self-similar phases of steady jet evolution.

To understand the general effect of the unsteady source condition on the rise rate over time, the rise behavior that is common to all experiments must be

determined. This common behavior can be elucidated from a collapse in the trends for all experimental conditions. In order to collapse the trends, the length and time scales which are characteristic to each condition are used to normalize the observed behavior for that condition. If the scales are chosen properly, then the normalized height and time curves for all experiments should overlap in one trend and thus achieve a collapse, or reduction, of the data. With the exception of the vortex rings, the height curves for all experiments collapse together when each curve is normalized by the scales h_0 and t_0 as shown in Figure 4.7.

All of these conditions are fit approximately by the expression $h/h_0 = \ln(t/t_0^*)$ where $t_0^* = \exp(-4)$. This expression is shown with the nondimensionalized height time series in Figure 4.8. The resulting value of the nondimensional time $t_0^* = 0.02$. However, it is unclear what controls this time scale and thus why it is common for all experiments.

4.3.3.2 Width

Width was easiest to define when the individual experiments were ensemble averaged (Figures 4.9a and 4.10a), and the typical shape of a starting jet emerged – a spherical cap followed by a conical plume. However, width was difficult to define for the individual experiments as it increased non-monotonically with distance from source over most of the observed duration as shown in Figures 4.9b and 4.10b. Ensemble averaged images were created by summing the pixel values of images at the same instant for all runs in a condition and then dividing that sum by the number of images that were averaged. While

the widths were easier to define for the ensemble case, they did not accurately represent changes associated with any individual experiment. Therefore width was considered for both the individual and ensemble averaged images.

For jets with flow boundaries that monotonically and linearly increase with height, the angle the jet boundary makes with the vertical flow axis can be approximated by calculating the change in width over the change in height for a time-averaged jet boundary. I therefore calculated the spreading rates for the unsteady jets in the same manner. For the individual jets, the spreading rate calculation procedure is illustrated in Figure 4.11 where the spreading angle, theta, was determined for the line connecting *a* and *a'*; *a* is located at the edge of the jet just above the orifice and *a'* is the location of the intersection between the maximum spread of the jet and the location of maximum height. A similar procedure was followed for calculating the spreading angle for the ensemble averaged jet image as shown in Figure 4.11b. Both, the change in the spreading angle for a given phase (dtheta) was calculated as well as the time-averaged spreading angle (theta) of the flow at that time.

The results for the spreading angle calculations are reported in Table 4.2 for the jet from the 3-mm diameter orifice and Table 4.3 for the jet from the 15-mm diameter orifice. The spreading angles for the jet in the ensemble averaged image are generally wider than the jet in the images of the individual experiments. For the experiment with the 3-mm diameter orifice the spreading angle is around 12.0^{o} for the ensemble while the individual experiment spreading angle is ~ 10.0^{o}.

The spreading angle for the ensemble of the second vortex, v2, in the 15 mm experiments is around 13.0^o while the value for the individual experiment is around ~ 7^o.

The time-averaged spreading angle (theta) for the individual 3-mm experiment has a maximum value of 11.3^o in the first instant; the angle decreases monotonically over time to 9.5^o at 1.0 seconds. A different trend is observed for the ensemble, where the angle starts at 12.0^o then decreases to its minimum value of 10.7^o at 0.3 seconds after which it increases to 12.0^o at 1.0 seconds. This trend observed for the 15-mm experiments is different. For the individual jet, the spreading angle is a maximum at the first instant at 10.9^o, a sharp drop to 7.0^o at 0.2 seconds, and then an increase to 7.8^o at 1.0 seconds. For the ensemble, the spreading rate starts at 12.5^o, then decreases abruptly to 10.5^o at 0.20 seconds before increasing to its maximum of 12.7^o at 1.0 seconds. The trends in the individual experiments (dtheta) are considerably more variable and show a slightly different trend. The angle decreases from 0.1 seconds to 0.2 s, then increases abruptly from 0.2 seconds to 0.3 seconds. The spreading angle varies considerably after that with no clear general trend.

Overall, the spreading angle changes with time in these flows. For all experiments, the general evolution of the spreading angle involves a decrease from 0.0 – 0.1 seconds to 0.1 to 0.2 seconds and then a subsequent increase.

4.4 Steady Scaling

To facilitate the analysis of the time dependence, the momentum flux was divided into 4 phases on the basis of the acceleration behavior shown in Figure 4.12. In the first phase from 0.0 to 0.1 seconds the acceleration is positive and increasing as the volume flux increases at a progressively faster rate. In the second phase from 0.1 to 0.3 seconds the acceleration is decreasing; however, from 0.1 to 0.2 seconds it is positive and from 0.2 to 0.3 seconds it is negative yielding a net acceleration for this phase that is approximately zero. Then in phase 3 the acceleration is negative and increasing as the momentum flux decreases at a progressively faster rate before it ceases. As the volume flux ceased, the source is 'off' and the acceleration is zero in phase 4.

I then assessed the relationship between height and time within each of these phases by attempting to find power law relationships that best fit each phase of the data. For the first phase, there does not seem to be a power law relationship between height and time and this will be discussed further below. For the second phase the height roughly scales with the square root of time for the 3-mm diameter experiments but scales with a power less than ½ for the 9-mm and 15-mm diameter experiments. By the end of phase 4, the asymptotic trend to a power of ¼ is approached for all experimental conditions although the exact timing and rate of the transition from phase 3 to phase 4 scaling varies with each condition. The values of these powers at each of these times are summarized in Table 4.5.

For phase 1, the power law relationships do not seem to approximate the data well as the values of the power are greater than 1.0 for all experimental

conditions and the residual is large indicating that the observed values deviate appreciably from the fit. By the time the jet enters phase 2, however, the residuals are considerably reduced and the power ranges from 0.43 to 0.74 with values for the 3- and 9-mm experiments clustering around 0.40 while the values for the 15-mm experiments exceed 0.50. These values suggest that some experiments approach the self-similar starting jet behavior indicated by a power of 0.50 in this phase. In phase 3, the power values fall in the range 0.30 to 0.50 which is generally less then starting jet scaling suggesting that this scaling should overpredict the motion of the unsteady jets in this phase. The minimum values around 0.3 are approaching the power expected for the puff scaling, 0.25. This value is not reached in 1.00 second by all of the experimental conditions whose power values are greater than 0.30. However, the values for the power in this phase 4 are lower than the values in the previous phase 3 suggesting that the flows are slowly approaching the behavior of a puff and a power value of 0.25.

These power law relationships are also part of the scaling laws that describe steady jet rise in terms of source characteristics. Considering variable nature of the best fit power law relationships, it is apparent that the scaling relationships will also vary over time. To better understand how the observations vary from the behavior predicted in equations 4.1 and 4.2, theoretical heights were calculated from these expressions. To determine the value of the constants, I rearranged equations 4.1 and 4.2 so that the values of the constants C_1 and C_2 could be calculated from the instantaneous values of the ensemble averaged

height and the time-average of the ensemble averaged source momentum flux, in the case of the starting jet, or the total momentum injected, in the case of the puff. Values of C_1 are shown as a function of time for all experimental conditions in Figure 4.13. I then took the maximum instantaneous values for C_1 and C_2 indicated by the red stars in Figure 4.13 and listed in Table 4.5.

The values for C_1 range from 3.6 to 5.4 which exceed the value of 3.0 that is typical for steady and starting jets with circular cross sections in the region of self-similar behavior [e.g., *Sangras et al*., 2002]. This difference may be related to the fact that the unsteady jet may not be in a state of self-similarity during the observation period. Values for C_2 are typically larger than those for C_1 and range from 3.8 – 6.1. Again, these are larger than the values for instantaneously released puffs with typical values around 2.6 [e.g., *Sangras et al*., 2002]. This difference is likely attributable to the fact that the injection duration is not instantaneous.

As shown in Figure 4.14, treating these flows as either starting jets or puffs does not adequately characterize the rise of the flow fronts over the duration shown. Starting jet scaling reasonably approximates the start of the rise (phases 1and 2) but significantly overpredicts the height thereafter. The overprediction at later times is most likely related to the fact that the source ends in the experiment but is assumed to be continuous in the model. In contrast, puff scaling overpredicts the start of the rise but reasonably approximates the asymptotic rise (phase 4). The overprediction at early times is most likely related to the fact that

material is released over a finite duration in the experiments and the model assumes it is instantaneously released.

4.5 Unsteady Scaling

The results from both the qualitative and quantitative analysis of the unsteady jet evolution suggest that jet properties vary in space and time over the observation duration. Jet properties likely change in response to internal dynamics with strongly varying time-dependence derived from the strongly varying source volume flux. Consequently, the scaling relationships used to understand the general relationships between key dynamic variables in steady flows may not be accurate for these highly unsteady flows. Thus, the observations of unsteady jet evolution are now used to understand the key dynamic variables for unsteady flows. Then, the general relationships between these variables are established to yield scaling relationships appropriate for unsteady flows.

This logarithmic relationship between height and time varies from the power law relationship typically assumed for these variables. To compare the power function with the logarithmic function, the logarithmic function can be written as

$$h/h_0 = (t/t_0)^n \tag{4.20}$$

where *n* is the value of the power. The derivative of this function with respect to time is

$$h'/h_0 = n(t/t_0)^{n-1} \tag{4.21}$$

for the power law where the prime denotes the time derivative. For the logarithm, the time derivative is

$$h'/h_0 = 1/(t/t_0) = (t/t_0)^{-1}. \quad (4.22)$$

By combining equations 18 and 19, h'/h_0 can be eliminated resulting in

$$(t/t_0)^{-1} = n(t/t_0)^{n-1} \quad (4.23)$$

which simplifies to

$$1 = n(t/t_0)^n \quad (4.24)$$

Solving for t/t_0 then yields

$$t/t_0 = (1/n)^{1/n}. \quad (4.25)$$

According to the steady scaling laws for starting jets (equation 1) and puffs (equation 2), height should evolve according to the ½ or ¼ power of time when the starting jet or puff, respectively, is in a self-similar state. According to equation 23, when n = ½, $t/t_0 = 4$ and when n = ¼, $t/t_0 = 16$. Thus, these power law relationships will be tangent to the logarithmic relationships at the nondimensional times of 4 and 16. For $t/t_0 = 4$, $h/h_0 = \ln(t/t_0) = 1.39$ and for $t/t_0 = 16$, $h/h_0 = \ln(t/t_0) = 2.77$.

These locations are plotted alongside the nondimensional height time series in Figure 4.15. It is interesting to note that the v1 curves deviate from the rest of the group at approximately the location where the puff power law fit ($n = 1/4, t/t_0 = 4, h/h_0 = 1.39$) intersects the logarithmic function of the data. It is also interesting to note that all the curves collapse together until the location where the starting jet power law fit ($n = 1/2, t/t_0 = 16, h/h_0 = 2.77$) at which

point the v1 curves deviate from the rest of the data. Perhaps the value of 4 used in the time scaling for the fit of all the experimental conditions is related to this nondimensional time at which all of the curves remain together. This would be consistent with the notion of a vortex formation time of approximately 4, a value that is in good agreement with other experiments [*Gharib et al.*, 1998]. At this time, the front vortex is expected to separate from the remaining flow. This is consistent with the observations for the 15-mm conditions but not for the 3- or 9-mm conditions which do not generate vortex rings.

To compare the form of the power laws with the observations, I found that the premultiplying constants of 1.4 for the puff scaling (blue dashed line) and 0.7 for the starting jet scaling (red dashed line) fit the data best. The results are shown in Figure 4.16. For early times, before the nondimensional time of 16, the puff scaling over estimates the observed heights but approximates them more reliably thereafter. In contrast, the starting jet scaling law approximates the observations well until a nondimensional time of 16 when it starts to overestimate them. The mismatch is smallest for the starting vortex rings (v1). The trajectory of the starting jet power law continues to approximate the starting vortex rings after the nondimensional time of 16. It is clear in this figure that the logarithmic fit (magenta solid line) approximates the data well for all values of nondimensional time and is therefore a better fit of the data as compared to the power laws.

The logarithmic evolution of the observed height behavior is best approximated by the steady starting jet model ($h \sim t^{1/2}$) for times before the

momentum flux peak is reached (phase 1), and then, in the late time limit (in phase 4), by predictions from the puff model ($h \sim t^{1/4}$). The power of ½ is tangential to the collapsed height data at the non-dimensional time of 4.00 which corresponds to the real time of 0.07 seconds, during the acceleration phase (phase 1) of the flow. The power of ¼ is tangential to the collapsed height data at a non-dimensional time of 16.00 which corresponds with a real time of 0.29 seconds, near the end of the deceleration phase (phase 3). The rise during phases 2 and 3 is not well approximated by either steady model.

The jets in this study have evolve according to the following:

(1) Acceleration: The jets are momentum-driven and maintain a continuous boundary layer. The flow has a spherical head and conical tail that is asymmetric about the centerline of the flow. Momentum flux controls the rise.

(2) Constant: The jets are momentum-driven though the rates that momentum is supplied to the jet vary over this phase, the net acceleration is effectively zero. The shear layer breaks and a large structure forms at the front of the flow. As this structure grows it isolates itself and a second structure is formed behind it. High-momentum fluid then accumulates in the second structure. Height changes very little for both structures during this time.

(3) Deceleration: The flow segments into many structures. The widths of the structures, particularly the second structure, grow dramatically

during this phase. Momentum continues to be added though at a decreasing rate. The first vortex is moving completely independently now. Height changes very little.

(4) Off: The flow starts to rise and spread at approximately equal rates. Each segment of the flow that formed a vortex structure is approximately spherical. The segment of the flow that did not form a vortex structure formed a narrow conical tail. As the vortex structures that sit atop the tail diffuse, the conical tail diffuses opposite the direction of rise – it diffuses toward the orifice. The total momentum injected controls the rise.

The evolution of the unsteady jet outlined above differs from that for a steady starting jet in a number of important ways. First, the unsteady jet shape varies over the duration whereas the steady jet shape remains approximately the same. Second, the width of an individual unsteady jet varies non-monotonically with distance from source while the width of a steady jet varies monotonically (linearly) with distance from source. As a monotonic increase in width underlies the criteria on which the similarity assumption is based, this suggests that rather than self-similar dynamics at every height, these flows have variable dynamics over their height. Each segment has a different history leading to a different evolution. While these segments appear interdependent, with the exception of the first structure, up to the deceleration phase, they appear to evolve independently thereafter. However, the scaling success suggests that the height of these flows is

not particularly dependent on these differences but can be accounted for by tracking the rate at which momentum accumulates and then the total amount. It is important to note that height is not an indicator of flux once the acceleration phase ends. Also, the width of the flow, rather than the height, is more indicative of changing source conditions, after the source acceleration phase. Furthermore, the width responds much more rapidly than the height so it should be the first indication that the source changed.

4.7 Implications for volcanic plumes

These findings suggest at least two phases of development may occur for volcanic plumes with source durations that are less than their rise times. In the first phase, the evolution will depend directly on conditions at the source. The front of the flow will evolve variably in time, and the incorporation of ambient fluid may vary along with source conditions. Thus, studies intending to characterize plume evolution from eruption conditions should document the plume motion from initiation as well as through the evolution. During the second phase, the source has no control on the dynamics and the flow will evolve dynamically as if it were instantaneously released. Consequently, studies estimating discharge rates from plume heights should confine their estimates to the duration of the eruption.

There are few studies which capture the motion of volcanic plumes at sufficiently high rates for use in analyzing their dynamics according to the detailed analysis of the experiments presented here. However, two studies provide

insight into the application of the experimental results to the understanding and interpretation of volcanic plume dynamics. In the first study, *Patrick* [2007] report an analysis of volcanic plumes generated during Strombolian-style eruptions at Stromboli volcano in Italy. Direct comparisons can be made between observations reported by *Patrick* [2007a] and those reported here. However, the *Patrick* [2007a] study lacks sequences of visual images showing the evolution of the plume rise. One such sequence is presented by *Mori and Burton* [2009] also for plumes from Stromboli volcano in Italy. I therefore begin the discussion with the analysis of the plume images from *Mori and Burton* [2009] using the summary of dynamics presented at the end of the unsteady scaling section. This comparison provides a base level test of the potential application of the ideas presented in that summary. Then, I discuss my findings in the context of those presented by *Patrick* [2007a] to derive a more general understanding of the applicability of these results.

The image sequence from *Mori and Burton* [2009] of the rise of a plume from one single eruption is shown in Figure 17. The images were collected with a camera and optics set up sensitive to the UV band and thus the images were color contoured by the authors to reflect the concentration of SO_2 in the plume; SO_2 is a common gas in volcanic plumes that is not common in the atmosphere which facilitates plume observations even for very low concentrations of SO_2. Assuming these images are calibrated correctly, the SO_2 concentration can then be used as a passive tracer for the plume dynamics. Areas of large SO_2 concentrations are red

and correspond to regions where the plume is not well mixed with the atmosphere. These regions will now be analyzed.

The plume images show the near vent evolution of the plume at 2-second intervals and include the initiation of the eruption at 14:28:48. At this stage in the eruption, a small plume is visible which appears to have a round spherical front. At 14:28:50, the front of the plume advances higher into the atmosphere and has a large concentration of SO_2 in a relatively spherical region at the front of the plume. The width of the plume is nearly uniform from the volcanic vent to the front of the plume. At 14:28:52, the plume continues to advance into the atmosphere and three regions of the plume can be distinguished; an oblate 'cap' at the front, an elongated spherical region in the middle, and a conical shaped region near the vent. Between the cap and the elongated sphere, the plume width narrows abruptly. At the edges of the elongated sphere, the plume boundary appears to be crenulated with variations that are larger than in the cap or the conical region below it. By 14:28:54, the cap structure starts to widen beyond the widths of the elongated oval structure and conical region, both of which are still identifiable. The height of the cap appears nearly equal to the height in the previous instant, however the elongated oval structure has lengthened and the conical region has shortened.

At 14:28:56, the oval structure appears to merge with the cap appears to merge with the cap. The width of the bottom of the oval structure is now the widest section of the plume and the conical region is no longer conical but

appears cylindrical. This implies a change in source conditions which may be an important observation considering the plume evolution changes dramatically at 14:28:58. These observations of plume behavior forming three flow regions of a cap, a middle oval, and a bottom cone, but remaining relatively uniform in width and axisymmetric about the axis of the jet for the period from 14:28:48 to 14:28:54, a duration of 6 seconds, are consistent with the acceleration phase of the unsteady jet experiments particularly those generated with the 15-mm diameter orifice. The change in the near vent behavior from conical shaped to cylindrical shaped at 14:28:56 (8 seconds after onset), I interpret to reflect a relative decrease in the injection rate. However, the front of the flow is still attached to the tail so the change in source conditions has yet to reach the front of the flow. This phase of the flow may be consistent with the constant injection phase near the peak in the discharge rate.

At 14:28:56 there is an asymmetry in the jet where the left side of the jet has large indentations beneath the cap and beneath the former elongate oval structure while the right side has a relatively uniform boundary. I interpret this to mean there is a prevailing wind in the ambient atmosphere which moves from the right side of the image to the left. Thus, the variations in the boundary on the right side of the jet are smoothed by the interaction of the jet boundary with the prevailing wind. This wind does not appear to be strong enough to bend the plume. The shape of the red contour in the cap region at 14:28:58 (10 seconds after onset), is similar to the shape of the jet fluid in the vortex ring structure in

the laboratory jets as the ring is separates from the flow. There is a narrow region of the red contour between the cap and the oval structure which looks like the structure formed between the separating ring vortices and the trailing jet region in the experiments with the 15-mm orifice diameter. Also, the second structure which was formerly elongate now appears to be contracting into a sphere with a region of peak SO_2 concentration near the center of the sphere. This is consistent with the formation and growth of the second vortex structure in the laboratory jets from the 15-mm condition. The fluid that formerly composed the conical region now appears to be dividing into flow segments. The shape of these segments is similar to the shape of the experimental flows when they are rotating about the central vertical flow axis. Due to the abrupt change in the flow behavior over the entire length of the flow and the change in the width of the flow near the vent, I interpret this time step to represent the onset of the deceleration phase of the injection.

At 14:29:00 (12 seconds after onset), the cap appears to be deforming on the right side in a way that is reducing the concentration of SO_2 and breaking up the structure. Both of these would be consistent with the interaction of these structures with a prevailing wind. On the left side, however, there is now a large region of lower concentration SO_2 which separates the cap and the structure behind it. That structure continues to grow in width, contract from the bottom to the top, and now has a very flat bottom. The individual structures are more visible in the region formerly described as conical. At 14:29:02 the cap structure appears

to be breaking up from the right to the left. The second structure is now nearly spherical and no longer contains a flat bottom. The structures in the former conical region have regions of very narrow width that separate them. Thus, due to the flow segregation near the vent, the flat bottom of structure 2, and the lobed structure of structure 1, I interpret this flow pattern as occurring after the end of the injection. This interpretation is supported by the fact that, if there is an influence from the prevailing wind, it does not seem to affect the plume motion before this instant but does seem to effect the plume motion in all time steps afterwards.

From 14:29:04 to 14:29:10 (16 – 22 seconds), the second structure continues to grow radially and maintain a high SO_2 concentration while the front structure and the structures in the former conical region become dilute. This observation of consistently high concentrations and growth rates that exceed other segments of the plume is consistent with the notion that the injection volume and momentum fill the second structure of unsteady jets from volume fluxes that increase and then decrease before ceasing. Also visible during this time is the bending of the plume to the left, consistent with the hypothesized wind direction. From 14:29:12 to 14:29:22 the second structure rotates out of the field of view and the concentration distribution of the second structure appears to diffuse relatively uniformly. This is consistent with this structure acting as a puff in the long time limit.

In short, the features and the evolution of this discrete volcanic plume are consistent with the features and the evolution of the unsteady laboratory jets from the 15-mm diameter orifice. This suggests that the dominant controls on the dynamics of small volcanic plumes such as these maybe reasonably captured by experimental set up. Furthermore, the features are characteristic of the individual experiments rather than the ensemble, which supports the consideration of both when trying to understand the dynamics of these flows. More observations of volcanic plumes which are similar to this study are needed to understand how often plumes with this evolution history are formed.

Mori and Burton [2009] describe this event as a Type 2a or gas-thrust plume according to the plume styles described by *Patrick* [2007a]. The rise velocity of plumes in this class decreases significantly within the first 100 meters from the volcanic vent after which they ascend at a relatively constant rate of 5 - 10 m/s. The relatively constant ascent is interpreted by *Patrick* [2007a] to indicate the transition to buoyancy-driven convective rise and is therefore now interpreted as such by many authors. However, the non-buoyant laboratory experiments exhibit a constant rise behavior once the asymptotic puff condition is reached. This suggests that turbulent structure rather than the mechanism of turbulence generation controls the constant rise behavior. It also suggests that the transition from momentum-driven to buoyancy-driven behavior may be gradual rather than abrupt and therefore difficult identify definitively in volcanic plume observations.

I then analyzed the rise behavior by measuring the height of the plumes in [*Mori and Burton*, 2009] at each time. The values of height I measured are listed in Table 4.6 and plotted against time in Figure 4.18a. I then used linear regression to fit the height and natural log of time and find the characteristic length scale h_0 = 66.5 meters and time scale t_0 = 1.35 seconds for the real plume. I then plotted the real heights against the best fit curve for the lab data in Figure 4.18b. The real data plot close to the relationship measured in the lab when nondimensionalized by the unsteady scaling law.

The observation that plumes from Strombolian-style eruptions can be classified as gas-thrust plumes (Type 2a) [*Patrick*, 2007a] indicates that momentum-driven dynamics are also an important component of the rise of these small scale plumes and may therefore be compared with the experimental results presented here. For the plumes they observed in this flow class, *Patrick* [2007a] found the average power law fit for height and time to be 0.62+/-0.03 which is greater than the value of 0.5 expected for a steady starting jet and greater than the fits for the experimental jets presented here. As the value expected for a starting plume is 0.75, the disagreement between the observations, theory and lab experiments may be attributed to the additional role that buoyancy may play in the rise of the volcanic plumes which is not considered in either the starting jet theory or the laboratory jets. Alternatively, it may be related to the time history of the eruption which may not be adequately characterized by the source conditions in the experiments or theoretical model. The average spreading rate of the

volcanic plumes was 7.3^{o} which is smaller than the average spreading rates I found for the laboratory jets which was generally above 10^{o}. The potential source of this disagreement is unknown but may be related to the fact that the volcanic plumes contain buoyancy and are more complex than the simplified experiments.

While the values for spreading angle and the power law fits for laboratory jets and the observations of Strombolian-plumes time do not agree, there is agreement between the evolution history of the two. This suggests that first order variables controlling the dynamics may be reasonably approximated by the experiments but the detailed processes contributing to the observable behavior may be oversimplified or simply different in the laboratory experiments. Nevertheless, the presence of a gas-thrust plume population for plumes from Strombolian-style eruptions suggests momentum driven dynamics should not be ignored for this eruption class. Furthermore, the similarity between the evolutions of unsteady laboratory jets and the Strombolian plumes suggests time-dependent dynamics should not be ignored.

4.8 Conclusion

Measurements of jet heights and spreading angles coupled with qualitative observations of jet morphology indicate that unsteady jets evolve over a sequence of stages that correlates with the sequence of stages in the momentum flux. Therefore, these observations show a varying dependence on time which indicates that variable discharge rates have first order effects on turbulent jet dynamics when the discharge fluctuations are on comparable time scales with the duration. I

hypothesize that variable discharge rates may introduce spatial and temporal variability in the mean volume flux in the jet, which may in turn affect the processes that directly depend on it, including turbulent mixing and entrainment, and thereby influence the jet rise and spreading characteristics. It follows then that models which treat rates of discharge, mean flow, mixing and dilution as time invariant may not adequately describe the evolution of turbulent jets driven by discharge rates that strongly vary in time. Therefore, by analogy, volcanic plume models which use constant eruption rates, mean flow, mixing and dilution may not adequately describe the evolution of volcanic plumes while eruption rates are strongly varying. Consequently, neglecting the dependence of volcanic plume dynamics on time-varying eruption rates may lead to grossly inaccurate hazard predictions for volcanic plumes from variable-rate eruptions, particularly those generated during Vulcanian-style eruptions.

Figure 4.1. Ensemble averaged momentum flux at the source as a function of time for experimental conditions H3 (black circles), L3 (gray circles), H9 (black squares), L9 (gray squares), H15 (black triangles), and L15 (gray triangles).

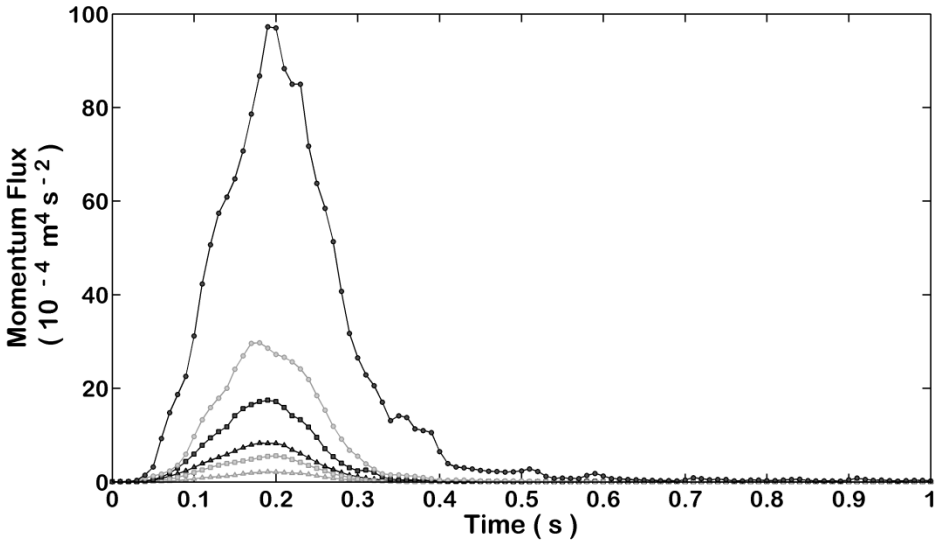

Figure 4.2. Ensemble averaged Reynolds number at the source as a function of time for experimental conditions H3 (black circles), L3 (gray circles), H9 (black squares), L9 (gray squares), H15 (black triangles), and L15 (gray triangles).

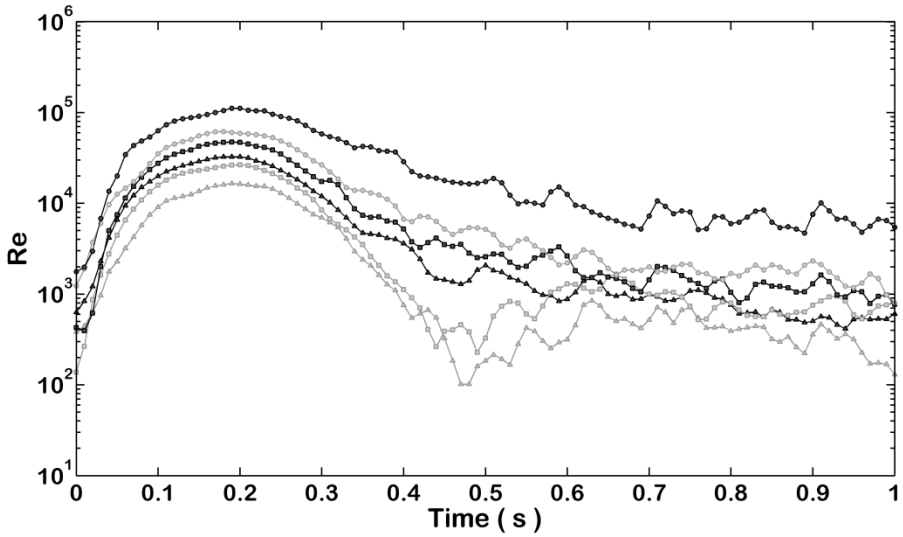

Figure 4.3. Ensemble-averaged source momentum flux normalized by the maximum value for experimental conditions H3 (black circles), L3 (gray circles), H9 (black squares), L9 (gray squares), H15 (black triangles), and L15 (gray triangles).

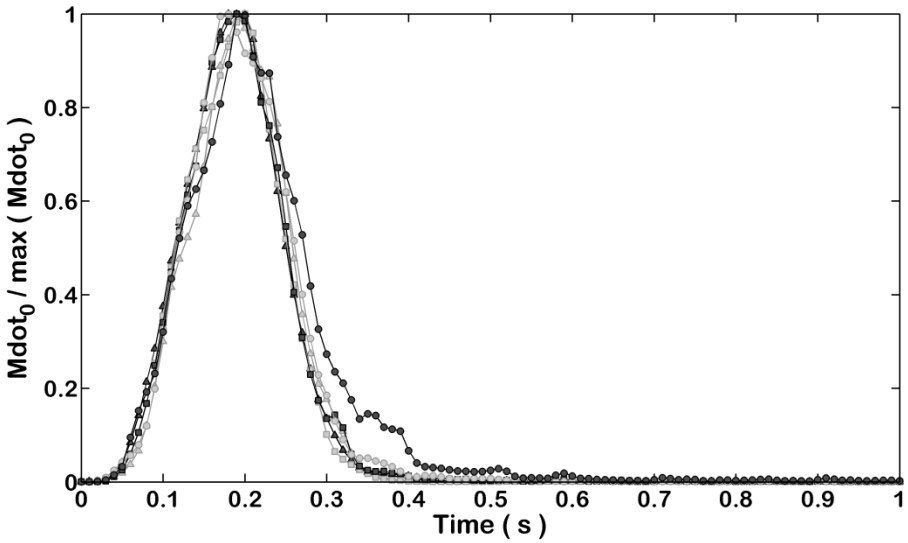

Figure 4.4. Jet (dark colored fluid) evolution in an individual experiment for conditions H3 (a) and H15 (b) at various instants. Scale on left indicates the distance from source in units of source diameters. Locations of vortex structures v1 and v2 are indicated in each frame.

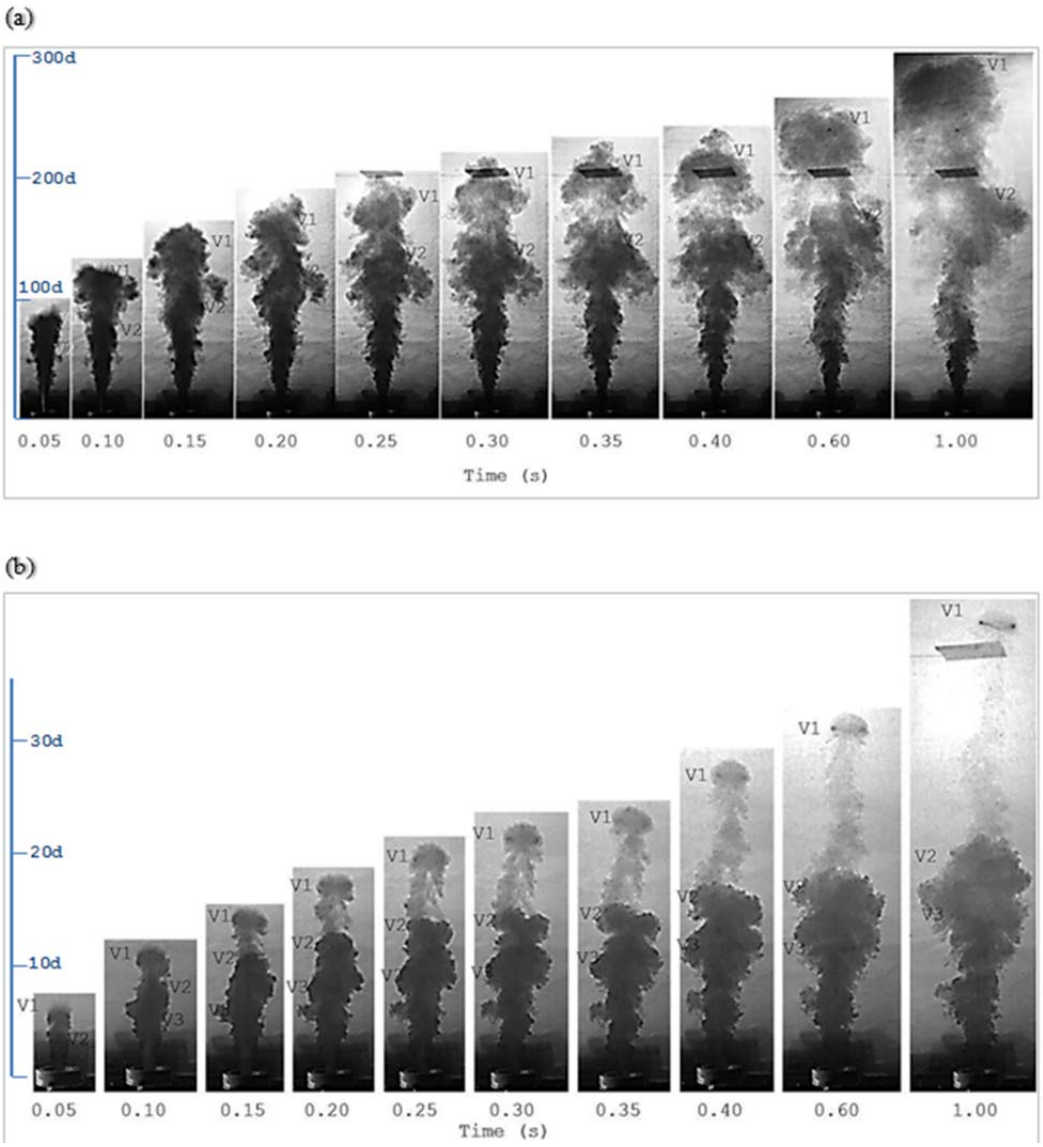

Figure 4.5. Ensemble-averaged jet height as a function of time for experimental conditions H3 (black circles), L3 (gray circles), H9 (black squares), L9 (gray squares), H15 (black triangles), and L15 (gray triangles).

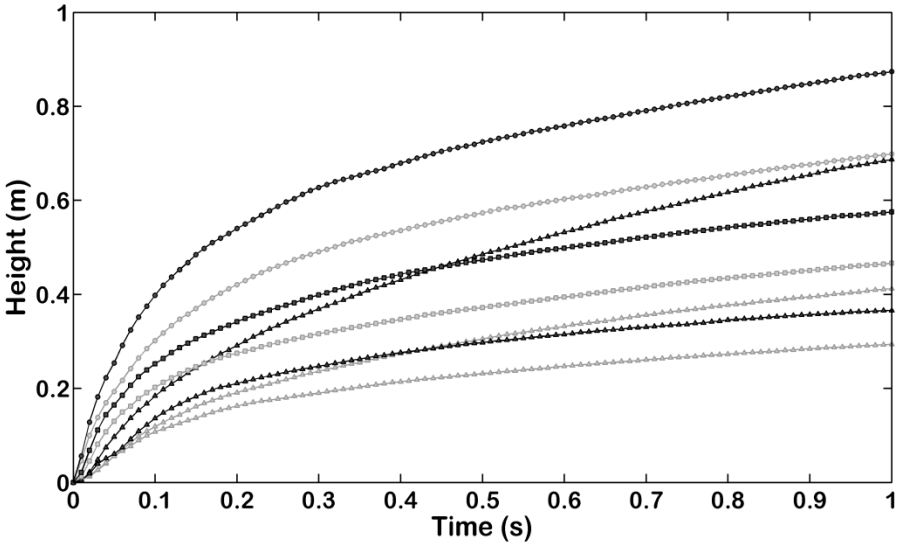

Figure 4.6. Comparison of the logarithmic fits (solid lines) of the height time series with the observations of height (shapes) for experimental conditions H3 (red), L3 (orange), H9 (green), L9 (blue), H15v1 (purple), H15v2 (cyan), L15v1 (magenta), and L15v2 (gray).

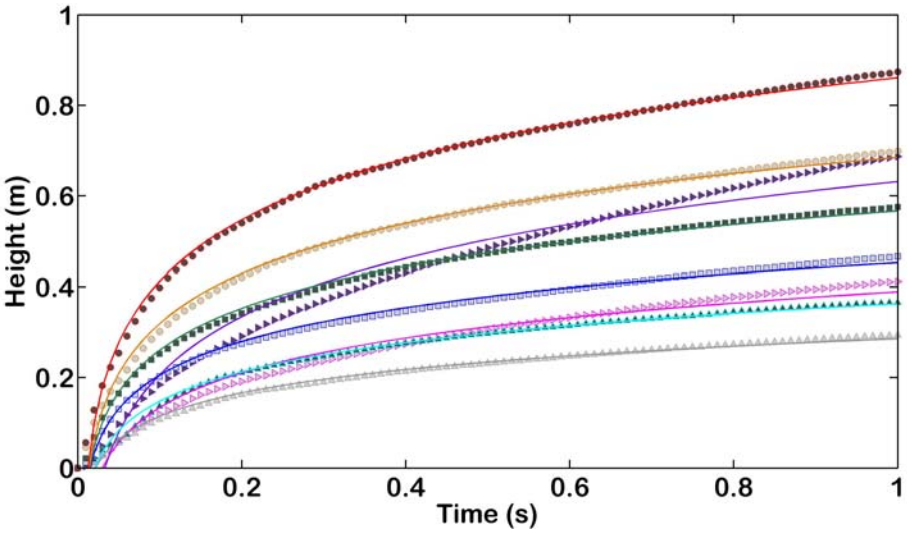

Figure 4.7. Normalized ensemble-averaged jet heights (see text) plotted against normalized time for experimental conditions H3 (black circles), L3 (gray circles), H9 (black squares), L9 (gray squares), H15 (black triangles), and L15 (gray triangles).

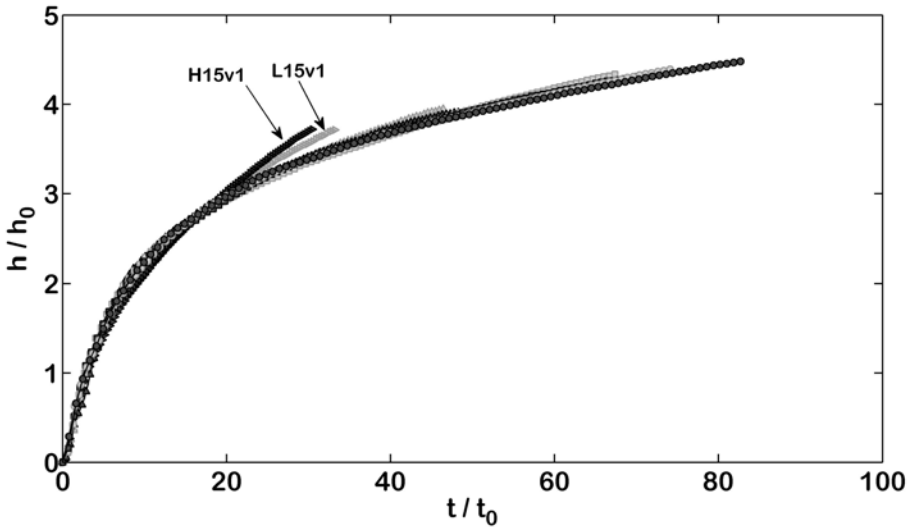

Figure 4.8. Fit (magenta line) of normalized ensemble-averaged jet heights (see text) plotted against normalized time for experimental conditions H3 (black circles), L3 (gray circles), H9 (black squares), L9 (gray squares), H15 (black triangles), and L15 (gray triangles).

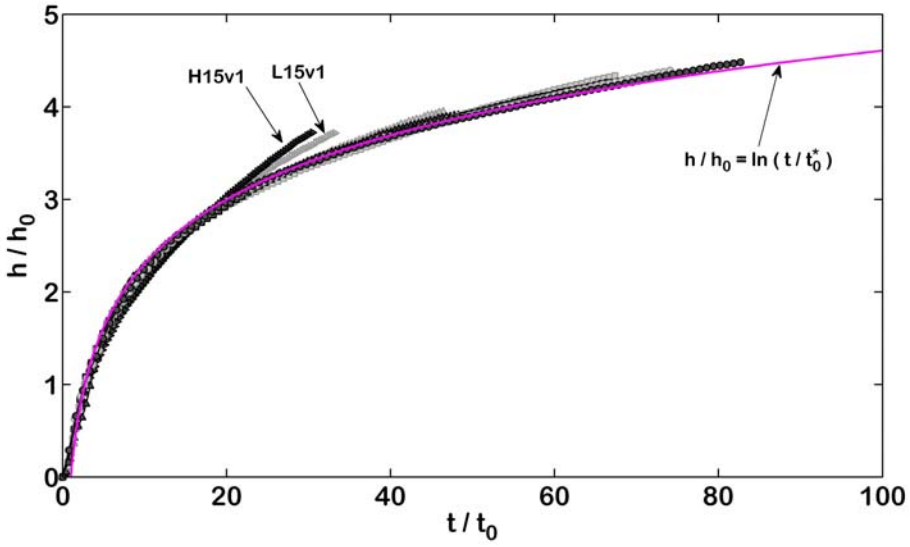

Figure 4.9. Jet outlines for the H3 condition showing the relationship between the ensemble images (a) and images for an individual run (b).

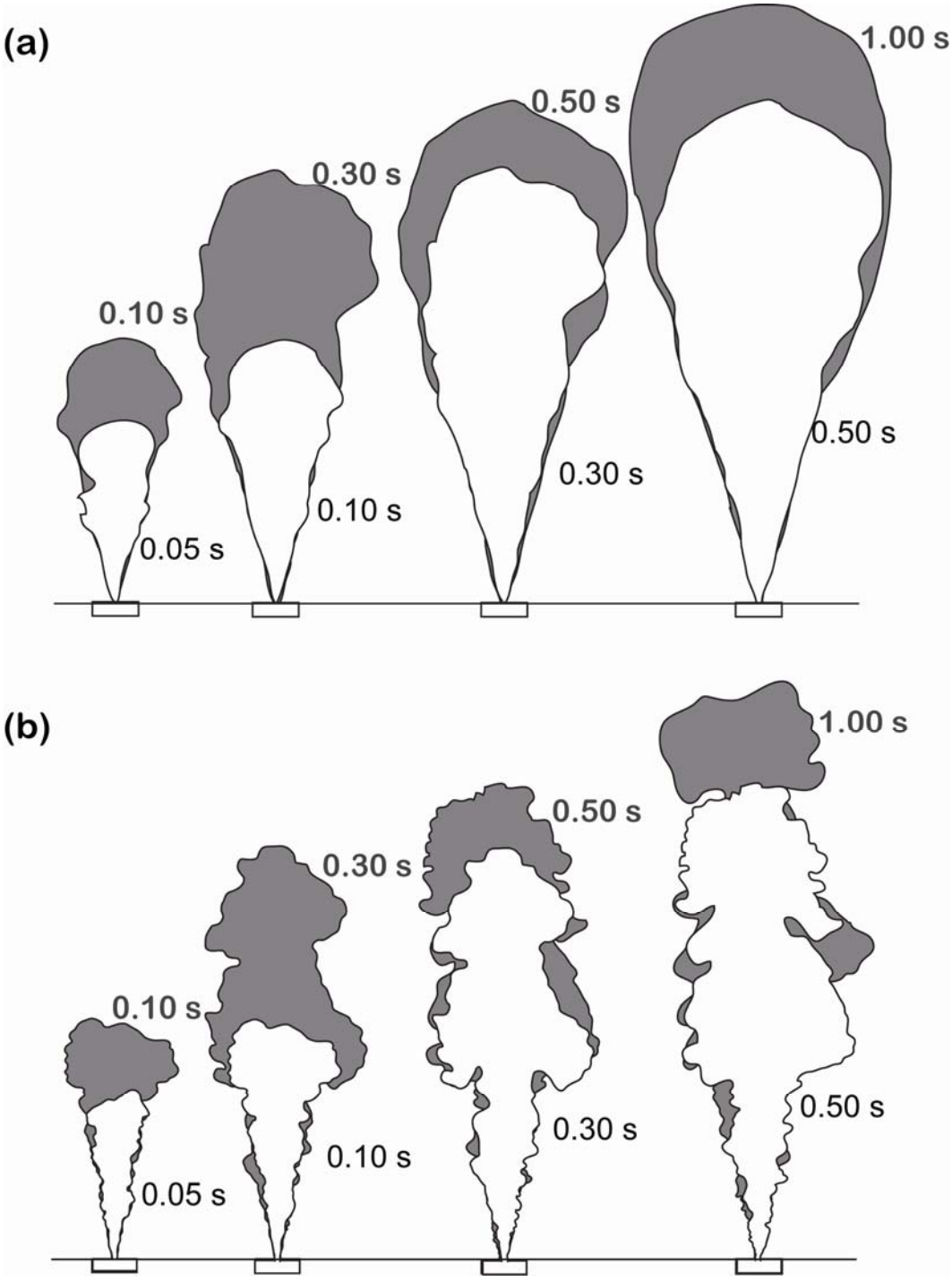

Figure 4.10. Jet outlines for the H15 condition showing the relationship between the ensemble images (a) and images for an individual run (b).

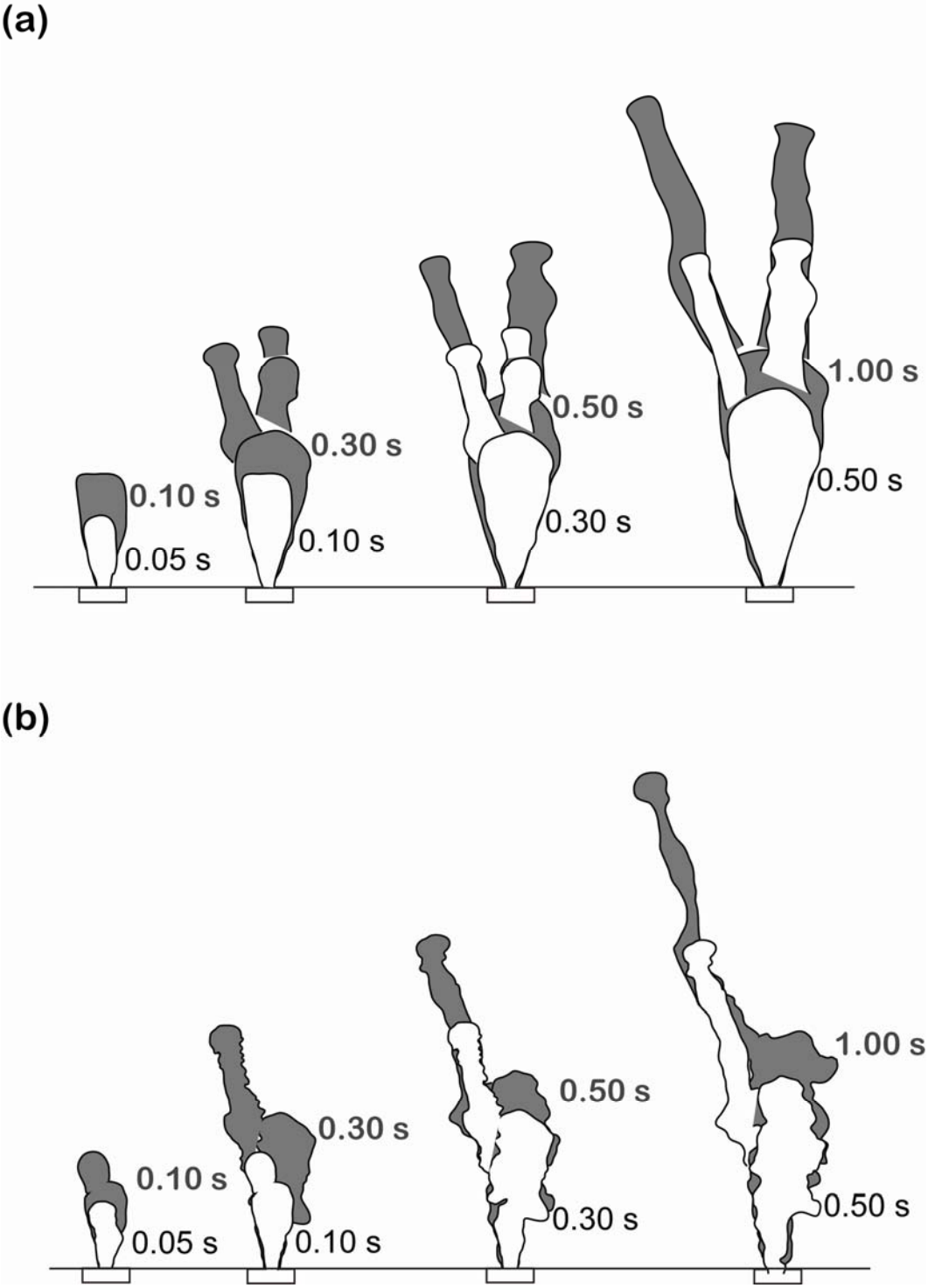

Figure 4.11. Schematic demonstrating the procedure for the spreading calculations. Height is indicated by the letter *h* and width by the letter *b*. Capital letters indicated the time averaged value and lower case indicate the instantaneous value.

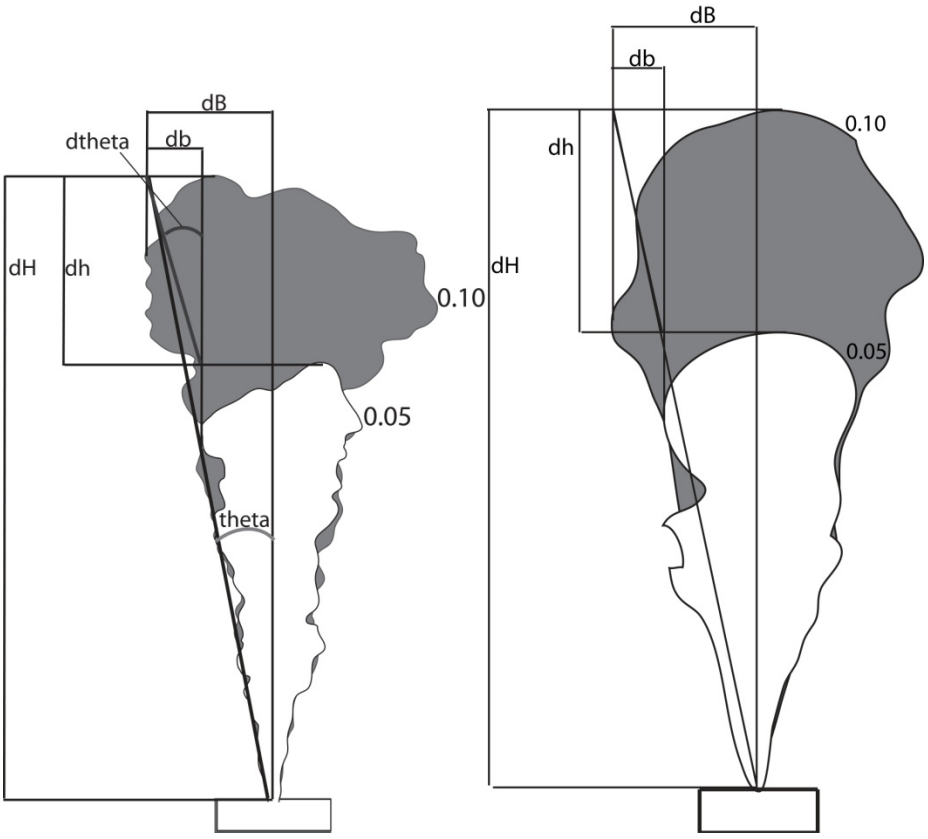

Figure 4.12. Ensemble-averaged source acceleration for experimental conditions H3 (inset, black circles), L3 (inset, gray circles), H9 (black squares), L9 (gray squares), H15 (black triangles), and L15 (gray triangles). Blue lines denote acceleration (1), constant (2), deceleration (3) and off (4) phases.

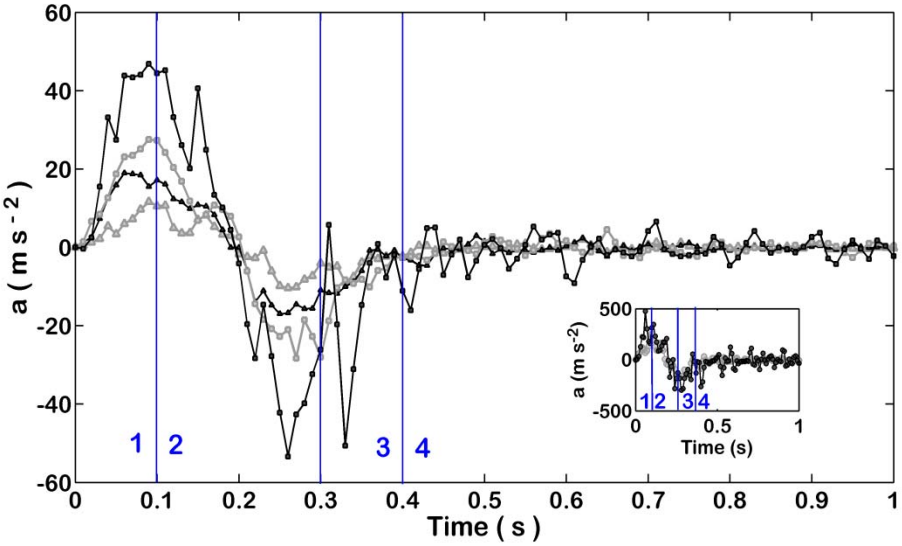

Figure 4.13. Calculated values of the constants C_1 and C_2 for the starting jet (a) and puff (b) models defined in equations 1 and 2, respectfully, for experimental conditions H3 (black circles), L3 (gray circles), H9 (black squares), L9 (gray squares), H15 (black triangles), and L15 (gray triangles). For the variable, M^*, the time-averaged momentum-flux is used in the starting jet model and the total amount of momentum injected is used in the puff model. Peak values are indicated by red stars.

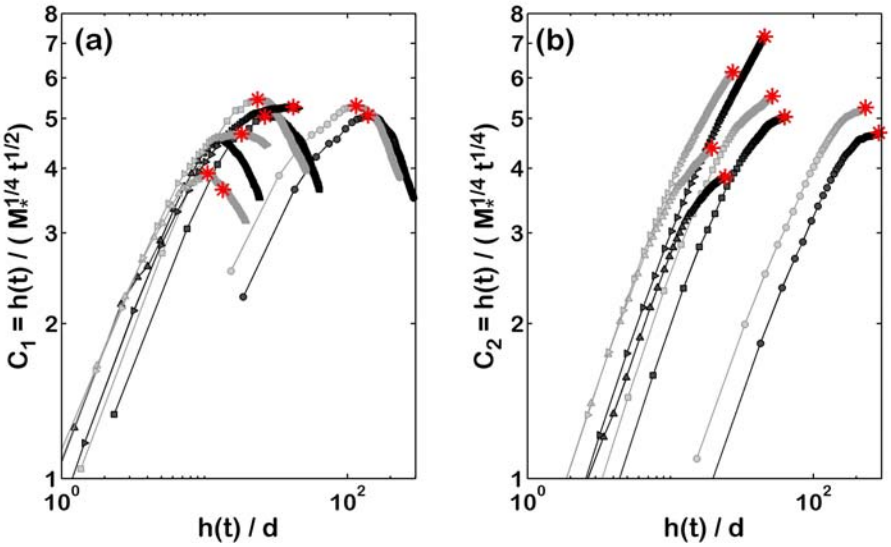

Figure 4.14. The instantaneous (blue dots), time-averaged (solid yellow line), and total (orange square) momentum flux for an individual experiment within the H3 (a) and the H15 (c) conditions. The resultant height estimates for the H3 (b) and the H15 (d) conditions.

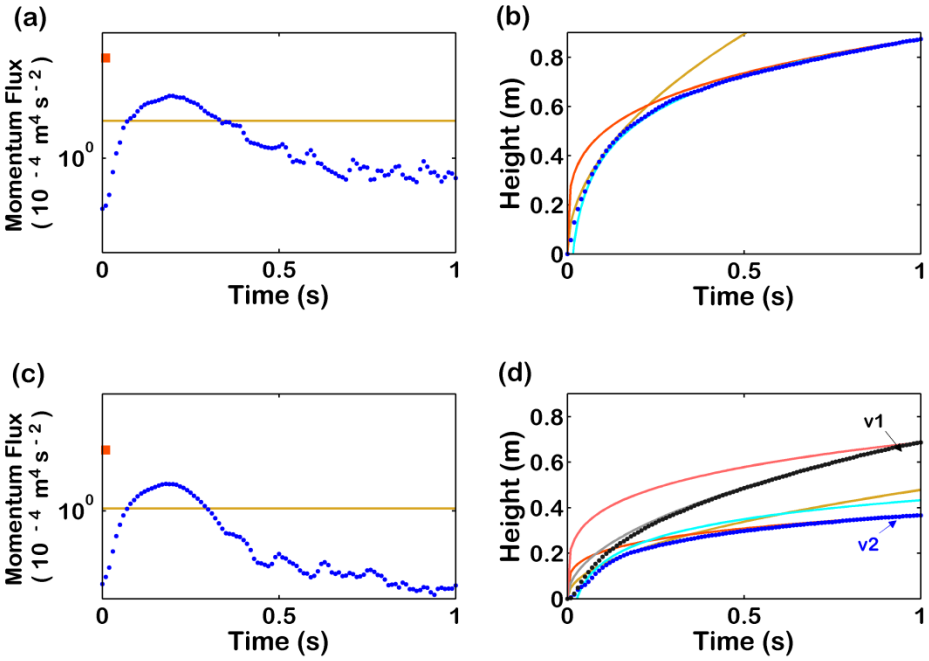

Figure 4.15. Locations (4, 1.39) and (16, 2.77) where laws with the powers of ¼ and ½, respectively, are tangent to the logarithmic function. Fit (magenta line) of normalized ensemble-averaged jet heights (see text) plotted against normalized time for experimental conditions H3 (black circles), L3 (gray circles), H9 (black squares), L9 (gray squares), H15 (black triangles), and L15 (gray triangles).

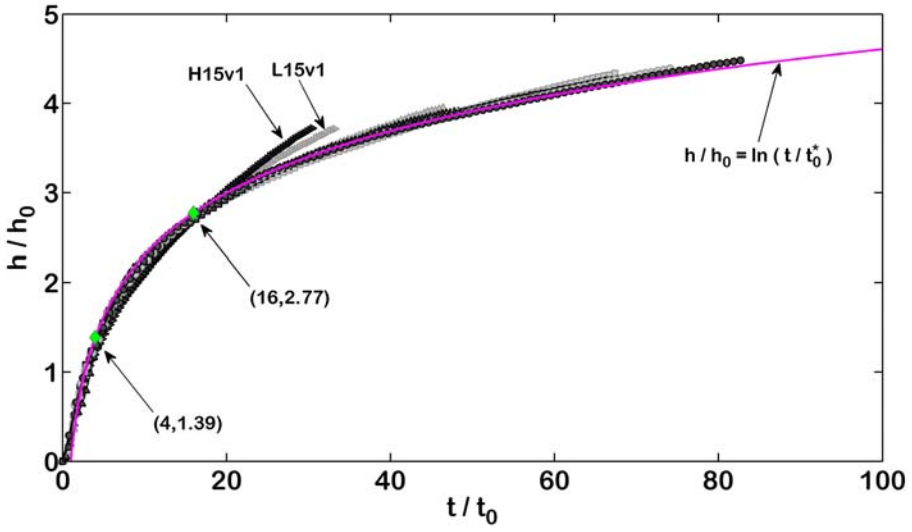

Figure 4.16. Power law functions $h/h_0 = 1.4\ (t/t_0)^{1/4}$ (blue dashed line) and $h/h_0 = 0.7\ (t/t_0)^{1/2}$ (red dashed line) that approximate the logarithmic function of the normalized ensemble-averaged jet height fit (magenta solid line).

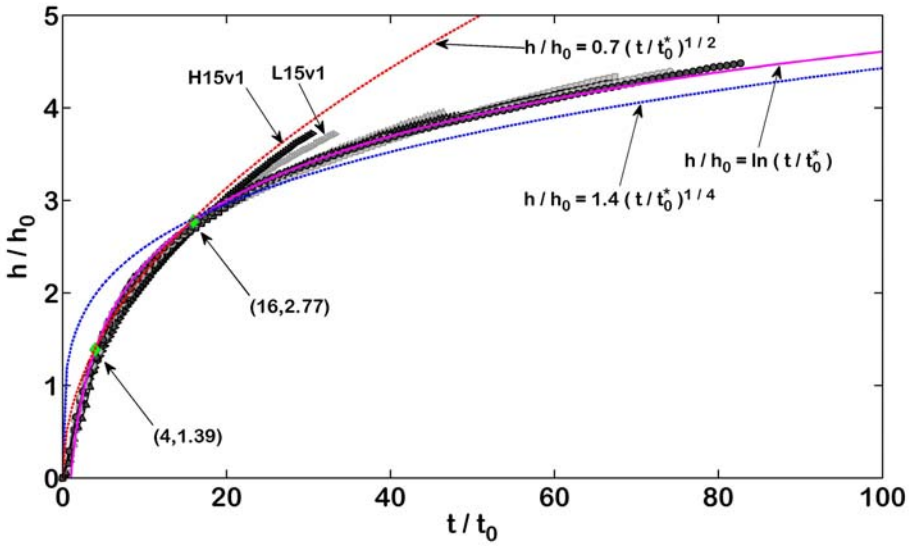

Figure 4.17. Figure from *Mori and Burton* [2009] showing the rise of a volcanic plume from Stromboli volcano. The colors indicate SO_2 concentrations within the plume.

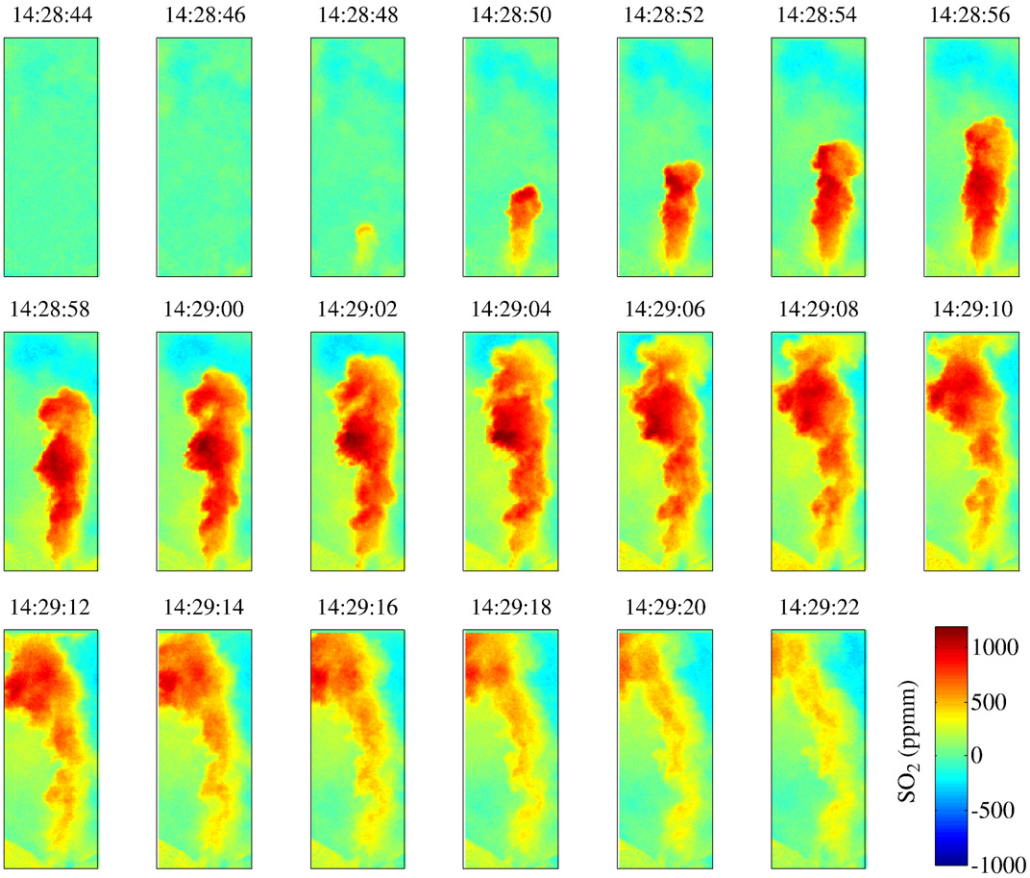

Figure 4.18. The height time series (a) of the volcanic plume imaged in *Mori and Burton* [2009]. The non-dimensional scaling law derived here (b) for the volcanic plume (circles) and the best fit curve of the experimental unsteady jets (solid line). For the volcanic plume, h_0 = 66.93 meters and t_0 = 1.53 seconds with a norm of residuals = 25.80. Thus, the characteristic velocity scale is h_0/t_0 = 43.75.

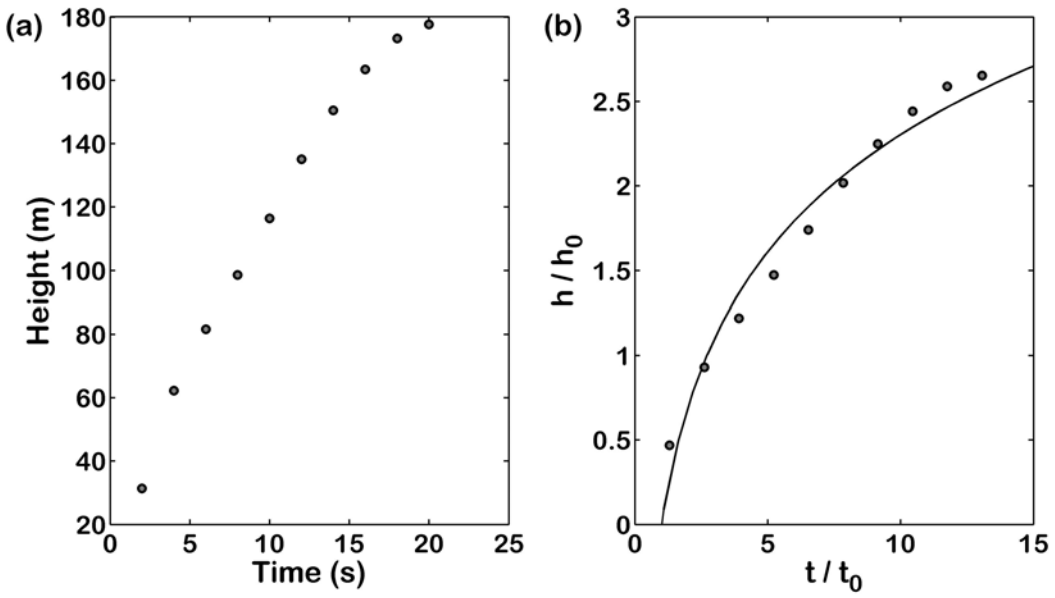

Table 4.1. Results from the linear regression analysis of the height time series.

Condition	$a = h_0$	b	Norm of residuals	b/a	$\exp(-b/a) = t_0$	$V_0 = h_0/t_0$
H3	0.20	0.86	0.12	4.42	0.014	14.29
L3	0.16	0.68	0.13	4.31	0.014	11.43
H9	0.13	0.57	0.09	4.26	0.012	10.83
L9	0.11	0.45	0.09	4.21	0.017	6.47
H15v2	0.09	0.36	0.09	3.88	0.018	5.00
H15v1	0.18	0.63	0.40	3.42	0.030	6.00
L15v2	0.07	0.29	0.08	3.84	0.016	4.38
L15v1	0.11	0.39	0.20	3.50	0.029	3.79

Table 4.2. Instantaneous (theta) and differential (dtheta) spreading angle calculations for an individual 3-mm experiment and the ensemble average of images.

Time (s)	Individual Experiment		Ensemble	
	Theta (degrees)	dtheta (degrees)	Theta (degrees)	dtheta (degrees)
0.00 – 0.10	11.3	16.3	12.0	13.0
0.10 – 0.20	10.8	0.90	11.0	10.0
0.20 - 0.30	10.1	22.9	10.7	22.9
0.30 – 0.40	10.0	40.3	11.5	15.1
0.40 – 1.00	9.5	2.50	12.0	18.9

Table 4.3. Instantaneous (theta) and differential (dtheta) spreading angle calculations for an individual 15-mm experiment and the ensemble average of images.

Time (s)	Individual Experiment		Ensemble	
	Theta (degrees)	dtheta (degrees)	Theta (degrees)	dtheta (degrees)
0.00 – 0.10	10.9	11.9	12.5	8.6
0.10 – 0.20	7.0	4.7	10.5	6.3
0.20 - 0.30	7.4	4.2	12.2	13.8
0.30 – 0.40	7.7	16.5	12.8	16.5
0.40 – 1.00	7.8	8.4	12.7	52.1

Table 4.4. Power law fit values

Condition	Phase	Time (s)	Power law fit	Residual
H3	1	0.01-0.06	$h = 1.8E2t^{1.27}$	0.29
	2	0.07-0.28	$h = 1.32t^{0.47}$	0.09
	3	0.29-0.48	$h = 0.74t^{0.29}$	0.01
	4	0.49-1.00	$h = 0.72t^{0.28}$	0.01
L3	1	0.01-0.10	$h = 14.8t^{1.02}$	0.36
	2	0.11-0.27	$h = 0.72t^{0.47}$	0.03
	3	0.28-0.41	$h = 0.46t^{0.32}$	0.01
	4	0.42-1.00	$h = 0.44t^{0.29}$	0.01
H9	1	0.01-0.09	$h = 93.3t^{1.38}$	0.66
	2	0.10-0.26	$h = 0.41t^{0.44}$	0.03
	3	0.27-0.42	$h = 0.33t^{0.38}$	0.01
	4	0.43-1.00	$h = 0.28t^{0.29}$	0.01
L9	1	0.01-0.09	$h = 1.7E2t^{1.57}$	0.75
	2	0.10-0.27	$h = 0.23t^{0.43}$	0.05
	3	0.28-0.44	$h = 0.17t^{0.34}$	0.01
	4	0.45-1.00	$h = 0.17t^{0.33}$	0.01
H15v2	1	0.01-0.08	$h = 1.7E3t^{2.11}$	0.54
	2	0.09-0.25	$h = 0.38t^{0.72}$	0.23
	3	0.26-0.47	$h = 0.11t^{0.38}$	0.01
	4	0.48-1.00	$h = 0.10t^{0.31}$	0.01
H15v1	1	0.01-0.06	$h = 3.4E5t^{2.77}$	0.73
	2	0.07-0.25	$h = 0.83t^{0.74}$	0.08
	3	0.26-0.47	$h = 0.45t^{0.55}$	0.01
	4	0.48-1.00	$h = 0.42t^{0.52}$	0.01
L15v2	1	0.01-0.09	$h = 43.7t^{1.66}$	0.29
	2	0.10-0.26	$h = 0.12t^{0.59}$	0.06
	3	0.27-0.41	$h = 0.07t^{0.42}$	0.01
	4	0.42-1.00	$h = 0.06t^{0.35}$	0.01
L15v1	1	0.01-0.06	$h = 1.5E2t^{2.77}$	0.30
	2	0.07-0.25	$h = 0.24t^{0.67}$	0.07
	3	0.26-0.47	$h = 0.15t^{0.53}$	0.01
	4	0.48-1.00	$h = 0.13t^{0.45}$	0.03

Table 4.5. Peak values of the constants C_1 and C_2 used to calculate values of height from the steady scaling laws in equations 1 and 2, respectively.

Condition	C_1	C_2
H3	5.1	4.7
L3	5.3	5.2
H9	5.0	5.0
L9	5.4	5.5
H15v2	3.6	3.8
H15v1	5.3	7.2
L15v2	3.9	4.4
L15v1	4.7	6.1

Table 4.6. Height time series measured from the images of *Mori and Burton* [2009].

Clock Time	Time from start (s)	Height (m)
14:28:46	0	00.00
14:28:48	2	31.32
14:28:50	4	62.24
14:28:52	6	81.57
14:28:54	8	98.58
14:28:56	10	116.37
14:28:58	12	135.06
14:29:00	14	150.52
14:28:02	16	163.40
14:28:04	18	173.20
14:28:06	20	177.58

Chapter 5

RESULTS FOR UNSTEADY JET INTERNAL EVOLUTION

5.1. Introduction

Chapter 4 presented the results of unsteady jet experiments in which the external behavior of the jet was found to vary in space and time in correlation with source conditions. As a result of the correlations, it was hypothesized that the source conditions lead to variations in the velocity distribution in the jet which, in turn, modified the external motion of the jet as observed. In this Chapter we use PIV to test these hypotheses and measure the effects of the unsteady discharge conditions on the distributions of velocity in the turbulent laboratory jets. The jets are generated under analogous conditions to those that may prevail in short-duration volcanic eruptions. These results are then used to improve interpretations of volcanic plume behavior in terms of eruption rate variations.

In turbulent flows, the overall motion of the flow may differ from the motion of the fluid elements that make up the flow. Fluid elements may undergo translation, rotation, linear deformation and angular deformation and the motion of a fluid element from one instant to the next may be due to one of these or some combination of any or all of them. As the overall motion of the flow is the net result of the individual motions of all of the elements, a greater understanding of the overall motion can be achieved by understanding the motion of the elements. The relative motion of fluid elements within a turbulent flow can be measured

using a technique called Particle Image Velocimetry (PIV) that involves adding particles to an otherwise clear fluid to make the motion of that fluid visible.

PIV is a measurement method used to measure the distribution of velocity within a moving fluid for the purpose of visualizing the structure of the flow and understanding the mechanics of its motion. This technique provides velocity measurements over a whole flow field at a particular instant in time; other techniques for measuring fluid motion involve measurements of the flow at a single location or over a large interval of time. Thus PIV captures snap shots of the continuous fluid motion. Analysis of these snap shots can then be used to inspect the mechanics of the continuous motion. The results of these measurements are typically represented as vector plots which show the differential motion of the fluid elements as well as the motion of the overall flow. These vectors plots can then be used to understand how the motions of the fluid elements combine to generate the overall motion of the flow.

PIV is also a nonintrusive measurement technique, as long as the particles do not interfere with the motion of the fluid, so the flow is not altered when taking the measurement. This feature is important for unsteady flows which may change abruptly and unsystematically by the presence of a measuring device in the field. The ability to make instantaneous measurements of the flow field is also an important feature for unsteady flows. Unsteady flows may involve the generation of very large instantaneous forces which may impact the motion of a fluid in a non-trivial way such that the motion cannot be understood without considering

the contribution from the unsteady forces. For example, the sudden opening of a valve in a water pipeline may lead to a burst pipe if the strength of the pipe material cannot withstand the large pressures that are generated in the pipeline during the valve opening. The average pressures in the pipeline, however, may remain below that peak value and thus a rupture would not be considered if the peak force was not considered. Consequently, making instantaneous measurements of the flow enables the measurement of large instantaneous forces.

To use PIV to understand unsteady dynamics, a set of experiments must be performed under conditions which are identical. Even for identical conditions, the inherent randomness in turbulent flow behavior will lead to variations in the measurements acquired from each individual experiment. Consequently, the contributions to the motion from variations in the measurements between different runs of that condition need to be eliminated before the motion can be analyzed. However, this must be accomplished without eliminating the contributions to the motion from time-varying dynamics. Ensemble averages are used for this purpose.

An ensemble average is computed for each instant that measurements are acquired. To compute the average, an instantaneous velocity distribution from an individual experiment is averaged with those at the same instant from all other experiments in the set. The result is an average velocity field that represents the average motion of a flow at a particular instant for a given experimental condition. This average is computed so that the mechanics of the flow that results

from a particular experimental condition can be studied rather than the mechanics of the flow that resulted from a single experiment.

The difference between velocity fields, or realizations, from an individual experiment and that from an ensemble average over all experiments in a set, or ensemble, is belabored here because each volcanic plume is essentially the result from a single experiment. Thus an understanding of the laboratory flows based on their ensemble average behavior may not provide information about the detailed dynamics of any single plume but rather information about the behavior common to an entire class of plumes generated from identical eruption conditions.

This fact presents some problems when trying to compare the laboratory data with volcanic plume observations because plumes are not classified in volcanology, eruption styles are. So while there are conceptual models for plumes formed during Vulcanian-, or Strombolian-style eruptions, each of these eruption styles can generate a wide variety of plume behaviors. *Patrick et al.* [2007] reported four different plume 'morphologies' - jets, starting plumes, thermals and rooted thermals - which they observed from Strombolian-style eruptions at Stromboli volcano in Italy. Each of these 'morphologies' is an individual class of turbulent flows with general theory and methods of solution specific to each class. Moreoever, each of these classes has a distinct source condition which implies that each of these 'morphologies' has a distinct source condition. However, these morphologies were defined based on observations of plumes without observations of the source conditions. While observations of 'source conditions' for volcanic

eruptions can be difficult to collect and interpret, let alone classify, it does present a problem when trying to understand how to model their dynamics. For example, it must be known whether each morphology class requires a separate set of equations or simply a change in the initial conditions of a single set of equations. However, with the exception of studies completed at the same volcano, the volcanology community has yet to publish plume observations according to this classification scheme. Thus, it is not yet understood if all of these morphologies are present or common at all volcanoes or if they are specific to Stromboli volcano in Italy. Moreover, *Gottsmann et al.* [2009] present evidence for two different plume types generated during Vulcanian-style eruptions at Soufriere Hills Volcano on the island of Montserrat in the British West Indies. Their analysis, however, was of the 'source condition' and they did not provide any detailed information about the plumes except to mention they were different. Moreover, publications which do consider plume behavior rarely consider the behavior common to more than 10 plumes, with the exception of *Patrick et al.* [2007] who used ~80 plumes on which they base their classification. Consequently, there is currently not enough plume observations in the literature to on which to define a distinct class of volcanic plumes.

Thus, this work considers the behavior common to a theoretical class of volcanic plumes which are generated at a variable rate during short-lived explosive eruptions and are driven by inertia. Both the results from individual experiments as well as ensemble-averages are considered here. This is to

facilitate, first, the understanding of what contributes to variability from the average behavior, and, second, the understanding of the evolution of an individual jet which may help identify which volcanic plumes may belong to this theoretical plume class.

5.2 Background

The results of experimental observations of jets and puffs are now discussed to inform the reader of what is known about velocity distributions in different types of turbulent flows. Three types of flows are considered here steady turbulent jets, puffs and unsteady jets. In all three of these flows turbulent motions are generated by momentum forces. They differ in their shapes and the dominant controls on their dynamics.

Steady turbulent jets are generated by a continuous source momentum. As jet fluid moves away from the source, it slows down and spreads wider. As it spreads, it incorporates ambient fluid into the jet through the process of turbulent entrainment. The rate at which jets slow, spread and entrain is governed by the rate momentum is supplied to the jet at the source. This momentum is diluted as the high-momentum jet fluid mixes with the low-momentum ambient fluid which causes the decrease in the jet velocity and the spread in the jet width.

Consequently, jets from steady source conditions have velocities that are large near the source and near center of the flow as shown in Figure 1. The vertical component of velocity along the centerline of the jet decreases with distance from source. The rate of decrease depends on the rate at which the jet

momentum is diluted by entrainment and mixing of ambient fluid. Close to the source of the jet, the velocity distribution across the jet is uniform; in other words, all of the fluid at the source has the same velocity. However, in the far field of the jet, the time-averaged vertical velocity distribution across the jet has a Gaussian spatial distribution. This distribution has a maximum velocity at the center of the jet and minima at the sides which represents the transfer of momentum from the center to the edges of the flow. This transfer occurs by the action of turbulent mixing. As the source momentum dissipates with increasing distance from source, the Gaussian cross-sectional distribution decreases in amplitude and increases in width. In between the near-field and far-field is the transitional region. In this region, large coherent structures are formed in the shear layer which separates the jet fluid from the surrounding ambient fluid. Coherent structures are regions of the flow where the fluid moves together in a pattern or coherently rather than moving at random. These structures dominate the dynamics in this region and control the rate at which ambient fluid is brought into the jet as well as the rate momentum is transferred throughout the flow. These large structures are formed by the large radial velocity gradients that form in the boundary layer between the high-velocity jet fluid and the ambient fluid. In steady jets, these gradients are reduced by the action of turbulent mixing which leads to the breakdown of the large structures in the transition region.

In unsteady jets, however, these large structures may persist rather than be broken down. This is because the unsteady conditions maintain the presence of

radial gradients in the velocity field. Unsteady jets are generated by source fluxes of momentum which vary in time. The factors which govern their behavior depend on the situation in which the jets were generated. Thus, to understand the effect of unsteadiness for a specific situation, experiments must be conducted in that situation. However, in general, the effect of source unsteadiness depends on whether the jet is being accelerated or decelerated. Relative to a steady jet, spreading and mixing are observed to decrease in accelerating laboratory jets [e.g., *Kouros et al*., 1993; *Zhang and Johari*, 1996], but increase in decelerating laboratory jets [e.g., *Boree et al*. 1996; *Johari and Paduano*, 1997; *Musculus*, 2009]. *Ruiz et al*. [2011] attributes the observed differences between steady and unsteady jets to the rate at which the shear layer between jet and ambient grows and forms the large-scale structures. *Ruiz et al*. [2011] observed that steady jets develop a slowly growing shear layer that rolls up approximately one diameter from the source into many small-scale structures. These observations are consist with previous observations of near-field structures in steady jets [e.g., *Crow and Champagne*, 1971; *Hussain and Husain*, 1989]. However, the shear layer from a pulsed jet – created by a sequence of pulses of fluid – develops more rapidly and forms large-scale coherent structures with characteristic length scales on the order of the total flow width [*Ruiz et al*., 2011]. They also observed that the magnitude of the vorticity near the source is increased in unsteady jets by over 50% compared to an equivalent steady jet [*Ruiz et al*., 2011].

These results suggest that unsteady discharge rates may lead to greater strain rates in the direction of flow within the fluid in the shear layer. These increased strain rates may in turn generate larger magnitudes of vorticity that lead to the observed large-scale structures. An alternative explanation proposed by *Soteriou et al.,* [2002], suggests that unsteady volume flux results in the production of local circulation maxima in the shear layer. While flow above the local maxima is decelerated by the presence of the local maxima, flow below it is accelerated and the difference in velocity induces the local flow to rotate around the maxima. *Soteriou et al.,* [2002] suggest local maxima do not occur in steady jets because the production of circulation in the shear layer increases monotonically with height at an approximately constant rate. *Soteriou et al.,* [2002] also propose that the magnitude of the circulation or the strength of the rotation depends on the relative rates between the local turbulent diffusion and convection processes. Turbulent diffusion acts to reduce gradients and prevent the development of local maxima so large rates of turbulent diffusion work against the generation of structures *Soteriou et al.*, [2002]. Convection may lead to large local strain rates and thus stretch the circulation in the direction of flow and prevent local maxima from forming *Soteriou et al.*, [2002].

In other experiments looking at unsteady vortex generation, *Olcay and Krueger* [2008] observed that accelerating a forming vortex results in a more tightly wound vortex with a smaller core as compared to the steady formation of a vortex. Similarly, decelerating flow during vortex formation results in a more

loosely wound vortex with a fatter core *Olcay and Krueger* [2008]. As observed by *Ruiz et al.* [2011] and noted by *Maxworthy* [1972], forming vortices entrain ambient fluid through advection whereas fully formed, steady vortex rings entrain ambient fluid through the much slower process of diffusion. The time over which vortices form then delineates the time during which entrainment occurs by advection. This time is commonly referred to as the 'formation time' following *Gharib et al*. [1998]. For steady flow conditions, in piston-cylinder driven experiments with smooth contraction nozzles *Gharib et al*. [1998] found that the formation time was affected only by the velocity of fluid that forms the vortex and the geometry of the outlet. Thus, if the vortex motion was non-dimensionalized on these scales, universal formation time resulted with a non-dimensional time around the value 4. However, other factors such as unsteady flow conditions, the specific vortex-generation mechanism, and the outlet type have all been shown to influence the formation time [e.g., *Ai et al*., 2005; *Yu et al*., 2007].

When pressure drives vortex generation, there seems to be an additional contribution of pressure to the circulation of the rings during the initial roll up phase [*Krueger*, 2005]. Because the propagation velocity of a vortex ring is directly related to circulation, pressure-driven rings should propagate faster than piston-cylinder or gravity-driven rings. Orifice plates tend to delay the formation time, that is, lengthen the duration of advective entrainment, and produce larger rings that persist for longer times than vortex structures formed by flow through smooth contraction nozzles or flat plate orifices [e.g., *Ai et al*., 2005; *Mi et al*.,

2007]. These observations suggest that pressure-driven rings generated in jets issuing from orifice plates should form rings that propagate further from the outlet before they finish forming, all the while entraining ambient fluid through advection.

The effect of unsteadiness on vortex formation depends on the nature of the unsteadiness. In general, acceleration tends to decrease formation time that results in structures forming close to the source. Deceleration results in an increase in the formation time with structures that form far from the vent. Flows that quickly accelerate and then slowly decelerate, entrain large amounts of ambient fluid and form rings with small cores [*Olcay and Krueger*, 2008]. Flows that slowly accelerate and then quickly decelerate form rings with fat cores that entrain less ambient fluid.

Vortex rings, turbulent puffs and jets may all be created by the impulsive injection of fluid through an outlet. To classify the flow that will result from a particular injection, the nondimensional parameter, P, was developed by *Hermanson et al.* [2000], and is defined as the cube root of the ratio of the total volume injected to the product of the outlet area and its diameter. Large P values result in the generation of starting jets whereas small P values generate vortex rings; puffs are generated by intermediate values. For a constant value of outlet area, the value of P is determined by the total volume injected alone, and thus the total volume injected determines the structure that forms during the injection.

Puffs and rings are generated by an instantaneous release of momentum and their motions are governed by the total amount of momentum imparted to the puff or ring during release. For small volume injections, vortex rings are formed and at intermediate volumes puffs are formed [e.g., *Olcay and Krueger*, 2008]. In the experiments of *Ghaem-Maghami and Johari* [2010] this difference was attributed to the presence of a tail of fluid in the puff case that was absent in the vortex ring case. The vortex ring entrains fluid across its bottom surface by advection and thus the presence of the tail limits the surface area across which fluid can be entrained [*Ghaem-Maghami and Johari*, 2010]. Entrainment at the sides of the puff tail occurred by diffusion [*Ghaem-Maghami and Johari*, 2010]. Furthermore, these experiments showed that above the cores of the structures fluid was always directed radially away from the structure, while below the cores fluid was brought into the structure, ambient fluid in the case of the ring and tail fluid plus ambient fluid in the case of the puff [*Ghaem-Maghami and Johari*, 2010]. For the ring, ambient fluid is incorporated into the structure at a greater rate than it is forced out at the top; conversely for puffs, the rate at which fluid is forced out the top is greater than the entrainment rate [*Ghaem-Maghami and Johari*, 2010]. Each of the *Ghaem-Maghami and Johari* [2010] experiments was conducted at the same constant velocity, which was maintained over the injection duration, and greater volumes were achieved simply by increasing this injection duration.

In contrast, in an unsteady jet, the injection rate may vary in time such that the volume flux may change considerably from one instant to the next. It is unknown whether such source conditions will result in flow structure evolution from ring to puff to jet over time. However, experiments by *Sangras et al*. [2002] observed that interrupted starting jets, jets where the source was on long enough to achieve starting jet behavior before the source was suddenly stopped, evolved from starting jets to puffs for short times after the source was stopped. This result suggests that a changing source condition may result in structure evolution through time.

The far-field velocity distributions for rings and puffs from steady sources were investigated by *Ghaem-Maghami and Johari* [2010] who found that velocity distributions were greatest in the center of a ring or puff and decreased radially from the center. Larger volume puffs also had the largest velocities near the center of the flow but had a velocity distribution that was elongated in the direction of the flow due to the presence of the head and the tail.

While most of the above experiments utilize constant velocity or schematic (e.g., trapezoidal) acceleration schemes, in natural flows the volume flux increases, gradually peaks, and then decreases before it stops. This volume flux is typical for jellyfish and squid locomotion, cardiovascular flows [e.g., *Querzoli et al*., 2011] and perhaps flows from some volcanic eruptions. As the injection time history is an important control on the formation of vortices in the near-field of these flows, the gradual changes in velocity are expected to affect the

formation of structures and the shear layer in nontrivial ways. Thus, it is important to understand the dynamics of the vortices generated from this type of unsteady source condition to understand the unsteady jet dynamics.

Consequently, this work aims to measure the internal velocity fields of jets generated under conditions which may prevail in short-duration volcanic plumes. The purpose of the measurements is to characterize the velocity structure of the unsteady jets over time. The evolution of the structure is then analyzed to improve the understanding of the mechanics of these flows.

5.3 Methods

Velocity field measurements were obtained using Particle Image Velocimetry (PIV). PIV is a non-invasive technique for measuring velocities within a flowing fluid. A schematic illustrating this process is shown in Figure 1. In this technique, particles are added to a fluid to provide a means to track the motion of the fluid which is otherwise not visible. Particles within a particular plane through the flow interior are then illuminated with a laser light sheet so the internal motion, rather than the motion of the edges, of the flow is visible. Images are then taken of the illuminated particles [*Adrian and Westerweel*, 2011]. Sequential images are then processed to determine the distance the particles moved between the times the images were taken. Processing involves dividing the image field of view into small subsections using a grid. Within each grid section, the average displacement of all the particles in a grid section is found by cross correlating the images. Velocities are then computed by dividing the average

displacement in that grid section over the time interval between the images. This computation is completed for all grid sections. The result is a velocity field for the flowing fluid in the plane of the laser [*Adrian and Westerweel*, 2011].

I conducted the PIV measurements at the Explosive Volcanology Laboratory Group at Arizona State University. The jets were created in the apparatus in Figure 3.1 which is described in Chapter 3.1. In contrast to the experiments described in Chapter 3.1 in which the jet issued from a flat plate orifice, in the experiments described here the jet issues from the open pipe; the flat plate orifices screw onto this pipe so they were simply not installed while these experiments were conducted. This decision was made to limit the number of unknowns in the problem as the behavior of steady jets, puffs, and vortex rings from open pipe experiments were discussed more extensively than those from orifice plates in the literature at the time these experiments were conducted, January and February 2010.

The PIV arrangement is shown schematically in Figure 3.2. This arrangement consisted of a laser, optics for creating a laser sheet across the image area and a digital camera for recording the PIV images. Silver-coated hollow glass spheres from Potters Industries were used to seed the source and ambient fluid. These particles had a diameter of 10 microns and a density of 1.1 grams per cubic centimeter. The laser sheet was created with a dual-powered double-pulse Nd:YAG laser from Litron, operated at a frequency of 14.1 hertz and power of 200 millijoules per pulse at a wavelength of 532 nanometers. The light sheet was

aligned with the center of the pipe to illuminate the motion in the center plane of the jet. The light sheet was approximately 1 millimeter thick and approximately 30 centimeters tall at the location of the pipe. The time between laser pulses was 0.0075 s. Synchronization of the camera and laser were controlled with a timing unit.

Images were then taken of the particles that were illuminated in the plane of the laser. Images were taken with a HiSense4M camera from Dantec Dynamics at a frequency of 14.1 hertz. The camera was operated in triggered double frame mode which means a pair of images was collected every 0.07 seconds after the camera was triggered. Images were collected for a total record length of 7.0 seconds. The CCD in the HiSense4M camera is 2048 pixels high by 2048 pixels wide; however, images for this study are 2048 pixels high by 1000 pixels wide to limit the field of view to the jet motion. The narrow field of view increases the number of velocity measurements within the jet region. The optics for the camera consisted of a Zeiss macro lens with a fixed focal length of 50 millimeters that was coupled to the camera with an F-mount adapter. The camera field of view was 302 millimeters tall by 142 millimeters wide such that each pixel corresponded to 0.15 millimeters. This provided measurements over the region $0 < y < 15d$ where y is the vertical distance from the pipe exit plane and d is the inner diameter of the pipe. The pipe inner diameter was 20 millimeters. The center of the field of view was offset from the center of the pipe to capture the motion of the ambient fluid surrounding the jet boundary. The measurements corresponded to a radial distance

of -2.5d < r < 4.5d where r is the radial coordinate and r = 0d corresponds to the center of the pipe. Separate high speed video measurements of this same flow condition in this apparatus yielded maximum jet front velocities of the order of 1 meter per second within this field of view immediately following jet initiation.

The PIV images were analyzed using an interrogation window size of 32 by 32 pixels with a 25% overlap. Image pairs were cross correlated and then filtered using a 3 by 3 pixel moving average filter. A multi-pass correlation algorithm was applied to minimize noise. This was set at 3 passes. The resulting vector fields have an array of 85 by 40 vectors (i.e., 3400 uniformly spaced vectors). For a single pass and without the moving average filter, there were erroneous vectors (outliers) in the PIV fields immediately following jet initiation. These outliers were usually located in the jet close to the pipe exit plane (y < 1d) or near the front of jet in the starting vortex. For times near the jet initiation the outliers in the jet are likely associated with a combination of the very high seeding density in the jet fluid as it exited and perhaps large velocity gradients in the jet fluid. For intermediate times, the outliers in the jet are likely associated with a combination of the very high seeding density in the jet, large velocity gradients in the jet fluid, and the rotation of the jet fluid into and out of the plane of the laser. The number of outliers in the jet decreased as the time after injection increased. Outliers in the starting vortex are likely associated with the three-dimensional motion of the vortex. Regions of high shear (steep velocity gradients) also appear

at various times and in various places throughout the flow which also contributed to the generation of spurious vectors.

After three passes and the application of the moving average filter, up to 70 % of the velocities in the fields consisted of interpolated vectors. This is attributed to the large dynamic range in the instantaneous velocity fields generated in these unsteady experiments. The error may be reduced by optimizing the PIV technique by identifying the spatial extent of the camera field of view, the timing between laser pulses, and the seeding density in the jet appropriate for each instant and location during the jet evolution. However, this optimization cannot be completed without *apriory* knowledge of the range of velocities which can be expected in the flow fields at different locations and at different times. This information was not known before this study was undertaken and it was therefore necessary to begin with a characterization of the flow behavior to establish a baseline. Due to the highly variable nature of the flows from this experimental setup this characterization was time consuming. Therefore, the work presented here lays the groundwork for additional studies in this setup which may yield improved velocity measurements. Nevertheless, the interpretation of the flow behavior presented here should not be significantly altered with these improved measurements. In other words, it is expected that improved measurements may refine the details of the motion within the context of the broader characterization of behavior presented here. This broad characterization, however, significantly improves the understanding of unsteady jets developed by the bulk visualization

presented in Chapter 4. Therefore the error in the measurements is considered acceptable for use in this purpose; it may be unacceptable for use in validating numerical models.

The experiments described here were conducted at approximately 3.4MPa, the low momentum condition described in Chapter 4. This maximized the time the jet front remained within the field of view of the camera. Instantaneous flow fields were measured for 100 experiments over a range of total injected volumes. The experiment conditions are summarized in Table 3. At first the velocity fields from all 100 experiments were ensemble averaged. However, the results were difficult to interpret. This was attributed to the fact that flows with different volumes generate structures in different locations with different strengths. As discussed in the introduction, the value of P, which is a parameter that identifies the structure that will form during a steady injection, depends only on total injected volume when the vent area remains constant. Thus, the total injected volume for each experiment was calculated according to equation 1. The frequency distribution of the calculated volumes is shown in Figure 4. The mean injected volume was 65.3 cubic centimeters and experiments within 5% of this mean were chosen to ensemble average. Ensemble averages were then calculated over the 27 experiments with total injected volumes that met the criteria. These averages were computed for each instant data was acquired.

The accuracy of an ensemble average improves when more experiments are part of the ensemble – this holds for experiments at the same condition which

would be defined by total volume injected in this situation. When a small number of realizations comprises the ensemble there may be areas of low coherence or data loss where velocities strongly vary between realizations. A universal number does not exist for the exact number of realizations that need to comprise the ensemble to prevent data loss. The value depends on the flow situation and the purpose of measurements. The purpose of this study was to investigate the evolution of the flow over time rather than achieve a statistically convergent data set and thus visual inspection of the ensemble of 27 experiments suggests it is sufficiently large for this purpose. However, areas of low coherence and data loss in the ensemble average field are expected with this ensemble size. The low coherence seems to effect the measurements in the jet more than the ambient fluid. Considering the low coherence in the ensemble for the motion of the jet fluid, an individual experiment was chosen to represent the evolution of all experimental runs in the ensemble and to illustrate the main features of the flow development that are not evident from the ensemble.

For perspective, a similar experimental study was published by *Ghaem-Maghami and Johari* [2010] after the completion of these experiments which found that 2000 experimental runs were needed for convergence of the ensemble statistics for *steady* finite-volume flows suggesting a much larger number would be required for unsteady flows. Based on the results from 100 experimental runs (realizations) in this apparatus, 30 experiments of every 100 would be similar enough to ensemble. Thus, to obtain the minimum of 2000 experiments for a

convergent ensemble average, over 6000 experiments would be required. At peak efficiency, I ran 1 experiment in 30 minutes, which suggests over 3000 hours of data collection alone would be required to obtain an experimental set of that size. This estimate does not include a number of additional steps that are required to obtain this data including data processing which takes about 4 times longer than data collection. In short, to obtain that type of data set in this apparatus would require a such a significant undertaking that it is cost prohibitive on the grounds that I've outlined only what may be required for the minimum number of experiments for a statistically convergent data set – there's no guarantee, however, this number would be sufficient to produce a statistically convergent set at that minimum for *unsteady* finite-volume flows. Furthermore, in the study referenced, the statistics converged for the velocity fields in the self-similar region of the far field which indicates nothing about the convergence anywhere else in the flows. And what's more, due to the significant time variation in these flows, statistical convergence would likely be achieved at a *different* number of experiments for *each* instant, particularly since some of the instants involve rotation of the flow about the flow axis while others do not – it would likely take longer for the instants with rotational flows to reach statistical convergence. Thus, statistically convergent data sets were not the objective of this study.

5.4 Results

The source momentum flux history is shown in Figure 5.1 for a representative individual experiment (a) and the ensemble of all chosen

experiments (b). The injection is characterized by a momentum flux that first increases, then reaches a maximum and decreases to zero as it ends. The injection sequence is divided here into five stages: (1) initiation and acceleration of the discharge rate which occurs from 0.00 to 0.10 s; (2) constant discharge rate from 0.10 to 0.30 s; (3) decelerating discharge rate from 0.30 s to 0.40 s; (4) a transition stage from 0.40 s to 0.60 s where the source ends and discharge is zero; and (5) the time well beyond the injection time from 0.60 s to 1.91 s. Due to limitations with the pulsing of the laser, velocity fields were collected at 14.1 Hz and thus each phase of the source corresponds with few velocity field measurements.

5.4.1. Instantaneous Velocity Vector Fields

During phases 1 – 4, the flow fields change quickly in time and space. To illustrate the flow development through these phases, a group of images is used for each instant within the phase. This group includes a photo which shows the cross sectional view of the flow in the plane of the laser for an individual experiment. The photo is a contrast-enhanced image used for the PIV analysis. The areas with high concentrations of white pixels show the extent of the jet fluid. The areas with low concentrations of white pixels indicate the location of the ambient fluid. Alongside the photo of the jet cross section is the velocity field that corresponds with the jet in the photo. This velocity field represents the motion in both the jet and ambient fluids at one instant and is thus referred to as the instantaneous velocity field. Finally, the instantaneous velocity field averaged

over the ensemble of experiments (the ensemble average instantaneous velocity field) is shown alongside the individual field.

The juxtaposition of the individual and ensemble fields facilitates the comparison of features of the velocity field which are common to all experiments (ensemble) at that instant with those that characterize an individual experiment. Large-scale turbulent structures are formed in each individual experiment. As I will demonstrate later in this chapter, the transient source conditions result in each individual experiment forming structures with different sizes and strengths, occurring at different spatial locations. This variability results in the details of the structures getting averaged out in the ensemble. However, the structures are important features of the dynamics for an individual flow and therefore both the instantaneous and ensemble velocity fields are presented for phases 1 - 4. During phase 5 the flow fields change slowly in time and space and four instants were chosen to represent this evolution. For this phase, the individual flow fields are similar to the ensemble flow fields and thus only the ensemble averaged velocity fields are presented for each instant.

5.4.1.1 Initiation and acceleration: Phase 1

Data that represent this phase were collected at 0.07 s. In the photo of the external flow (Figure 5.2a), the jet is three vent diameters tall (3.0d) tall and is composed of a circular flow front with a maximum width of 2.0d followed by a column of approximately 1.0d in width over its entire length. The circular-shaped flow front is formed by the first fluid to exit the pipe, that generates an organized,

vortical structure. In the photo of the flow (Figure 5.2a), the vortex structure appears as the circular shaped flow front centered around the centerline of the flow (r/d = 0.0) and extends from height y/d = 2.0 to y/d = 3.0, where y/d is the height above the vent normalized by the vent diameter. The velocity field of a vortex core is shown schematically in Figure 2.4. In the corresponding instantaneous velocity field (Figure 5.2b), this structure appears as two counter rotating vortices that extend from y/d = 0.0 to y/d = 5.0 with a maximum width of 4.0d. Given that the extent of the structure is much larger than its visible boundary in the photo, this flow field represents both the motion of the jet fluid and the induced velocity field in the ambient fluid. In the ensemble velocity field (Figure 5.2c), this structure appears as the region of radiating fluid centered around the linear region of low velocity fluid at y/d = 3.0 that extends from r/d = -1.0 to r/d = 1.0.

The instantaneous velocity field (Figure 5.2b) shows that the centers of the vortices, or the cores, have low velocities and are located at r/d = -0.5, y/d = 3.0 and r/d = 1.5, y/d = 2.0. The locations of the cores are asymmetric with respect to the axis of the flow. The line which connects the cores is rotated 27^{o} to the horizontal. Above this line, fluid radiates out from the vortex but below the line fluid moves from the outer edges of the structure toward the centerline of the structure. While the ensemble velocity field (Figure 5.2c) at this time also shows a vortex structure, the structure is symmetric about the centerline and there are no vortices clearly shown. Instead, there is a linear region of near zero velocity at y/d

= 3 that extends from r/d = -1.0 to r/d = 1.0. Above this region fluid moves radially away from the line, but below the line fluid moves from the outer edges at r/d = -2.0 and r/d = 2.0 toward the centerline to r/d = -1.0 and r/d = 1.0, respectively. The streamlines in both the individual (Figure 5.2b) and ensemble (Figure 5.2c) velocity fields reflect the rotation associated with the starting vortex and the radial velocity pattern in the ambient.

The velocity pattern at 0.07 s is indicative of an impulsively started jet. Ahead of the jet, the ambient fluid is moved in a radial pattern directed away from the jet. This radiation pattern is consistent with the pattern of a point source or a monopole which has a decay rate inversely proportional to the distance from the source. At the jet front, a starting vortex forms. The formation process is illustrated in the schematic in Figure 2.3 and occurs due to the interaction of the jet fluid with the wall of the pipe and the still ambient fluid. The interaction with the wall of the pipe and the jet source fluid creates a boundary layer internal to the jet source fluid. In this layer, the fluid closest to the pipe wall is slowed relative to speed of the fluid in the center of the pipe. Once the jet fluid exits the pipe, the still ambient fluid the boundary layer separates the moving jet fluid from the sill ambient fluids. This velocity difference across the interface of the jet and ambient fluids is an unstable property configuration for fluids and classified as a Kelvin-Helmholtz instability. To eliminate the instability, the fluid rotates away from the jet center around the interface between the fluids. Consequently, this process is described as a roll-up of the jet shear layer. The interface of two fluids moving at

different velocities is called a shear layer whereas the interface between a fluid and a solid boundary is called a boundary layer. For circular exit conditions, the jet shear layer has an annular shape. When the annulus rolls, a torroid or ring is formed. This torroid is the core of a toroidal vortex or vortex ring which forms at the jet front due to the impulsive starting conditions; it is therefore referred to as a starting vortex. Toroidal vortices have a velocity pattern similar to a dipole source. As this rings form, they also move the ambient fluid with them.

The two-dimensional velocity pattern associated with the starting vortex consists of two counter rotating vortices. The circular vortices are cross sections of the ring or toroidal core. The extent of the velocity pattern involves the motion of both ambient and jet fluid as evidenced by the difference in size between the visible boundary of the jet fluid in the photo and the extent of the rotational pattern in the velocity field. The flow pattern in the ensemble field (Figure 5.2c) indicates the structure has significant movement in three dimensions – two within the plane of the laser, and one between the plane of the laser and the camera. The three dimensional pattern is indicated in Figure 5.2c by the presence of the linear feature of low velocity and the seemingly negative fluid velocities below it. The linear feature is likely the location of the toroidal-shaped core of the vortex where low fluid velocities would be expected. The vectors below the core indicating fluid motion back toward the source are likely a projection effect related to the three-dimensional circulation pattern of the vortex out of the plane of the laser and toward the camera. While this structure is symmetric about the centerline in

the ensemble field it is asymmetric in the individual field. The source of the asymmetry this close to the vent is most likely related to the velocity distribution in the source fluid before it exits the pipe. Since this asymmetry is absent in the ensemble, asymmetries in the individual structures must average out over multiple experiments. The analysis of the velocity field results in a similar conclusion to the analysis of the bulk boundary of the fluid presented in Chapter 4. However, it was not apparent in the bulk flow images that the highest velocities in the flow are at the center of starting vortex structure.

By 0.14 s, the jet rises to 6.0d and is ~2.0d wide at its maximum width as indicated by the photograph in Figure 5.3a. The jet width is non-uniform over the height and can be divided into three regions. Near the source (y/d = 0.0 to y/d = 2.0), the jet has a uniform width of 1.0d. Then, the jet widens to 2.0d from y/d = 2.0 to y/d = 5.0. From y/d = 5.0 to y/d = 6.0 a ‘neck’ of fluid connects the fluid below y/d = 5.0 to the starting vortex at y/d = 6.0. The ‘neck’ is wide at y/d = 5.0 and narrows up to the bottom of the vortex ring. As compared to the previous instant, the ring structure now has a much wider section of fluid between the vortex cores and the cores appear to have smaller diameters.

The individual velocity field at 0.14 s (Figure 5.3b) shows the region of radial velocity is ahead of the jet above y/d = 7.0. The starting vortex is cores are both at approximately y/d = 6.0 whereas in the previous time (Figure 5.2b) they were offset. The cores are located at ~r/d = -1.0 and r/d = 1.5, nearly symmetric about the vertical centerline, and separated by a distance of 3.5d; the ring is now

wider than at the previous time. There is a region of high velocity in between the cores that is asymmetric about the vertical centerline. On the right side of the field (+ r), the streamlines indicate the presence of a 'D' shaped circulation pattern [*Kovasznay*, 1975] which extends from the front of the starting vortex at y/d = 7.0 to the bottom of the second structure at y/d = 3.0. Velocities at the center of the jet are high throughout this length. There is a discontinuity near y/d = 4.0 in the velocity contours for the peak velocity magnitude. Also occurring at this height, is the contact of the streamlines of the D vortex with the jet fluid. Below y/d = 3.0 velocities in the narrow tail (between y/d = +/- 1.0) are vertical and notably lower than those in the second structure. The ensemble velocity field at 0.14 s (Figure 5.3c) show a similar pattern as the instantaneous indicating the individual experiments have similar features at this time. The motion of the ambient fluid below the D vortex and outside of the jet (beyond y/d = +/- 1.0) is different from the individual experiment. The region has a predominately radial orientation with motion directed toward the center of the jet.

Based on the patterns in the velocity fields at this time, there appear to be five main regions in the flow field. The first is the radiating velocity pattern ahead of the jet which results from the movement of the ambient fluid to allow the jet to rise. The second region is the starting vortex which appears to retain some three dimensional component because there are still arrows in the center of the vortex that are directed opposite the flow direction. In this region in the individual experiment there is no clear evidence that ambient fluid separates the starting

vortex from the flow behind it. However, when the velocity field is overlaid on the photo as shown in Figure 5.4, the cores of the D vortex structures correspond with the regions of ambient fluid between the front vortex and the tail. Thus the large scale structures in this flow are wider than the flow and nearly as long. The third region is the main jet region located between r/d = +/- 0.5 at heights between y/d = 0.0 and y/d = 5.0 in the ensemble field. This region has a velocity peak near y/d = 4.0 in the ensemble field due to the presence of the second structure. Fourth is the ambient fluid outside of y/d = +/-1.0 where the flow field is predominately inward-directed radial flow. This region appears to represent motion of the ambient fluid induced by the jet motion. Finally, there are two narrow regions of low velocities in the ensemble field at locations where the radially oriented velocities in the ambient meet the vertically oriented velocities in the jet. These regions are adjacent to the jet-like structure below the vortex ring; they are roughly defined by outwardly angled lines that span from y/d = 1.0 at r/d = +/- 0.5, to y/d = 5.0 at r/d = +/- 2.0. These zones are interpreted to represent the shear layer between the jet and ambient fluids. The velocity gradients that likely exist in this region result in a loss of data during PIV processing which may lead to the low velocities in the ensemble field.

The presence of the ‘D’ vortex or the circulation pattern that extends from the front of the flow to the tail of the second structure is not evident in the bulk flow images or the photos in these images. It indicates that starting vortex is still interacting with the fluid behind it. Also the fact that momentum is concentrated

in the second structure is supported by the large magnitudes of the velocities in this region relative to other regions. However, this may also be an artifact of the quality of this data. The velocity field in the tail at this time needs to be better resolved to test this hypothesis.

5.4.1.2. Constant acceleration: Phase 2

At 0.21 s, the photo shows that the starting vortex is moving away from the tail (Figure 5.5a). This movement is indicated by the presence of more ambient fluid between the starting vortex and the tail as well as the difference between the positions of the vortex front and the front of the tail. The front of the vortex is now at y/d = 9.0 and the front of the tail of fluid is at y/d = 6.5; a total distance of 3.5d. In the previous instant, the front of the staring vortex was at y/d = 7.0 and the front of the tail was at y/d = 5.0; a total distance of 2.0d. The starting vortex has a maximum width of 3.0d at this instant and the tail has three regions of varying width. Closest to the outlet, from y/d = 0.0 to y/d = 1.0, the tail has a constant diameter of 1d. The sides of the tail in this region appear to be parallel and straight. From y/d = 1.0 to y/d = 3.0 the flow has an uniform width of 2.0d. Above that, from y/d = 3.0 to y/d = 6.5, is a region that is approximately spherical (circular in the plane of the laser) shaped with a diameter of 1.5d. The front of the leading vortex ring moved from y/d = 6.5 to y/d = 10.0 since the last frame (time elapsed of 0.07 s), equivalent to a rise rate of 1.0 m/s. The front of the tail moved from y/d = 5.0 to y/d = 7.0 over the same interval, indicating a slower rise rate of 0.6 m/s.

At 0.21 s, the individual instantaneous velocity field (Figure 5.5b) shows that the starting vortex continues to dominate the flow field. At this time it is again asymmetric, although angled 20^{o} from horizontal in the opposite direction. The radiating velocity field in the ambient fluid ahead of the jet is visible above y/d = 9.0. This pattern is now angled from the vertical. This orientation is different from the previous time steps. Though the vortex cores were not offset at 0.14 seconds, they were at 0.07 seconds but the radiation pattern ahead of the flow was symmetric about the centerline of the flow. However, the ensemble velocity field (Figure 5.5c) shows that, on average, the radiation pattern ahead of the flow remains symmetric. The vortex cores are at y/d = 7.0, r/d = -1.0 and y/d = 8.0, r/d = 1.5, in the individual field (Figure 11a) and are separated by a distance of 3d. The ensemble velocity field (Figure 11c) shows a similar pattern though the vortex appears symmetric about the centerline and there are now vortices in the flow field with cores at y/d = 8.0. At y/d = 7.0, there are regions of high velocity directed into the bottom of the starting vortex. The streamlines show evidence that a large D vortex structure still exists above y/d = 5.0 but with a width that extends beyond the field of view. The streamlines surrounding the vortex core however suggest the D structure is now confined to the starting vortex. In both the individual and ensemble velocity fields, there appears to be mostly vertically directed velocity beneath y/d = 8.0 in the jet region between r/d +/- 1.0. Outside of that region, flow is radial and directed toward the jet centerline. The distribution of radial flow appears discontinuous in the individual field with

regions of high radial flow surrounded by regions of lower magnitude. This distribution appears relatively continuous in the ensemble field with high radial velocities at the base of structure 2, y/d = 3.0.

The presence of vortex cores in the ensemble flow fields suggests the motion of this structure is now relatively consistent over all the individual experiments. Otherwise, the structure would not be resolved when the flow fields were averaged as is the case in the previous time steps. The significant radial motion beneath the vortex in both the ensemble and individual fields suggest the starting vortex is now inducing a stronger flow field in the ambient. As the vortex separates from the tail, it appears to induce a 'sucking' motion in the ambient fluid and perhaps also in the tail fluid. This motion may be responsible for the large vertically-directed velocities at the center of the tail in the individual field. The low velocity zones at y/d = 5.0 correlate with the location of the front of the tail in the photo. The streamlines in the individual field also suggest they correlate with the formation of a second structure as evidenced by the streamline that crosses y/d = 5.0 and r/d = 2.0. The velocity field near this streamline indicates the motion is away from the jet from r/d = 2.0 to r/d = 3.0 and then back toward the jet along the streamline located at y/d = 4.0. There is also a feature in the individual field at y/d = 9.0 where many streamlines seem to converge from the bottom and diverge out the top.

5.4.1.3. Deceleration: Phase 3

At 0.28 s, the starting vortex appears to be independent of the trailing jet fluid as there is no longer a ‘neck’ which connects them (Figure 5.6a). The starting vortex core is at y/d = 11.0 and has a width of ~ 2.0d; this width has been 2.0d since formation indicating it is not growing wider as it is moving. The separation distance between the starting vortex and the tail has now increased to ~4.0d indicating that the vortex is moving independently of the tail. The tail continues to rise and its front is now at y/d = 7.0. The three regions of the trailing jet are still visible though each has a different character than in the previous time step. The region near the vent that extends from y/d = 0.0 to y/d = 1.0 no longer has a uniform width; instead the width decreases with height and then expands to 2.0d. This feature is interpreted to be a small vortex with a height of y/d =1.0. The second region has a uniform width of 2.0d and extends from y/d = 1.0 to y/d = 5.0. This indicates the length of this structure doubled from 2.0d at 0.21 seconds to 4.0d at 0.28 seconds without a change in width. In contrast, the front spherical structure appears to have contracted from a diameter of 1.5d at 0.21 seconds to a diameter of 1.0d at 0.28 seconds. The front of this structure also moved from y/d = 6.0 to y/d = 7.0. The front of the leading vortex moved from y/d = 10.0 to y/d = 14.0 in 0.07 s, indicating a rise rate of ~0.9 m/s.

At 0.28 s, the individual instantaneous velocity field shows that the starting vortex is indeed separated from the tail by a region of fluid with high vertical velocity (Figure 5.6b). Previous to this time step the peak velocity contours were continuous across the first structure and the tail. Now, there are

multiple isolated regions with similar peak velocities. This discontinuous structure is consistent with the interpretation that the first structure is separating. This interpretation is also supported by the fact that at later times, the distance between this structure and the tail grows. The fluid across the bottom surface of the starting vortex is directed toward its centerline. Both vortex cores are located at y/d = 10.0 in the individual velocity field although they are not centered on the vertical axis. The cores are now separated by a distance of 3d indicating the structure is growing wider. The streamlines indicate the circulation pattern is now circular rather than D shaped. The area of induced inward-directed flow at the bottom of the vortex extends from y/d = 8.0 to y/d = 10.0. Streamlines converge below the structure with a high density of streamlines occurring near the left core. This linear feature indicates strong motion along that line. Beneath this structure is a high velocity region at y/d = 6.5 that is associated with a D vortex. Below this structure at y/d = 5.0 there is vertically-directed flow in the tail between r/d = -1.0 and 1.0, that is asymmetric about the vertical centerline. Outside the tail at y/d = 5.0 is a region of flow directed toward the center of the tail with large radial and vertical components. This radial flow is associated with the D vortex structure.

The ensemble velocity field (Figure 5.6c) also shows the starting vortex structure as separated from the trailing jet and the structure is again symmetric about the flow axis. The cores are located at y/d = 10.5 and are separated by a distance of 3.0d. The high concentration of streamlines over the core on the right

indicates the core strength is much larger on this side. The streamlines have the shape of a flattened sphere. The region of large induced velocity toward the underside of the vortex extends from y/d = 7.0 to y/d = 10.0. From y/d = 5.0 to y/d = 7.0 there appears to be a low velocity zone for all values of r/d. The streamlines indicate these regions are associated with the centers of vortices. These vortices have a geometry that is in between oval and D shaped which suggests they are in a transitional state. Below y/d = 5.0 there a zone of predominantly vertical velocity from r/d = +/- 1.0 in the tail and a radially directed flow toward the centerline outside of that.

At this time, the starting vortex is moving independently of the tail and is growing wider. This supports the idea that this structure starts to separate near the peak of the injection around 0.20 seconds and finishes sometime between 0.21 seconds and 0.28 seconds. The starting vortex is inducing relatively high-velocity fluid motion into the structure all along its bottom surface. At the same time, a second structure forms at the front of the tail. The centers of these structures are associated with very low velocity fluid and the streamlines indicate they have a transitional structure between D and circular. In the ambient, the second structure induces radial velocities toward the center of the tail. The structure at the front of the tail contracts while the structure in the middle of the tail lengthens; both occur without a significant change in width. This contrasts the observations from the bulk flow experiments which suggest the deceleration phase is associated with a significant increase in width.

At 0.35 s, the photo shows (Figure 5.7a) the starting vortex reaches y/d = 12.0 and the cores are now visible due to the low concentration of particles surrounding the ring. The starting vortex and the tail are separated by a distance of 4.0d, which is similar to the previous instant. The space between is filled with ambient fluid as evidenced by the dark color in this region in the image. The tail extends from y/d = 0.0 to y/d = 9.0 and still contains three flow regions. The small vortex near the vent is no longer symmetric about the centerline of the outlet but is skewed to the left (r/d < 0). It still has a width of 1.0d but it now extends to y/d = 2.0. The base of the second region has moved from y/d = 1.0 to y/d = 3.0 though the front has moved y/d = 5.5. This suggests this structure is also contracting in the vertical direction while maintain an approximately constant at a width of 2.0d. The base of the oblate structure at the head of the trailing jet is still located at a height of y/d = 5.0 and the front is at y/d = 8.0. This is only a small change in the position of the structure from the previous instant.

At 0.35 s in the individual instantaneous velocity field (Figure 5.7b) shows that the starting vortex continues to move independently as an isolated vortex ring. The vortex cores, however, no longer appear circular but are oblate or tear-drop shaped instead. There is radially directed flow out the top of the ring and into the bottom of it. The distributions are similar for the flow out the top in the individual and ensemble (Figure 5.7c) fields but the distribution for the flow out into the bottom is more elongate in the ensemble field. Furthermore, there is high vertical velocity along the centerline in this region in the ensemble field but there

is no evidence for this linear feature in the individual field. The pattern at the front of the tail in the individual field is also different from the pattern in the ensemble. In the individual field the front of the tail has a high velocity region that is bullet shaped and located between the cores of the vortex. This region had low velocity in the previous instant. In the ensemble field, this region has a circular shape. The high streamline density around the core of this second vortex indicates that this structure is stronger at this instant. The cores appear to be transitioning from a more D-like structure to a more circular structure. Below the second structure at y/d = 6.0, the tail region between r/d = +/- 1.0 continues to have predominantly vertical velocity. The ambient region outside the tail continues to have predominantly radial velocity directed toward the center of the tail.

At 0.35 seconds there are two zones of high velocities that were not present at 0.28 seconds, one behind the starting vortex and one at the front of the tail. The increase in velocity may be due to the increased distance between the starting vortex and the tail region. While the starting vortex was close to the tail it may have been stretching and straining the fluid in the tail in the direction of the flow. Once the vortex moved sufficiently far from the tail the strain may have reduced sufficiently which allowed the second vortex to rapidly form. This formation then resulted in the increase in the velocity at the front of the tail.

5.4.1.4 Transition: Phase 4

At 0.42 s (Figure 5.8a), the core of the first structure is no longer visible in the photo and the front of the tail reaches y/d = 9.0. The spherical structure at the

front of the tail has a diameter of 1.5d which is similar to the previous instant. Behind the tail front, is another structure with a width of 1.0d and a length of 2.0d. At the bottom of this structure is a trail of fluid which stretches to the vent and has a meandering centerline.

The cores of the first structure are still visible in the individual velocity field (Figure 5.8b) and located at y/d = 14.0. The set of cores is at y/d = 6.0. Between them is a region of high velocity that was bullet shaped in the previous instant and now appears diamond shaped. This same region is oval-shaped in the ensemble field (Figure 5.8c) with a lower peak velocity. The starting vortex continues to have a region of high outward directed velocity ahead of it and inward and upward directed velocity behind it. The region behind it is smaller than it was previously. This distribution is still different from the ensemble field wherein this region is elongate and centered along the centerline. The velocities in this region have decreased in the ensemble.

The shape and dimensions of the tail in the photos at 0.49 (Figure 5.9a) and 0.56 seconds (Figure 5.10a) are similar to those at 0.42 seconds (Figure 5.8a). The velocity pattern in the tail front of the individual experiment is also similar at 0.42 (Figure 5.8b), 0.49 (Figure 5.9b) and 0.56 seconds (Figure 5.10b) although the magnitude of the peak velocity decreases in time. For the ensemble velocity, the distribution of peak velocity lengthens and the magnitude of the velocity increases from 0.42 (Figure 5.8c), 0.49 (Figure 5.9c) and 0.56 seconds (Figure 5.10c). The distribution in the tail at 0.56 seconds (Figure 5.10c) has an oval

shape that is 2.0d wide between y/d = 5.0 and y/d = 8.0 and a narrow region that is 1.0d wide between 2.0d and 5.0d.

During the transition region from 0.42 to 0.56 seconds, an individual tail has a diamond shaped velocity distribution with a peak velocity that decreases over time. The ensemble field has an oval shaped velocity distribution with a peak velocity that increases over time.

5.4.1.5 Source off: Phase 4

Following the increase in peak velocity in the ensemble field between 0.42 and 0.56 seconds (Figures 5.8-5.10c), the magnitude decreases from 0.56 to 0.63 seconds (Figure 5.11a). The decrease continues for the duration of the flow shown here at 0.70 (Figure 5.11b), 0.75 (Figure 5.11c), and 1.25 seconds (Figure 5.11d). The peak distribution changes from oval shaped at 0.42 seconds to circular at 0.75 seconds as the velocity decreases. The narrow region below the peak decreases more quickly and is absent by 1.25 seconds when there is still some velocity in the peak region. During the asymptotic phase, the ensemble velocity field distributions (Figure 5.11) show that there is a circular region with a high-velocity core at the front of the tail which rises from y/d = 7.0 at 0.63 s to y/d = 11.0 at 1.25 s. While it rises, the velocity dissipates in the bottom region before it decays at the head region as shown by the evolution in Figure 5.11a-d.

5.4.2 Instantaneous Velocity Profiles

Profiles of the vertical velocity, v, along the centerline (r/d = 0.0) are shown for an individual experiment in Figure 5.12. These profiles are shown for

various times during and immediately following the injection as indicated by the arrows. From y/d = 0.0 to y/d = 15.0, peaks in the profiles at early times correspond with structure 1 (indicated by arrows in Fig. 5.12a) and peaks in the profiles at later times correspond with structure 2 (arrows in Fig. 5.12b). While the profiles have variable distributions at early times (Fig. 5.12a), they are relatively constant in time at later instances (Fig. 5.12b, 0.35 s – 0.56 s), displaying an approximately linear increase in velocity from y/d = 0.0 to y/d = 6.0, with a peak at ~y/d = 6.0 corresponding to the location of structure 2. Above structure 2 is a nearly linear decrease in velocity from y/d = 7.0 up to the base of structure 1 which occurs at different locations for each instant. The increasing distance between the two peaks in Figure 5.12b as time proceeds highlights the point that the leading structure is moving independently and away from the second structure. The peak velocity at early times (Fig. 5.12a), representing the leading structure, increases in magnitude from 0.07 s to 0.14 s, and then decreases from 0.14 s to 0.28 s. Similarly, the peak velocity at late times (Fig. 5.12b), representing the second structure, increases in magnitude from 0.35 s to 0.42 s, and then decreases from 0.49 s to 0.56 s. The largest changes in peak velocity in the leading structure occur between 0.14 s and 0.21 s (Fig. 5.12a), and in the second structure, the largest changes occur between 0.42 s and 0.49 s (Fig. 5.12b). These times correspond with a) the first structure beginning to separate from the second, and b) the first structure moving far enough away from the second structure to end their mutual interaction.

Profiles of the vertical velocity, v, along the radial coordinate are shown in Figure 5.13 for the individual experiment. Profiles are shown for several distances from the source of the injection and at several times. For early times (Figure 5.13a), the cross-sectional profiles show the vertical propagation of the first structure, and at late times (Figure 5.13b), the cross-sectional profiles show the vertical propagation of the second structure. The position of the peak in each velocity profile is inferred to be the centerline of the flow or structure at that distance from source. At early times, the position of this peak moves between r/d = - 2.0 and r/d = +2.0 indicating that the first structure is moving to the left and right of the central axis, r/d = 0.0. The cross-sectional profiles at late times indicate that the second structure oscillates about the central axis, moving between r/d = -1.0 and r/d = +1.0. There is considerable variability in the shape and symmetry of the cross-sectional profiles associated with the first structure, whereas the second structure tends to have more symmetrical, more centered distributions. In profiles corresponding to the second structure, both the peaks and widths of the cross-sectional distributions increase with distance from source. The velocities are greater than zero for y/d = 3.0 and y/d = 5.0 but are less than zero (downward) at the edges of the distribution at later times (r/d = +/-1.5, y/d = 7.0, t = 0.49, 0.56). Overall, for these spatial locations at late times, the cross-sectional profiles through the second structure, at each instant are very similar to one another. On the other hand, at early times, cross-sections through the first structure vary considerably.

The cross-sectional profiles of the normalized instantaneous vertical velocity, v / v_{max}, for an individual experiment at various distances from the source of the injection are shown in Figure 5.14. Velocity was normalized by v_{max}, the maximum value of the vertical velocity along the cross section at the specified distance from the source. Comparisons of the profiles of normalized vertical velocity at late times (Figure 5.14b), to profiles in the literature indicate that at y/d = 3.0 the distribution is similar to that observed in a jet rotating about the central axis [*Seo et al*., 2002]. At y/d = 5.0 the profile has a distribution that is skewed to the left side (r/d < 0.0) suggesting the rotation continues at that level, and the flow is wider, as evidenced by the wider velocity distribution. At y/d = 7.0 the normalized distribution is similar to that expected for a pair of opposite rotating vortices where there is a negative dip in the profile at r/d = +/- 2.0, corresponding to the location of the vortex cores. When the negative dips have different strengths, as at 0.56 s where the dip at r/d = 2.0 is greater than the peak at r/d = -2.0, the center peak is skewed toward the side of the stronger vortex, in this case toward r/d = 2.0.

In Figure 5.15, the cross-sectional profiles of the normalized vertical and radial velocities for the ensemble of experiments are shown at various distances from source at t = 1.0 s. The profiles of vertical velocity indicate that velocities are greatest at the center of the flow and increase with distance from source until the location of the second vortex. Above the vortex, velocities are low. Profiles of radial velocity have peaks on both sides of the centerline which increases and

widens with distance from source. These peaks in radial velocity indicate the location of the shear layer. For distances close to the source the profiles are generally ‘v’ shaped which indicates the shear layer reaches the centerline. At vertical locations close to the vortex the profiles are ‘u’ shaped which indicates that there is a core of fluid with little to no radial velocity and thus dominated by vertical velocity. Also these plots indicate that the ratio of peak radial velocity to peak vertical velocity vary with distance from source; the peak velocity ratio associated with the four lower panels in Figure 5.15 varies from bottom to top, where the value is 0.10 in the bottom panel (y/d = 3.0), 0.20 in the next panel (y/d = 5.0), 0.25 in the next (y/d = 7.0), and 0.10 in the fourth (y/d = 9.0). This variation in velocity ratio suggests that the rate at which radial velocity carries ambient fluid into the jet changes with height.

5.4.3 Time-Averaged Velocity Vector Fields

According to the instantaneous velocity fields, the unsteady jet is characterized by two organized, toroidal vortical structures, the starting vortex and the vortex at the front of the tail. Velocity profiles suggest that the velocity distributions should change significantly within the first structure over time but less so in the second structure. Two main events occur as the flow evolves. First the leading structure separates from the trailing flow, and second, the second structure begins to move in isolation of the first. This information was then used to time-average the instantaneous velocity fields in the following way: the first instant, 0.07 seconds, is unique and thus not averaged, the instants from 0.14 s to

0.28 seconds occur before the isolation of the first and second structures, the instants from 0.35 s to 0.56 seconds occur after the isolation and while the flow fields are still changing with time, and the instants later than 0.56 seconds show little change with time. Next I present the time-averaged velocity fields for each structure in each dynamic phase along with the corresponding streamlines, distributions of the radial and vertical velocity components, and the vorticity fields. Vorticity is a property of a moving fluid used to describe the rotational characteristics of the fluid [e.g., Adrian and Westerweel, 2011]. Vorticity results from variations in velocity in directions perpendicular to the velocity. Here vorticity, ω, is computed according to the expression

$$\omega = \frac{dv}{dr} - \frac{du}{dy} , \qquad (10)$$

where a positive value corresponds with clockwise rotation about the *z* axis; the z axis is orthogonal to the plane in which the velocity measurements were made.

For the first phase, at 0.07 s, only the first structure exists in the flow field and is shown in Figure 5.16 for the individual experiment (top) and the ensemble (bottom). This structure is asymmetric in the individual experiment but symmetric about the vertical axis in the ensemble. Vertical velocities are greatest at the center of the structure where the contours in the viewing plane for the individual experiment have a circular shape. The radial velocities are greatest ahead of the structure and show that the structure is moving in the positive r/d direction (to the right). The vorticity indicates the structure is two counter-rotating vortices with opposite-signed vorticity.

The patterns in the ensemble reflect the motion of the ambient fluid which is moved away from the structure as indicated by the vertical velocity contours and the vector field. The vorticity plot shows a more complex flow pattern which may reflect the fact that the location of vortex formation varies from experiment to experiment. In the vertical and radial components of velocity, there is a peak in values on the positive r/d side (right) that does not exist on the negative r/d side (left) indicating that asymmetry about the vertical axis also exists for all experiments.

Structure 2 is imaged in Figure 5.17 using the time-average of an individual experiment, from t = 0.14 s to t = 0.35 s. The first structure has not been imaged in this way over this time period because its position varied significantly, preventing a reasonable time-average. Figure 5.17 shows that the second structure has a core of high velocity that is centered between the two imaged vortices (at the center of the three-dimensional vortex ring). The imaged vortices extend the length of this high-velocity core as indicated by the extent of the rotating streamlines and the radial velocity pattern. The vorticity occurs in two elongate bands located at approximately r/d = +/- 1.0. Vorticity would be generated by the velocity gradients in the shear layer and thus this plot indicates the extent of the shear layer. The distribution on the –r/d side is continuous whereas the distribution on the +r/d side is not.

The first (top) and second (bottom) structures are imaged in Figure 5.18 using the time-average from 0.14 s to 0.35 s of the ensemble experiments. The

first structure appears to be moving as vortex ring as indicated by the closed contours of vorticity at the center of the rotational structures visible in the streamlines. However, the structure is not moving in isolation from the second structure as indicated by the continuous distribution of vertical and radial velocity. The radial vorticity distribution shows a complex pattern of oppositely signed closed contours. An elongated contour in the cross stream direction is above the complex pattern. Below it is an elongated contour in the streamwise direction of opposite sign. This pattern suggests the top of the structure is moving toward the camera while the bottom is moving away indicating that the structures in the middle reflect motion into and out of the plane of the laser on a smaller scale. This pattern suggests the discarded vorticity in the first structure is rotating from top to bottom while the discarded vorticity is rotating from left to right, both rotations in and out of the plane of the laser.

Figure 5.18 (bottom) shows a much less complex pattern for the second structure. The regions of high vertical velocity are concentrated in a circular core at the top of the structure where the radial velocity also peaks along the lateral edges of the structure. Regions of high radial velocity extend along the whole length of the structure (from y/d = 1.0 to y/d = 5.0) with lower magnitudes near the base of this field of view, in the tail of the flow. This pattern supports the interpretation that fluid is being brought into the jet at a much higher rate near the base of structure 2 than in the tail of fluid behind it. The vorticity plot has peaks within structure 2 and the radial vorticity plot indicates that this structure is three

dimensional and the sense of movement is opposite that of the first structure (above); fluid in the bottom of structure 2 is moving toward the camera, and fluid at the top is moving away from the camera. The streamlines indicate the ambient fluid is moving toward the jet at different angles depending on height (compare lines at y/d = 1.0 and y/d = 5.0). Below the region of high vorticity (below y/d = 3.5) the streamlines are nearly perpendicular to the main axis of the flow while above y/d = 3.5 they are curved.

The time-average of the individual experiment from 0.42 s to 0.56 s highlights structure 2 in Figure 5.19. At this phase in the flow the region of peak vertical velocity has contracted to a circular region near the top of the second structure. The radial velocity pattern is more complex and may reflect the fact that the fluid is rotating around the central vertical axis.

The time-average from 0.42 s to 0.56 s for the ensemble is shown in Figure 5.20 for structures 1 (top) and 2 (bottom). The vertical velocity distribution in Structure 1 looks similar to the previous average plot (Figure 18, top), although now the linear region of high vertical velocity along the vertical axis in the lower half of this field of view is more pronounced. Also note that the radial vorticity in this region indicates that the flow is moving into the plane of the laser. The vorticity plot also indicates closed contours of vorticity of a single sign beneath the cores of the structure suggesting the torroidal structure maybe rotating around its central axis while sucking up fluid through the center of the torroid.

The time-average from 0.42 s to 0.56 s of the ensemble in Figure 5.20 (bottom) highlights structure 2 and shows a pattern of high vertical velocity at the core of the structure that is divided into two regions one centered at y/d = 6 and one at y/d = 4. Centered in the zone between these two regions are radial velocity peaks at y/d = 5 and r/d = 2 and -1.5. This pattern supports the interpretation that structure 2 is rotating in the azimuthal direction in the same direction as the first vortex. This interaction and rotation is supported by the streamlines which show that the rotational motion does not complete a circular structure. The streamlines are approximately perpendicular to the central axis beneath y/d = 5 but curve above that.

For late times, only the ensemble time average is shown as it is similar to the patterns observed in the individual flow. In Figure 5.21, the time average is from 0.56 s to 1.91 s and shows the evolution of structure 2. The vertical velocity field indicates a compact and circular region of high vertical velocity centered at y/d = 9, on r/d = 0 at the base and r/d = 0.5 near the top. The vorticity plot shows two peak regions near the top of the structure which are associated with movement into and out of the plane of the laser as indicated by the radial vorticity plot. The streamlines show that the velocity is angled toward the central axis, with increasing curvature of the streamlines closer to the flow axis.

5.4.4 Time- and Space-Averaged Velocity Vector Fields

The previous section discussed data for experiments that fell within a narrow range of volumes. Here I discuss the near source evolution of the flow for

an ensemble of experiments with different total volumes injected, in order to illustrate the specific effect of volume of flow characteristics. These experiments were conducted with a slightly different vent condition; a 15-millimeter orifice plate was secured on top of the 20-milimeter open pipe. However, the flows display similar bulk flow evolution, which suggests that their velocity fields are similar in space and time. Ensembles of experiments with different volumes should produce continuous contours of vertical velocity in places where correlations are high for all experiments (regions where vertical velocity varies only slightly in magnitude and sign) and discontinuous ones in places where correlations are low (where vertical velocities vary greatly in magnitude and sign).

The resulting fields are shown in Figure 5.22. At the first instant, 0.07 seconds (Figure 5.22a), when the discharge is accelerating there is one region of nearly uniform width that has an approximately round top and discontinuous sections of higher velocity. As indicated by the previous analysis, this time step is dominated by the first structure, and this pattern indicates that the first structure likely varies according to different injection rates. The next time step, 0.14 seconds (Figure 5.22b), where the discharge rate is still increasing but at lower rate (flattening injection curve with positive slope), shows both the first and second structures. Close to the vent there is a region of very high velocity (red-white contours) that appears approximately uniform (equal magnitude) across the cross section. This region is 1.0d tall. At the edge of this region is a region of

lower vertical velocity that widens with distance from source. This region likely represents the shear layer outside the jet. Then coherence is drastically lost after the uniform velocity region above 1.0d. This suggests either that there are large velocity gradients in this location or that there are significant variations in the structure among the experiments in the ensemble. Also above this region the width does not vary much with height along the rest of the visible contours. By the next instant, 0.21 seconds (Figure 5.22c), near the peak of the injection curve, there is a linear region of high velocity near the flow center that decreases toward the edges. This region extends to 6d from the source where the velocity also decreases with distance from source in the vertical direction. This region of high velocity has two parts, one below y/d = 2.0 and one above y/d = 2.0d. By the next instant, 0.28 s, near the end of the injection, the high velocity regions are no longer visible and there are some isolated regions of higher velocity near the flow center. The next time step, 0.35 seconds (Figure 5.22d), at the end of the injection shows that these regions were dissipated and the velocities in the regions above and below the former peak region were drastically reduced. Once the injection ends, represented by the time step at 0.42 seconds (Figure 5.22e), the flow momentum dissipates from the edges of the flow toward the center, as indicated by the higher velocity regions at the center of the flow and the lower velocity regions along the flow margins.

5.5 Summary and Discussion

Ultimately the velocity field data collectively (Figures 5.2 – 5.22) support the interpretation of the following sequence of events: (1) a starting vortex is formed at 0.07 s whose location with respect to the source depends on the acceleration conditions but whose width depends on the diameter of the vent; (2) this vortex is convected away from source by the accelerating fluid behind it which forms a jet; this vortex remains constant in width throughout the flow duration; (3) there is a transition from jet-dominated motion in the near-field of the source, to puff dominated motion in the intermediate region, and vortex dominated motion in the far field; (4) once the source ends, puff motion dominates; the core of the second structure has high velocity which decreases radially away from the center; this structure is elongate just before the end of the injection, and becomes compact and round after the injection. After the injection ends, the structure remains relatively stationary but grows in width, suggesting that subsequently injected fluid is contributing to increasing the structure width, but not causing much continued vertical propagation. Thus unsteady jets with increasing and decreasing momentum flux generate a sequence of structures separated by a region of jet-driven flow that ultimately dissipate as finite volume structures.

The findings from the velocity fields are consistent with the interpretation of the flow behavior using the bulk flow observations presented in Chapter 4, and support the interpretation which characterizes the flows as starting jets during the initial phases of injection, but as finite volume puffs in the asymptotic limit. These

findings also support that the timing of the transition from jet to puff motion is coincident with the end of the source. Once the source ends, the second structure fills fluid that has relatively high-momentum and spreads wider rather than grows taller. The filling event appears to coincide with an internal reconfiguration of the flow front.

The main features of the velocity distribution and its evolution in time can be inferred from the PIV measurements presented here. The velocity structure of unsteady jets consisted of two sets of two counter-rotating vortices that move away from the source. The vortices dominate the distribution of momentum in the flow and are therefore significant to the dynamics in this region. This double vortex pair also has long lasting consequences as it is responsible for an increased momentum dilution rate for the overall jet relative to starting jets and decreased momentum dilution rate relative to puffs in still environments; vertical velocity decayed more slowly/quickly than starting jets/puffs in the self-preserving state at similar streamwise distances from the source.

It follows from these variations in the velocity structure, that the flow field changes in space and time while the source is on. This supports earlier observations that found the flow boundaries to vary in space and time while the source was on. Consequently, the flow boundaries were therefore a good proxy for the flow field changes that resulted from the source condition changes in these experiments. Furthermore, once the source ends the distributions of velocity approach an asymptotic regime where they appear to approximate finite volume

flows. This also supports this interpretation from the observations of the flow boundary.

The vortex ring has a similar structure to forming, and unsteady, vortex rings such as those investigated by *Maxworthy* [1972] and *Kovasznay et al*. [1975]. The separation appeared to start at or before 0.14 s when the acceleration in the source velocity would have peaked. This is consistent with the observation of *Querzoli et al*. [2010] who observed that jets driven with a Gaussian-like injections over time had a break in the shear layer that formed beneath the first structure at the time in the injection that the acceleration peaked. This would suggest that the circulation rate is greater than the rate at which the shear layer is convecting.

The fluid that comprises the second structure starts with a jet-like uniform velocity distribution in the exit plane. As the fluid travels away from the source, the velocity distribution transitions to a distribution similar to that for elongated puffs [*Ghaem-Maghami and Johari*, 2010]. Once the source shuts off, the elongated velocity distribution transitions to a compact velocity distribution similar to that for a small-volume, compact puff [*Ghaem-Maghami and Johari*, 2010]. Consequently, though the momentum flux varies in time, the flow at any single instant can be characterized according to a combination of structures which form in constant velocity experiments. These structures have varying rates, distributions, and mechanisms for entrainment which suggests that modeling entrainment in these flows may not be well-characterized by simple linear

constants of the vertical velocity. This is especially important near the peak of the injection when many different dynamic regions characterize the spatial distribution of the flow.

However, the general trend from jet to elongated puff to compact puff may explain the broad agreement with finite volume thermal models in describing the behavior of volcanic plumes from short duration eruptions [e.g., *Caplan-Auerbach et al.*, 2009; *Yamamoto et al*., 2008]. However, it also implies that the arrival, in space and time, of the flow at puff behavior will be delayed in eruptions which last for significant durations of the rise. This may account for the observation of *Caplan-Auerbach et al*. [2009] who found that a thermal model with a displaced virtual origin best explained their observations of the 2006 Vulcanian-style eruptions of Augustine volcano in Alaska (US). The duration of these 13 eruptions ranged from 55 to 350 seconds [*Caplan-Auerbach et al*., 2009]. These durations are consistent with the class of short duration eruptions discussed here. The need to invoke a displaced virtual origin supports the idea that material was not erupted all at once, as is assumed in a puff model, but over a finite duration requiring the coupling of the instantaneous model with a displaced starting position that is in the direction of the flow. In physical space this origin is above the surface of the earth and perhaps corresponds with the distance over which the plume had a starting jet-like behavior.

The results here also suggest that volcanic plumes will have zones with high entrainment rates that will be indicated by places where the width of the flow

changes very quickly over a small height, simply referred to as a ‘corner’ here but is the same feature called ‘indentations’ by *Hu et al*. [2012]. Such features delineate the largest scales of motion of the flow. The scales of the first structure may be set by the geometry of the vent and the velocity of eruption as well as its evolution over the eruption initiation, and thus may contain information about the initial pressure in the conduit, though more experimental work would be needed to confirm the existence of such a relationship.

The fact that the velocity distribution changes significantly as the source changes implies that variations in discharge rate will have a first order effect on the resultant turbulent flows. Acceleration and constant phases are important for generating large structures and preventing their full formation. The forming vortices entrain ambient fluid via advection in contrast to formed vortices which entrain fluid by the slower process of diffusion. Deceleration and shut off are particularly important for promoting large-structure growth. The decreasing jet velocity results in slower rates of break down and turn over time such that growth of vortices may occur [e.g., *Hu et al*., 2012].

The velocity fields indicate that the rotational motion around these vortices extends all the way to the jet interior. This observation has two consequences. First, the engulfed ambient fluid has low momentum relative to the jet fluid which means the flow has to expend momentum in order to impart momentum to the entrained fluid. Second, as these vortices are the same scale as the jet width, they represent the largest scales of the flow. These scales generally

depend on the boundary conditions of the flow which suggests that the boundary conditions control the entrainment process in the decelerating jet.

This fact has important implications for flows which must achieve buoyancy reversal in order to prevent collapse. It suggests that for situations where the discharge rate decreases in time, the boundary conditions may critically impact the stability of the jet by modifying the large structures which form in the shear layer. Under situations which support the formation and persistence of large scale structures, local regions of high entrainment may result. These regions may distort the boundary of the jet resulting in indentations which extend into the flow interior [*Hu et al*., 2012]. This may enhance entrainment and mixing and thus, in turn, the process of buoyancy reversal.

On the other hand, there may be situations where large scale structures do not form or persist, such as the case with open pipes in quasi-steady jet conditions where the structures are weak and thus broken down quickly by the gradients in velocity in the vertical direction [*Mi et al*., 2001]. For this situation, a decreased rate of injection may correspond with the absence of structures, rather than regions of high entrainment beneath large scale structures, and thus decreased entrainment. This situation may therefore promote collapse in response to a decelerating injection rate.

This interpretation is consistent with the mechanism of increased entrainment in unsteady jets that was proposed by *Johari and Paduano* [1997] which attributes increased rates of entrainment to the fact that more ambient fluid

is entrained rather than jet fluid in the structures in decelerating jets. It is also consistent with the mechanism of decreased entrainment for accelerating jets proposed by *Breidenthal* [2008] that relatively more jet fluid than ambient is entrained by vortices in accelerating conditions. This would also be the case when large scale structures are not formed or are broken into smaller structures, as they would effectively entrain more jet fluid relative to ambient fluid. Unsteady jets also involve variations in the size and strength of the structures that are formed and the size and strength change in time. The structures are imparted different amounts of momentum and are therefore moving relative to one another; structures with large amounts of momentum can become increasingly separate from slower moving structures.

Overall, unsteady discharge rates introduce the possibility for considerably more variables to enter into the natural problem since anything which may significantly modify the boundary conditions, the generation of large structures or the amount of ambient fluid which is brought into a large structure, may also influence the unsteady jet stability. Potential contributors from within a volcanic jet may include the presence of ash-particles or lapilli (larger fragments of magma), variations in the volume fraction of ash over time, and the sedimentation of ash at the jet margins. Potential contributors from outside a volcanic jet may include changes to vent geometry and wind patterns in the surrounding atmospheric air. However, the potential impact of any of these contributors, from inside or outside the unsteady volcanic jet, on the jet stability is difficult to assess

without a better understanding of the unsteady conditions that may prevail in the volcanic jets.

The velocity values measured during this PIV analysis may not represent the absolute values reached by the flowing fluid under these unsteady conditions. This is a consequence of the fact that the analysis involves spatial averages of the flow field, on the order of the interrogation grid size, and the velocity fields generated during the unsteady conditions have gradients on the order of the grid size that may not be represented well by an average value. For example, an interrogation box at the edges of the flow represents fluid that is moving very quickly in the jet and relatively more slowly outside of it and their average will be a velocity value that neither the jet or ambient fluid is moving. In other words, the velocity values that result from the PIV analysis of unsteady flows will depend on the optimization of the technique so as to minimize the gradients present in any one interrogation grid box. Consequently, if the flows generated here were analyzed at a different resolution of the velocity field then the values in the velocity structure may be different from the analysis presented here. As a result, relationships such as the ratio of the radial velocity at the flow boundary to the vertical velocity at the flow centerline may also differ between the analyses. However, the new analysis would likely still indicate the generation of multiple structures at approximately the same locations as the analysis presented here, for experiments of the same initial condition. The determination of which conditions are the same seems to require consideration of both the total volume injected and

the injection history for PIV analysis of the unsteady jets generated in this apparatus. This new analysis is also expected to support the evolution of unsteady jets over the same sequence of events observed here.

Unsteady jet velocity distributions vary in time and space in correlation with variations in discharge over time. However, if the source ends before the jet momentum completely dissipates, then the internal structure of the flow reconfigures to eliminate internal gradients. The reorganization results in a velocity distribution that remains structurally similar as the remaining jet momentum slowly dissipates. In this limit the velocity distributions are similar to those for a turbulent puff. This observation is consistent with the trends observed in the analysis of the external behavior where the motion of the flow front changes quickly in time while the discharge varies and then more slowly thereafter. The reorganization of the velocity field correlates in time with the stalling of the front rise rate and widening of the second structure. The evolution of the flow with the puff-like velocity distribution correlates in time with the approach of the front rise rate to the asymptotic final state that is reasonably approximated by the scaling law for puffs. Consequently, the external motion of the unsteady jets is a good indicator of the interior dynamics. This fact suggests that analysis of volcanic plume observations may yield information about the interior dynamics even though they are not directly observable. I suggest the significance of this result can then be extended further by noting that the exterior flow dynamics correlated well with the source evolution and thus, by analogy, the

observations of volcanic plumes may yield dynamic information about their sources; this parameter is difficult to study by other methods and thus plume observations may help improve the interpretation of these data sets.

Figure 5.1. Source momentum flux (a) and Reynolds number (b) over time for the representative experiment (stars) and ensemble (open circles) experiments used for the internal flow measurements.

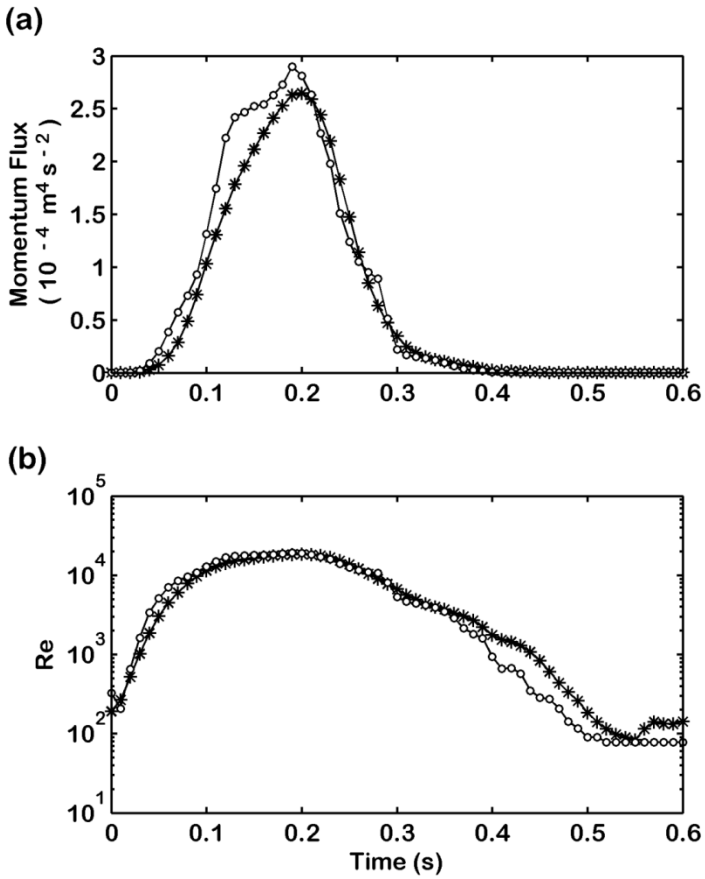

Figure 5.2. Individual jet photo (a), along with the individual (b) and ensemble (c) velocity fields at 0.07 s. Vectors are magnified 5x and 50% of those measured are displayed. Contours of velocity magnitude, V, and streamlines (solid grey lines) and are based on the total vector field.

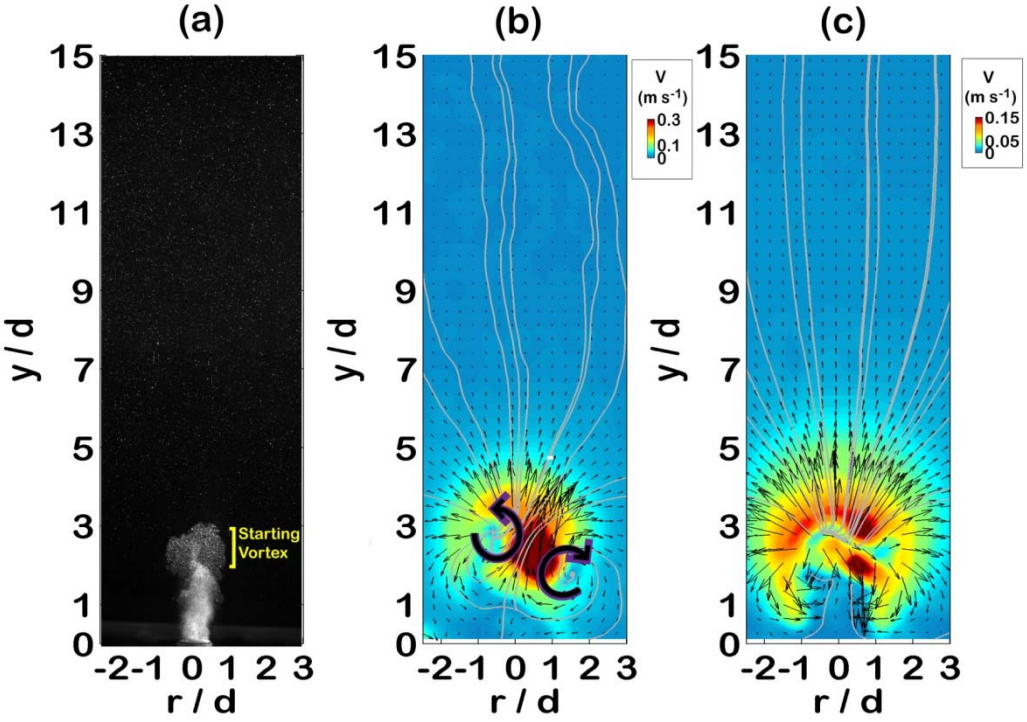

Figure 5.3. Individual jet photo (a), along with the individual (b) and ensemble (c) velocity fields at 0.14 s. Vectors are magnified 5x and 50% of those measured are displayed. Contours of velocity magnitude, V, and streamlines (solid grey lines) and are based on the total vector field.

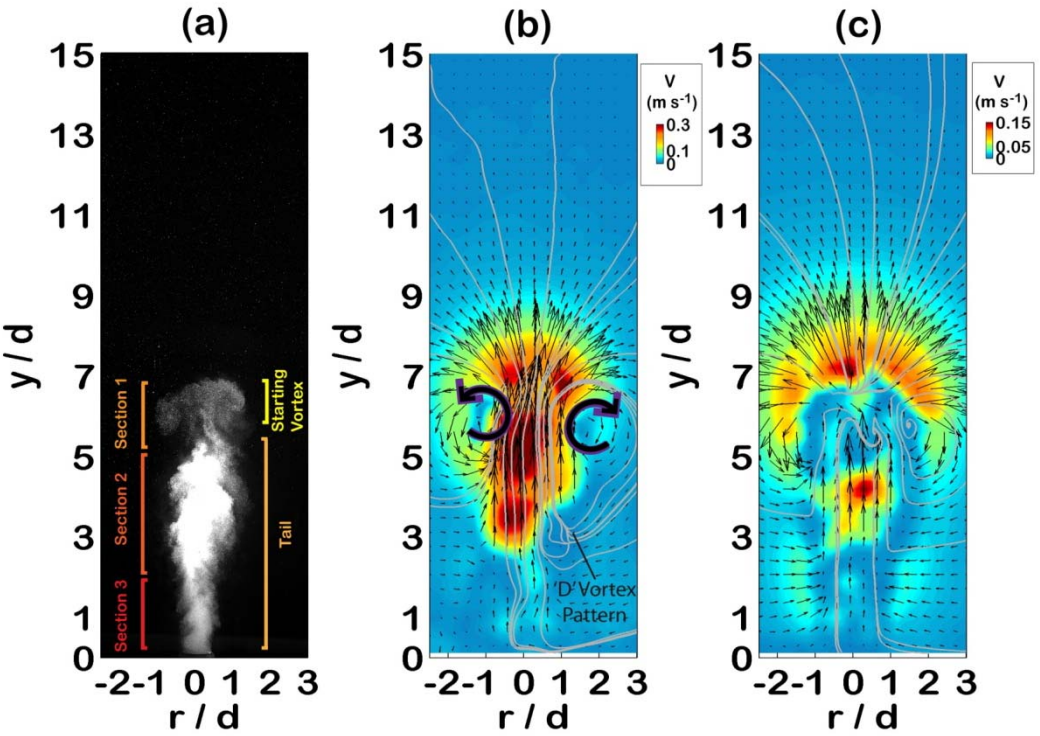

Figure 5.4. Individual jet photo (a) under the individual (b) velocity field at 0.14 s. Vectors are magnified 5x and 50% of those measured are displayed. Contours of velocity magnitude, V, and streamlines (solid grey lines) and are based on the total vector field.

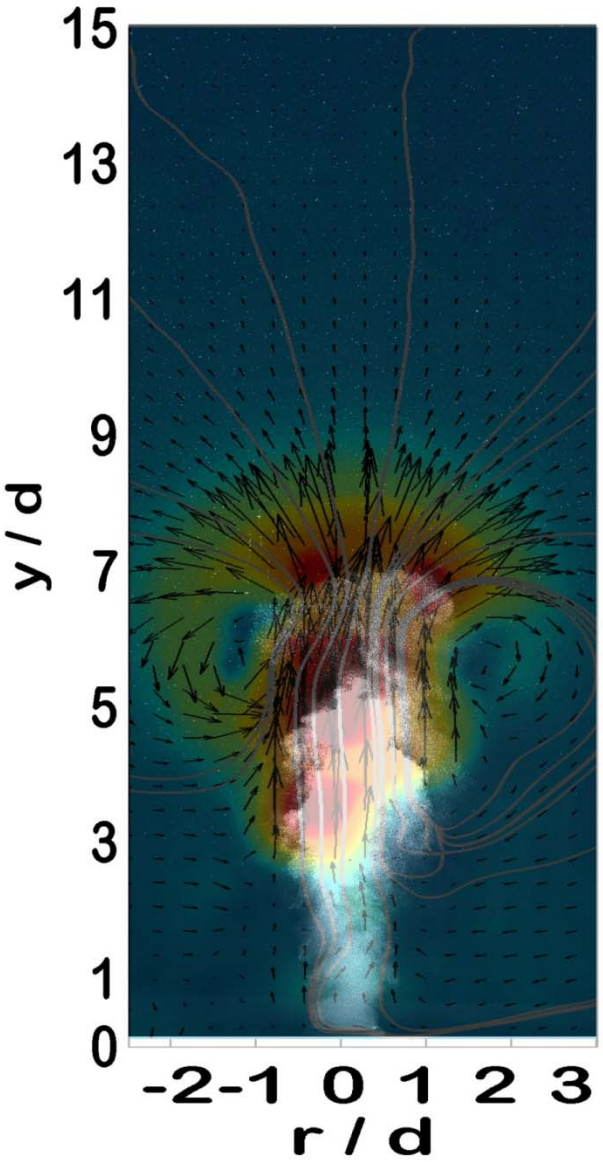

Figure 5.5. Individual jet photo (a), along with the individual (b) and ensemble (c) velocity fields at 0.21 s. Vectors are magnified 5x and 50% of those measured are displayed. Contours of velocity magnitude, V, and streamlines (solid grey lines) and are based on the total vector field.

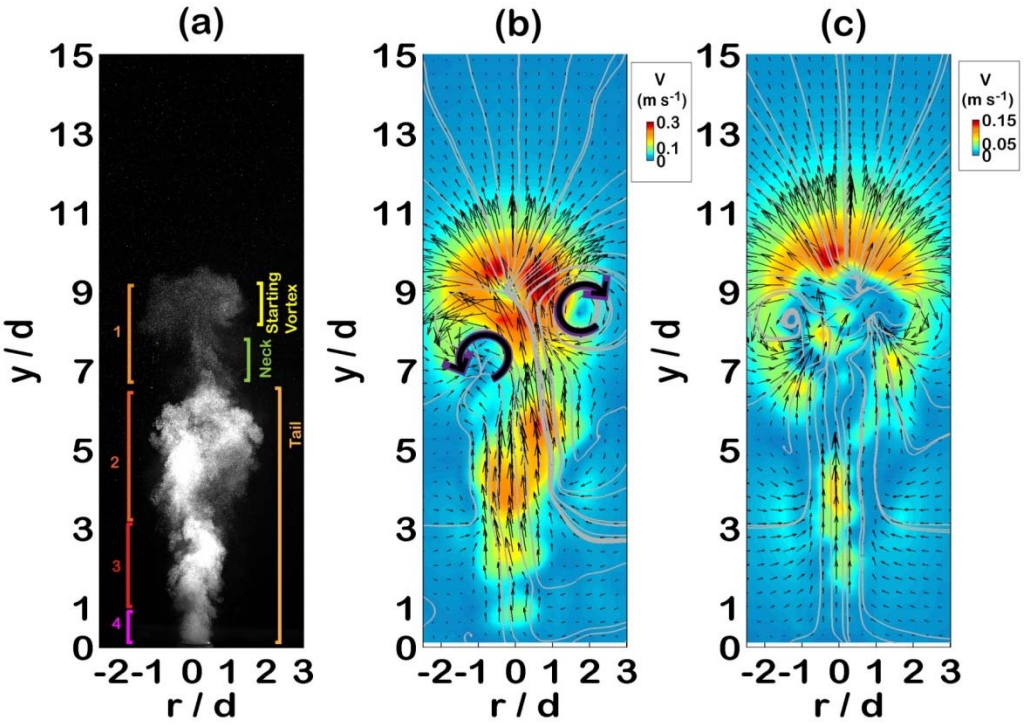

Figure 5.6. Individual jet photo (a), along with the individual (b) and ensemble (c) velocity fields at 0.28 s. Vectors are magnified 5x and 50% of those measured are displayed. Contours of velocity magnitude, V, and streamlines (solid grey lines) and are based on the total vector field.

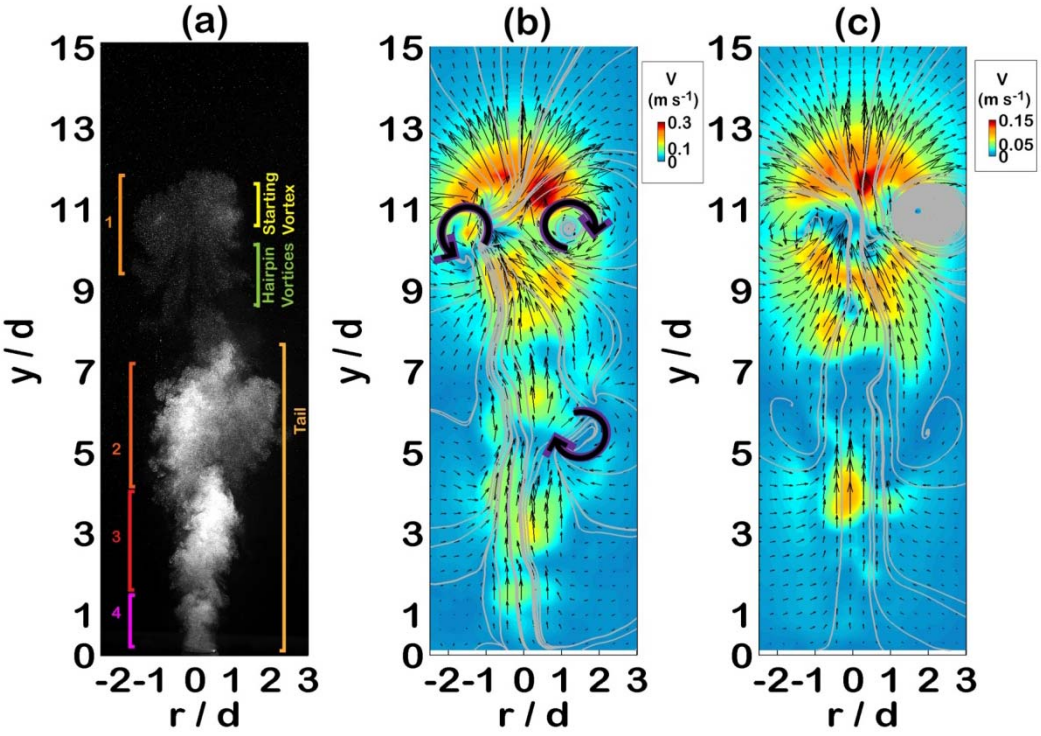

Figure 5.7. Individual jet photo (a), along with the individual (b) and ensemble (c) velocity fields at 0.35 s. Vectors are magnified 5x and 50% of those measured are displayed. Contours of velocity magnitude, V, and streamlines (solid grey lines) and are based on the total vector field.

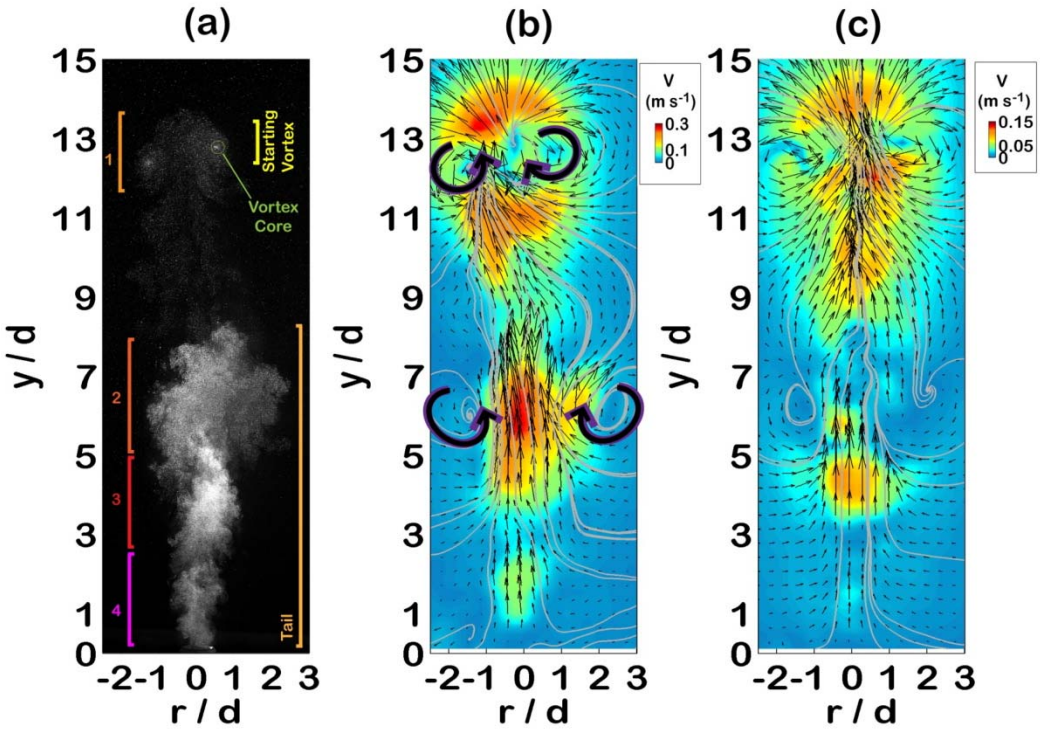

Figure 5.8. Individual jet photo (a), along with the individual (b) and ensemble (c) velocity fields at 0.42 s. Vectors are magnified 5x and 50% of those measured are displayed. Contours of velocity magnitude, V, and streamlines (solid grey lines) and are based on the total vector field.

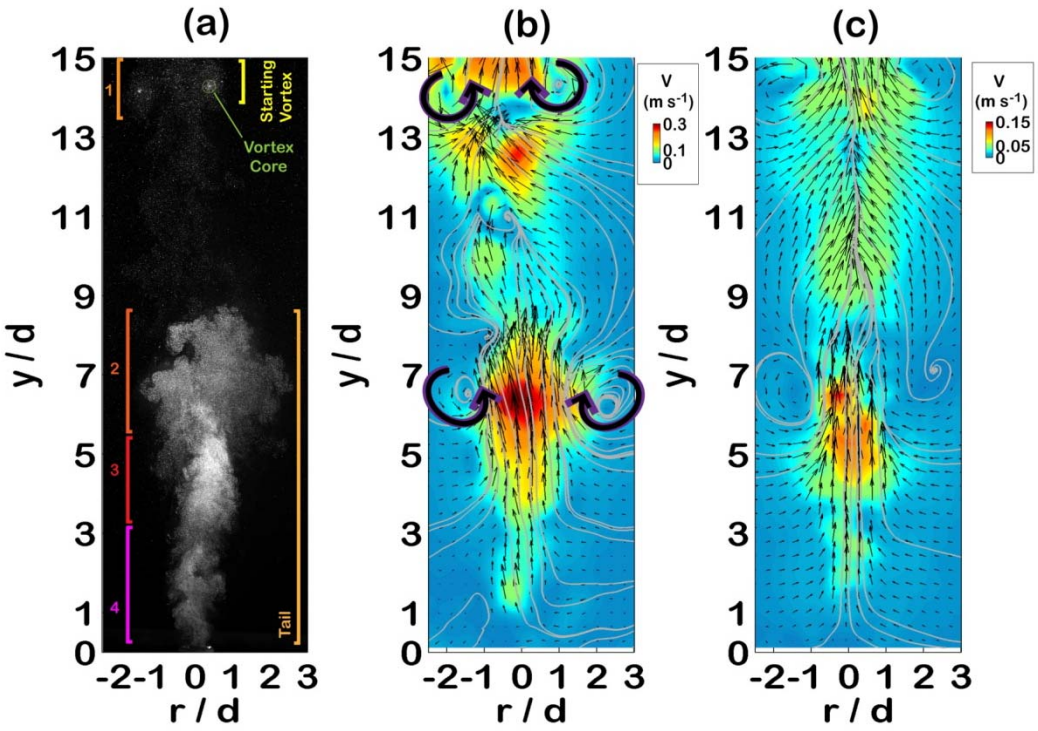

Figure 5.9. Individual jet photo (a), along with the individual (b) and ensemble (c) velocity fields at 0.49 s. Vectors are magnified 5x and 50% of those measured are displayed. Contours of velocity magnitude, V, and streamlines (solid grey lines) and are based on the total vector field.

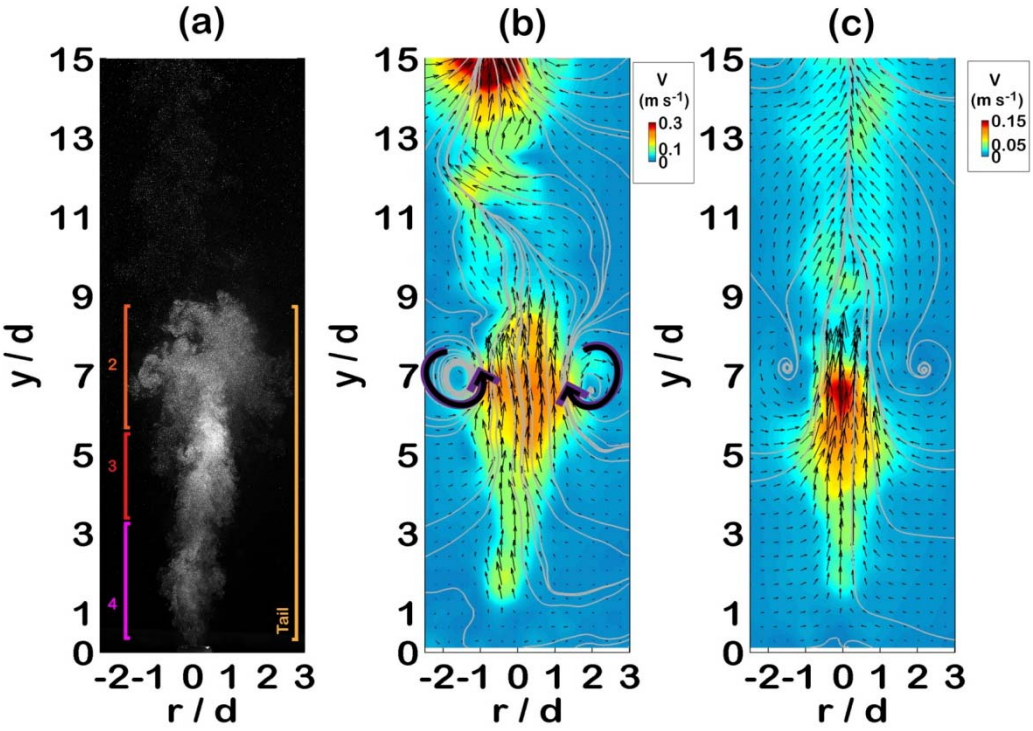

Figure 5.10. Individual jet photo (a), along with the individual (b) and ensemble (c) velocity fields at 0.56 s. Vectors are magnified 5x and 50% of those measured are displayed. Contours of velocity magnitude, V, and streamlines (solid grey lines) and are based on the total vector field.

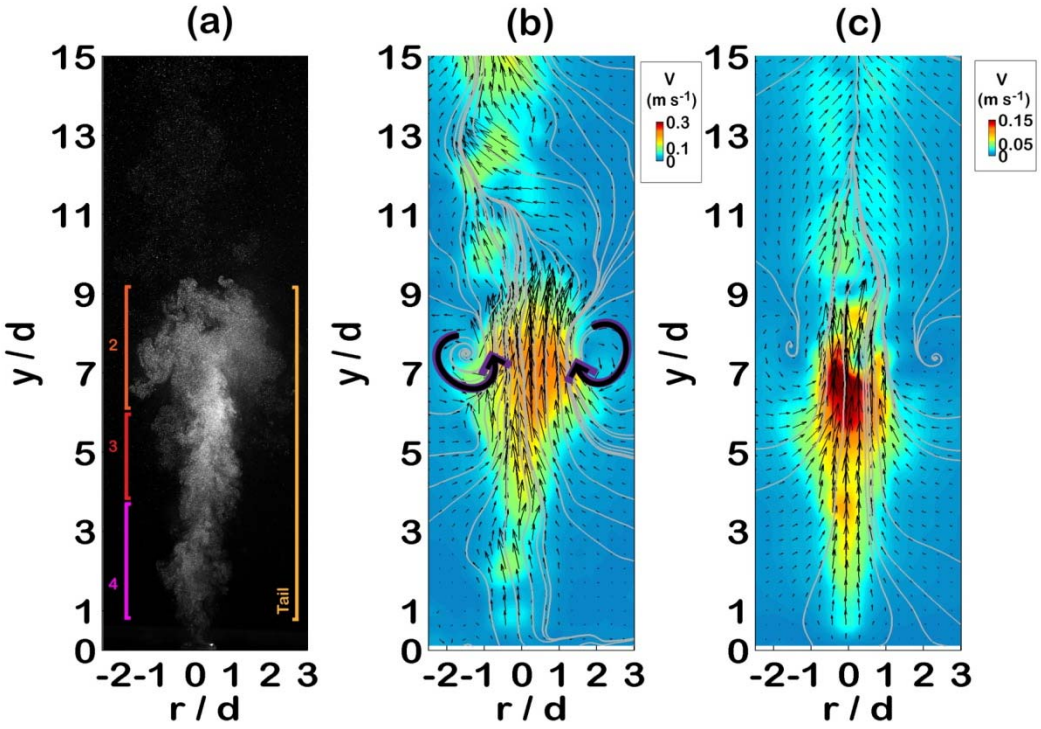

Figure 5.11: The ensemble average velocity field over all experiments for t = 0.63 s (a), 0.70 s (b), 0.75 s (c) and 1.25 s (d). Velocity vectors are magnified five times and only 50% of the vectors measured are plotted for clarity. Contours represent the magnitude of the velocity vector and are based on the total number of vectors. Streamlines are shown in solid grey lines and are based on the total number of vectors.

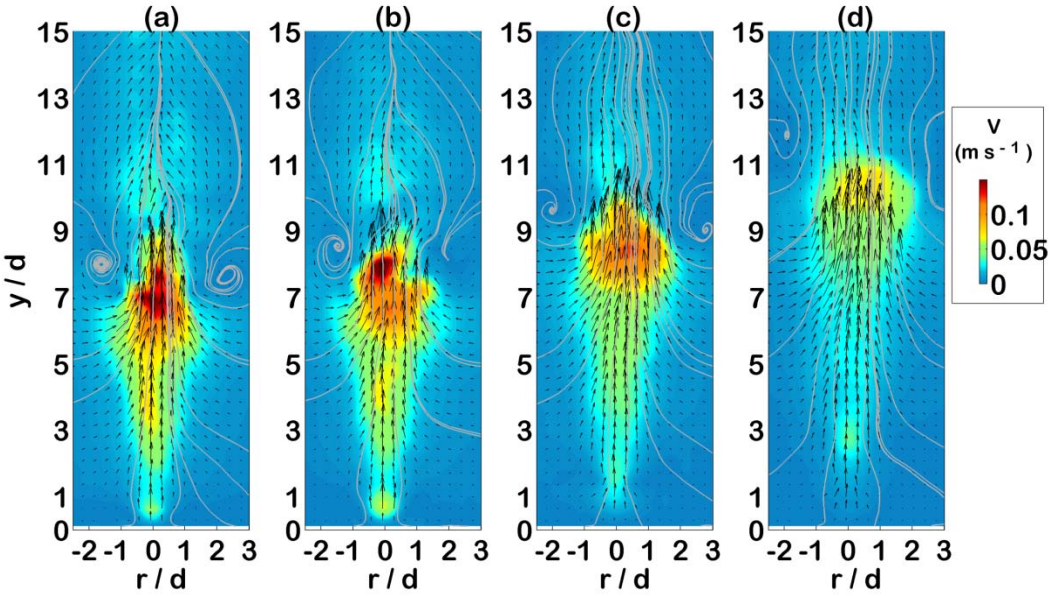

Figure 5.12: Profile of the instantaneous axial velocity, v, for the individual experiment along the centerline (axial coordinate y/d = 0) at times during the injection (a) and times at and following the end of the injection (b) as indicated by the arrow labels.

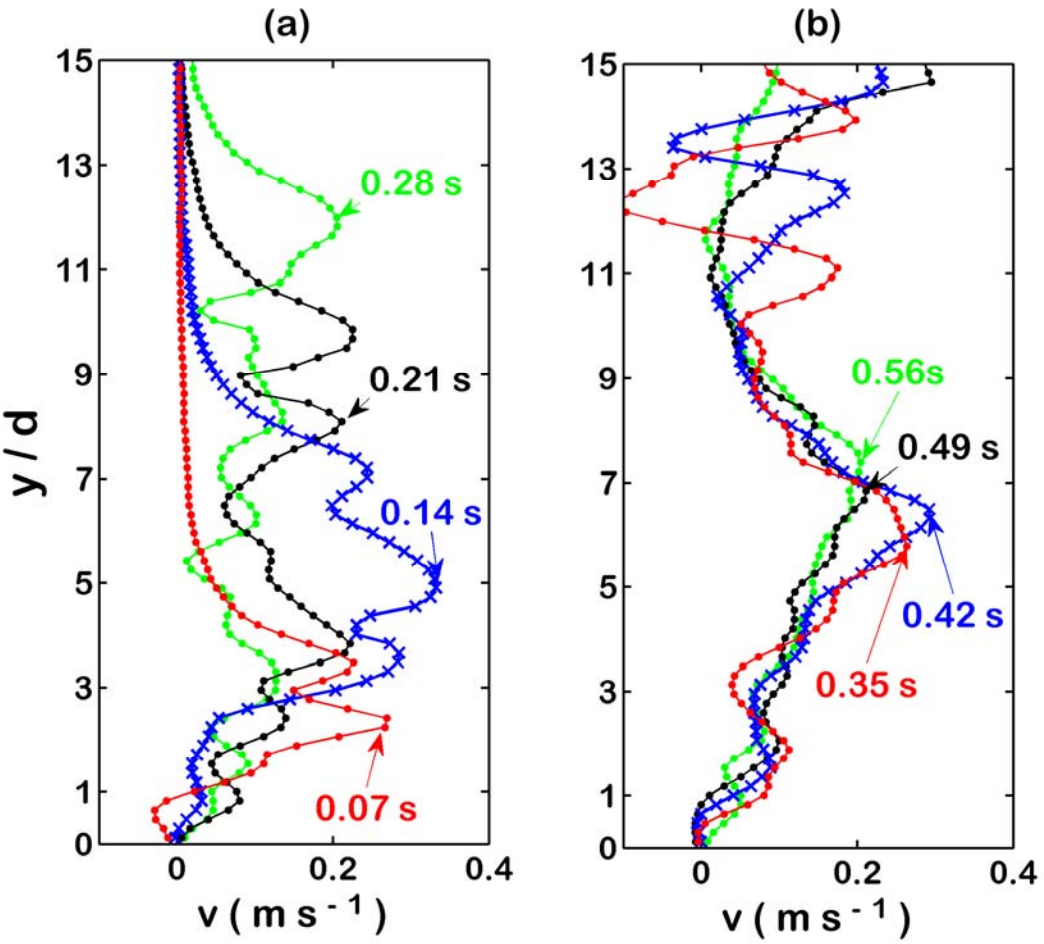

Figure 5.13: Cross-sectional profiles of the vertical velocity, v, for the individual experiment at a distance of 7d (top), 5d (middle), and 3d (bottom) from the vent for early times (a) and late times (b) indicated by the legend.

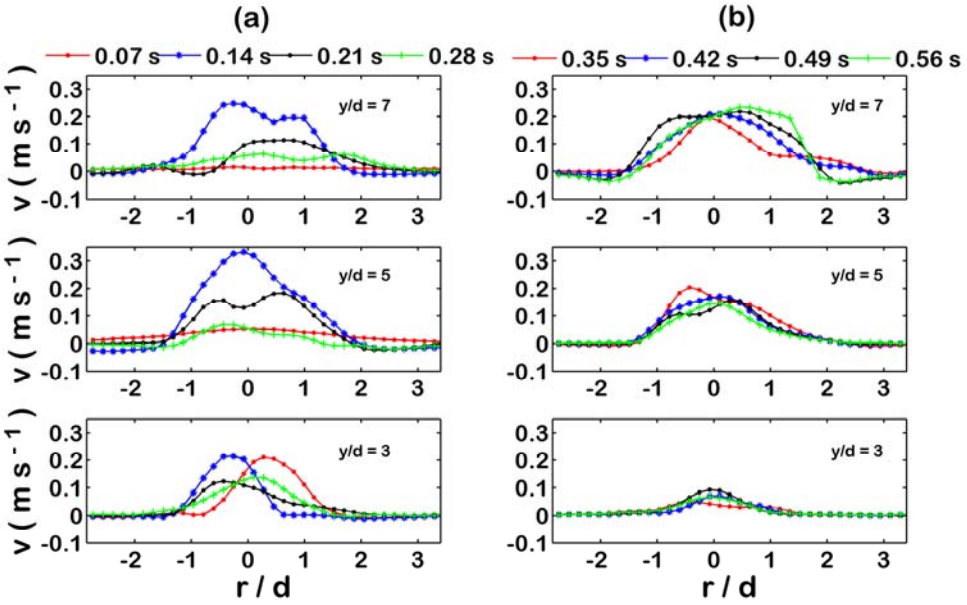

Figue 5.14: Cross-sectional profiles of vertical velocity, v / v_{max}, for the individual experiment at a distance of 7d (top), 5d (middle), and 3d (bottom) from the vent for early times (a) and late times (b) indicated by the legend. Velocity was normalized by the maximum value of the axial component of velocity along the cross section, v_{max}, at the specified distance from the source.

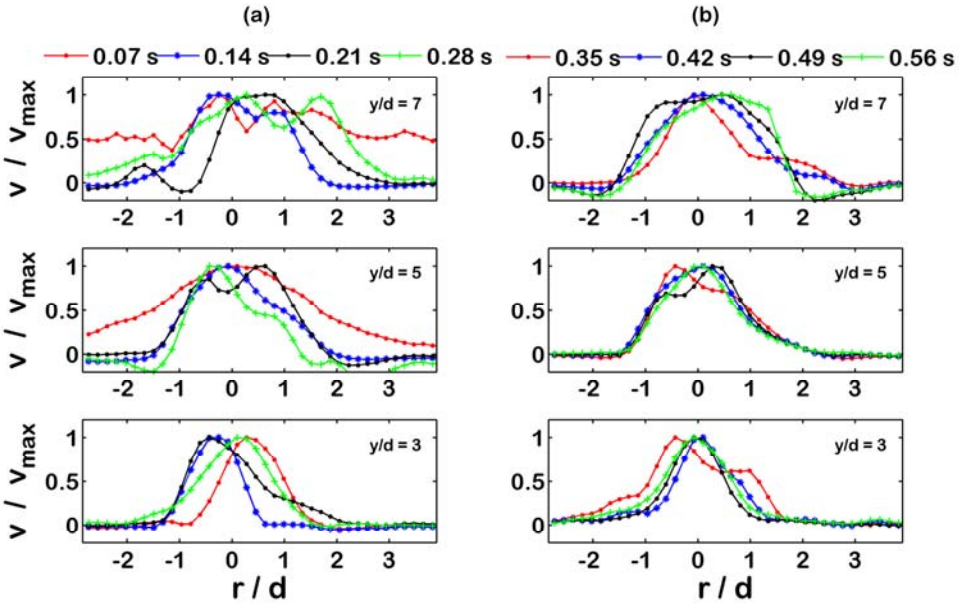

Figure 5.15: Cross-sectional profiles of the axial component of the normalized instantaneous velocity, v/v_{max}, (a) and the normalized magnitude of the radial component of the instantaneous velocity, $|u|/|u|_{max}$, (b) for the ensemble of experiments at various distances from source as indicated by the lines.

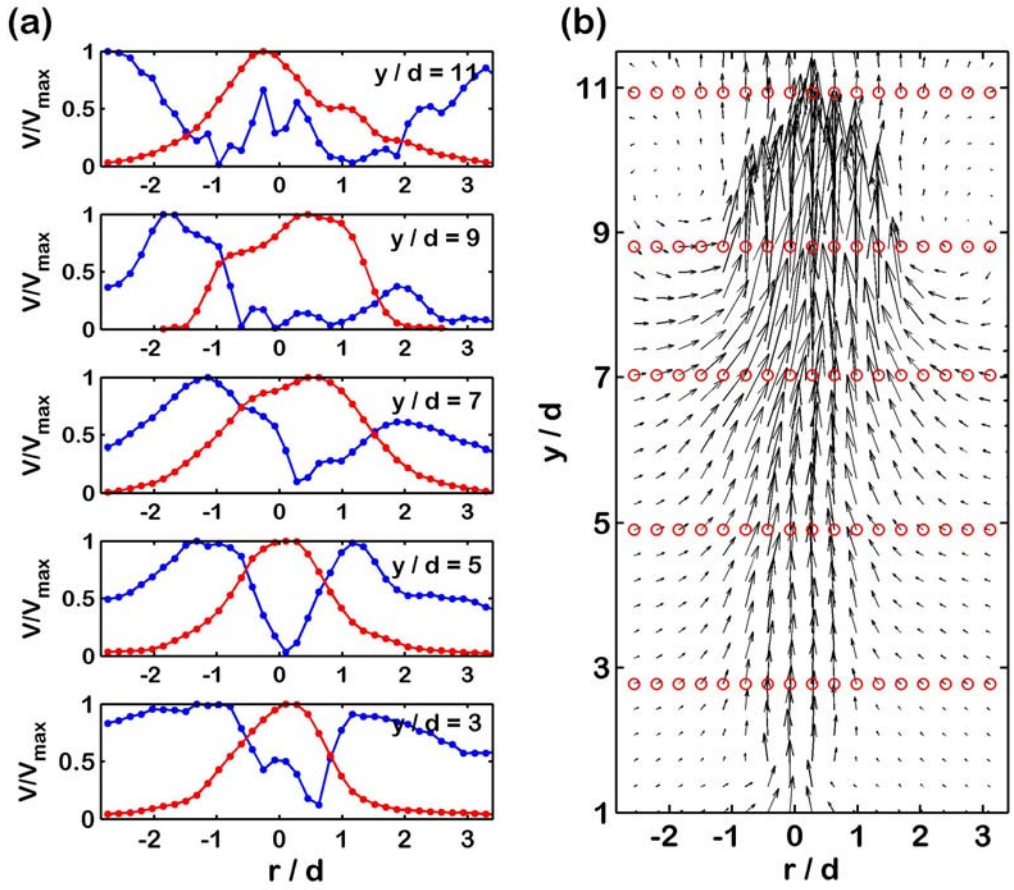

Figure 5.16: Instantaneous velocity fields at 0.07 seconds showing structure 1 in the individual experiment (a) and for the ensemble (b).

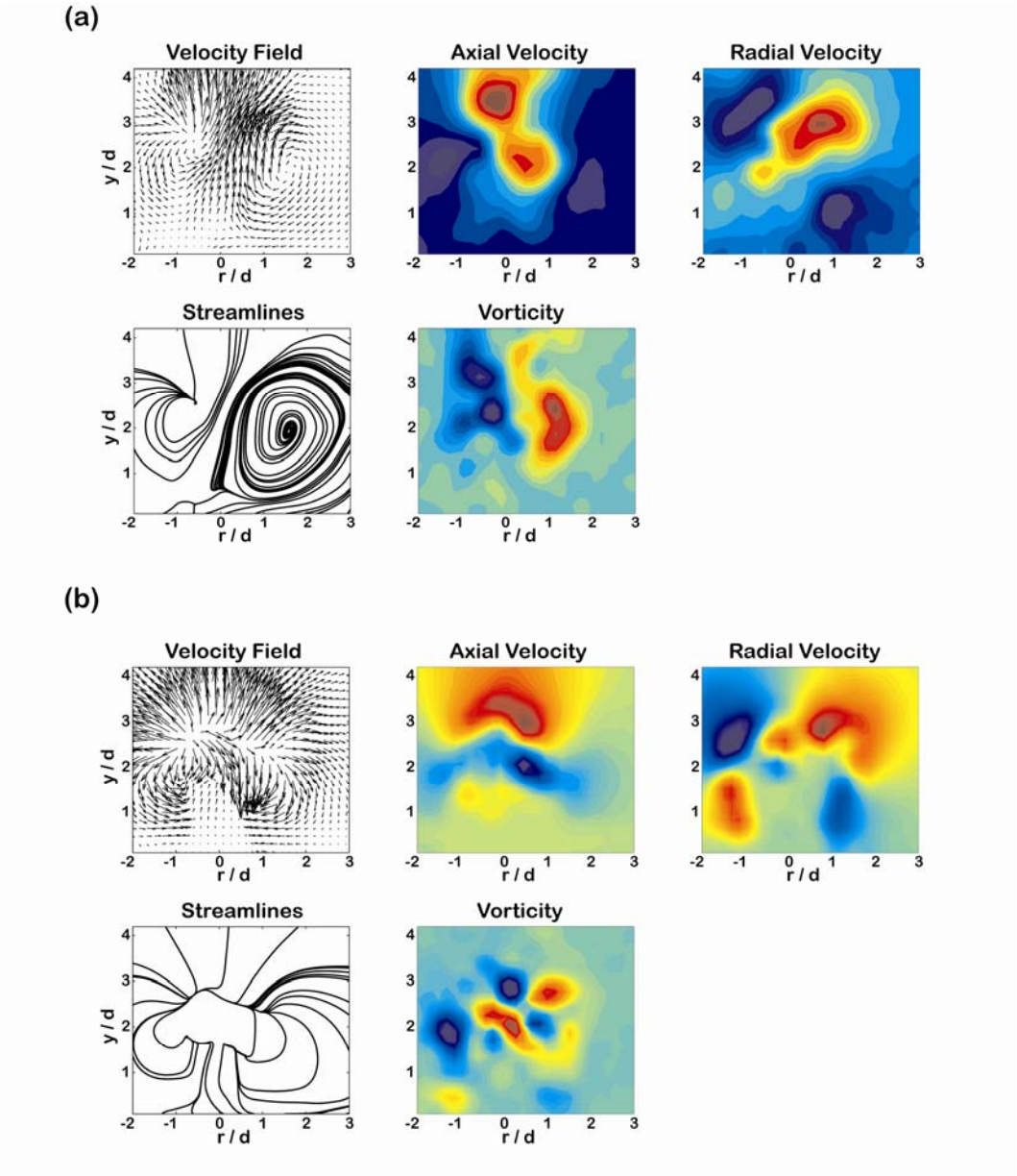

Figure 5.17: Time-averaged velocity for the individual run from 0.14 s to 0.35 s

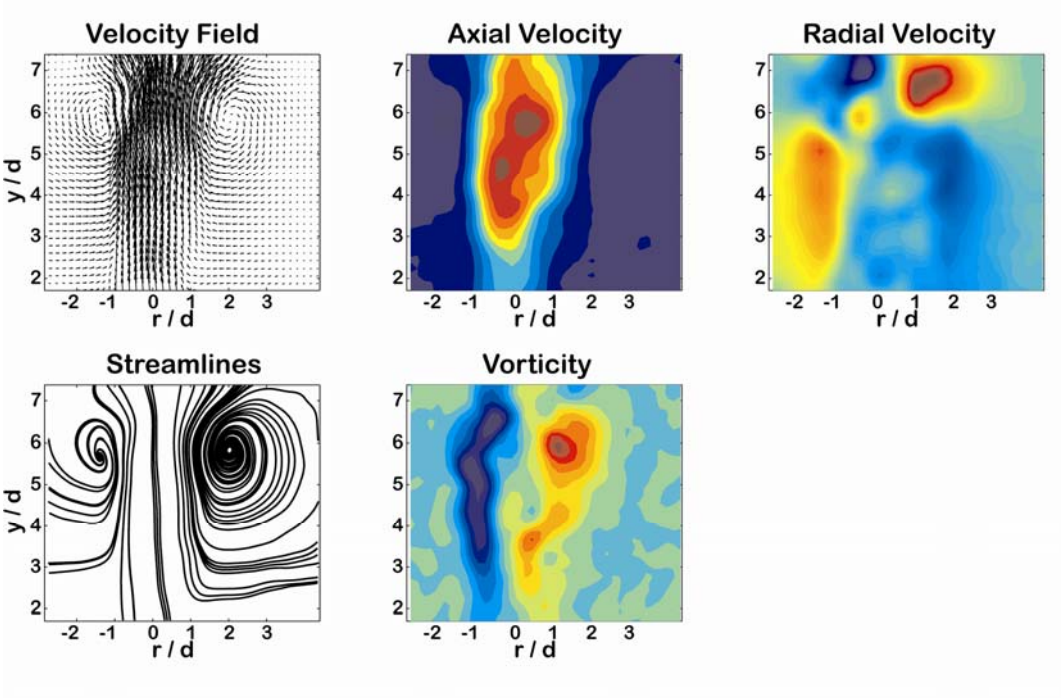

Figure 5.18: Time-averaged velocity for the individual run from 0.14 s to 0.35 s showing structures 1 (a) and 2 (b).

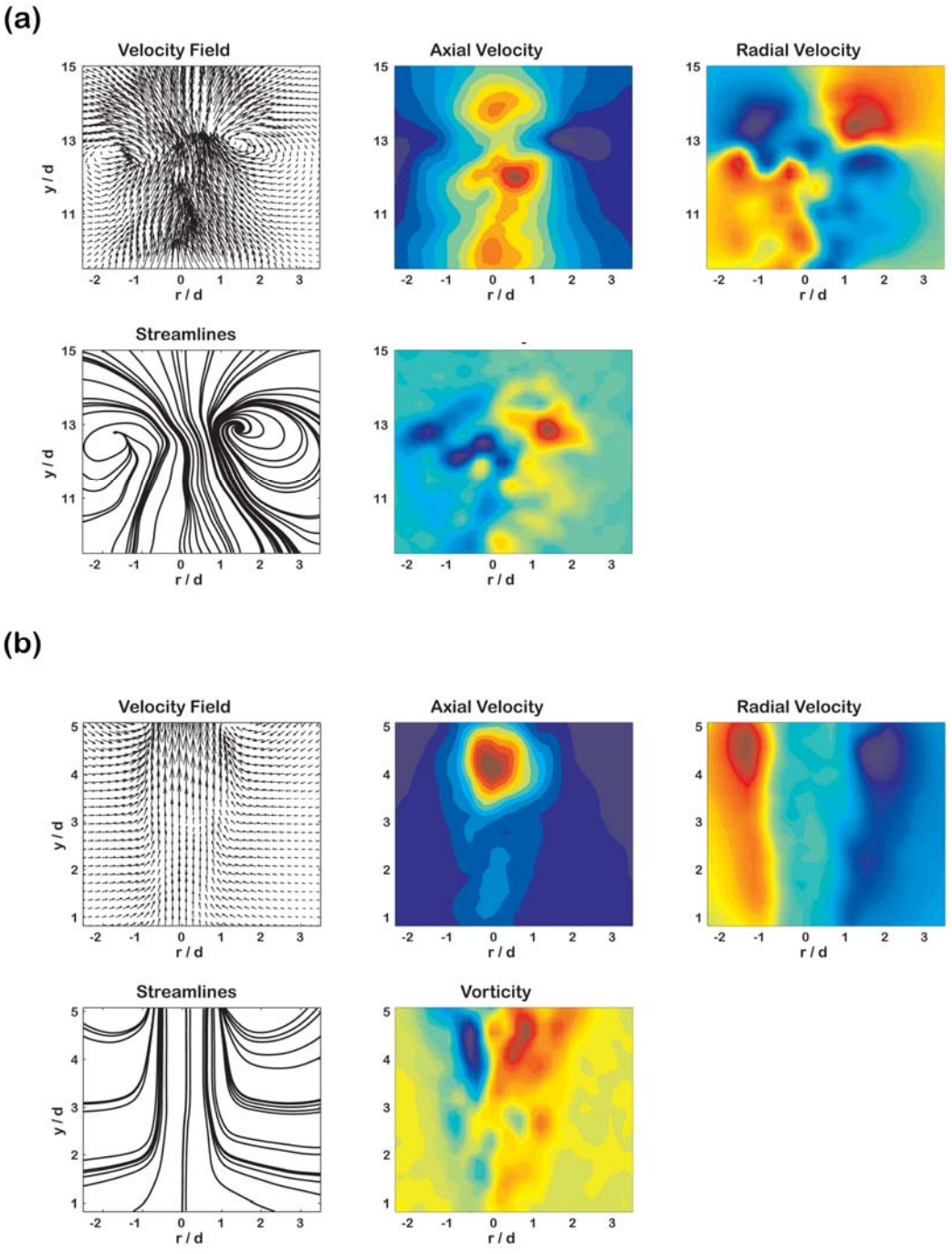

Figure 5.19: Time-averaged velocity for the individual run from 0.42 s to 0.56 s

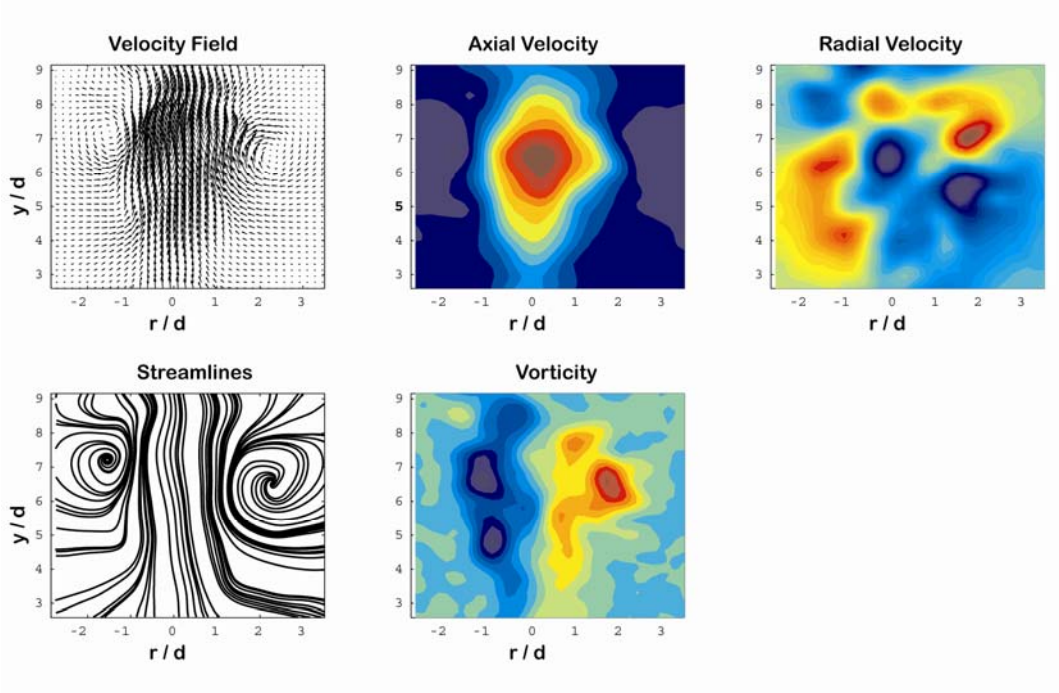

Figure 5.20: Time-averaged velocity for the ensemble from 0.42 s to 0.56 s showing structures 1 (a) and 2 (b).

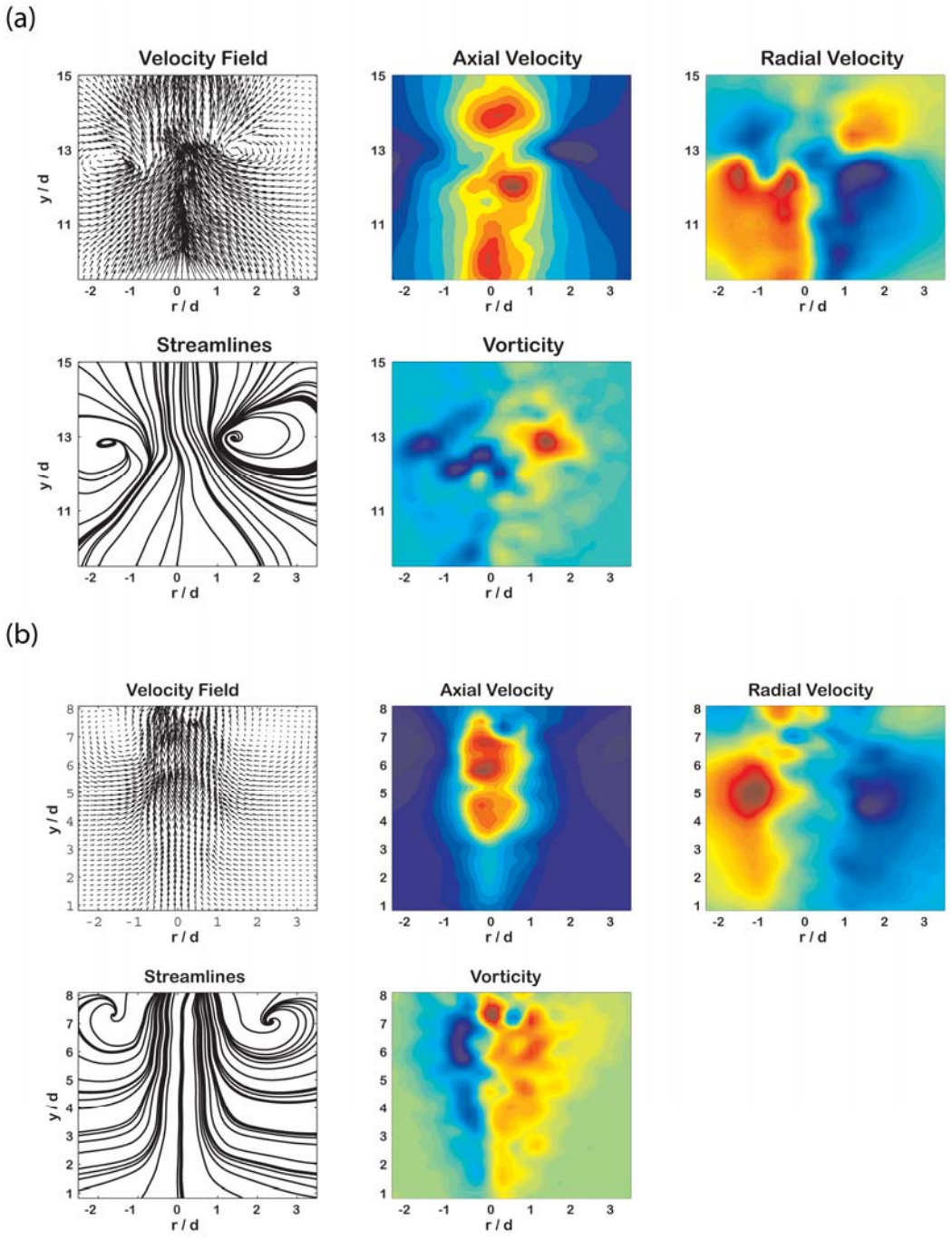

Figure 5.21: Time-averaged velocity for the ensemble from 0.63 – 1.25 s

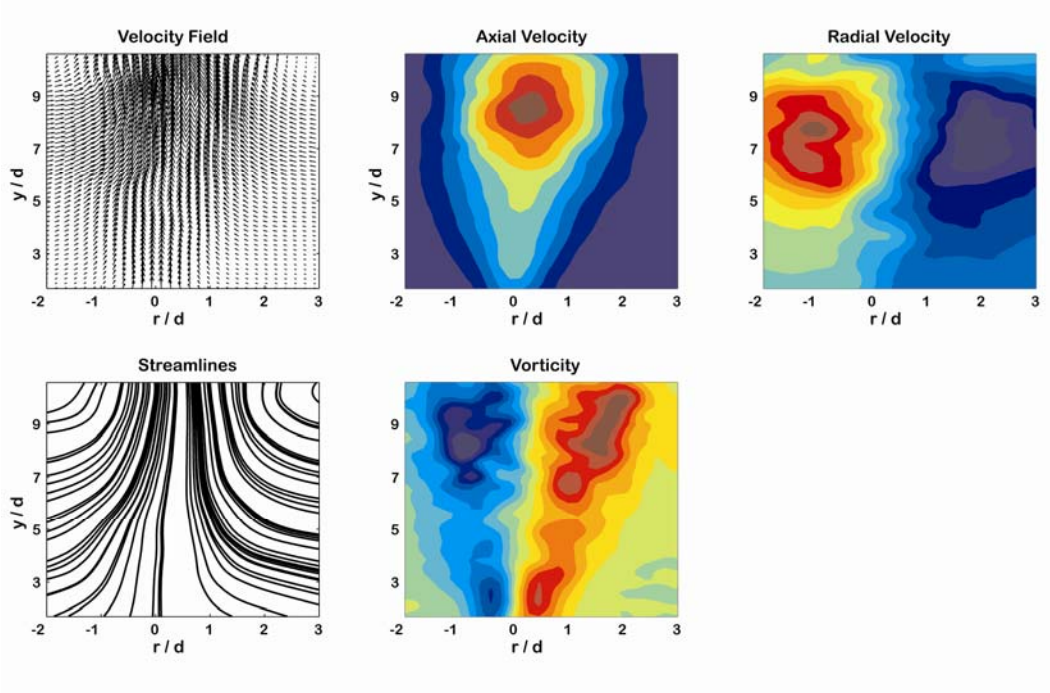

Figure 5.22. The evolution of an ensemble of multiple experiments in the near field of an experiment with a 15 mm orifice from y/d = 0 to y/d = 10. Contours represent the magnitude of the axial component of velocity were red is high and blue is zero. The ensemble consists of 3 experiments.

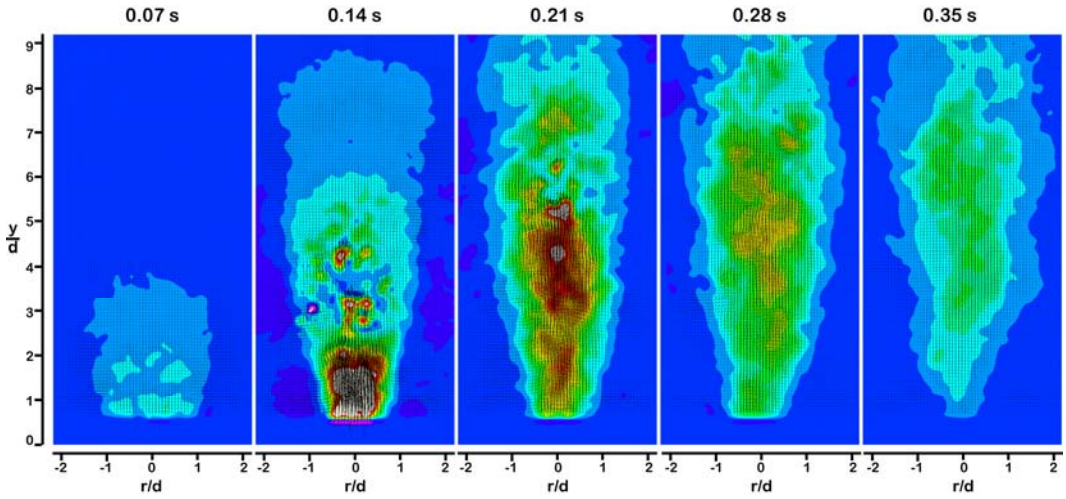

Chapter 6

RESULTS FOR UNSTEADY BUOYANT JET EVOLUTION

6.1 Introduction

Volcanic plumes are injected into the atmosphere with high velocities and densities that are different from atmospheric air. Thus, they begin with both initial momentum and buoyancy. In Chapter 5, I examined the role of unsteadiness on the evolution of jets that have only initial momentum. Now I consider the additional role of buoyancy. In jets that include buoyancy, buoyancy contributes to the production of baroclinic vorticity due to the density gradients between the jet and ambient fluids [*Turner,* 1962]. In starting jets, baroclinic vorticity is produced in addition to vorticity generated by the velocity gradient at the source [e.g., *Turner*, 1962; *Ai et al*., 2006; *Bond and Johari*, 2010].

Flows that begin impulsively, such as starting jets, generate a head vortex and a trailing stem of fluid or tail [*Gharib et al.*, 1998]. In the jets generated in this apparatus, the head vortex takes on the structure of a vortex ring or puff when the jet is non-buoyant. In the presence of buoyancy, the structure and development of the starting vortex ring is modified [*Bond and Johari*, 2005]. Buoyancy contributes to the vertical stretching of the ring due to buoyant acceleration [*Bond and Johari*, 2005]. It also results in the elimination of the internal structure of the ring [*Bond and Johari*, 2005]. *Bond and Johari* [2005] also observed that jet fluid released with momentum and buoyancy tends to end up in a single structure, for injections that are steady with nearly instantaneous injection times. An additional

difference between buoyant and non-buoyant rings is that the centerlines of buoyant vortex rings have zero vorticity [*Bond and* Johari, 2010].

When buoyancy is present in the vortex ring, *Bond and Johari* [2010] demonstrate that the spreading rate of buoyant vortex rings depends on the ratio of circulation generated by baroclinicity and the vortex generator. The spreading rate of vortices is small for those without buoyancy, and comparable with the spreading rates expected for vortex rings [*Bond and Johari*, 2010]. For those with buoyancy, spreading rates are large [*Bond and Johari*, 2010] with a maximum at 0.25 for a thermal [*Turner*, 1969]. Thus, the spreading rate for any given buoyant vortex depends on the ratio of buoyancy and momentum [*Bond and Johari*, 2010]. There is not, however, a quantitative relationship that predicts this spreading rate as a function of initial momentum and buoyancy [*Bond and Johari*, 2010].

Thermals involve only the generation of baroclinic circulation. Thermals also dilute rapidly [*Turner*, 1969]. This rapid dilution was observed by *Bond and Johari* [2010] to be due to Rayleigh-Taylor instabilities at the front of thermals and starting jets due to the density difference across the interface between the jet and ambient fluids. These instabilities contribute to mixing of the jet and thermal fluid and result in large spreading and dilution rates [*Bond and Johari*, 2010]. As compared to non-buoyant rings, buoyant rings rapidly entrain ambient fluid near to the vent and then expand quickly [*Bond and Johari*, 2010]. This result may be critically important for volcanic plumes. To achieve a state of buoyant rise, volcanic plumes must generate a sufficient degree of entrainment to achieve

buoyancy reversal [e.g., *Sparks and Wilson*, 1976; *Woods*, 1988; *Sparks et al.*, 1997]. This result is contrast to the near vent behavior of steady jets which have, on average, lower rates of entrainment near the vent [e.g., *Solovitz and Mastin*, 2009].

6.2 Methods

Much work has been done to understand the behavior of starting buoyant jets in the far field where the flow reaches a self-similar state that can be described with similarity theory [e.g., *Diez et al*., 2003]. However, less is known about the near field behavior [*Bond and Johari*, 2010]. To understand the role of buoyancy in the near field of unsteady turbulent jets, I ran a set of experiments at conditions similar to those described in Chapter 5 but with a positively buoyant fluid jet fluid. In the experiments described in Chapter 6 the jet fluid has a density of 970.0 +/- 5.0 kg/m^3 and consists of an aqueous mixture of methanol.

For the buoyant jets, the relative importance of buoyancy to inertia can be estimated with the densimetric source Froude number, Fr_0. This parameter is defined as

$$Fr_0 = \frac{V_0}{\sqrt{g_0' d_0}}, \tag{6.1}$$

where V_0 , g_0' , and d_0 are the source velocity, reduced gravity, and diameter, respectively. The reduced gravity is defined as

$$g_0' = \frac{(\rho_\infty - \rho_j)}{\rho_\infty} g, \tag{6.2}$$

where ρ_∞ and ρ_j are the ambient and jet fluid densitities, respectively, and g is the gravitational acceleration. For large values of this parameter, the inertia dominates the buoyancy force. For the buoyant experiments, $\rho_j = 970\ kg\ m^{-3}$ and $g_0' = 0.3$. The maximum values of the Froude number for each experimental condition with buoyancy are listed in Tables 3.3 and 3.4. These values indicate that the maximum Fr_0 is greater than 10 for all conditions considered here. According to these values, momentum will likely dominate the buoyant jets.

6.3. Source Characteristics for External Measurements

The ensemble averaged momentum flux rates for all experimental conditions are plotted in Figure 6.1a. For all conditions, momentum flux increased for approximately the first 200 milliseconds, then decreased for 200 milliseconds and terminated at approximately 400 milliseconds. Momentum flux was greatest for smaller vent diameters and larger initial pressures. Momentum flux values were less than those at the same condition for the non-buoyant jet. For example, the H3 condition peaked at 95 x 10^{-4} m^4 s^{-2} and 60 x 10^{-4} m^4 s^{-2} in the non-buoyant and buoyant cases, respectively. When each ensemble momentum flux time series is normalized by the peak value of the momentum flux for that time series, all of the curves collapse together as shown in Figure 6.1b. There appears to be a slight variation (t < 0.05 seconds) in the timing of the peak according to momentum flux; higher momentum flows peak at later times. This was not observed in the non-buoyant jet experiments.

The variation of the Reynolds number at the vent with time is shown in Figure 6.1c. Minimum Reynolds numbers were observed at the start of the flow and had values on the order of 10^2 to 10^3. Maximum Reynolds numbers were observed at the flow rate peak and had values on the order of 10^3 to 10^5 which are approximately similar in shape and magnitude to those for the non-buoyant jets. Accelerations (Figure 6.1d) are also approximately similar in magnitude, with the 3-mm conditions being much greater than the 9- or 15-mm conditions, and the timing of the phases are consistent with those in the non-buoyant jets. In the first phase, from 0.00 to 0.10 seconds, the acceleration is positive and increasing. Then in the second phase, the acceleration is decreasing though at first it is positive from 0.10 to 0.20 seconds and then it becomes negative during 0.20 s to 0.30 seconds. During the third phase from 0.30 to 0.40 seconds the acceleration is negative but increasing. Finally, the source ends at around 0.40 seconds and there is zero acceleration of jet fluid from the vent.

6.4. Unsteady Buoyant Jet Development

6.4.1 Qualitative Observations of Jet Boundaries

Buoyant jets also generated flows with and without vortex rings. Vortex rings occurred during the same 15-mm conditions. Features of the buoyant jet evolution are described below.

6.4.1.1 Flows without leading vortex rings

Jets from the 3-mm and 9-mm vents evolved similarly according to the pattern shown in Figure 6.2a for a representative 3-mm experiment with a large

momentum flux. During the first 0.30 seconds the jets without rings rapidly ascend and spread radially. At 0.05 s the flow appears to be symmetric about the axis of injection and the width spreads linearly with distance from source. This pattern is consistent through 0.15 seconds. At 0.20 seconds, however, there is a visible structure to the flow that consists of a flattened oval cap, marked v1 for vortex structure 1, followed by a conical tail. The cap is not much wider than the projected width of the tail to that height and there is not a clear distinction between the cap and the tail.

From 0.20 to 0.25 seconds there is significantly less dye concentrated in structure v1. The front of this structure appears to have rotated toward the +r/d direction and the front of a similarly-sized structure immediately below it appears to have rotated in the –r/d direction. The second structure seems also to have appeared at 0.20 seconds, though it is difficult to distinguish it from the trailing fluid at that time step. It is more distinguishable at 0.25 seconds due to its higher dye concentration relative to the first structure. At 0.30 seconds the flow appears to be dividing into a sequence of structures, producing a meandering appearance of the jet centerline. The dye concentration in the first and second structures continues to become more dilute.

At 0.35 seconds, there are 3 visible regions to the flow. The first is the front structure, v1, which continues to spread and become more dilute and the front of v1 appears to rotate in the +r/d direction. This structure accounts for most of the fluid above 150.0d. The third region is the fluid near the vent (below

100.0d) which retains a relatively high concentration of dye at this time step. This region appears to be a nearly conical jet in form but has a centerline that appears to be meandering. Between 100.0d and 150.0d there is a region that has almost a cylindrical form but contains two individual units one above and one below 125.0d. These three flow regions are present for the remainder of the evolution although each evolves in a different manner.

The first region (structure v1), continues to widen, rotate and become more dilute between 0.40 and 1.0 seconds. The third region increases in height between 0.35 and 0.60 seconds, reaching a height of over 100.0d at 0.60 seconds, while maintaining a jet-like shape. At 1.0 seconds, however, the front of this third region appears to have been reduced to a height of 75.0d. The second region in between the first and third regions grows wider and considerably more diffuse over time to the point where it is difficult to define its edges at 1.0 second. By 1.0 second the first region (structure v1) appears to have a larger concentration of dye than the second region.

6.4.1.2 Flows with leading vortex rings

Conditions H15 and L15 are characterized by starting vortex rings that separate and evolve independently from the remaining/trailing source fluid. Photographs in Figure 6.2b show a representative 15-mm experiment with a large momentum flux. For buoyant jets, the first structure v1, forms by 0.05 seconds and is already separate by 0.10 seconds. By 0.10 seconds, the second structure, v2, is also formed at the front of the trailing fluid. At 0.15 seconds, the first

structure appears to move independently from the second structure and the tail fluid. At 0.20 seconds, there appears to be three main regions of the tail. From 0.0d to 5.0d is one region that grows in width with distance from source and has a similar dye concentration throughout. In the second region, near ~ 5.0d, the jet narrows considerably and then sharply widens slightly above 5.0d. The third region is one of approximately uniform width, starting above the constriction at 5.0d to the trailing jet flow front at approximately 12.0d. These three regions remain in the flow for the remainder of its duration.

The first structure v1 moves independently of the rest of the flow. It remains a constant width until after 0.40 seconds when it begins to grow as evidenced by its progressively larger sizes at 0.60 s and 1.0 s. The fluid around the core of the vortex no longer has a high dye concentration and therefore the core is visible as a ring at 0.60 and 1.0 seconds. The second structure, v2, grows wider from 0.35 to 0.40 seconds but does not grow taller during this time. It is taller at 0.60 seconds indicating that it has started to move again between 0.40 and 0.60 seconds. At 1.0 second, v2 appears to be rotated off-axis and is nearly spherical. The fluid at the base of the jet appears to increase in height and width throughout the rest of the observation duration. The structure at the front of the tail region, however, appears to widen and become spherical.

6.4.1.3 Summary of Flow Morphology

All the unsteady, short-duration flows with buoyancy are similar in that they create a sequence of distinct round structures as they evolve. The structures

grow in height and width, at various rates as they travel from the source. However, the different sets of experiments differ in the relative sizes (i.e. fluid volumes) of each of those structures. Also the dilution pattern of each subsequent structure appears to vary such that the middle regions of the flows dilute more quickly than the front (v1) and the tail region appears to dilute most slowly.

The typical evolution of the unsteady buoyant jets is characterized by the formation of one or more toroidal vortices, the first of which is labeled v1 in the images. The vortices form as the source fluid initially exits the round orifice and are then driven away from the vent by the fluid injected after their formation. Flow conditions with the highest discharge velocities generate vortex structures that propagate farthest from the source during the time of the acceleration. During the initial rapid ascent, the flow remains symmetric about the axis of the flow. This period of high ascent rates corresponds in time with the acceleration phase at the source, between 0.05 seconds and 0.20 seconds after flow initiation.

At 0.20 seconds, the flow appears to contain three regions; a near-source region that is concentrated in dye and roughly jet-shaped; a middle region which contains structures that become very dilute (as in the 3-mm case) and are spherical (as in the 15-mm case). As the flow continues, each of these regions evolves according to its own structure. As the flow breaks up into individual structural elements during the source deceleration phase, flow asymmetry arises as each structure moves in a direction opposite to that of the structure ahead of it.

During the 0.60 seconds time step, the source is off, and the flows are in a transitional state that is characterized by the continued radial growth of the individual structures that developed during the deceleration stage. The starting vortex v1 also evolves to a radial growth stage during this time. Finally, the flow arrives at its final dynamic state characterized by radial growth of all the source fluid injected. This period has low propagation and spreading rates. The cores of the rings that are formed in the 15-mm condition are visible.

6.4.2 Quantitative Observations of Jet Boundaries

6.4.2.1 Height

Jet height was measured for each run at 0.01 second intervals for the first 200 milliseconds of each experiment and at irregular intervals after that. Each height time series was then interpolated to a regularly-spaced time axis using the *interp* function in Matlab. A linear interpoloation was used over a 1.0 second interval. The interpolated time series were then ensemble averaged to determine the average height time series for each experimental condition. The ensemble-averaged height time series are shown in Figure 6.3a for all experiment conditions.

Jet height for the 3-mm and 9-mm experiments is coincident with the starting vortex, labeled v1 in Figure 6.1a; for the 15-mm experiments, height corresponds with the front position of structure 2 that is labeled v2 in Figure 6.2b. The rise of these buoyant jets evolves in a similar fashion to the non-buoyant jets in that all flows ascend very rapidly in the initial stages (t = 0.0 to 0.2 seconds)

and then slow at an increasing rate until they begin to asymptote in height around 1.0 second. Flows with smaller vent sizes and larger pressures – high momentum conditions – have larger values of height at any given time.

The distribution of flow-front height versus time is logarithmic and the trends in the 3-mm, 9-mm, and v2 of the 15-mm experiments are nearly parallel. To scale these data according to the unsteady scaling procedure I discussed in Chapter 4, I used linear regression analysis to fit the interpolated height time series to the natural log of time. From the fit, I found the characteristic length and time scales for the unsteady buoyant jets and these values are listed in Table 6.1. The results are plotted in Figure 6.3b. These scales also collapse all the data for the unsteady buoyant jets to a single trend described with the equation

$$h/h_0 = \ln(t/t_0), \tag{6.1}$$

where t_0 = exp(-4.2). The value of 4.2 is the average ratio of b/a for all conditions.

A comparison of the heights attained by the buoyant and non-buoyant unsteady jets are shown in Figure 6.4. In general, buoyant and non-buoyant jet heights are nearly identical for all times. Similar rise behavior despite the presence or absence of buoyancy likely indicates that momentum dominates the dynamics during the observation period and for the experimental conditions considered here. The relative importance of buoyancy can be estimated with the densimetric Froude number at the jet source. The values of this parameter for the buoyant jets are listed in Table 3.3. These values are all above 10, suggesting momentum dominates the rise behavior.

Identification of the jet height in each buoyant experiment was complicated by the dilution of the dye. The dye marking the jet boundary dilutes considerably more in the buoyant jet experiments perhaps making it more difficult to identify the front position. Furthermore, other experimental work looking at concentration distributions in buoyant starting vortex rings indicates that mixing occurs at the front of the rings as well as the back [e.g., *Bond and Johari*, 2010]. The mixing at the front is attributed to Rayleigh-Taylor instabilities associated with the different densities of the jet and ambient fluids at the front boundary [e.g., *Bond and Johari*, 2010]. The mixing at the back is related to the large scale eddy motion in the jet.

6.4.2.2 Width

Width was more difficult to define for the buoyant jets due to the significant dye dilution. The outlines of jets from the representative experiment in Figure 6.2a are shown in Figure 6.5b along with outlines from the ensemble of experiments for the H3 condition (Figure 6.5a). The ensemble shape of the jet has a spherical front and a conical tail with a width that grows nearly linearly with distance from source. This shape is maintained throughout the duration of observation. The shape of the individual run is similar to a conical tail and spherical front, but the width varies more over the height with large indentations in the middle region of the jet behind the first structure and in front of the conical shaped tail. The indentations caused by the second structure in the buoyant jets are smaller than those observed for the nonbuyoant jets. In the individual H3

experiment the first structure is the largest. The second structure seems to form but it is not as big as the first and the width increases approximately linearly with height from the source to the second structure. This observation contrasts with the trend observed for the non-buoyant H3 jets that were characterized by a narrow tail of fluid behind the second structure that was much wider.

Outlines from the representative 15-mm shown in Figure 6.2b are shown in Figure 6.6b along with outlines from the ensemble of experiments for the H15 condition (Figure 6.6a). Near the source, especially at early times, both the ensemble and individual shapes of the jet have spherical fronts and conical tails with widths that grow nearly linearly with distance from source. The shape of the individual run is similar to the ensemble but has large undulations in the flow boundary beginning at t = 0.30 s, particularly in the middle region of the jets (behind the first structure and in front of the conical shaped tail).

The spreading angles of the jet were measured for each phase of the source condition (described initially in Chapter 4) and are listed for the representative and ensemble 3-mm experiments in Table 6.2. The jet width is greater for the ensemble, and the width changes over time. Near the end of the injection, at 0.30 seconds, the width of the ensemble is less than its value before and after that time step. A similar width minimum is observed in the individual experiment at 0.50 s. The spreading angles for the 15-mm individual and ensemble of experiments are list in Table 6.3. Spreading angles were calculated by measuring the maximum width at the base of the flow and the maximum

height of the second structure. For the individual experiment an increase in width occurs at 0.30 s rather than a decrease, as occurred for the other experiments discussed above. There is an increase in angle at 0.30 seconds, however, in the ensemble. The spreading angles for the near jet in the 15-mm experiments exceed the spreading angle in the 3-mm experiments.

Overall, the spreading angle changes with time in both the buoyant and non-buoyant unsteady jets. The individual flows have more variability than the ensembles due to the presence of large scale structures within the flow. The presence of buoyancy appears to modify the formation of the structures in the tail more significantly than the starting structure. Indentations in the flow boundary are reduced in the tail relative to those observed for the non-buoyant jets in the same experimental conditions.

6.4.2.3 Comparison of buoyant and non-buoyant jets

The evolution of the jet boundary (morphology) occurs in a similar dynamic sequence for both the buoyant and non-buoyant jets. The resultant plume shapes however look rather different as shown in Figure 6.7 for the 3-mm condition. While both the non-buoyant and buoyant jets divide into a head, body and tail regions in the early stages ($t < 0.2$ seconds), the structures in the non-buoyant flows appear to be more compact and round (less elongate) than those in the case with buoyancy. The buoyant jets appear to have a larger height at a given time than the non-buoyant jets and have two main flow regions, rather than three, in the long time limit. On the other hand, the plume shapes look very similar for

the 15-mm condition, as shown in Figure 6.8. There appears to be less variation of the flow boundaries at the edge of the buoyant jets. The observation of the linear growth in width with height in the buoyant unsteady jets is different from the change in width over the height of the non-buoyant unsteady jets that involved a drastic change in width associated with the second structure.

6.4.3 Jet Interior

To understand the role of buoyancy on the velocity field evolution, experiments with buoyancy were run and PIV measurements were made (methods described in Chapters 3 and 5). These experiments were identical in source condition as the non-buoyant jets such that direct comparisons can be made of the measurements.

6.4.3.1 Source Characteristics

The source conditions for these experiments are summarized in Table 3.4. The injection curves are shown in Figure 6.9. The Reynolds number varied from 10^2 to a maximum above 10^4 and then decreased.

6.4.3.2 Jet Velocity Fields

The velocity vector fields measured at 0.07 seconds for the unsteady buoyant jets are shown in Figure 6.10 for a representative individual experiment and the ensemble. The source is on and the flowrate is increasing at this instant. The photo of the individual experiment is also shown (Figure 6.10a). The jet reaches a height of y/d = 3.0 within the first 0.07 seconds and remains at an approximately uniform width of 1.0d. The flow front does not appear visible. In

the individual velocity field (Figure 6.10b) the motion of the first vortex structure is illustrated by the pattern of velocity vectors. The velocity decreases from the interior of the jet towards its edges. There are vectors near the center of the structure which point toward the vent. This pattern is associated with the three-dimensional propagation of this structure toward the camera which gives the appearance of downward motion. The ensemble shows that this structure occurs at approximately y/d = 2.0 at this time step for all experiment conditions. The velocity magnitude also appears to be very large.

At 0.14 seconds the first structure is visible at y/d = 6.0 (Figure 6.11). This structure appears to still be connected to the trailing fluid behind it, as there is no break in the light intensity in between the two (Figure 6.11a). This image shows the reflectivity of the methanol in the laser and its large concentration within the jet as compared to the ambient fluid results in an over-exposed image. Thus unfortunately velocities within the jet region may not accurately reflect real values during these stages. The individual velocity field (Figure 6.11b) shows that there are two regions of peak velocity, one within the first vortex and one within the region at the front of the trailing flow. The cores of the front vortex appear to be rotated off the axis of the flow. In the ensemble (Figure 6.11c), however, the flow field shows more symmetry about the vertical axis. There is high magnitude velocity directed toward the center of the jet below the base of the leading vortex structure, stretching from y/d = 1.0 to y/d =5.0. In the ensemble, like in the

individual experiment, there is a zone of high velocity in the fluid at the front of the trailing jet.

At 0.21 seconds, the peak of the vent discharge has been reached and the flow is just beginning to decline. At this stage (Figure 6.12a), the leading vortex has broken away from the remaining fluid and entrained ambient fluid, as is evidenced by the decrease in the intensity of light reflection in the separated structure. As a result a well-defined vortex structure with width 2.0d becomes evident near y/d = 9.0. There is still high momentum fluid at the centerline of this structure as evidenced by the elongated patch of peak velocity near the center of the vortex in the individual velocity vector field (Figure 6.12b). The region of peak velocity appears larger and to have reached a larger peak value relative to the previous time step. The trailing jet at this time appears to have three structures. The region nearest the vent has poor vector resolution potentially due to the high concentration of particles near the vent. The middle region of the jet has a large high-velocity region at approximately y/d = 3.0 in the individual velocity field, corresponding to a region of largely inward-directed radial velocity in the ensemble field (Figure 6.11c). The peak radial velocities occur just above the peak in the velocity at the center of the flow. Finally, I note here that the first structure continues to propagate at a high velocity.

At 0.28 seconds, the source is on but decreasing in time. Analysis for this time step (Figure 6.13a) shows that the first structure continues to propagate independently of the trailing fluid and maintains a constant width. This structure

appears to be oriented symmetrically about the vertical flow axis. The trailing fluid has a round top which extends from y/d = 4.0 to y/d =7.0, over which it has a uniform width of approximately 2.0d. The tail region is below y/d = 4.0. The velocity in the second structure is visible in the individual velocity field (Figure 6.13b) and has high velocities at the core. The leading ring structure now at y/d = 12.0 has flow moving vertically upward through its bottom surface, suggesting that the ring is moving as an isolated structure. There is a decrease in width in the jet at y/d = 4.0 in the photo that corresponds with a region of high jet velocity in the individual velocity field and a region of high inward-directed radial velocity in the ensemble (Figure 6.13c).

At 0.35 seconds the source flux is just ending. By this time step the starting vortex structure continues to move away from the vent as shown in Figure 6.14 (cores at a height of y/d = 14.0) but now the velocity distribution is large at the bottom of the structure rather than at the top. The structure from y/d = 5.0 to y/d = 8.0 is associated with large structures in the velocity field that are not apparent in the photo. The region of constricted flow at y/d = 5.0 is also associated with large vertical jet velocities in the individual image and large ambient inward-directed radial velocities in the ensemble. The leading ring structure continues to have very high velocities at its core.

By 0.42 seconds the source is off and the flow changes character as shown in Figure 6.15. The first structure is out of the field of view of the photo but its trailing tail is still visible in the individual and ensemble velocity fields. This

leading structure is still visible in the ensemble velocity field. According to the photo the main jet has three regions at this instant: one from y/d = 5.0 to y/d = 9.0, one from y/d = 3.0 to y/d =5.0, and one from y/d = 0.0 to y/d = 3.0. These regions are separated by a decrease in width of the visible flow boundary. The highest velocities in the jet are located in the first region from y/d = 5.0 to y/d = 9.0 and are largely vertically directed; the largest local velocities in the ambient also occur here and are radial and inward-directed. The largest velocities in the individual and ambient are associated with the motion of the first structure. The ensemble velocity field can be divided into 4 regions. The first is associated with the first structure with cores at y/d = 14.0. This motion extends down to y/d = 9.0. The cores of the second structure are at y/d = 8.0 (consistent with the velocity field from the individual experiment). The flow below this can be divided into the jet region between r/d = +/- 1.0 and the ambient region beyond r/d = +/- 1.0. There is no evidence in the ensemble that flow contained three structures at this time.

At 0.49 seconds the first structure at the head of the jet (centered around y/d = 8.0) appears to be changing form into a sphere (Figure 6.16a). A small, region of moderate velocity is visible below it around y/d = 3.0 (Figure 6.16b), and corresponds in space with the very narrow portion of the jet visible in the photograph (Figure 6.16a). The flow below (upstream of) that has a different character in that the dyed fluid appears to be more dilute. In the individual velocity field the second structure at ~y/d = 8.0 is increasing in strength as evidenced by the larger velocities at the center of the vortex. The ensemble field

continues to show the high velocity associated with the passage of the starting vortex. The region of peak velocity in the jet in the individual and ensemble fields is associated with a narrow region of fluid in the photo.

By 0.56 seconds (Figure 6.17) the magnitude of the velocity behind the leading vortex ring structure decreases and the second structure continues to grow in both height and width, although still centered around y/d = 8. The region of peak velocity now appears to be internal to the structure. This region is also associated with large ambient velocities that have a significant vertical component. There is a region of peak velocity in the ensemble field at y/d = 6 that corresponds with the base of this second structure v2.

From 0.63 to 1.25 seconds the velocity fields transition from being dominated by the ambient flow to being dominated by the jet flow, as shown by the ensemble velocity fields shown in Figure 6.18. Note that there is a region of high velocity at the center of the jet at later times. This region extends from the flow base to the front of the second structure. Also at this time are very large vorticies, which bring in ambient fluid at an angle to the vertical. This creates the ‘wing’ pattern of radial velocity at the edges of the jet. This motion is still high amplitude at 1.0 seconds.

6.4.3.3 Jet Velocity Profiles

The profile of the instantaneous vertical velocity, v, for the individual experiment along the centerline is shown in Figure 6.19 for various instants during and immediately following the injection. From y/d = 0.0 to y/d = 15.0,

peaks in the profiles at early times (a) correspond with structure 1 and peaks in the profiles at later times (b) correspond with structure 2. While the profiles show variable distributions during early times (a), the profiles show more consistency at later times (b) with an approximately linear increase in velocity from y/d = 0.0 to y/d = 7.0, then a peak corresponding to the location of structure 2 which remains between y/d = 7.0 and y/d = 9.0 at all of the later times. Above structure 2 is a region of nearly constant velocity from y/d = 7.0 to the base of structure 1 which occurs at different locations for each instant. The peak velocity at early times (left side) increases between 0.07 and 0.21 seconds when it is a maximum, and then decreases rapidly between 0.21 and 0.28 seconds. Similarly, the peak velocity for structure 2 increases (late times, right side) between 0.35 and 0.49 seconds when it reaches a maximum, and then decreases rapidly between 0.49 and 0.56 seconds. The changes in velocity occur gradually at later times without a large jump in the values.

The cross-sectional profiles of the vertical velocity, v, for the individual experiment at various distances from the source of the injection are shown in Figure 6.20. For early times (a), the cross-sectional profiles show the propagation of the first structure, and at late times (b), the cross-sectional profiles show the propagation of the second structure. Note that there is considerable variability in the shape and symmetry of the cross-sectional profiles of the first structure while the second structure has a consistent distribution in which velocity increases from the flow edges toward its center and is generally centered about the central axis.

For the vertical velocity in the second structure, both the peak magnitudes and the widths of the cross-sectional distributions increase with distance from source. The distribution is broad and rounded, however, and it is difficult to discern the jet motion from that of the ambient in these figures.

The cross-sectional profiles of the normalized vertical velocity, v / vmax, for the individual experiment at various distances from the source of the injection are shown in Figure 6.21. Velocity was normalized by the maximum value of the vertical velocity along the cross section, vmax, at the specified distance from the source. There are very large negative normalized velocities for both the first and second structures. The centerline of both wavers as is evidenced by the variability in the locations of the peaks.

In Figure 6.22, the distributions of vertical and horizontal velocity across the jet are shown for the ensemble of experiments at various distances from source at t = 1.0 second. Vertical velocities are greatest at the center of the flow and increase with distance from source until the location of the first vortex (structure 1). Above the vortex, the velocity is very low. The profiles for the radial component of velocity indicate that there is a peak in the radial component on either side of the centerline, which increases and widens with distance from source. Radial velocity peaks in the location of the shear layer and decreases toward the flow centerline and again toward the ambient fluid. For distances close to the source the radial velocity profiles make a ‘u’ shape which may indicate the shear layer does not reach the centerline. Alternatively this may mean there is

little velocity measured within the jet. These plots also indicate that the ratio of the peak radial component of velocity varies to the peak in the axial component vary along the distance from source.

6.4.3.4 Time-Averaged Velocity Vector Fields

The time-averages of the velocity fields can be used to examine the flow structures. There are two main structures in each flow, the starting vortex and then a second vortex. At the first instant, 0.07 seconds, the starting vortex dominates both the individual and ensemble vector fields as shown in Figure 6.23. The vertical velocities are high at the flow center and lower at edges. Though the pattern is not symmetric about the vertical centerline for the individual case, it does appear symmetric in both the vertical and radial velocity components in the ensemble. The vorticity shows a complex wave form with multiple regions of localized vorticity.

The time-average from 0.14 to 0.35 seconds of the second structure in the individual experiment is shown in Figure 6.24. This structure has a vortex ring at the front and a region of high vertical velocity near its base. There is radial velocity all along the sides of the structure and high vorticity along two linear regions at the edges of the flow. The ensemble (Figure 6.25) at this time has two structures. However, the structure moves considerably in space so the time average shows that the sequential location of the vortex progressed too far to get a good average. Thus there is a complex pattern of localized regions of high vertical and radial velocity as well as vorticity. Structure 2 on the other hand, has a very

distinct jet-like structure with a very strong border along the jet. This border is visible in the radial velocity contours. There is a region of high velocity and vorticity near the center of the flow.

The time-average for the transitional time between the source on and off phases, is shown in Figure 6.26 for the individual experiment and in Figure 6.27 for the ensemble. The vertical velocity structure has a region at the flow center with a peak velocity. There also seems to be a movement of the jet toward the –r/d direction in all contour plots. There are two main regions of vorticity associated with the structure at the flow front. The velocity patterns show an isolated vortex for the first structure in the ensemble images. The second structure is similar to a puff but with very high ambient velocities at the base of the head of the structure at y/d = 5.0.

The time-averaged structure for late times (Figure 6.28) has large vertical velocities at the center of the flow around which the radial velocity is also large. Vorticity occurs throughout the jet and opposite signed vorticity crosses the centerline.

6.5. Discussion

The results for the external and internal motion of unsteady buoyant jets do not lead to a clear resolution of the role of buoyancy in modifying unsteady jet behavior. On the one hand, buoyant unsteady jets reach similar heights as the non-buoyant unsteady jets of the same initial condition for all times during the observation duration. This observation suggests that buoyancy does not modify

the front velocities of the unsteady jets significantly for the flow conditions observed here. Also, the internal velocity distributions were similar to those in the non-buoyant jets for all times during the observation duration in the region $y/d < 12$. These results may indicate that the momentum dominates the velocity distribution and rise velocity of the unsteady jets for the length and time scales considered here. Alternatively, it may be that buoyancy effects the concentration distribution more significantly than the velocity distributions in these flows.

Evidence for buoyancy modifying the concentration distribution is indicated by the different buoyant jet morphology and dye concentrations that were observed in the buoyant as compared to the non-buoyant unsteady jets. Buoyant jets appeared to divide into fewer structures than non-buoyant jets. This observation is consistent with the observation by *Bond and Johari* [2005] that all of the fluid seems to eventually end up in one structure. Also the first structure appeared to be less structured and larger in the buoyant as compared to the non-buoyant unsteady jets. This observation is consistent with buoyancy eliminating the internal structure of vortex rings [*Bond and Johari*, 2005] and modifying the starting vortex structure [*Bond and Johari*, 2005]. The presence of buoyancy seemed to dilute the buoyant unsteady jets faster and to a greater extent than the non-buoyant jets. This observation is consistent with mixing enhancement by the presence of positive buoyancy as observed by *Bond and Johari* [2010].

A clearer understanding of the role of buoyancy may be derived from a study that considers the evolution of jets over a range of momentum to buoyancy

ratios. If these jets vary from one another and from the non-buoyant jets, then the effects of buoyancy may be more detectable. The inclusion of flows with maximum densimetric Froude numbers close to 1 may be the most informative. This would be difficult to accomplish in this apparatus. Based on the velocities and orifice diameters that are considered in this study, to achieve a Fr near 1 would require a large density difference between the ambient and jet fluids. These differences are above the threshold ~3% that the Boussinesq approximation is expected to be valid. This may add considerable complexity to the dynamics, and, thus, require the measurement of the internal concentration distribution over time in conjunction with the internal velocity distribution. By measuring both, the relative dependence of either distribution on buoyancy can be investigated. And, as the results presented in this chapter suggest, the significance may vary for each distribution. Also, a better match of the indices of refraction between the buoyant jet and non-buoyant ambient fluids may improve the velocity measurements [e.g., *Adrian and Westerweel*, 2011].

If buoyancy does not contribute significantly to the near field evolution of buoyant jets, then momentum dominates the process of near field entrainment. This means the process of buoyancy reversal as well as the stability of the jet are functions of the dissipation of source momentum, alone. This result lends support to the study of momentum-only jets to better understand the dynamics in these regions in volcanic plumes. However, care must be taken when extending the results of buoyancy in this study as it has a very limited scope. Most importantly,

these results involve a positively buoyant jet whereas volcanic plumes are thought to sometimes have negative buoyancy on their initiation [e.g., *Sparks et al*., 1997]. However, *Patrick* [2007b] argues that there may be a subset of these short-lived volcanic plumes that are initiated with positive rather than negative buoyancy. As this parameter is difficult to measure, its value, spatial distribution and evolution over time remains relatively unconstrained.

Yet, *Marchetti et al*. [2009] suggest buoyancy may be an important indicator of the source mechanisms for short-lived plumes. They argue that Vulcanian-style plumes may have more initial buoyancy than Strombolian-plumes and both styles have similar ranges in initial momentum. This would imply the eruption mechanisms for these styles impart a different amount of buoyancy without imparting a different amount of source momentum. Fragmentation of hot magma into small fragments that quickly transfer their heat to the surrounding air may be one way to accomplish a larger buoyancy flux. This condition may exist for Vulcanian-style eruptions that are thought to produce more fine grained particulates than Strombolian-style eruptions [e.g., *Sparks et al*., 1997]. However, finer-grained material is also thought to be the result of strong explosions, thus, implying a larger momentum flux when the buoyancy flux is large. By implying that the buoyancy flux is independent of the momentum flux, these authors also imply that the source mechanisms for these fluxes are independent. If true, this suggests there is a very large range of buoyancy and momentum fluxes that may be possible for any given eruption plume. Thus, future experiments should work

to systematically characterize the potential role of buoyancy over a range of momentum fluxes.

A conservative conclusion to draw from these results is that momentum will likely dominate the near field behavior of some volcanic plumes. Buoyancy may contribute to second order and modify mixing processes for times near the initiation. These second order effects may lead to changes in large-scale structures and the morphology of the plume.

Figure 6.1. Source momentum flux (a), normalized source momentum flux (b), Reynolds number (c), and acceleration (d) over time for experimental conditions H3 (black circles), L3 (gray circles), H9 (black squares), L9 (gray squares), H15 (black triangles), and L15 (gray triangles).

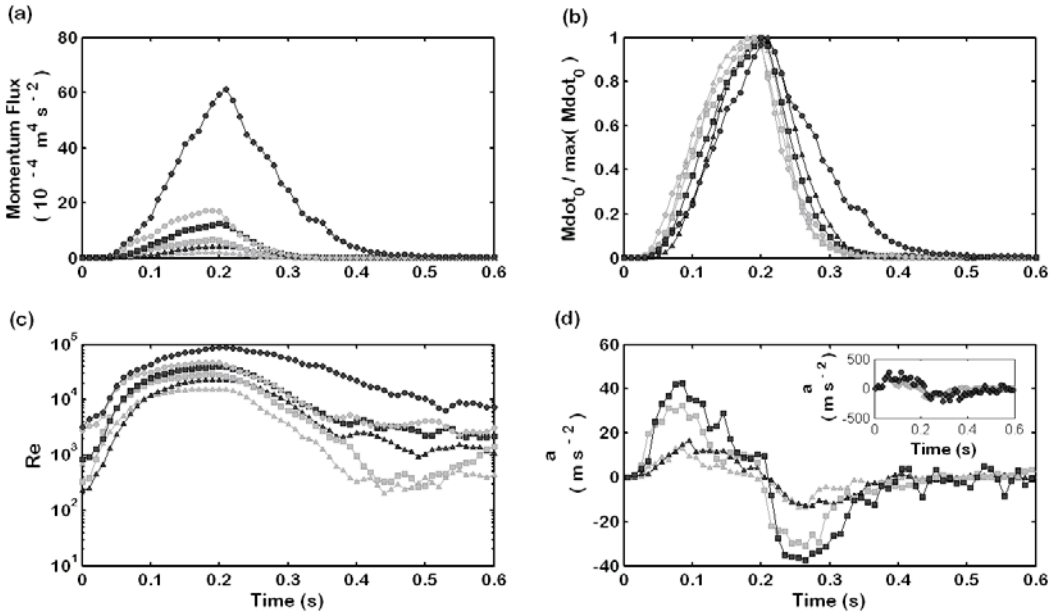

Figure 6.2. Jet (dark colored fluid) evolution in an individual experiment for conditions H3 (a) and H15 (b) at various instants. Scale on left indicates the distance from source in units of source diameters. Locations of vortex structures V1 and V2 are indicated in each frame.

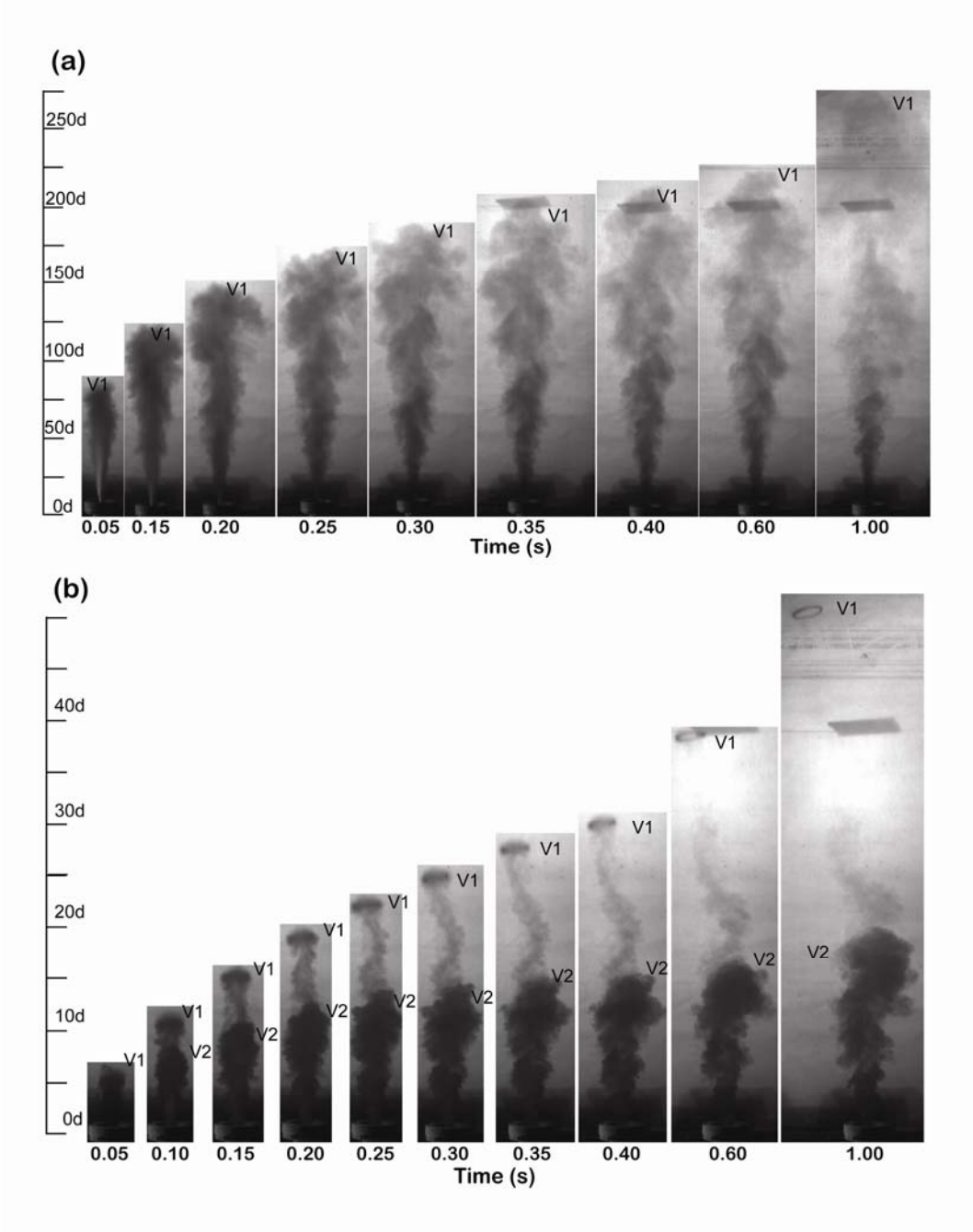

Figure 6.3. Unsteady buoyant jet height as a function of time (a) normalized by the scales h_0 and t_0 (b) for all runs in experimental conditions H3 (black circles), L3 (gray circles), H9 (black squares), L9 (gray squares), H15 (black triangles), and L15 (gray triangles). The best fit curve for the unsteady scaling (magenta line) is also shown (b).

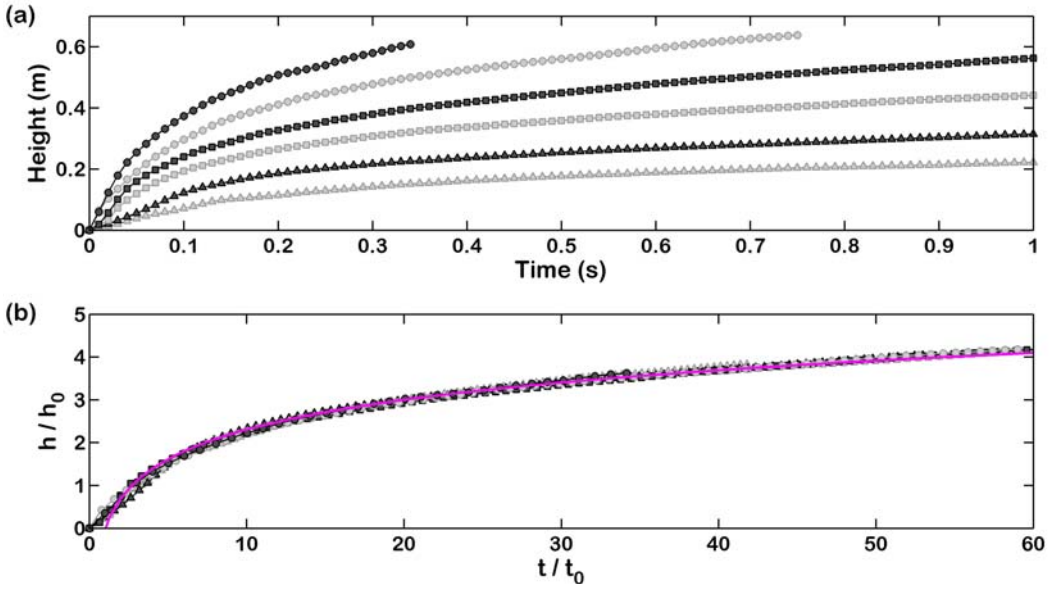

Figure 6.4. Comparison between ensemble-averaged buoyant (magenta crosses) and non-buoyant (black line) unsteady jet height as a function of nondimensional time.

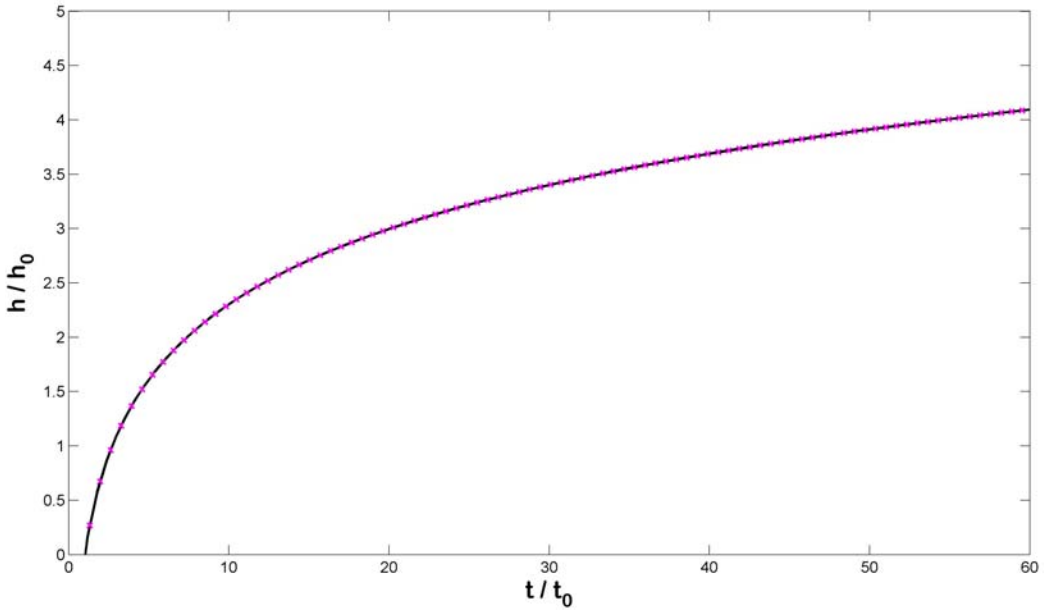

Figure 6.5 Jet outlines for the H3 condition showing the relationship between the ensemble images (a) and images for an individual run (b).

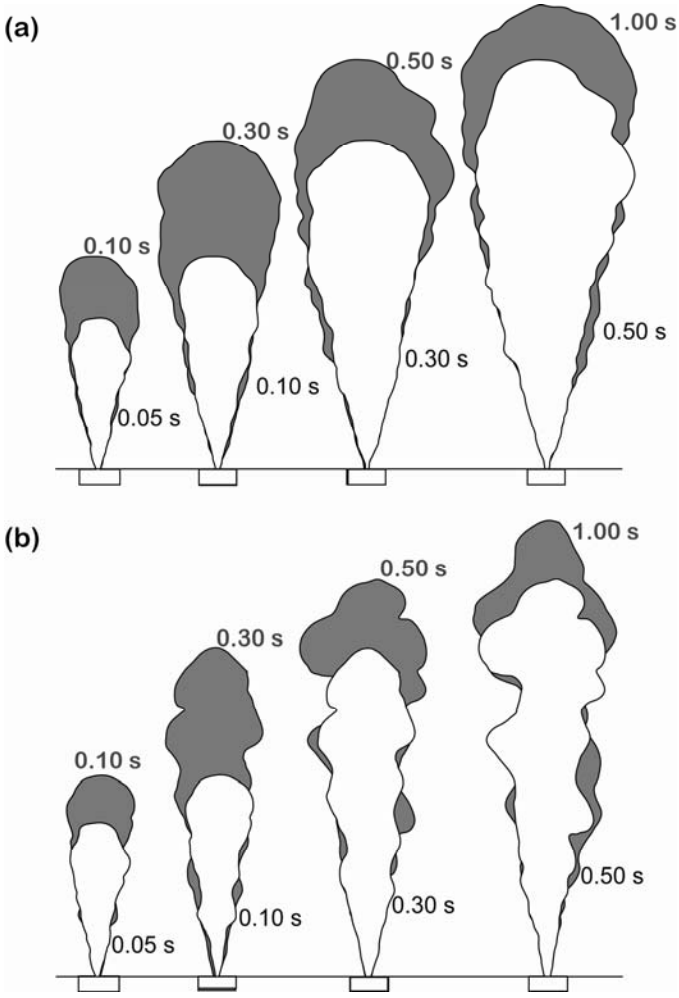

Figure 6.6 Jet outlines for the H15 condition showing the relationship between the ensemble images (a) and images for an individual run (b).

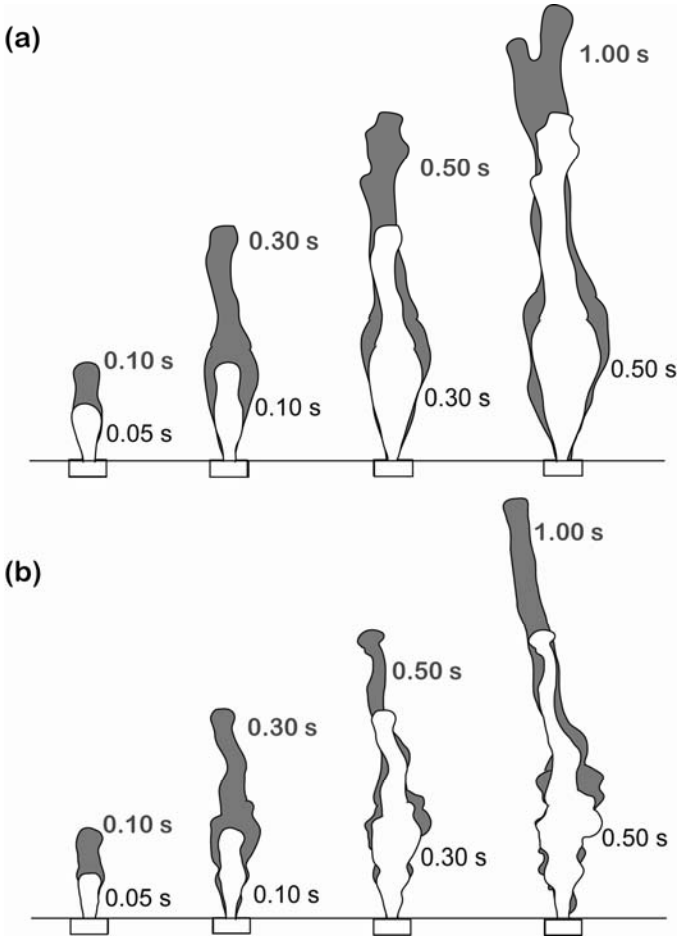

Figure 6.7. Comparison between buoyant and non-buoyant jets for the 3-mm condition.

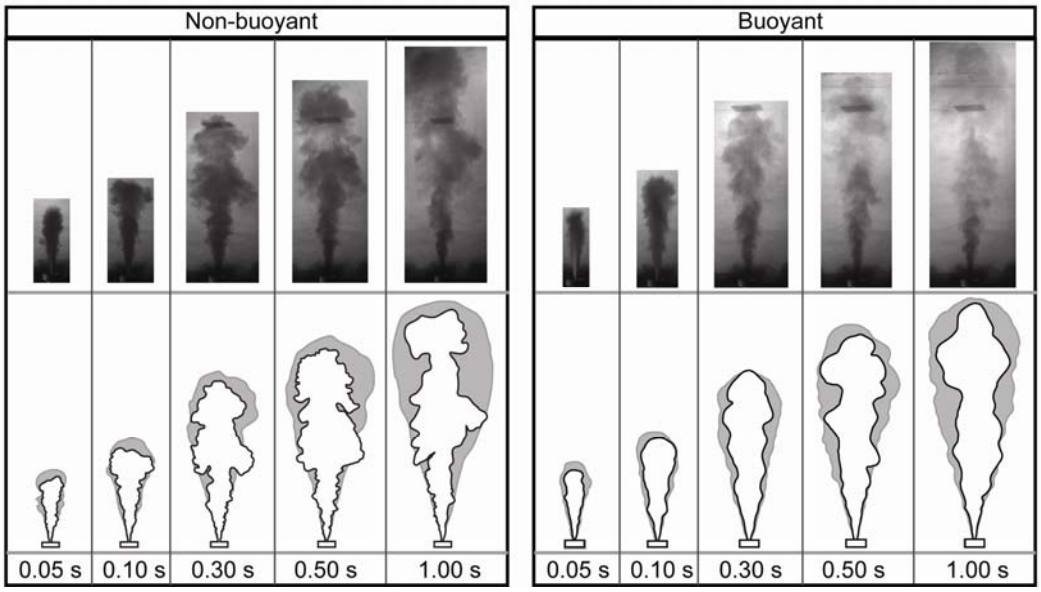

Figure 6.8. Comparison between buoyant and non-buoyant jets for the 15-mm condition.

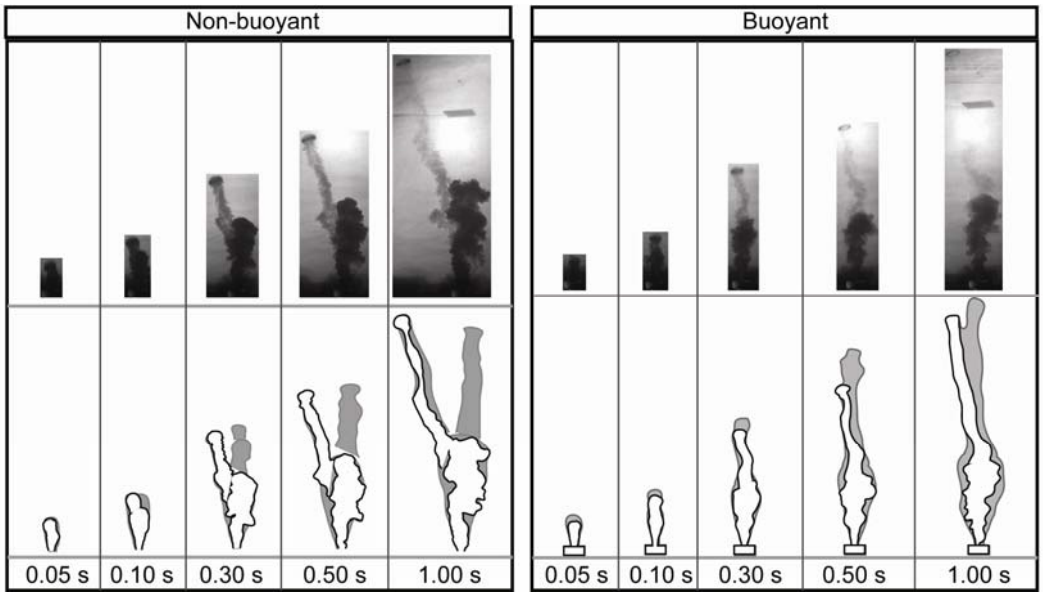

Figure 6.9. Source momentum flux (a) and Reynolds number (b) over time for the representative experiment (stars) and ensemble (open circles) experiments used for the internal flow measurements.

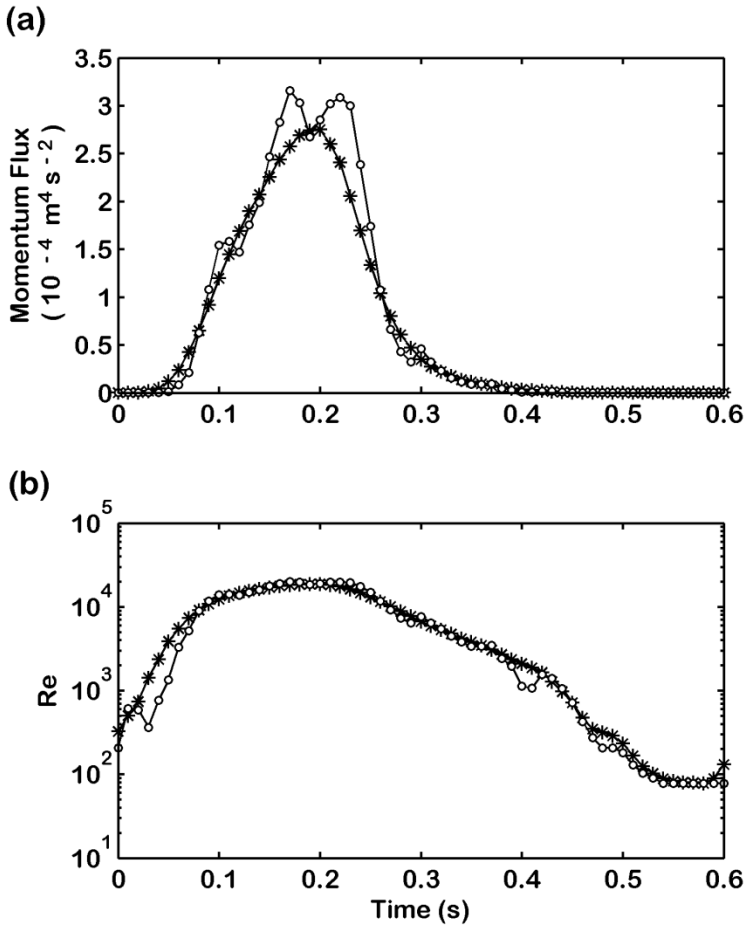

Figure 6.10. Individual jet photo (a), along with the individual (b) and ensemble (c) velocity fields at 0.07 s. Vectors are magnified 5x and 50% of those measured are displayed. Contours of velocity magnitude, V, and streamlines (solid grey lines) and are based on the total vector field.

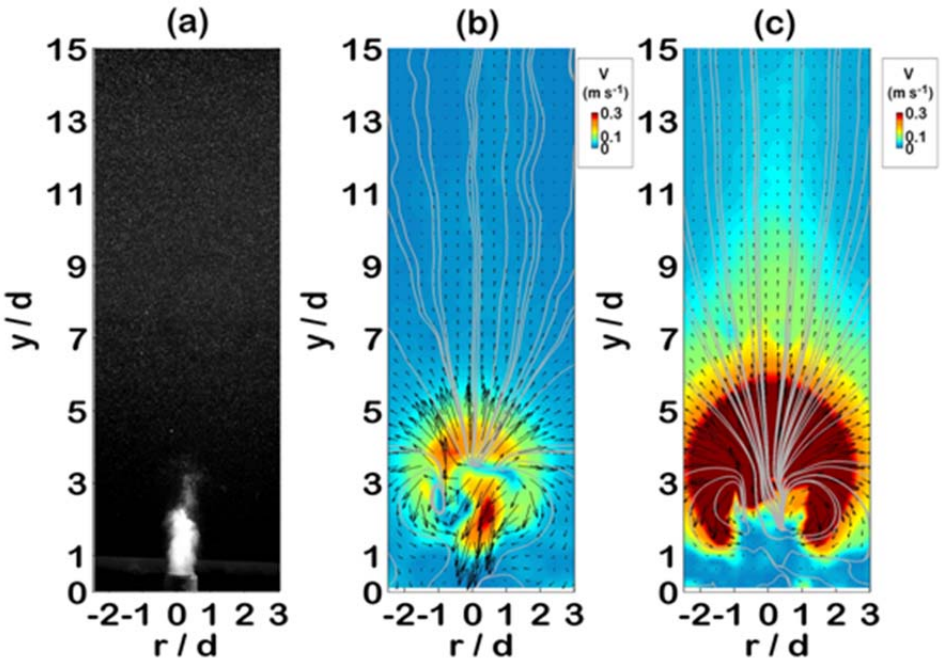

Figure 6.11. Individual jet photo (a), along with the individual (b) and ensemble (c) velocity fields at 0.14 s. Vectors are magnified 5x and 50% of those measured are displayed. Contours of velocity magnitude, V, and streamlines (solid grey lines) and are based on the total vector field.

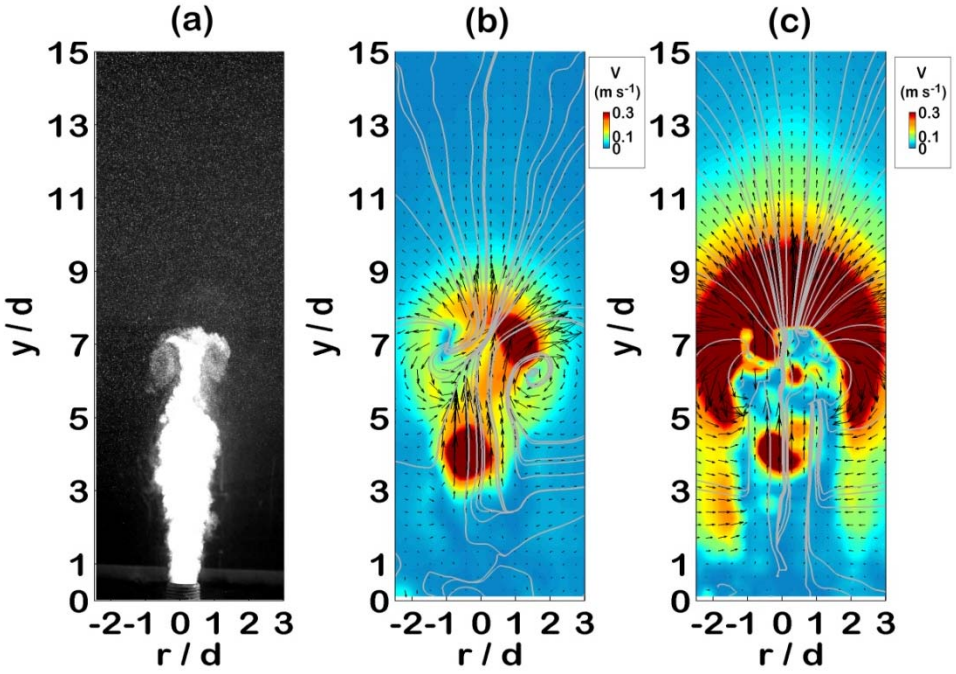

Figure 6.12. Individual jet photo (a), along with the individual (b) and ensemble (c) velocity fields at 0.21 s. Vectors are magnified 5x and 50% of those measured are displayed. Contours of velocity magnitude, V, and streamlines (solid grey lines) and are based on the total vector field.

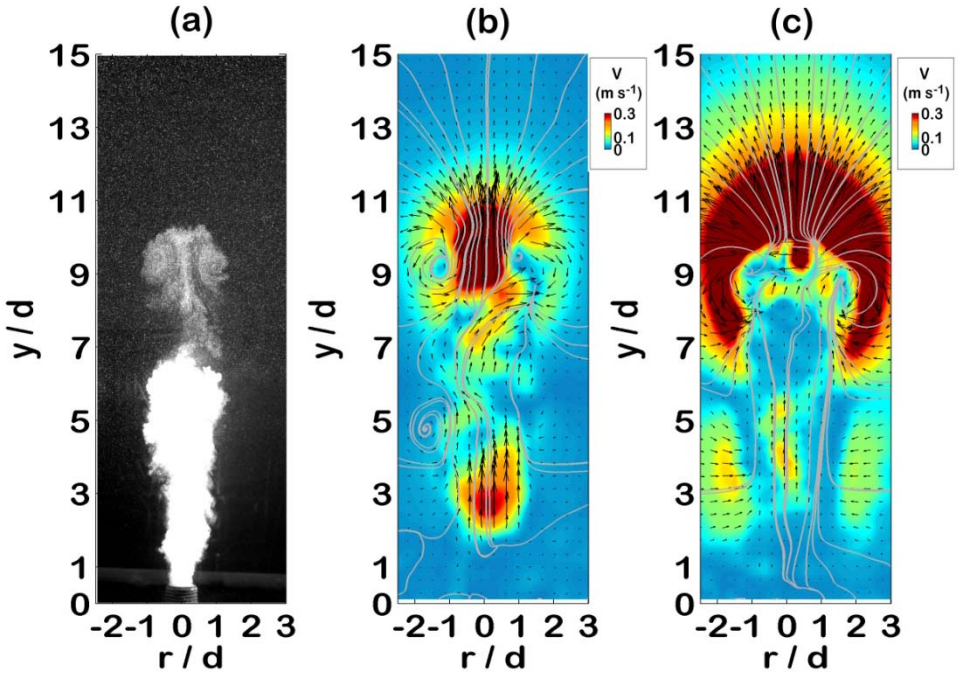

Figure 6.13. Individual jet photo (a), along with the individual (b) and ensemble (c) velocity fields at 0.28 s. Vectors are magnified 5x and 50% of those measured are displayed. Contours of velocity magnitude, V, and streamlines (solid grey lines) and are based on the total vector field.

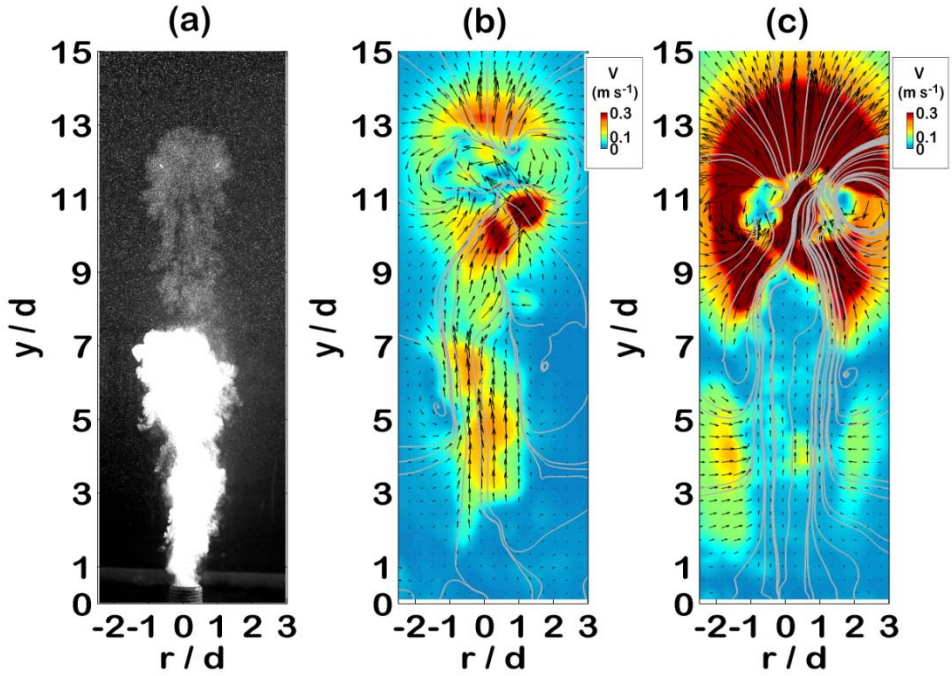

Figure 6.14: Individual jet photo (a), along with the individual (b) and ensemble (c) velocity fields at 0.35 s. Vectors are magnified 5x and 50% of those measured are displayed. Contours of velocity magnitude, V, and streamlines (solid grey lines) and are based on the total vector field.

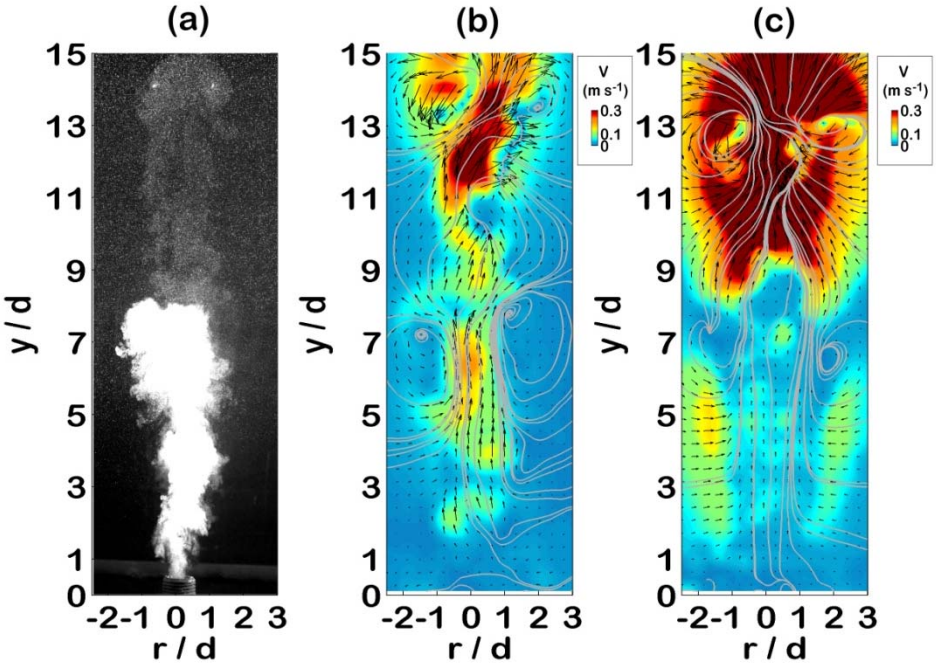

Figure 6.15: Individual jet photo (a), along with the individual (b) and ensemble (c) velocity fields at 0.42 s. Vectors are magnified 5x and 50% of those measured are displayed. Contours of velocity magnitude, V, and streamlines (solid grey lines) and are based on the total vector field.

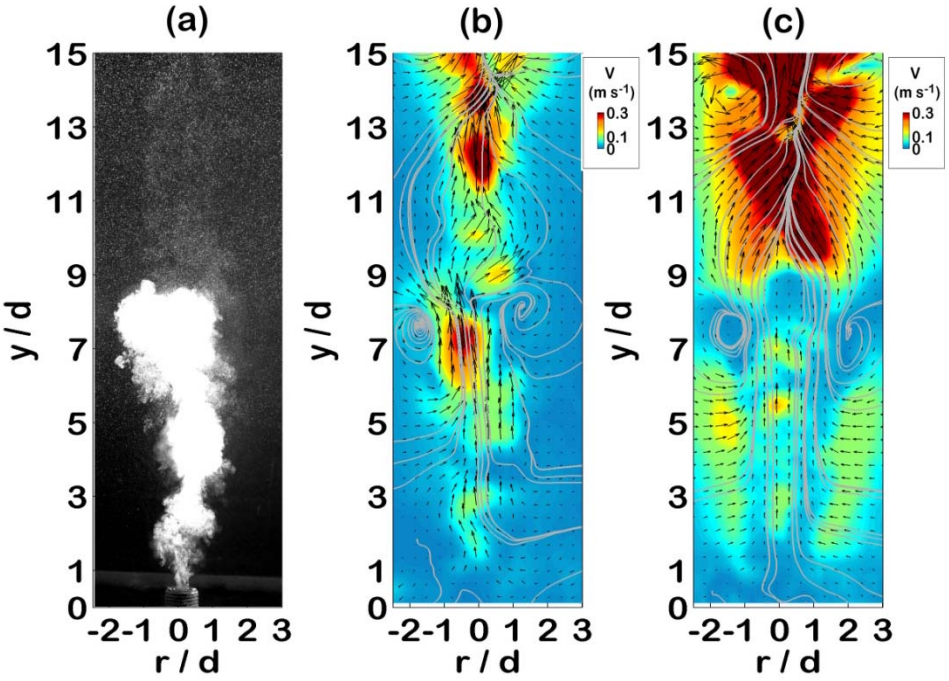

Figure 6.16: Individual jet photo (a), along with the individual (b) and ensemble (c) velocity fields at 0.49 s. Vectors are magnified 5x and 50% of those measured are displayed. Contours of velocity magnitude, V, and streamlines (solid grey lines) and are based on the total vector field.

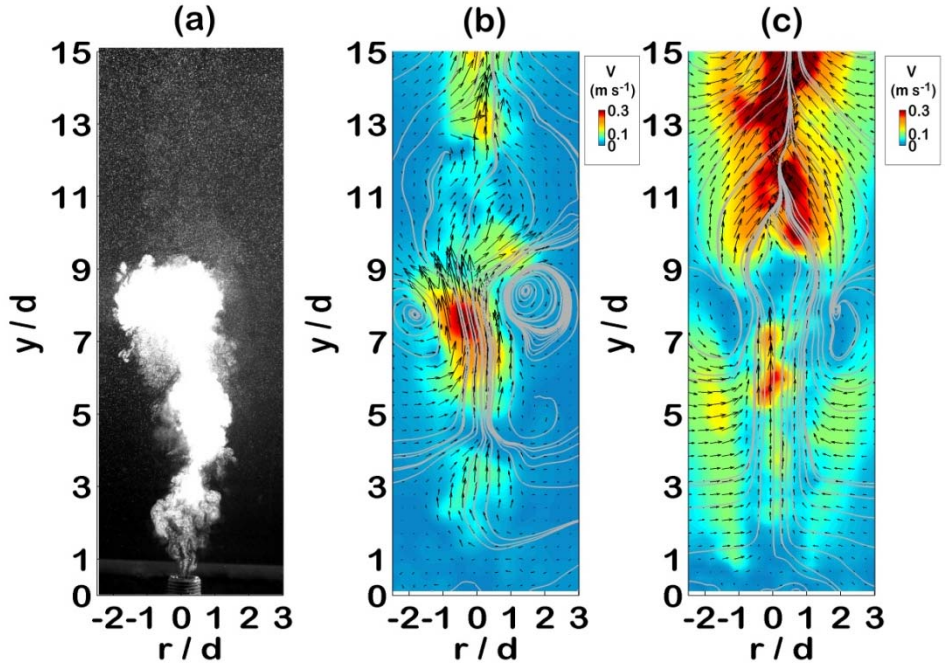

Figure 6.17: Individual jet photo (a), along with the individual (b) and ensemble (c) velocity fields at 0.56 s. Vectors are magnified 5x and 50% of those measured are displayed. Contours of velocity magnitude, V, and streamlines (solid grey lines) and are based on the total vector field.

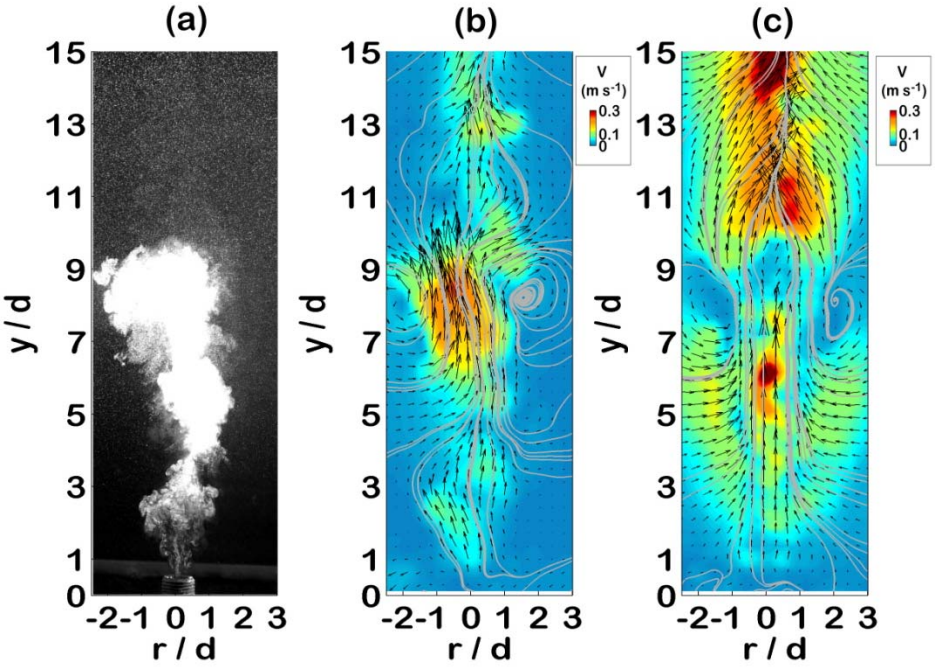

Figure 6.18. Ensemble average velocity fields for t = 0.63 s (a), 0.70 s (b), 0.75 s (c) and 1.25 s (d). Vectors are magnified 5x and 50% of those measured are displayed. Contours of velocity magnitude, **V**, and streamlines (solid grey lines) and are based on the total vector field.

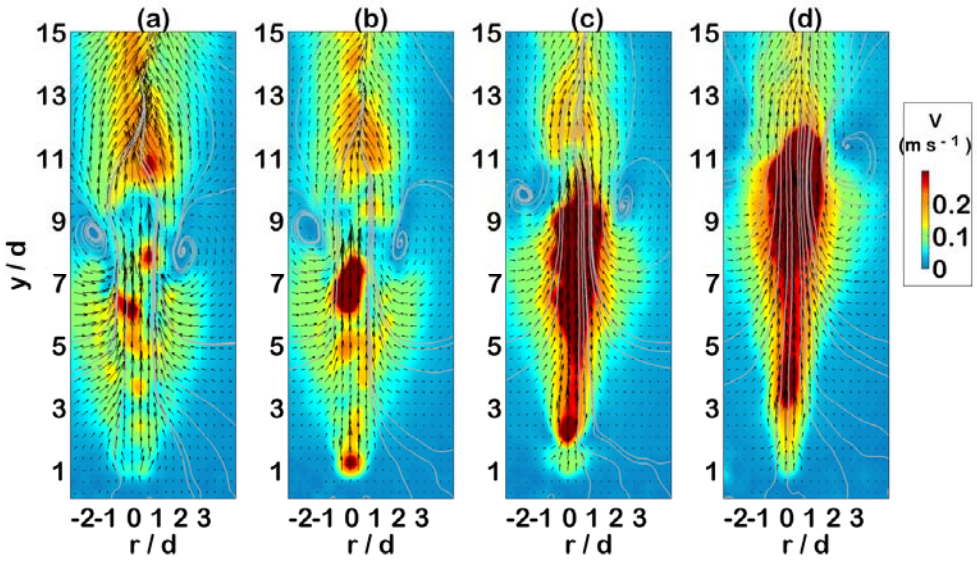

Figure 6.19. Profile of the instantaneous vertical velocity, v, for the individual experiment along the centerline at times during the injection (a) and times at and following the end of the injection (b) as indicated by the arrow labels.

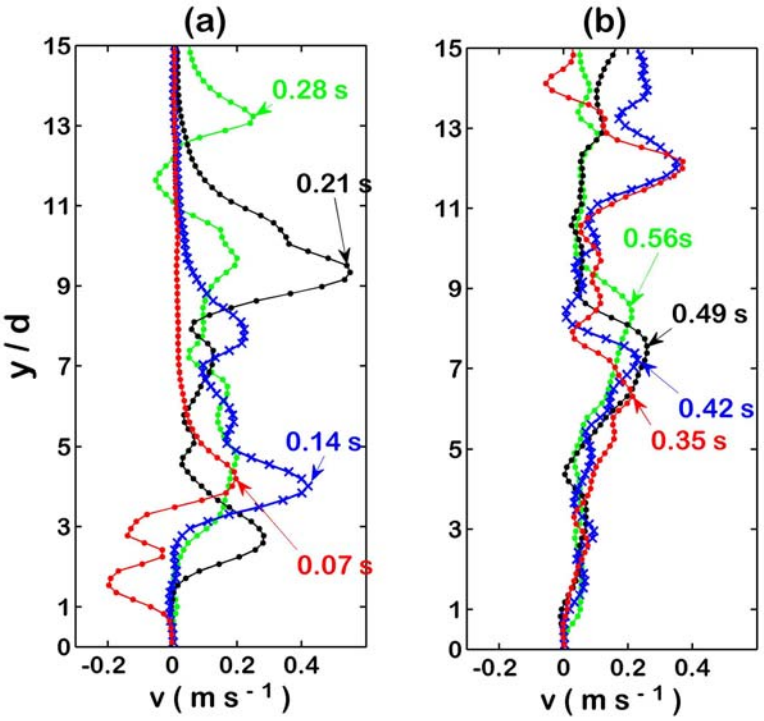

Figure 6.20. Cross-sectional profiles of the vertical velocity, **v**, for the individual experiment at a distance of 7d (top), 5d (middle), and 3d (bottom) from the vent for early times (a) and late times (b) as indicated by the legend.

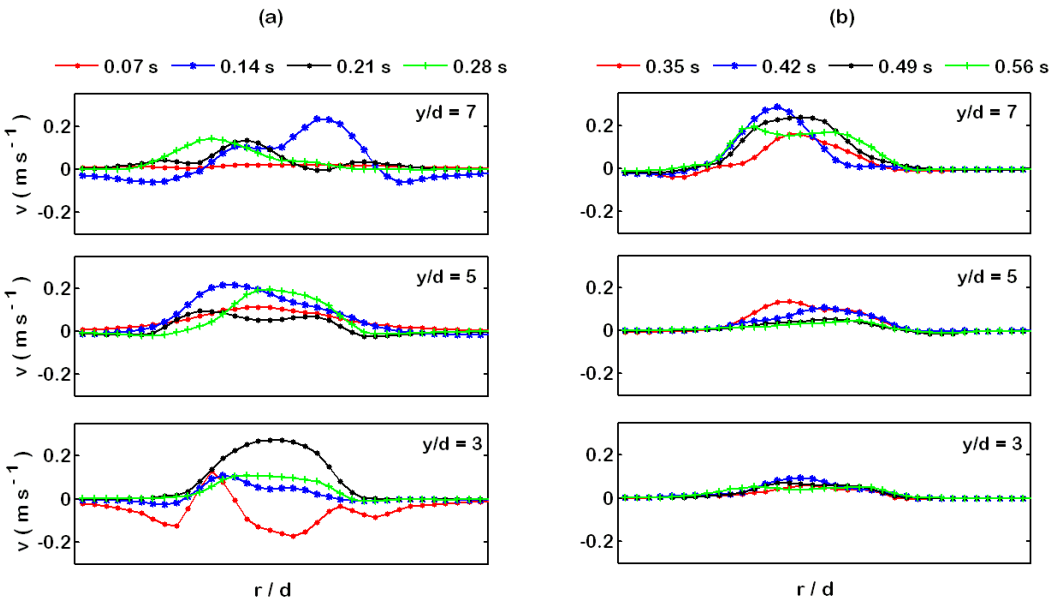

Figure 6.21. Cross-sectional profiles of the normalized axial component of the instantaneous velocity, v / v_{max}, for the individual experiment at a distance of 7d (top), 5d (middle), and 3d (bottom) from the vent for early times (a) and late times (b).

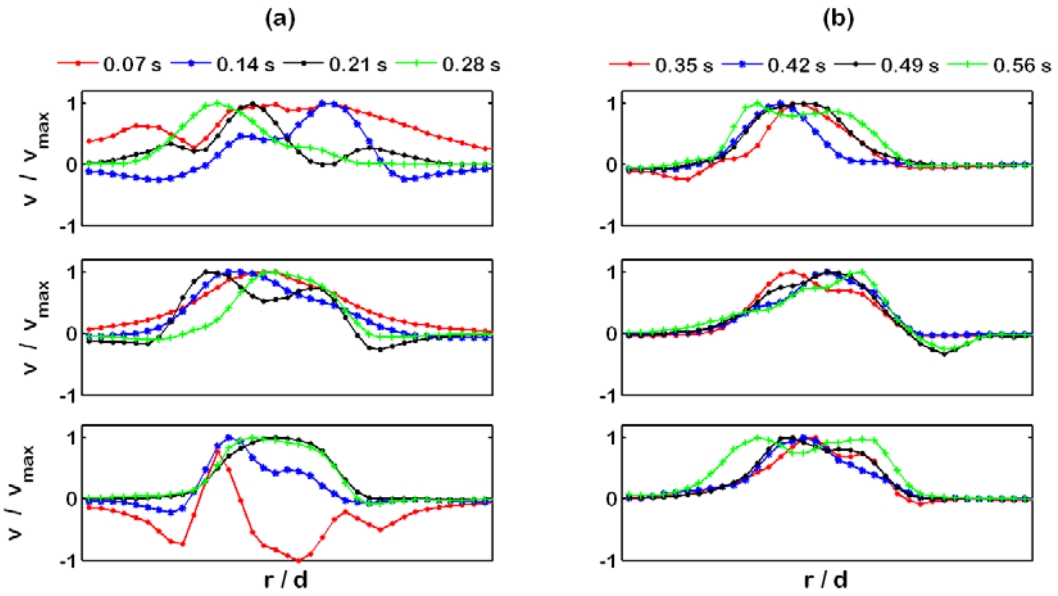

Figure 6.22. Cross-sectional distributions (a) of normalized axial, v/v_{max} (red), and radial. $|u|/|u|_{max}$ (blue), velocity for the ensemble-averaged flow. Profiles were taken at heights indicated by the red circles (b) in the whole flow field.

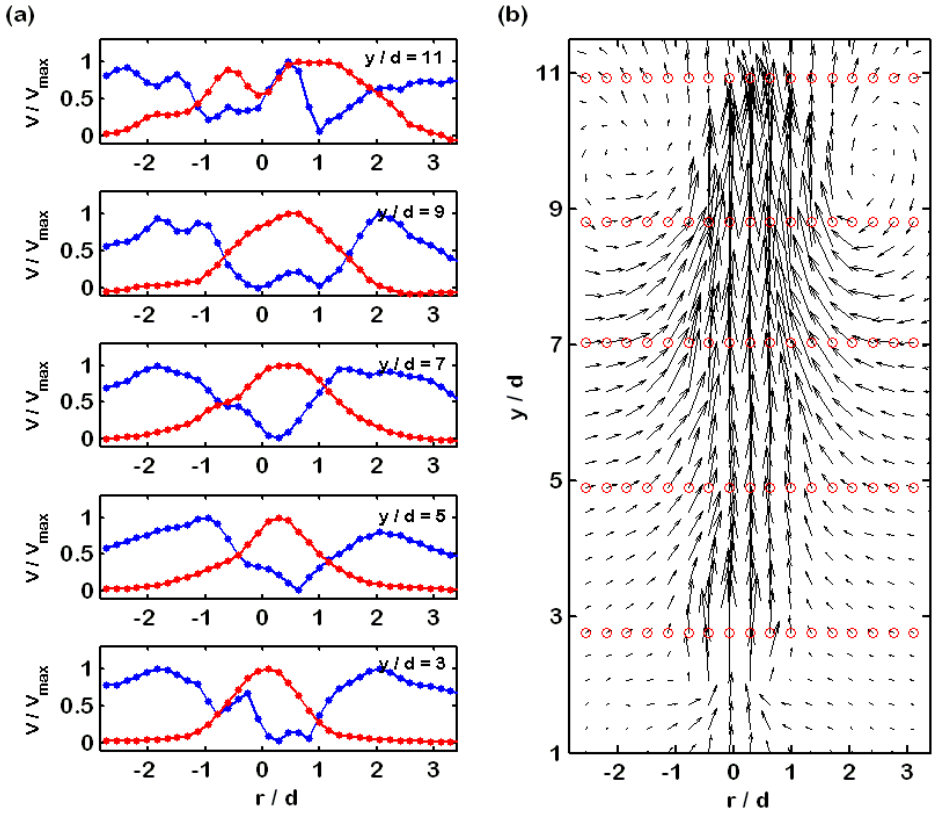

Figure 6.23. Velocity fields at 0.07 s for the (a) individual experiment and the (b) ensemble.

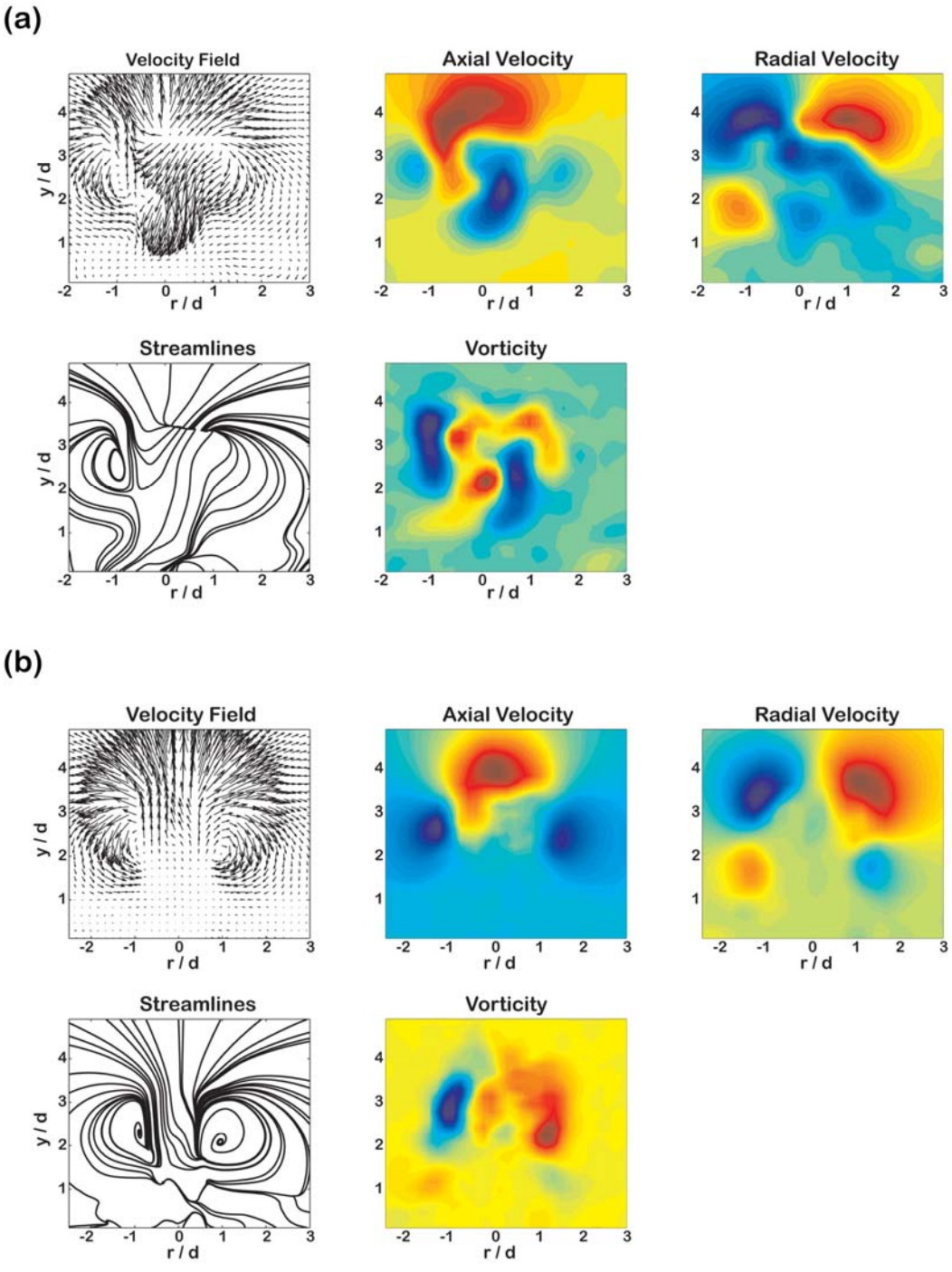

Figure 6.24. Time-averaged velocity for the single run from 0.14 - 0.35 s

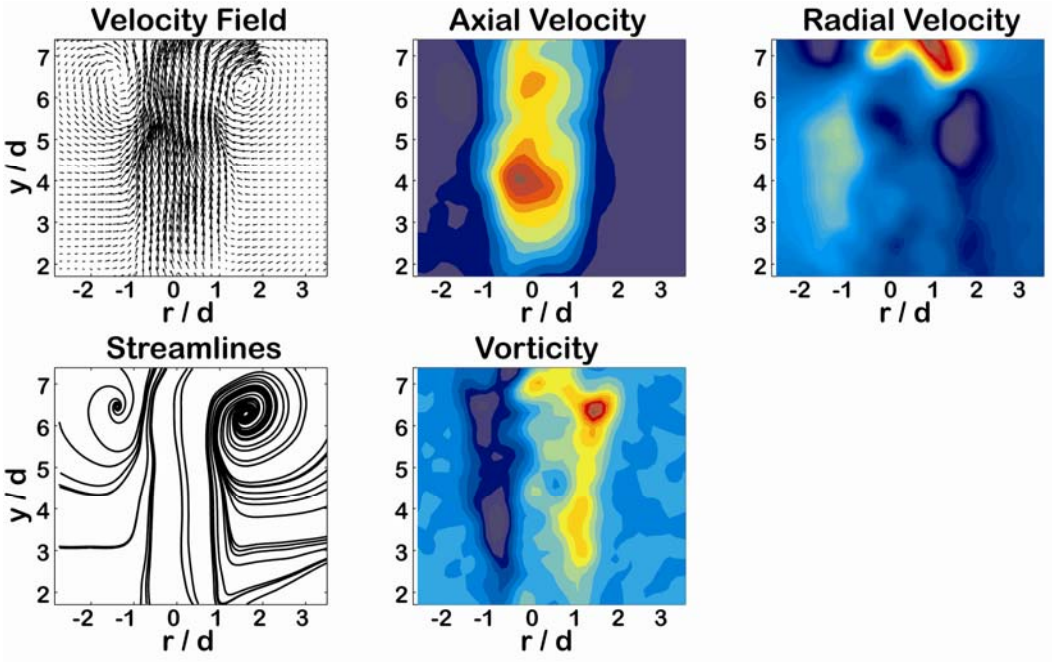

Figure 6.25. Time-averaged velocity for the ensemble from 0.14 - 0.35 s showing structures 1 (a) and 2 (b).

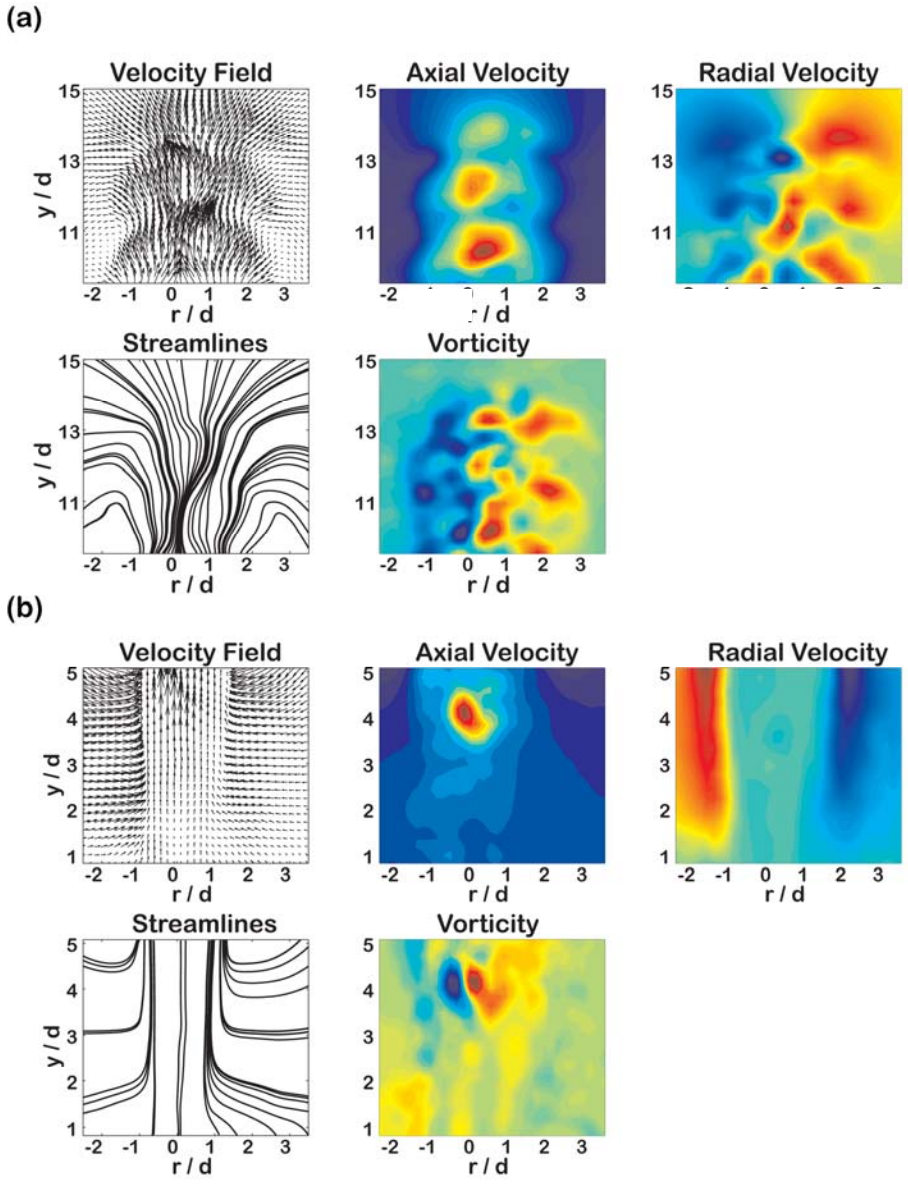

Figure 6.26. Time-averaged velocity for the single run from 0.42 - 0.56 s.

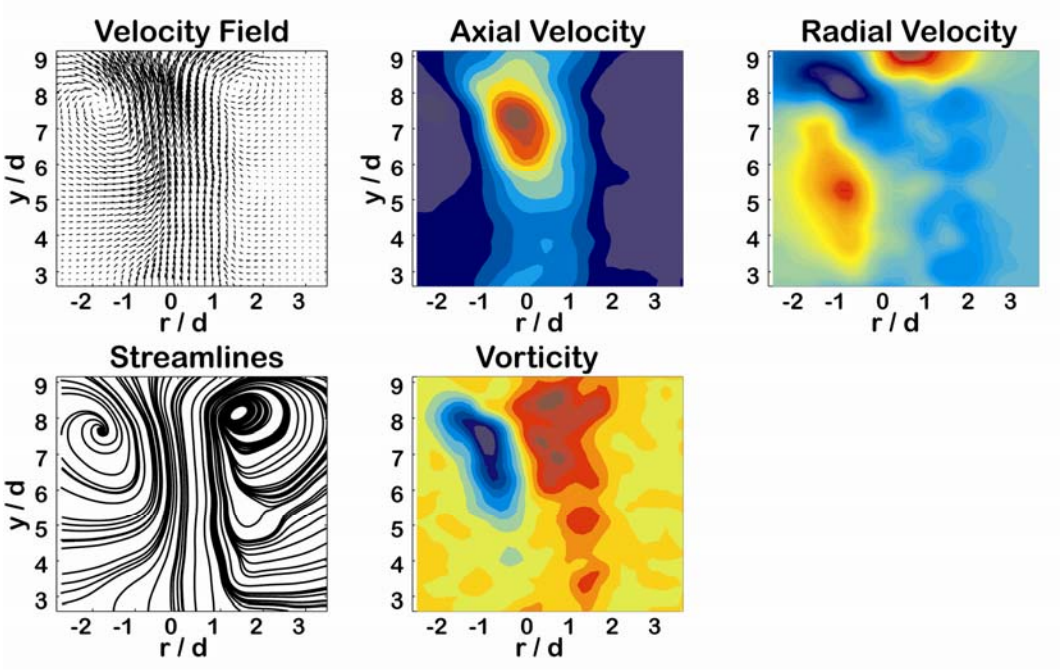

Figure 6.27. Time-averaged velocity for the ensemble from 0.42 - 0.56 s showing structures 1 (a) and 2 (b).

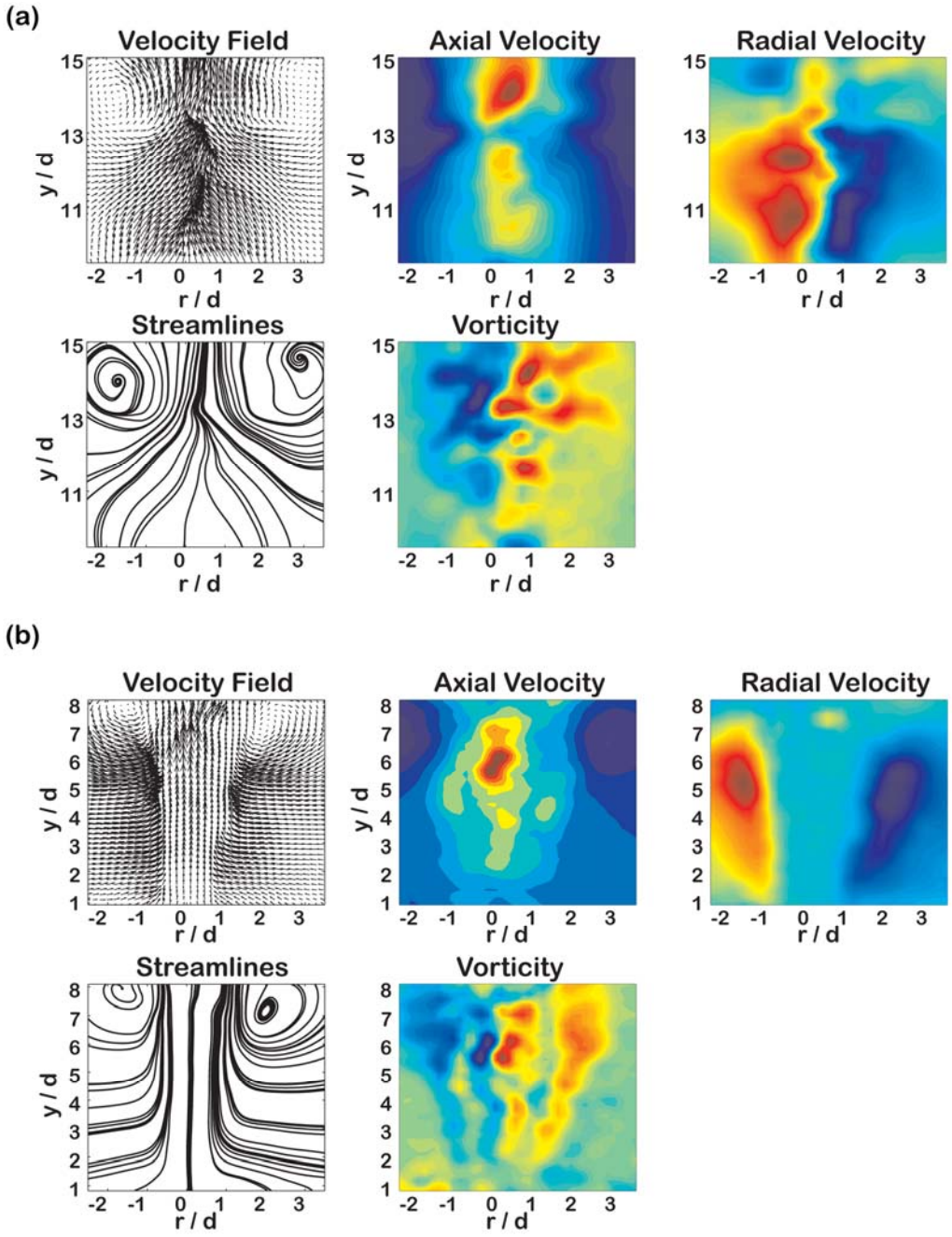

Figure 6.28. Time-averaged velocity for the ensemble from 0.56 s - 1.91 s.

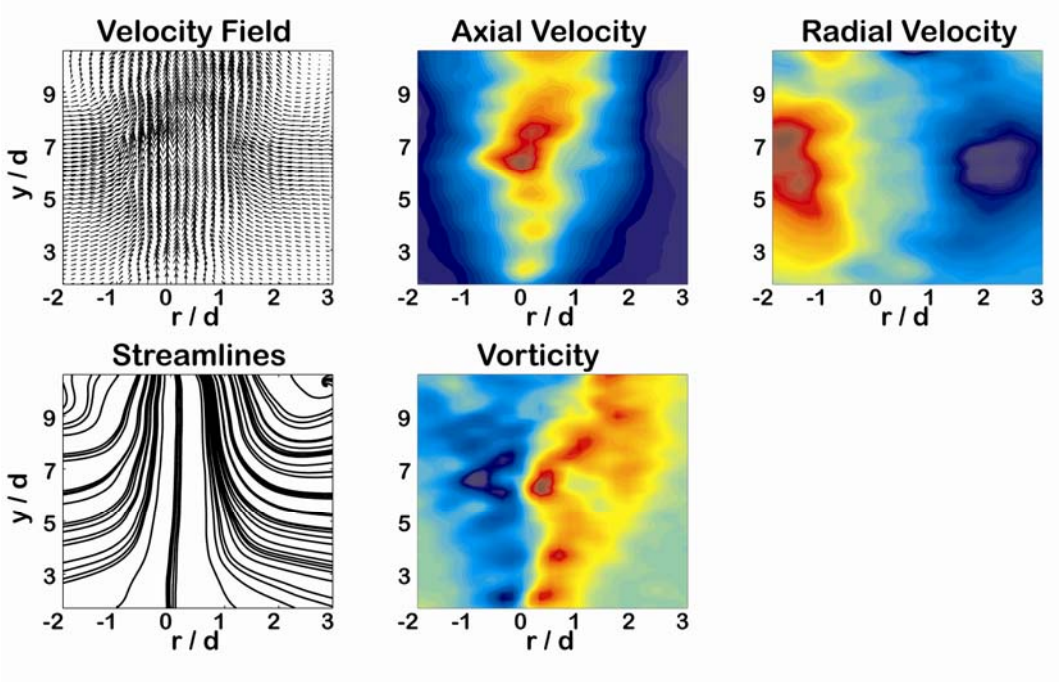

Table 6.1. Results from linear regression analysis

Condition	$a = h_0$	b	Norm of residuals	b/a	$\exp(-b/a) = t_0$	$V_0 = h_0/t_0$
H3	0.17	0.78	0.08	4.59	0.010	17.00
L3	0.15	0.67	0.14	4.47	0.013	11.54
H9	0.13	0.55	0.11	4.23	0.015	8.67
L9	0.10	0.43	0.06	4.30	0.015	6.67
H15	0.08	0.31	0.08	3.88	0.019	4.21
L15	0.06	0.22	0.08	3.67	0.024	2.50

Table 6.2: Spreading angle calculations for an individual 3-mm experiment (left column) and the ensemble average of images (right column).

t (s)	Individual	Ensemble
	Theta (degrees)	Theta (degrees)
0.05	9.1	15.0
0.10	11.5	15.0
0.30	11.7	12.9
0.50	9.7	14.0
1.00	11.2	14.6

Table 6.3: Spreading angle calculations for an individual 15-mm experiment (left column) and the ensemble average of images (right column).

t (s)	Individual	Ensemble
	Theta (degrees)	Theta (degrees)
0.05	9.4	17.3
0.10	12.4	14.4
0.30	15.6	15.4
0.50	12.7	12.9
1.00	12.5	19.7

Chapter 7

DISCUSSION AND CONCLUSION

7.1 Discussion

To understand the potential consequences of the time-varying momentum flux on volcanic plumes generated during short eruptions, I conducted a set of analogue experiments on turbulent laboratory jets with time-varying injection rates. I measured the injection characteristics and the resultant jet rise, spread, shape and internal velocity distributions as functions of time, for various source diameters, source Reynolds numbers and amounts of injected source fluid.

I found that unsteady jets evolve through a series of stages in which multiple large vortex structures are formed. These structures then evolve through the following sequence of dynamic phases: generation, motion, growth, self-similarity, dilution. Structures persist through the jet development and cause large indentations in the flow boundaries. These indentations are locations of increased entrainment in forming or destabilizing vortex structures. Each structure has a different amount of momentum, vorticity, circulation and volume such that each evolves independently to an asymptotic state that is similar to a puff. In this state, the remaining momentum and vorticity is broken down and dissipated from the outside of the structure to the center. Dissipation of the jet occurs until there is no distinguishable difference between the source and ambient fluids.

I then compared measurements of unsteady jet heights with predictions from steady similarity theory to assess the applicability of the theory to unsteady

conditions. Good agreement was found between starting jet theory and unsteady observations while the momentum flux was continuously increasing, and puff theory once the source ended; neither model captured the jet evolution in the deceleration phase. However, an unsteady scaling law, based on logarithmic rather than power law dependence between height and time, was able to capture unsteady jet behavior over the entire observation duration. Moreover, this scaling law collapsed the results from all experimental conditions to a single trend that was consistent with observations of a single, well-documented volcanic plume. This consistency lends confidence that the experiments capture first-order dynamics of short-lived volcanic plumes.

Measurements of the unsteady jet internal velocity distributions were compared with published distributions for steady source conditions in similar experiments. The comparison supports the interpretation from the external observations that the flows evolve over a sequence of stages from jet-like to puff-like behavior. The velocity fields also indicate that unsteady jet behavior is governed by large, coherent structures. Following the acceleration phase of the source, these structures continue to act as forming vortices and entrain ambient fluid by large-scale motions (engulfment). Once the source ends, these structures become fully formed and entrain fluid by small-scale motions (nibbling) before they break down and dissipate. The event sequence indicated by the internal velocity fields is supported by the evolution of the jet height; rapid changes in

height occur at the initiation of the flow and then change less rapidly as the source momentum flux decreases and eventually stops.

Buoyancy does not appear to modify unsteady jet velocities significantly for the flow conditions observed here as evidenced by the indistinguishable rise rates between the buoyant and non-buoyant unsteady jets. The internal velocity distributions of the buoyant jets are also similar to the non-buoyant jets. However, mixing is enhanced by the presence of positive buoyancy. This effect contributes to variations in the flow morphology and concentration dilution between buoyant and non-buoyant jets, without affecting the velocity distribution. Thus, this enhanced mixing must play a secondary role in the momentum dilution process in these unsteady jets. Alternatively, enhanced mixing may play a larger role in the dynamics of the jet when the jet fluid is much further from the source.

My findings suggest that momentum dissipation in unsteady jets with Gaussian-like injection histories differs from the behavior of experimental jets with constant injections and the predictions of steady theory. As turbulent mixing and entrainment were the only processes which can account for this discrepancy, I therefore conclude that the turbulent mixing and entrainment were influenced by the time-varying source conditions. Turbulent mixing, entrainment and momentum dissipation are fundamental and important controls for volcanic plume rise, transport and stability. My findings suggest all of these may be influenced by unsteady momentum fluxes in short-duration eruptions.

Additionally, these findings suggest at least two phases of development may occur for volcanic plumes with source durations that are less than their rise times. In the first phase, the evolution will depend directly on conditions at the source. The front of the flow will evolve variably in time, and the incorporation of ambient fluid may vary along with source conditions. Thus, studies intending to characterize plume evolution from eruption conditions should document the plume motion from initiation as well as through the evolution. During the second, source-off phase, the time-dependence of the source has no control on the dynamics and the flow will evolve dynamically toward a state expected from an instantaneous release, or a puff. Consequently, studies estimating discharge rates from plume heights should confine their estimates to the duration of the eruption.

Implications also exist for the Gaussian-like time history of the injection. The acceleration followed by a deceleration in momentum flux results in the growth of large vortex structures beyond the scales that would form for constant injection histories. At the bottom of these large structures, ambient fluid is entrained into the jet at a fast rate by large-scale motions. These motions extend all the way to the jet interior as indicated by the internal velocity fields. This observation has two consequences. First, the engulfed ambient fluid has low momentum relative to the jet fluid which means the flow has to expend momentum in order to impart momentum to the entrained fluid. Second, as these vortices are the same scale as the jet width, they represent the largest scales of the flow. These scales generally depend on the boundary conditions of the flow which

suggests that the boundary conditions control the entrainment process in jets with Gaussian-like injection histories.

This fact has important implications for flows which must achieve buoyancy reversal in order to prevent collapse. If the boundary conditions modify the large structures which form in the jet, then the stability of the jet may critically depend on these conditions, when the momentum flux has a Gaussian-like history. Under situations which support the formation and persistence of large scale structures, local regions of high entrainment may result. These regions may distort the boundary of the jet resulting in indentations that extend into the flow interior. This may enhance entrainment and mixing and thus, in turn, the process of buoyancy reversal. On the other hand, there may be situations where the boundary conditions prevent the formation or persistence of large-scale structures. In the absence of structures, the associated regions of high entrainment are also absent, and, therefore, jet buoyancy reversal may not be sufficient to avoid collapse during the deceleration phase.

In reality, the size and strength of the structures are changing in time due to their formation from the time-varying momentum flux. Each structure is imparted a unique amount of mass and momentum, allowing for the relative movement of structures. Thus, structures with large amounts of momentum can become increasingly separate from slower moving structures. This motion has implications for jet morphology and dynamics as well as their evolutions in time.

Furthermore, the decrease in jet velocity results in slower break-down rates and turn-over times for each structure, allowing for the large structure sizes.

Three features distinguished the unsteady lab jets: (1) a starting vortex structure at the flow front; (2) the breakdown of the flow into segments; and (3) the middle of the flow mixing more than the front or rear. I can therefore use these attributes as a guide when looking for evidence in volcanic plumes of unsteady momentum flux. Leading vortex structures can be readily observed in photographs and videos of plumes during eruption initiation, such as the images in Figure 1.1. However, evidence of the first structure separating is less common. I found at least one image where it appeared a second structure, in a two structure sequence, exhibited more mixing than the first [*Schraff et al*., 2012]. I also found at least one sequence of plume images where the plume appeared segmented beyond an identifiable first structure [*Mori and Burton*, 2009]. Consequently, these attributes are common to both the lab and natural plumes, suggesting they may be used to assess the source behavior from the plume observations.

Source flux changes could be detected by monitoring the jet rise behavior, according to steady theory. However, my findings suggest that the width of the plume and its velocity near the source will more accurately reflect changing momentum flux. This finding may provide a much more reliable criterion for monitoring changing source conditions. Additionally, the width near the vent changes relatively quickly in response to the changing source conditions (i.e., there is little delay), so width may provide the earliest warning that conditions are

changing. Severe changes in source flux or changes that persist for a sufficient amount of time will likely lead to observable changes in the plume behavior. On the other hand, some source flux changes may change in a way that allows the plume to adapt while the source is changing; therefore, one might not see the effects of time-varying source conditions in all plumes.

7.2 Conclusion

The relationship between source conditions and plume evolution is critical for developing accurate, as well as predictive, models of volcanic plumes. This relationship has not been established for short-duration eruptions with variable source conditions. I therefore undertook a laboratory investigation of turbulent jets to examine the role that time-dependent momentum flux plays in the generation and development of the resulting turbulent flows.

I generated turbulent single-pulsed jets in the laboratory by injecting pressurized water into a tank of still water. Injections were Gaussian-like in time with durations shorter than jet rise times. The injection was tested over a range of exit conditions corresponding to an order of magnitude change in vent Reynolds number (10^3-10^5), a parameter that characterizes the relative effects of inertia to viscous forces. These vent Reynolds numbers correspond to those expected for smaller volcanic plumes, which is the range of applicability for the results of this study. The evolution of the flow boundaries and the internal flow fields were investigated using experimental techniques, flow visualization and particle image velocimetry, respectively, best suited to each subject.

The evolution of turbulent flows from Gaussian initial conditions had three main phases of development − an injection phase which correlated with the source duration, a transition phase immediately following the source termination, and a final phase during which the source was off. The injection phase was further subdivided into two distinct sub-phases − acceleration and deceleration. Scaling of the results indicated that individual characteristic velocities dominated each of the acceleration, deceleration, and transition phases of the short-lived unsteady jet development. However, the final phase of development tended toward the behavior of a finite-volume release of momentum, or a puff. As such, it was determined that time-dependent source conditions have dominant first order effects on flow evolution during the injection and transition phases but had little control over dynamics during the final phase where the integrated total volume injected played a dominate role.

In addition to variable characteristic velocities, each flow phase had a unique velocity distribution. During the accelerating phase, the flow field reflected expansion of the source fluid into the ambient fluid and also indicated significant movement of the ambient fluid in front of the source fluid. During the decelerating phase, the flow field was dominated by two large-scale vortices at the front of the flow with multiple smaller scale vortices near the vent. The motion of the front of the large-scale vortices was consistent with expansion but the motion at their rear indicated significant movement of ambient fluid into the flow (entrainment) at that location. Motion of ambient fluid into the flow was also

observed for the smaller scale trailing vortices though at a much smaller scale. This flow pattern indicates that two types of ambient fluid entrainment operated during this phase: large-scale advective entrainment (engulfment) following the largest eddies and small-scale diffusive entrainment (nibbling) following the smaller eddies. Once the source was off, the flow was dominated by a large number of small- scale vortices. Evidence for small-scale diffusive entrainment was visible at the rear of the eddies at the flow boundaries.

The flow fields indicate the following sequence of events in the evolution of the flows: 1) Initially the high pressure of the source fluid causes it to expand vertically and radially into the ambient without entraining much ambient fluid. 2) Once the flowrate at the source starts to wane, the flow becomes unstable and begins breaking up into eddies of two main sizes: large-scale at the flow front and small-scale near the source. The flow simultaneously entrains a significant amount of ambient fluid though two different modes of entrainment associated with the two eddy sizes. 3) After the source ends, the flow becomes more unstable and begins to break into a large number of small eddies and then dissipates.

The sequence of events indicated by the internal velocity fields is supported by the evolution of the flow front where the flow front changes rapidly at the initiation of the flow and then continues to change less rapidly as the flowrate decreases and eventually stops. Once the source turns off the height evolves constantly in time according to theory for an instantaneous release of fluid. Scaling arguments indicate that height depends on the momentum injection

rate in the acceleration phase, then the cumulative momentum of the injection during the deceleration phase, and the total momentum injected once the source is off.

There are many implications of this work for the volcanic system. Most importantly there are at least two phases of development for plumes with source durations that are less than their rise times. In the first phase, the flow evolution will depend directly on conditions at the source and the front of the flow will evolve variably in time. During the second phase, the time-dependence of the source has no control on the dynamics and the flow will evolve dynamically as if it were driven by an instantaneous source. Therefore, plume dynamics record time-dependent source conditions only in the initial phases of eruptions. In other words, eruption initiation must be captured and well-characterized by studies intending to characterize plume evolution from initial conditions. Furthermore, vent characteristics must be well characterized at the same time that plume behavior is well-characterized if the intent is to relate the source and plume motion. Another implication is the limit of geophysical observations for use in predicting the magnitude or final rise height of a short-lived plume. The final rise height will depend on the total amount of momentum (and buoyancy among other potential variables) injected into the plume so this must be parameterized before total rise heights can be estimated. This model is expected to scale well to the natural system by comparison with an appropriate field data set that

simultaneously constrains vent and plume behavior in a calm ambient environment.

7.3 Future Work

The experiments presented here were conducted with insight provided by experiments I do not present in the previous chapters. This additional work is listed in Table 7.1 and was conducted for one of three main reasons: repeatability, optimization, and interpretation. Repeatable experimental conditions were necessary to generate experiments with nearly identical initial conditions. The initial pressure, vent opening style and buoyancy were all considered in developing the technique used here for repeatable results. I did not, however, systematically consider the role of the hose volume, injection duration or the smoothness of the injection curve. Each of these could be followed up in more detail. This work would greatly benefit from a comparison of these unsteady results with steady experimental results in the same apparatus. This would require a different style pump; the current pump pulses rather than deliver a constant flow rate. As the pump is one of the main features of the apparatus, it is likely that a pump change would also require a new repeatability test.

In addition to new tests, I recommend a few modifications to the existing setup for future work. I recommend installing a mesh screen between the valve and the pipe opening to remove swirl imparted to the flow by the passage through the tee upstream of the valve. This screen would act to break up the three dimensional swirl that causes motion into and out of the plane of the laser in the

PIV experiments. I also recommend and alternative chemical for use in generating buoyancy in the PIV experiments. This chemical should have an index of refraction closer to that of water so that better data can be collected for the buoyancy experiments. Also, to use the planar laser fluorescence capabilities of the lab, a new tank should be built that is made of a different side material. This material should not be tinted or scratch as easily as the current material. Furthermore, the plumbing into the tank should allow for interchangeable parts at the bottom. This would allow for cleaning of the plumbing as well as modifications to the outlet.

In addition to hardware modifications, I recommend some ways to optimize the data. These experiments evolve very quickly in time in the first second. Thus, if this is the time-scale of interest in future experiments, data should be collected at a faster rate than 100 samples per second. It would be interesting to test the Gaussian-like injection history for a broader range of positive and negative density fluids. Then, it would be good to test a different injection history curve and compare the results with the Gaussian-like injection history. This may be accomplished mechanically by adding an accumulator or a different type of injection system. Alternatively, a vent valve could be purchased with a mechanism that differs from a ball valve or one with a longer opening time. Finally, I recommend an investigation of the velocity near the exit plane of the pipe or orifice. This should provide more information on the controls of the length and time scales in the unsteady scaling law.

Table 7.1. Previous experiments

Date	Purpose	Data Description
2005-2006	Scaling law - some data featured in *Clarke et al*.[2009]	External jet behavior: video, flowmeter, particles, manual valve, Lab on 4th floor of PSH-Wing
2006-2007	PIV optimization – Redlake System	Mostly momentum only & mostly videos, various test conditions, not systematic
2008		135 momentum only, backlit, manual, Lab in basement of PSH-Wing
2009	Define repeatability in apparatus for ensemble averages in PIV data	opening experiments at different pressures with 3 and 15 mm vent diameters Manual vs automatic vent opening; flowmeter velocity vs jet velocity; positive vs negative vs neutral buoyancy; ~150 experiments over all conditions
2010	Dantec System: PIV data (Dissertation); 9 mm external and internal data	October 2010 – compilation of data for BMOMO_LOMO9mm (dye), BMIX_LOMO9mm (dye), MOMO_LOMO_9mm (PIV), flowmeter, height, video, which vent valve?
2011	External data (Featured Here); Other	January: ‘tests’ ~ 20; February: BMIX 1-5 video;
2012	External data for internal data interpretation	Open pipe, 39 runs, video, flowmeter, some height

REFERENCES

Adrian, R. J. (1991), Particle-imaging techniques for experimental fluid mechanics, *Annu. Rev. Fluid Mech.*, *23*, 261-304.

Adrian, R. J. and J. Westerweel (2011), *Particle Image Velocimetry*, 558 pp., Cambridge University Press, New York, New York.

Adrian, R. J. (1984) Scattering particle characteristics and their effect on pulsed laser measurements of fluid flow: speckle velocimetry vs. particle image velocimetry, *Appl., Opt., 23*, 1690 -1691.

Ai, J. J., S. C. M. Yu, A. W. Law, and L. P. Chua (2005), Vortex dynamics in starting square water jets, *Phys. Fluids*, *17*, 014106, doi:10.1063/1.1823532

Bernard, P. S., and J. M. Wallace (2002), *Turbulent flow: Analysis, measurement, and prediction*, 512 pp., Wiley, Hoboken, New Jersey.

Boree, J., N. Atassi, and G. Charnay (1996), Phase averaged velocity field in an axisymmetric jet subject to a sudden velocity decrease, *Exp. Fluids*, *21*, 447-456.

Bonadonna, C. and J. C. Phillips (2003), Sedimentation from strong volcanic plumes, *J. Geophys. Res., 108*, 2340, doi:10.1029/2002JB002034.

Bonadonna, C., J. C. Phillips, and B. F. Houghton (2005), Modeling tephra sedimentation from a Ruapehu weak plume eruption, *J. Geophys. Res., 110*, B08209, doi:10.1029/2004JB003515.

Bond, D., and H. Johari (2005), Effects of initial geometry on the development of thermals, *Exp. Fluids*, *39*, 589−599, doi:10.1007/s00348-005-0997-1.

Bond, D., and H. Johari (2010), Impact of buoyancy on vortex ring development in the near field, *Exp. Fluids*, *48*, 737 – 745.

Bluth, G. J. S., and W. I. Rose (2004), Observations of eruptive activity at Santiaguito volcano, Guatemala, *J. Volcanol. Geotherm. Res., 136*, 297 – 302.

Breidenthal, R. E. (2008), The effect of acceleration on turbulent entrainment, *Phys. Scr., T132*, 014001, doi:10.1088/0031-8949/2008/T132/014001.

Caplan-Auerbach, J., A. Bellesiles, and J. K. Fernandes (2010), Estimates of eruption velocity and plume height from infrasonic recordings of the 2006 eruption of Augustine Volcano, Alaska, *J. Volcanol. Geotherm. Res.*, *189*, 12 – 18.

Carazzo, G., E. Kaminski, and S. Tait (2008), On the dynamics of volcanic columns: A comparison of field data with a new model of negatively buoyant jets, *J. Volcanol. Geotherm. Res.*, *178*, 94–103.

Carey, S., and R. S. J. Sparks (1986), Quantitative models of the fallout and dispersal of tephra from volcanic eruption columns, *Bull. Volcanol.*, *48*, 109 – 125.

Calvari, S., R. Buttner, A. Cristaldi, P. Dellino, F. Giudiccpietro, M. Orazi, R. Peluso, L. Spampinato, B. Zimanowski, and E. Boschi (2012), The 7 September 2008 Vulcanian explosion at Stromboli volcano: Multiparametric characterization of the event and quantification of the ejecta, *J. Geophys. Res.*, *117*, B05201, doi:10.1029/2011JB009048.

Clarke, A. B., A. Neri, G. Macedonio, B. Voight, and T. H. Druitt (2002), Computational modeling of the transient dynamics of the August 1997 Vulcanian explosions at Soufriere Hills volcano, Montserrat influence of initial conduit conditions on near-vent pyroclastic dispersal, In: Druitt, T. H. & Kokelaar, B. P. (eds) *The Eruption of the Soufrière Hills Volcano, Montserrat, from 1995 to 1999. Geological Society, London, Memoirs* 21, 319–348.

Clarke, A. B., J. C. Phillips, and K. N. Chojnicki (2009), An investigation of Vulcanian eruption dynamics using laboratory analogue experiments and scaling analysis, From: Thordarson, T., Self, S., Larsen, G., Rowland, S. K. & Hoskuldsson, A. (eds) *Studies in Volcanology*: *The Legacy of George Walker.* Special Publications of IAVCEI. 2, 155–166. Geological Society, London.

Crow, S. C., and F. H. Champagne (1971), Orderly structure in jet turbulence, *J. Fluid Mech.*, *48*, 547 – 591.

Dobran, F., A. Neri, and G. Macedonio (1993), Numerical simulation of collapsing volcanic columns, *J. Geophys. Res.*, *98*, 4231 - 4259.

Donne, D. D., and M. Ripepe (2012), High-frame rate thermal imagery of Strombolian explosions: Implications for explosive and infrasonic source dynamics, *J. Geophys. Res.*, *117*, B09206, doi:10.1029/2011JB008987.

Diez, F. J., L. P. Bernal, and G. M. Faeth (2003), Round turbulent thermals, puffs, starting plumes and starting jets in uniform crossflow, *J. Heat Trans.*, *125*, 1046 – 1057.

Druitt, T. H., S. R. Young, B. Baptie, C. Bonadonna, E. S. Calder, A. B. Clarke, P. Cole, C. Harford, R. A. Herd, R. Luckett, G. Ryan, and B. Voight (2002), Episodes of repetitive Vulcanian explosions and fountain collapse at Soufrière Hills volcano, Montserrat. In: Druitt, T. H. & Kokelaar, B. P. (eds) *The Eruption of the Soufrière Hills Volcano, Montserrat, from 1995 to 1999. Geological Society, London, Memoirs* 21, 281–306.

Fischer, H. B., E. J. List, R. C. Y. Koh, J. Imberger, and N. H. Brooks (1979), *Mixing in Inland and Coastal Waters*, 483 pp., Academic Press, Inc., Orlando, Florida.

Formenti, Y., T. H. Druitt, and K. Kelfoun (2003), Characterisation of the 1997 Vulcanian explosions of Soufrière Hills volcano, Montserrat, by video analysis, *Bull. Volcanol.*, *65*, 587 – 605.

Gottsmann, J., S. De Angelis, N. Fournier, M. Van Camp, S. Sacks, A. Linde, M. Ripepe (2011), On the geophysical fingerprint of Vulcanian explosions, *Earth Planet. Sci. Lett.*, *306*, 98 – 104.

Ghaem-Maghami, E., and H. Johari (2010), Velocity field of isolated turbulent puffs, *Phys. Fluids*, *22*, 115105, doi:10.1063/1.3504378.

Gharib, M., E. Rambod, and K. Shariff (1998), A universal time scale for vortex ring formation, *J. Fluid Mech.*, *360*, 121–140.

Gouhier, M., and F. Donnadieu (2008), Mass estimations of ejecta from Strombolian explosions by inversion of Doppler radar measurements, *J. Geophys. Res.*, *113*, B10202, doi:10.1029/2007JB005383.

Gilbert, J. S., and S. Lane (2012), The consequences of fluid motion in volcanic conduits, In: Lane, S. J. & Gilbert, J. S. (eds) *Fluid Motions in Volcanic Conduits: A Source of Seismic and Acoustic Signals. Geological Society, London, Special Publications, 307*, 1-10, doi:10.1144/SP307.1

Hermanson, J. C., R. Dugnani, and H. Johari (2000), Structure and flame length of fully-modulated, turbulent diffusion flames, *Combust. Sci. Tech.*, *155*, 203 - 205, doi:10.1080/00102200008947290.

Hort, M., and R. Seyfried (1998), Volcanic eruption velocities measured with a micro radar, *Geophys. Res. Lett.*, *25*, 113 – 116.

Hu, B., M. P. B. Musculus, and J. C. Oefelein (2012), The influence of large-scale structures on entrainment in a decelerating transient turbulent jet revealed by large eddy simulation, *Phys. Fluids, 24*, 045106, doi:10.1063/1.3702901.

Hussain, F., and H. S. Husain (1989), Elliptic jets. Part 1. Characteristics of unexcited and excited jets, *J. Fluid Mech., 208*, 257 – 320.

Iguchi, M., H. Yakiwara, T. Tameguri, M. Hendrasto, and J. Hirabayashi (2008), Mechanism of explosive eruption revealed by geophysical observations at the Sakurajima, Suwanosejima and Semeru volcanoes, *J. Volcanol. Geotherm. Res., 178*, 1-9.

Johari, H., and R. Paduano (1997), Dilution and mixing in an unsteady jet, *Exp. Fluids, 23*, 272 – 280.

Johnson, J., M. C. Ruiz, J. M. Lees, and P. Ramon (2005), Poor scaling between elastic energy release and eruption intensity at Tungurahua Volcano, Ecuador, *Geophys. Res. Lett., 32*, L15304, doi:10.1029/2005GL022847.

Kaminski, E., S. Tait, and G. Carazzo (2005), Turbulent entrainment in jets with arbitrary buoyancy, *J. Fluid Mech., 526*, 361– 376.

Kaminski, E., S. Tait, F. Ferrucci, M. Martet, B. Hirn, and P. Husson (2011), Estimation of ash injection in the atmosphere by basaltic volcanic plumes: The case of the Eyjafjallajokull 2010 eruption, *J. Geophys. Res., 116*, B00C02, doi:10.1029/2011JB008297.

Kieffer, S. W. (1982) Fluid dynamics of the May 18 blast at Mount St. Helens, *U.S. Geol. Surv. Prof. Pap. 1250*, 379 - 400.

Kieffer, S. and B. Sturtevant (1984), Laboratory Studies of Volcanic Jets, *J. Geophys. Res., 89*, B10, 8253-8268.

Kitamura, S., and I. Sumita (2011), Experiments on a turbulent plume: Shape analyses, *J. Geophys. Res., 116*, B03208, doi:10.1029/2010JB007633.

Kouros, H., R. Medina, and H. Johari (1993), Spreading rate of an unsteady turbulent jet, *AIAA J., 31*, 1524-1526.

Kovasznay, L. S. G., H. Fujita, and R. L. Lee (1975), Unsteady turbulent puffs, *Adv. Geophys., 18*, 253-263.

Krueger, P. S. (2005), An over-pressure correction to the slug model for vortex ring circulation, *J. Fluid Mech.*, *545*, 427-443, doi:10.1017/S0022112005006853.

Lyons, J. J., G. P. Waite, W. I. Rose, G. Chigna (2009), Patterns in open vent, strombolian behavior at Fuego volcano, Guatemala, 2005-2007, *Bull. Volcanol.*, *72*, 1-15, doi:10.1007/s00445-009-0305-7.

Marchetti, E., M. Ripepe, A. J. L. Harris, and D. D. Donne (2009), Tracing the differences between Vulcanian and Strombolian explosions using infrasonic and thermal radiation energy, *Earth Planet. Sci. Lett.*, *279*, 273−281.

Mastin, L. G., et al. (2009), A multidisciplinary effort to assign realistic source parameters to models of volcanic ash-cloud transport and dispersion during eruptions, *J. Volcanol. Geotherm. Res.*, *186*, 10–21, doi:10.1016/j.jvolgeores.2009.01.008.

Matoza, R. S., D. Fee, M. A. Garces, J. M. Seiner, P. A. Ramon, and M. A. H. Hedlin (2009), Infrasonic jet noise from volcanic eruptions, *Geophys. Res. Lett.*, *36*, L08303, doi:10.1029/2008GL036486.

Maxworthy, T. (1972), The structure and stability of vortex rings, *J. Fluid Mech.*, *51*, 15–32.

Mays, L. W. (1999) *Hydraulic design handbook*, 1024 pp., McGraw-Hill, New York.

Mi, J., G. J. Nathan, and D. S. Nobes (2001), Mixing characteristics of axisymmetric free jets from a contoured nozzle, an orifice plate, and a pipe, *J. Fluid Eng., Trans. ASME*, *123*, 878 – 883, doi:10.1115/1.1412460.

Morton, B. R., G. I. Taylor, and J. S. Turner (1956), Turbulent gravitational convection from maintained and instantaneous sources, *Proc. R. Soc. London, Ser. A*, *234*, 1–23.

Mori, T., and M. Burton (2009), Quantification of the gas mass emitted during single explosions on Stromboli with the SO2 imaging camera, *J. Volcanol. Geotherm. Res.*, *188*, 395 – 400. doi:10.1016/j.jvolgeores.2009.10.005.

Musculus, M. P. B. (2009), Entrainment waves in decelerating transient turbulent jets, *J. Fluid Mech.*, *638*, 117 – 140.

Nadeau, P. A., J. L. Palma, and G. P. Waite (2011), Linking volcanic tremor, degassing, and eruption dynamics, *Geophys. Res. Lett., 38,* L01304, doi:10.1029/2010GL045820.

Neri, A. and G. Macedonio (1996), Numerical simulation of collapsing volcanic columns with particles of two sizes. *J. Geophys. Res., 101,* 8153 - 8174.

Newhall, C. and S. Self (1982), The Volcanic Explosivity Index (VEI): An estimate of explosive magnitude for historical volcanism, *J. Geophys. Res., 87,* 1231-1238.

Nishimura, T., M. Iguchi, R. Kawaguchi, Surono, M. Hendrasto, and U. Rosadi (2012), Inflations prior to Vulcanian eruptions and gas bursts detected by tilt observations at Semeru Volcano, Indonesia, *Bull. Volcanol., 74,* 903-911, doi:10.1007/s00445-012-0579-z.

Olcay, A. B. and P. S. Krueger (2008), Measurement of ambient fluid entrainment during laminar vortex ring formation, *Exp. Fluids, 44,* 235–247.

Ogden, D. E., G. A. Glatzmaier, and K. H. Wohletz (2008), Effects of vent overpressure on buoyant eruption columns: Implications for plume stability, *Earth Planet. Sci. Lett., 268,* 283 - 292.

Ogden, D. (2011), Fluid dynamics in explosive volcanic vents and craters, *Earth Planet. Sci. Lett., 312,* 401-410.

Papanicolaou, P. N., and E. J. List (1988), Investigations of round vertical turbulent buoyant jets, *J. Fluid Mech., 195,* 341−391.

Patrick, M. R. (2007a), Dynamics of Strombolian ash plumes from thermal video: Motion, morphology, and air entrainment, *J. Geophys. Res., 112,* B06202, doi:10.1029/2006JB004387.

Patrick, M. R. (2007b), The gas content and buoyancy of strombolian ash plumes, *J. Volcanol. Geotherm. Res., 166,* 1-6.

Peterson, G. N., H. Bjornsson, and P. Arason (2012), The impact of the atmosphere on the Eyjafjallajökull 2010 eruption plume, *J. Geophys. Res., 117,* D00U07, doi:10.1029/2011JD016762.

Querzoli, G., M. Falchi, and G. P. Romano (2010), On the flow field generated by a gradually varying flow through an orifice, *Euro. J. Mech. B/Fluids, 29,* 259 - 268. doi:10.1016/j.euromechflu.2010.03.004.

Richards, J. M. (1965), Puff motions in unstratified surroundings, *J. Fluid Mech*., *21*, 97 – 106, doi:10.1017/S002211206500006.

Ripepe, M., M. Rossi, and G. Saccorotti (1993), Image processing of explosive activity at Stromboli, *J. Volcanol. Geotherm. Res*., *54*, 335 – 351.

Ruiz, L. A., R. W. Whittlesley, and J. O. Dabiri (2011), Vortex-enhanced propulsion, *J. Fluid Mech*., *668*, 5 – 32, doi:10.1017/S0022112010004908.

Sangras, R., O. C. Kwon, and G. M. Faeth (2002), Self-preserving properties of unsteady round non-buoyant turbulent starting jets and puffs in still fluids, *J. Heat Trans*., *124*, 460 – 469, doi: 10.1115/1.1421047.

Sahetapy-Engel, S. T. and A. J. L. Harris (2009), Thermal-image-derived dynamics of vertical ash plumes at Santiaguito volcano, Guatemala, *Bull. Volcanol*., *71*, 827-830, doi:10.1007/s00445-009-0284-8.

Scase, M. M. (2009), Evolution of volcanic eruption columns, *J. Geophys. Res*., *114*, F04003, doi:10.1029/2009JF001300.

Scharff, L., M. Hort, A. J. L. Harris, M. Ripepe, J. M. Lees, and R. Seyfried (2008), Eruption dynamics of the SW crater of Stromboli volcano, Italy – An interdisciplinary approach, *J. Volcanol. Geotherm. Res*., *176*, 565 – 570. doi:10.1016/j.jvolgeores.2008.05.008.

Seo, I. W., S. Lyu, and Y. S. Park (2002), Experimental investigation of the velocity and turbulent structures of turbulent jets using PIV, In: H. Ninokata, A. Wada, and N. Tanaka (eds) *Advances in fluid modeling and turbulence measurements*, World Scientific, New Jersey, 185-192.

Soteriou, M. C., Y. Dong, and B. M. Cetegen (2002), Lagrangian simulation of the unsteady near field dynamics of planar buoyant plumes, *Phys. Fluids*, *14*, 3118, doi:10.1063/1.1491248.

Solovitz, S. A. and L. G. Mastin (2009), Experimental study of near-field air entrainment by subsonic volcanic jets, *J. Geophys. Res*., *114*, B10203, doi:10.1029/2009JB006298.

Sparks, R. S. J., and L. Wilson (1976), A model for the formation of ignimbrite by gravitational column collapse, *J. Geol. Soc. Lond*., *132*, 441 – 451.

Sparks, R. S. J., and L. Wilson (1982), Explosive volcanic eruptions – V. Observations of plume dynamics during the 1979 Soufriere eruption, St. Vincent, *Geophys. J. R. Astr. Soc*., *69*, 551 – 570.

Sparks, R. S. J., M. I. Bursik, S. N. Carey, J. S. Gilbert, L. S. Glaze, H. Sigurdsson, and A. W. Woods (1997), *Volcanic Plumes*, 524 pp., John Wiley, Chichester, U. K.

Suzuki, Y. J., T. Koyaguchi, M. Ogawa, and I. Hachisu (2005), A numerical study of turbulent mixing in eruption clouds using a three-dimensional fluid dynamics model, *J. Geophys. Res.*, *110*, B08201, doi:10.1029/2004JB003460.

Suzuki, Y. J. and T. Koyaguchi (2010), Numerical determination of the efficiency of entrainment in volcanic eruption columns, *Geophys. Res. Lett.*, *37*, L05302, doi:10.1029/2009GL042159.

Terada, A. and Y. Ida (2007), Kinematic features of isolated volcanic clouds revealed by video records, *Geophys. Res. Lett.*, *34*, L01305, doi:10.1029/2006GL026827.

Tupper, A., C. Textor, M. Herzog, H. Graf, and M. S. Richards (2009), Tall clouds from small eruptions: the sensitivity of eruption height and fine ash content to tropospheric instability, *Nat. Hazards*, *51*, 375 – 401, doi:10.1007/s11069-009-9433-9.

Turcotte, D. L., H. Ockendon, J. R. Ockendon, and S. J. Cowley (1990), A mathematical model of Vulcanian eruptions. *Geophys. J. Int.*, *103*, 211-217.

Turner, J. S. (1962), The ‘starting plume’ in neutral surroundings, *J. Fluid Mech.*, *13*, 356 – 358.

Turner, J. S. (1986), Turbulent entrainment: The development of the entrainment assumption, and its application to geophysical flows, *J. Fluid Mech.*, *173*, 431−471, doi:10.1017/S0022112086001222.

Valentine, G. (1998), Eruption column physics, In *From Magma to Tephra : Modeling Physical Processes of Explosive Volcanic Eruptions*, edited by A. Freundt and M. Rosi, pp. 318, Elsevier, Amsterdam; New York.

Valentine, G. A. and K. H. Wohletz (1989), Numerical models of Plinian eruption columns and pyroclastic flows, *J. Geophys. Res.*, *94*, 1867-1887.

Valentine, G. A., K. H. Wohletz, and S.W. Kieffer (1991) Sources of unsteady column dynamics in pyroclastic flow eruptions, *J. Geophys. Res.*, *96*, *21*,887 – 21,892.

Walker, G. P. L. (1973), Explosive Volcanic Eruptions - a new classification scheme, *Geol. Rundsch., 62*, 431-446.

Watson, I. M., V. J. Realmuto, W. I. Rose, A. J. Prata, G. J. S. Bluth, Y. Gu, C. E. Bader, and T. Yu (2004), Thermal infrared remote sensing of volcanic emissions using the moderate resolution imaging spectroradiometer, *J. Volcanol. Geotherm. Res., 135*, 75 − 89, doi:10.1016/j.jvolgeores.2003.12.017.

Wilson, L., R. S. J. Sparks, T. C. Huang, and N. D. Watkins (1978), The control of volcanic column heights by eruption energetics and dynamics, *J. Geophys. Res., 83*, 1829– 1836.

Williams, S. N. (1983), Plinian airfall deposits of basaltic composition, *Geology, 11*, 211-214, doi: 10.1130/0091-7613(1983)11.

Wilson, L. and Self, S. (1980), Volcanic explosion clouds: density temperature and particle content estimates from cloud motion. *J. Geophys. Res., 85*, 2567-2572.

Woods, A. W. (1988), The fluid dynamics and thermodynamics of eruption columns, *Bull. Volcanol., 50*, 169 – 193.

Woods, A. W. (1995), A model of vulcanian explosions, *Nuclear Engineering and Design, 155*, 345-357.

Yamamoto, H., I. M. Watson, J. C. Phillips, and G. J. Bluth (2008), Rise dynamics and relative ash distribution in vulcanian eruption plumes at Santiaguito Volcano, Guatemala, revealed using an ultraviolet imaging camera, *Geophys. Res. Lett., 35*, L08314, doi:10.1029/2007GL032008.

S. C. M. Yu, A. W. Law, and J. J. Ai (2007), Vortex formation process in gravity-driven starting jets, *Exp. Fluids, 42*, 783–797.

Zhang, Q. and H. Johari (1996), Effects of acceleration on turbulent jets, *Phys. Fluids, 8*, 2185 - 2195.